ELECTROCHEMICAL IMPEDANCE SPECTROSCOPY EXPERIMENTS, ANALYSIS AND MODELS FOR NEURAL–STIMULATION ULTRAMICROELECTRODES

By

CYNTHIA CHIAMAKA ELUAGU

A DISSERTATION PRESENTED TO THE GRADUATE SCHOOL
OF THE UNIVERSITY OF FLORIDA IN PARTIAL FULFILLMENT
OF THE REQUIREMENTS FOR THE DEGREE OF
DOCTOR OF PHILOSOPHY

UNIVERSITY OF FLORIDA

2025

To my parents, Bernard and late Theresa, my husband, Innocent, and my daughter, Oluomachi

ACKNOWLEDGEMENTS

I am thankful to God for his grace, blessings, and the gift of life that carried me through my doctoral studies. My sincere appreciation goes to my advisor, Professor Mark E. Orazem, for his invaluable support, advice, teaching, encouragement, ideas and expertise, during my doctoral studies. I am forever grateful for his recommendations, peer-review referrals, internship support, and the honour to work under his guidance and supervision.

Many thanks to my committee members, Professor Kevin J. Otto, Professor Won Tae Choi, and Professor Sumant Patankar for their support, ideas and guidance. I thank my research collaborators, Professor Stuart Cogan, Jamille Hetke, Qiwei, Elizabeth, Xander, and Yupeng for the time we spent together and the ideas that fostered the project.

I am especially grateful to my former labmates, Dr. You, Dr. Jacobs, Jammy Goh, Kelsey Sinclair, and Henry Lutz for their help and support at the early stage of my research. I extend my sincere appreciation to my current group members Yunhan Chuai, and Bernard Biney for their company and support. I express my gratitude to my former undergraduate mentee, Taskina Gui and my current mentee, Daniel Avalos for their assistance in modeling and analysis. I appreciate Mrs. Jennifer Peterson for her care and support.

I remain forever grateful to my loving husband, Innocent for his love, care and support in both good and bad times of my doctoral journey. I owe all my achievements to my husband, and will prove how much that means to me for the rest of my life with him. I appreciate my lovely daughter, Oluomachi for her sweet smiles that makes life beautiful. To my late mum, Theresa, forever grateful for her love and strength throughout this journey. To my amazing dad, Bro. Bernard, thanks for giving me the opportunity to have good education. I remain forever grateful to him. I thank my elder brother, Bonaventure for his support and guidance.

This work was supported by the National Institute of Health (NIH) under the UO1NS126052-01 “Engineering the Neural Response to Electrical Microstimulation”. The electrodes were custom-designed and manufactured by the NeuroNexus Company.

TABLE OF CONTENTS

page

LIST OF TABLES

LIST OF FIGURES

LIST OF ABBREVIATIONS

Roman

$_i$ electrode constants related to inverse Tafel slope

capacitance

$_{eff}$ effective capacitance

$_i$ concentration of species i

eff effective resistance

$_{eff}$ effective capacitance

f frequency

F Fardays Constant

f_c characteristic frequency

$_C$ charging current

$_F$ faradaic current density for reaction i

j imaginary number

$_i$ faradaic current density for reaction i

$_i$ heterogeneous rate constant for reaction i

$_i$ homogenous rate constant for reaction i

number of electrons exchanged for heterogeneous reaction

$_i$ flux for species i

CPE parameter

$_d$ diffusion resistance

$_e$ electrolyte resistance

$_i$ homogenous reaction rate for reaction i

$_t$ charge transfer resistance

time

double layer potential

$_{max}$ Maximum reaction velocity at excess substrate concentration

distance from electrode

impedance

$_F$ faradaic impedance

$_i$ ionic charge of species i

Greek

-1/ ' dimensionless diffusion impedance

CPE phase angle modifer

dielectric constant

$_o$ permtiviity of vacuum, 8.854×10^{-14} F/cm

Γ_i surface concentration of species i

Γ_T total surface concentration

Debye length

angular frequency

Φ potential

phase angle

frequency dependent variation of impedance

time constant

Subscript

j imaginary component of variable

ox oxidized form of species

m electrode

r real part of variable

ref reference

General

Im{ } imaginary part of

Re{ } real part of

$\bar{}$ steady-state of variable

$\tilde{}$ phasor of variable

Abstract of Dissertation Presented to the Graduate School
of the University of Florida in Partial Fulfillment of the
Requirements for the Degree of Doctor of Philosophy

ELECTROCHEMICAL IMPEDANCE SPECTROSCOPY EXPERIMENTS, ANALYSIS AND MODELS FOR NEURAL–STIMULATION ULTRAMICROELECTRODES

By

Cynthia Chiamaka Eluagu

December 2025

Chair: Mark E. Orazem
Major: Chemical Engineering

The objective of the present work was to identify the electrochemical properties of sputtered iridium oxide (SIROF) ultramicroelectrodes intended for neural stimulation. Ultramicroelectrodes (UMEs) are designed at sizes comparable to neuronal somas to enhance spatial selectivity, reduce tissue encapsulation, and improve long-term stability during neural stimulation and recording. Their reduced surface area result in high impedance, susceptibility to noise, and variability in signal quality. The interfacial reactions between these electrodes and electrolyte/tissue can be characterized using electrochemical impedance spectroscopy (EIS).

Through in vitro impedance spectroscopy measurements, a physical model was identified that accounted for an ohmic resistance, the mass transfer-influenced faradaic reduction of oxygen, the capacitive behavior of the SIROF electrode that accounted for time-constant dispersion, and the oxidation and reduction of iridium. Regression of the model to impedance data required consideration of the parasitic capacitance associated with the contribution of cables and connectors to the impedance response. Accuracy contour plots were used to evaluate the high-impedance and low-impedance limitations of the potentiostat and the influence of hardware connectors on the electrode’s impedance. The accuracy contour plots were obtained by measuring the impedance of open-lead and shorted-lead configurations associated with the electrochemical systems under study.

The model parameters were used to guide development of a mathematical model for the transient response of ultramicroelectrodes to current pulses consistent with those used for neural stimulation. The Laplace's equation was incorporated to account for variations of potential in the electrolyte. Finite element method (FEM) simulations of mass-transfer influenced faradaic reactions on the impedance response of ultramicroelectrodes revealed the effects of geometry-induced non-uniform current and potential distributions on the impedance spectra.

CHAPTER 1
INTRODUCTION

Neural stimulation is widely employed in the treatment of neurological disorders such as Parkinson's disease, essential tremor, epilepsy, paralysis, stroke, and depression. Brain-stimulation systems consist of implanted electrodes, a pulse generator, and connecting leads, integrated to deliver controlled electrical pulses to targeted neural regions. Traditional macroelectrodes can stimulate large populations of neurons; however, certain neurological disorders require higher-precision stimulation and spatial selectivity achievable with microelectrodes and ultramicroelectrodes. The performance of these devices is governed by electrode–tissue interfacial reactions, which can be characterized through electrochemical impedance spectroscopy (EIS). EIS is a non-invasive tool applied since the early 1960's to evaluate the impedance behavior of neural-stimulation electrodes, providing insights into the electrode stability, and capacitive behavior.

The effectiveness of neural-stimulation microelectrodes (with geometric surface areas of 100 to 1000 m^2) and ultramicroelectrodes (with geometric surface areas (GSA) of 20 to 80 m^2) depends on their ability to deliver both capacitive and faradaic currents during stimulation, without undergoing degradation. Electrochemical impedance spectroscopy is therefore required to characterize the interfacial reactions, electrode capacitance, and tissue response. The objective of this work was to evaluate the performance of high-density (HD) multi-electrode arrays (MEAs) and ultramicroelectrode arrays (UMEAs) with unique sites and materials, through impedance spectroscopy measurements, measurement model analysis, and process modeling of electrochemical reactions at the electrode/electrolyte interface. The analysis was coupled with finite-element modeling (FEM) of impedance, current flow and transient electrochemical responses during stimulation, to predict the influence of design parameters on the electrode sizes and function.

Electrochemical impedance spectroscopy describes the electrode, electrolyte, and electrode-tissue interface in terms of resistive elements, capacitance and mass-transfer reactions. The technique has been employed in neural stimulation for over 25 years, to evaluate changes in

electrode's impedance due to encapsulation, and establish safe charge-injection limits for device performance. EIS fits equivalent electrical circuits to experimental data to characterize the physical or chemical processes within the electrochemical system. The overview of neural stimulation, EIS applications to neural stimulation, review of neural electrodes, rudimentary use, and recent advances of EIS in neural applications are discussed in Chapter 2. The theory and key fundamentals of electrochemical impedance spectroscopy, and analysis of impedance spectra are introduced in Section 2.5 of Chapter 2.

The design and fabrication methods for the electrode devices evaluated are presented in Chapter 3. Three generations of electrode arrays (generation 1 to generation 3 (G1-G3)) manufactured by NeuroNexus were analyzed along with platinum disk ultramicroelectrodes. The impedance spectroscopy measurements were performed for the generation 1 (G1) devices in both in vitro and in vivo environments. The impedance spectra obtained from in vivo and in vitro experiments were analyzed through the measurement model to extract key electrode parameters, which were used to estimate capacitance and guide improvements in the impedance modeling of subsequent generations (G2 and G3) in phosphate-buffered saline.

Accuracy contour plots for the evaluation of usable frequency and impedance range of experimental data are discussed in Chapter 4. Electrochemical systems inherently combine contributions from the electrode, potentiostat, and connectors. Cables introduce additional parasitic capacitance, especially at high frequencies, which can distort the impedance measurement. Accuracy contour measurements were performed to systematically map the domains where impedance data can be acquired within specified accuracy limits. By visualizing the frequency limits where accurate impedance measurements are possible and identifying regions affected by instrumental artifacts or cable capacitance, accuracy contour plots provide guidance for interpreting impedance spectra and optimizing electrochemical setup.

Experimental methods for the characterization of electrode devices are presented in Chapter 5. This includes the impedance spectroscopy measurements, measurement modeling approach, measurement limitations, and solutions to current-range issues. Impedance

measurements apply a small-amplitude voltage or current perturbation to the electrochemical system across a wide frequency range and measures the systems sinusoidal response (current or voltage). The measurement enables the distinction between resistive, capacitive (charge-transfer), and faradaic contributions to the electrode impedance, which is crucial for optimizing stimulation parameters [1]. Capacitive reactions include redistribution of charged chemical species in the electrolyte, while, faradaic reactions allow the transfer of electrons between the electrode and electrolyte, resulting in reduction or oxidation of chemical species in the electrolyte [2].

Interpretation of impedance response requires the regression of a measurement model and a mechanistic model that describes the physical and chemical processes in the system. The measurement model developed by Agarwal et al.[3, 4] was used to quantify the stochastic error structure from replicated impedance data, and assess the consistency with the Kramers–Kronig relations. Goh et al.[5] showed that Kramers–Kronig relations is used to evaluate the conditions of linearity and stationarity of EIS measurements. Frequency points affected by external phenomena were removed. This includes parts of data inconsistent with the Kramers–Kronig relations or may be corrupted by measurement transients, particularly at high frequencies. Analysis and interpretation of impedance spectra for the high-density microelectrode array (generation 1 (G1)) is presented in Chapter 6. The model accounted for the mass-transfer influenced oxygen-reduction reactions and the constant-phase element behavior of the electrode.

The impedance spectroscopy behavior of the high-density ultramicroelectrode arrays (generation 2) is discussed in Chapter 7. The process model was selected to account for physical phenomena, and for parasitic capacitance if necessary. The electrode capacitance is estimated from regression results based on the assumption that the constant-phase-element (CPE) behavior arises from a surface distribution of time constants. Impedance spectroscopy characteristics of the ultra-thin high-density microelectrode arrays (generation 3) in phosphate-buffered saline is discussed in Chapter 8. Two process models were formulated to interpret the impedance response between porous and rough electrodes. Both models accounted for the constant-phase-element

characteristics of the electrode, the changes in iridium oxidation state, and the effects of parasitic capacitance at high frequency points.

The impedance response of platinum-disk ultramicroelectrodes are discussed in Chapter 9. Linear sweep voltammetry and polarization measurements were used to evaluate the steady-state and transient response of platinum electrodes in phosphate-buffered saline. The interpretation model accounted for the faradaic reactions in the system and the capacitive behaviour consistent with distribution of time constants along the surface of the electrodes.

Stimulation by ultramicroelectrodes is envisioned to enable precise control for activation of the target neural population. While not a direct representation of the stationary electrodes used for neural stimulation, the rotating disk electrode (RDE) geometry has the advantage of well-defined mass transfer characteristics for modeling electrochemical reactions at the electrode-electrolyte interface. Finite-element method (FEM) simulations of current and potential distributions and transient electrochemical responses on a rotating disk electrode geometry are presented in Chapter 10. The model guided development of more specific models for neural stimulation. The model accounted for the cathodic reduction of oxygen reaction on the surface of the electrode and the influence of mass transfer. Laplace's equation was used to account for variation of potential in the electrolyte.

Finite element method (FEM) simulations of mass transport effects on non-uniform potential and current distribution and the impedance response to the disk electrodes are discussed in section 10.4 of Chapter 10. You et al.[6] published the experimental observation for ohmic impedance. The present work adapt You's model to study the mass-transfer influenced Oxygen-reduction reaction and oxidation of Ferrocyanide on the impedance and ohmic impedance of disk electrode. Conclusion is presented in Chapter 11 and suggestions for future work are discussed in Chapter 12.

CHAPTER 2
BACKGROUND

2.1 Neural Stimulation

Neurological disorders such as epilepsy, Parkinson's disease, stroke, dementia, are leading global health challenges. Over the last three decades, the prevalence of brain disorders has surged by 65%, rising from approximately 2 billion cases in 1990 to 4 billion cases in 2021 [7]. In the United States alone, about 6.9 million adults aged 65 and older have Alzheimer's dementia as of 2024 [8]. These figures emphasize the substantial patient populations eligible for brain-stimulation therapies, particularly in cases where pharmacological treatments are inadequate.

Neural stimulation has advanced in both research and clinical practice for treatment of brain disorders [9]. The method uses electrical, magnetic, or optical signals to modulate the activities of target neurons in the brain [10, 11]. Electrical brain stimulation applies controlled electrical currents directly to the brain tissue, either through implanted electrodes (invasive) or scalp electrodes (non-invasive), to activate or modulate neural activity. Experiments by Fritsch & Hitzig in 1870 is a landmark in the history of electrical stimulation. Fritsch & Hitzig applied a pulse of direct current to platinum electrodes implanted on the surface of the cerebral cortex of dogs, and observed large movements [12, 13, 14]. Subsequently, studies reported the application of high-frequency electrical stimulation to treat a variety of disorders, including dyskinesia [15], parkinsonian and essential tremor [16], cerebral palsy [17], and convulsive disorders [18]. In 2003, the FDA approved brain stimulation for treatment of neurological movement disorder such as dystonia [19]. Microstimulation involving implantation of microelectrodes have been developed to deliver reliable small, controlled electrical currents to targeted neurons, allowing precise activation of neuronal populations and experimental probing of brain function [20]. However, there is risk of electrode and tissue damage associated with several parameters including polarity (i.e. cathodal versus anodal), current amplitude, frequency range, current density, and high impedance. Electrochemical impedance spectroscopy (EIS) is a non-invasive technique

The work presented in this chapter is submitted for publication to the Current Opinion in Electrochemistry

employed to characterize the electrode-tissue interface and electrode's impedance. EIS can be used to evaluate the changes in impedance that may indicate electrode degradation, or inflammatory tissue responses, and can guide the optimization of stimulation parameters to maintain safe neural activation.

2.2 EIS Application to Neural Stimulation

EIS is a non-invasive tool used to characterize the chemical properties of materials and interfaces over a range of frequency. In neural interfaces, where microelectrodes are chronically implanted into brain or peripheral nervous tissue, EIS offers a non-destructive approach to evaluate the conditions of the electrode–tissue interface [21], electrode capacitance, mass-transfer and tissue responses over time [22, 23, 24].

2.2.1 History

Early neural-stimulation researchers used impedance spectroscopy to evaluate electrode-tissue interface, monitor electrode degradation, and establish safe charge-injection limits for device performance during electrical stimulation. In 1962, Adey et al.[25] performed impedance measurements in brains of cats using chronically implanted coaxial electrodes to investigate the electrophysiological properties of brain tissues. By applying very small electrical signals and a current density of 10^{-13} amperes per square micron of electrode surface at 1000 cycles/seconds, they observed changes in the impedance which was related to alterations in neural activity or glial formation. In 1964, Porter et al.[26] measured impedance of the human brain using stainless-steel tubing and a Wheatstone bridge, and reported that impedance measurements may serve as indicators of microscopic abnormalities in tissue structure for patients with movement disorders. In 1990, notable work by Rose and Robblee [27] established safe charge-injection limits for platinum electrodes, influenced by multiple factors including electrode size, surface characteristics, pulse duration, and the electrode-tissue interface chemistry.

In 1990, McCreery et al.[28] identified combinations of charge density and charge per phase as damaging and non-damaging. In 1992, Shannon et al.[29] developed safe levels for electrical stimulation based on current flow principles and damage mechanisms in macroelectrodes,

following the work of McCreery et al.[28]. Subsequent work by Butterwick et al.[30] in 2007, demonstrated that current thresholds for macroelectrodes and microelectrodes scaled with electrode size at a transition point from 200 m and 300 m in electrode diameter. Cogan et al.[31] has reviewed the damage thresholds of tissue during electrical stimulation therapies.

Safe charge-injection limit is the maximum charge deliverable per phase (C/cm^2) without causing tissue damage or harmful faradaic reactions such as water electrolysis. Polarization of electrodes beyond these limits increases the risk of electrode degradation, glial scar formation [22] and high impedance, which reduces the efficacy of stimulation and recording. Grill and Mortimer [32] demonstrated that encapsulation tissues significantly increased the resistivity and impedance of the surrounding tissues and implants. Merrill et al.[2] detailed faradaic and non-faradaic mechanisms underlying electrode and tissue damage, emphasizing the need for safe charge delivery during neural stimulation. Neural stimulation studies [33, 34, 23] have reported that increase in impedance over time is attributed to the formation of fibrous encapsulation tissue around implanted electrode arrays. Several strategies have been developed to improve neural implant longevity, reduce tissue encapsulation, and maintain low impedance. Electrode miniaturization to ultra-smaller dimensions (< 10 m) [35] decreases acute tissue damage during insertion and reduces inflammatory response.

Rejuvenation offers an alternative solution for reducing electrode's impedance. Controlled voltage biases are applied to electrodes to reverse some tissue encapsulation effects and restore signal quality without implant replacement. Otto et al.[36] showed that large voltage pulses of 4 seconds applied to chronically implanted neural microelectrodes doubled the signal-to-noise ratio and reduced the 1-kHz impedance by over 60%. These pulses lower the resistive influence of tissue components at the interface. O'Sullivan et al.[37] have recently reported a decrease in impedance response associated with rejuvenation, consistent with previous work by Johnson et al.[38] and Otto et al.[36]. Studies have demonstrated that small voltage pulses and potential-biased asymmetric waveforms up to 1 ms [39, 40] can enhance the charge-injection capacity of neural electrodes.

2.2.2 Neural Stimulation and Recording Electrodes

Neural electrodes are conducting metals or polymers used for stimulation or recording. Brain-stimulation electrodes are used to deliver biphasic current pulses to targeted cells in the brain tissue to modulate neural activity. Recording electrodes are used to monitor and measure the electrical potentials generated by neurons and axons within the brain. Different neural electrode sizes and designs have been developed to improve neural recording and stimulation. Neural-stimulation electrodes are mostly selected to alter neural activities, reduce impedance, and minimize tissue damage [41]. The first sets of macroelectrodes have geometric surface areas (GSA) around 0.001 cm^2 or greater [42], and were made from materials like platinum as reflected in the works of Shannon [29] and McCreery [43].

Macroelectrodes are usually positioned on the surface of the targeted neural tissue; they have high-charge per phase but relatively low-charge density thresholds, hence does not undergo electrode degradation caused by stimulation at clinically relevant charge levels. However, the high-charge per phase delivered by these electrodes can pose a greater risk of tissue damage, which is typically a more significant concern [42]. Subsequent advances in neural stimulation fostered the use of microelectrodes with geometric surface areas around 10,000 m^2 as a better alternative.

Microelectrodes and ultramicroelectrodes offer a better advantage for penetration of neural targets. They can stimulate smaller, more precise amount of neural tissues, which can enhance selectivity and improve the spatial resolution of tissue responses. However, they exhibit high-charge densities which can lead to both electrode degradation and tissue damage [42]. Studies have shown that microelectrodes (with GSA ≤ 2000 m^2) have a narrow safe levels for charge per phase of around 1 nC/phase [43, 44]. Ultramicroelectrodes with GSA of 20 and 80 m^2, as shown in Figure 2-1 a and e) can enhance spatial selectivity for stimulation and recording [45]. Ghazavi et al.[45] evaluated the charge-injection capacity of ultra-small (20 m^2 to 1960 m^2) SIROF electrodes and found that they are at levels above some reported thresholds for microelectrodes. However, another major concern is high electrode impedance and low signal to noise ratio.

Many materials shown in Table 2-2 and 2-1, such as Gold [46, 47], Platinum [48, 49, 50], SIROF [51], AIROF [52], Titanium Nitride (TiN) [53], PEDOT:PSS [54, 55], sputtered ruthenium oxide (RuO_x) [56], are selected for high charge-injection and low impedance performance of both microelectrodes and ultramicroelectrodes. Cogan et al.[57, 58] showed that SIROF coatings demonstrate high charge-injection capacity with increasing film thickness. Reviews on electrode materials can be found elsewhere [42].

2.2.3 Electrochemical Impedance Spectroscopy Measurements

EIS is performed in vitro or in vivo to characterize the electrode-electrolyte or electrode-tissue interface. A schematic representation of the experimental setup for electrochemical impedance spectroscopy and neural stimulation, taken from Dong et al.[59], is presented in Figure 2-1. An ultramicroelectrode device, shown in Figure 2-1(a), has electrodes ranging in diameter from 5 to 50 m. In vitro EIS is conducted using three-electrode setup as shown in Figure 2-1(b). Potentiostats provide a small-amplitude sinusoidal potential across a broad frequency range and measure the resulting current. Typical perturbation amplitudes and electrolytes used for in vitro studies are shown in Table 2-1. Impedance spectra of neural implants are commonly reported at a single frequency of 1 kHz due to its physiological relevance to neuronal spike timing; however, full spectra of frequency sweeps across 10 mHz to 100 kHz are required to capture time-constants associated with double-layer capacitance, charge-transfer resistance, and diffusion effects.

The illustration in Figure 2-1(c) suggests a typical in vivo application. The in vivo EIS device shown in Figure 2-1(d) was miniaturized for easy implantation, minimizing tissue damage and inflammation. Most in vivo studies shown in Table 2-2 use a two-electrode configuration, though some employ a three-electrode set-up for electrophysiological analysis. Electrophysiological analyses are performed to measure the electrical activity of neural tissue [60]. The perturbation amplitudes of impedance measurements are selected to maintain linearity while allowing sensitivity to interface changes. In Vivo EIS is conducted in humans [61, 62] and animal models, including rats [63, 63], mice [55, 64] cats [65], and monkeys [66, 67, 33].

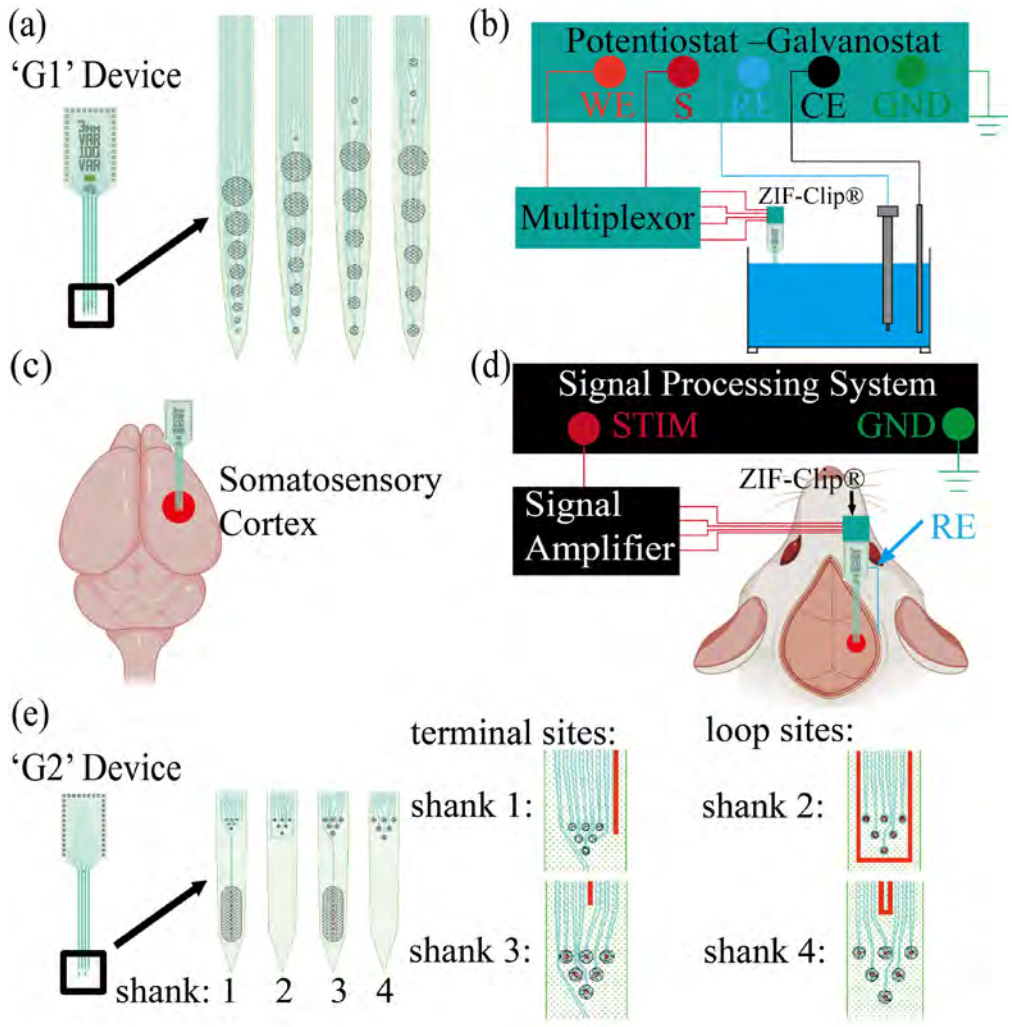

Figure 2-1. A schematic representation of the experimental setup for electrochemical impedance spectroscopy and neural stimulation, taken from Dong et al.[59]: (a) G1 device, consisting of a silicon-based substrate with 4 shanks and 32 sites, ranging from 5 m to 50 m in diameter; (b) in vitro three-electrode EIS setup where the working/working sense are connected to a multiplexer for channel selection; (c) somatosensory cortex of a rat brain, the target area for neural interfacing; (d) signal processing system setup for in vivo EIS, including the stimulator connected to the signal amplifier and the ground (GND) reference, the ZIF-Clip® headstage connected to the implanted UMEA with an additional RE placed on the skin; and (e) G2 device, silicon-based substrate with 4 shanks and 24-ultramicroelectrode sites of 5 m or 10 m diameter. The terminals and loops are highlighted.

Table 2-1. In Vitro EIS Parameters Applied in Neural Stimulation Studies. All studies referenced employ three electrodes. Details on the electrolytes and electrodes employed can be found in the cited references.

Researcher(s)	Electrolyte	Electrode	Electrochemical set-up	Perturbation amplitude	Frequency range	Process model	Error analysis
Three-electrode configuration							
Franks et al.[68]	PS,0.9% NaCl	Platinum, Pt black, TiN	CE: Large-area Pt, RE: SCE	10 mV	10 mHz – 100 kHz	Yes	Yes
Negi et al.[51]	PBS	SIROF or Platinum	CE: Large-area Pt wire, RE: Ag/AgCl	10mV	1 Hz– 100 kHz	Yes	No
Cogan et al.[48]	PBS	AIROF and PtIr microelectrodes	CE: Large Pt mesh, RE: Ag/AgCl	50 mV	20Hz– 100 Hz	No	No
Lewis et al.[69]	PBS, 0.01 M	Pt, IrOx, nanoPt, and PEDOT	CE: Not specified, RE: Ag/AgCl	100 mVpp	0.1 Hz – 100 kHz	No	No
Lempka et al.[67]	0.9% NaCl	DBS with platinum/iridium contacts	CE: Ag/AgCl wire	25 mV rms	0.5 Hz—10 kHz	Yes	Yes
Cogan et al.[57]	CBS/PBS	SIROFs on Gold substrates on flexible MEAs	CE: Large Pt, RE: Ag/AgCl	5 mV rms	0.05 – 100 kHz	No	No
Lutz et al.[70]	PBS	SIROF	CE: not specified, RE: Ag/AgCl	10 mV rms	40 mHz – 100 kHz	Yes	Yes
Ghazavi et al.[71]	model-ISF	SIROF	CE: Large Pt mesh, RE: Ag/AgCl	10 mV rms	1 Hz– 100 kHz	No	No
Meyer et al.[72]	PBS	Electrodeposited IrOx	CE: Pt wire, RE: Ag/AgCl	10 mV rms	0.05 Hz – 100 kHz	No	No
Dong et al.[59]	PBS	Gold coated with SIROF	CE: Pt wire, RE: Ag/AgCl	0.01 V rms	1 Hz– 100 kHz	No	No
Castagnola et al.[64]	PBS / ASCF	PEDOT:PSS	CE: not specified, RE: SCE	0.05 V rms	1–10 kHz	No	No

Table 2-1. Continued

Researcher(s)	Electrolyte	Electrode	Electrochemical set-up	Perturbation amplitude	Frequency range	Process model	Error analysis
Castagnola et al.[50]	PBS	Planar Pt electrodes uncoated or coated with PPy-CNTs, PEDOT-CNTs, PEDOT-agar, Au-CNT, Au-agar	CE: Pt wire, RE: Ag/AgCl	10 mV rms	1 Hz– 100 kHz	No	No
Weiland et al.[53]	PBS	IrOx and TiN	CE: not specified, RE: SCE	5 mV rms	1 Hz– 100 kHz	No	No
Vomero et al.[73]	PBS	Polyimide-based shank with SIROF and PEDOT/PSS coating	CE: Pt, RE: Ag/AgCl	10 mV rms	10- 100 kHz	No	No
Wills et al.[74]	PBS	IrOx, and PEDOT on arrays with Ir sites	CE: large-area Pt wire, RE: SCE	5 mV rms	1 Hz — 1 MHz	No	No

PBS, Phosphate Buffered Saline; SIROF, Sputtered Iridium Oxide Film; CE, Counter Electrode; RE, Reference Electrode; Pt, Platinum; Ag/AgCl, Silver/Silver Chloride; SCE, Saturated Calomel Electrode; PtIr, Platinum–Iridium Alloy; CBS, Carbon Black Substrate; MEAs, Microelectrode Arrays; IrOx, Iridium Oxide; ASCF, Artificial Cerebrospinal Fluid; ISF, Interstitial Fluid; PEDOT:PSS, Poly(3,4-ethylenedioxythiophene):Polystyrene Sulfonate; Ppy-CNTs, Polypyrrole–Carbon Nanotubes Composite; PEDOT-CNTs, Poly(3,4-ethylenedioxythiophene)–Carbon Nanotubes Composite; PEDOT-agar, Poly(3,4-ethylenedioxythiophene) embedded in Agar Hydrogel

Impedance measurements capture contributions from cables and connectors as well as the electrochemical system of interest. These configurations introduce to the measurement a capacitive or inductive behavior that can confound interpretation of the impedance data. The best approach is to ensure that the measurement does not include the influence of leads and connectors. Accuracy contour plots (ACPs) are used to evaluate the usable impedance and frequency ranges for different instrument setups. Hazelgrove et al.[21] emphasized the importance of accuracy contour plots in their review paper. Dong et al.[59] plotted accuracy contour plots for the Autolab PGSTAT12 (Metrohm, Utrecht, Netherlands) by itself and when connected to a neural implant via a connection hardware, emphasizing the importance of assessing the accuracy contour plot using the cables and connectors associated with the system under investigation. It is not enough to report the accuracy contour plot provided by the vendor.

2.2.4 Interpretation of Impedance Data

The effective use of EIS requires not just measurements but regression of mathematical models for accurate data interpretation. Circuit-based mathematical models enable interpretation of impedance spectra based on physical and chemical phenomena occurring in the system. Interpretation relies on two principal models: (i) a physicochemical model describing electrode and tissue interactions, and (ii) a measurement model for error structure analysis and assessment of data consistency with Kramers–Kronig relations. The Kramers–Kronig relations [75] were developed for optics and adopted by electrochemists to evaluate the self-consistency of impedance measurements. The measurement model is a Kramers–Kronig consistent model established by Agarwal et al.[4] for analyzing impedance data. Lutz et al.[70] used the measurement model to analyze replicated impedance spectra of SIROF microelectrodes for neural applications. Process models are not unique, multiple circuits can fit same impedance data, and the passive elements are assumed to act independently. Review by Vivier and Orazem [76] highlighted wide a range of electrical circuits used to model EIS data (including Randles [77] and Warburg [78] models).

Table 2-2. In vivo EIS parameters applied in neural stimulation studies.

Researcher(s)	Animal	Electrode	Electrochemical set-up	Perturbation amplitude	Frequency range	Process model	Error analysis
Three-electrode configuration							
Abbott et al.[79]	Rat	Amorphous silicon carbide (a-SiC) with SIROF sites	CE: Platinum wire, RE: Ag/AgCl	10 mV rms	1 Hz–100 kHz	No	No
Alba et al.[80]	Rat	PEDOT/MWCNTCE: Platinum, RE: and Pt/Ir elec- Ag/AgCl trodes		10 mV rms	10 Hz–32 kHz	Yes	No
Cogan et al.[52]	Rabbit	AIROF	CE: Platinum, RE: Ag/AgCl	50 mV	0.01 Hz–100 kHz	No	No
Two-electrode configuration							
Hughes et al.[61]	Human	Platinum and SIROF microelectrodes	CE: not specified	10 nA peak-to-peak	1 kHz	No	No
Barrese et al.[66]	Monkey	Silicon microelectrodes with platinum sites	CE: not specified	50 pA peak-to-peak	1 kHz	No	No
Kane et al.[65]	Cat	Sputtered iridium oxide (SIROF) electrode sites	CE: Platinum mesh, RE: Ag/AgCl	10 mV rms	1 Hz–100 kHz	No	No
O'Sullivan et al.[81, 37]	Monkey	Deep brain stimulation (DBS) and electrocorticography (ECoG) electrodes	CE: titanium screw/rod	0.01 V	10 Hz—100 kHz	Yes	Yes

Table 2-2. Continued

Researcher(s)	Animal	Electrode	Electrochemical set-up	Perturbation amplitude	Frequency range	Process model	Error analysis
Otto et al.[36]	Rat	Silicon-substrate microelectrode with iridium site	CE: stainless steel bone screw	25 mV rms	100 Hz–10 kHz	Yes	No
Purcell et al.[82]	Rat	Silicon probes with iridium recording sites	CE: stainless steel bone screw	25 mV rms	10 Hz–10 kHz	No	No
Urdaneta et al.[83]	Rat	Silicon-substrate microelectrode array	CE: stainless steel bone screw	15 mV peak-to-peak	10 Hz–100 kHz	No	No
Prasad et al.[84]	Rat	Pt/Ir microelectrode arrays	CE: not specified	4 mV peak-to-peak	1 Hz–2 kHz	No	No
Malaga et al.[33]	Monkey	Platinum site	CE: not specified	Not specified	1 kHz, 100–2050 Hz	No	No
Patel et al.[85]	Rat	Silicon probes with carbon fiber arrays	CE: stainless steel bone screw	10mV	10 Hz–31 kHz	No	Yes
Ludwig et al.[63]	Rat	PEDOT	CE: stainless steel bone screw	25 mV rms	10 Hz–10 kHz	Yes	No
Black et al.[86]	Rat	SIROF	CE: stainless steel bone screw	10 mV rms	1 Hz–100 kHz	No	No
Opie et al.[87]	Corriedale ewes	platinum recording electrodes	CE: stainless steel bone screw	10 mV rms	1 Hz–1 MHz	Yes	Yes

SIROF, Sputtered Iridium Oxide Film; CE, Counter Electrode; RE, Reference Electrode; Pt, Platinum; AIROF, Activated Iridium Oxide Film; Ag/AgCl, Silver/Silver Chloride; PtIr, Platinum–Iridium Alloy; CBS, Carbon Black Substrate; MEAs, Microelectrode Arrays; IrOx, Iridium Oxide; PEDOT:PSS, Poly(3,4-ethylenedioxythiophene):Polystyrene Sulfonate; Ppy-CNTs, Polypyrrole–Carbon Nanotubes Composite;PEDOT-CNTs, Poly(3,4-ethylenedioxythiophene) –Carbon Nanotubes, Composite; PEDOT-agar,Poly(3,4-ethylenedioxythiophene) embedded in Agar Hydrogel

Constant-phase elements (CPE) are frequently used to model non-ideal capacitive behavior caused by surface roughness, porosity, or resistive distributions [88]. Hirschorn et al.[89] developed methods to extract film thickness and effective capacitance from CPE parameters. These approaches are evident in neural studies on PEDOT [90] and porous SIROF microelectrodes [70]. Some neural studies [91] used Randles circuits [77] to fit impedance spectra. Other studies incorporated Warburg diffusion and resistive films to describe chronic tissue effects [92].

2.3 Rudimentary Use of EIS in Neuroscience: A Survey and Critique

Studies in neural stimulation often apply EIS in a rudimentary way primarily by reporting impedance magnitude and phase without modeling the electrode-tissue interfacial reactions. Researchers measure and report the impedance at 1 kHz because this frequency corresponds to the typical range of neural spikes and stimulation pulses. However, impedance is a frequency-dependent property that reflects both the resistive and capacitive contributions of a system. A single-point measurement at 1 kHz does not capture the electrochemical reactions across a wide frequency spectrum. Purcell et al.[82] measured impedance at 1 kHz to investigate how flavopiridol improved the performance of iridium electrodes in rats over 28 days. Their results showed reduced impedance at 1 kHz with flavopiridol, but did not account for complex electrode-tissue interactions. Wang et al.[93] used impedance at 1 kHz to assess electrode performance and tissue response, but did not apply process model to interpret the impedance spectra. Hughes et al.[61] measured impedance at 1 kHz to investigate long-term neural stimulation and recording performance of SIROF and platinum electrode arrays, in human sensorimotor cortex over 1500 days. Their results showed that stimulation through SIROF-sensory electrodes maintained lower impedances than platinum-motor electrodes due to material differences and charge injection. However, their study did not account for the faradaic and charge reactions associated with the electrochemical systems. Similarly, Woeppel et al.[62] used impedance measurements at 1 kHz to assess the influence of tissue encapsulation and chronic recording performance of explanted Utah electrode arrays in human cortex, but did not apply a process model to interpret their impedance spectra. While measuring at a single frequency

is fast and convenient for clinical monitoring, it cannot be used to analyze the relevant physicochemical processes such as charge transfer, double-layer capacitance, diffusion, and tissue encapsulation. Advanced interpretation of impedance data across a broad frequency range is necessary to truly separate properties of the electrode from biological tissue responses.

A major gap in neuroscience literature [46] is the lack of quantitative analysis of error structure and assessment of consistency with Kramers–Kronig relations [4], a test of linearity and stationarity [5] in EIS measurements. Most published neural EIS studies shown in Table 2-1 and 2-2 do not assess error structure of impedance data. Notably, reviews by Boehler et al.[94] and Schiavone et al.[95] did not discuss the importance of error structure analysis for EIS interpretation. Regression of mathematical models and error weighting are essential to extract statistically significant parameters describing electrode and tissue behavior. Agarwal et al.[4] developed a Kramers–Kronig -consistent measurement model for EIS data regression. The model uses a superposition of Voigt-circuit elements (RC circuits) to represent impedance data without requiring direct Kramers–Kronig integrations. This approach incorporates error analysis [96] and enables precise extraction of electrode-tissue parameters. Bias errors in neural stimulation could arise from instrumentation, biological artifacts [22], and non-stationary effects. Few studies [37] meet these standards. Lutz et al.[70] used the measurement model program [97] to analyze impedance spectra of SIROF microelectrodes. The maximum number of Voigt elements that yielded statistically significant parameters was employed for regression. They included error analysis to interpret and extract physical parameters of flat substrates and pore walls following de Levie's [98] approach.

Interpretation of impedance data is often overlooked. Some studies [91] apply electrical circuit models to neural EIS data but fail to integrate error structure to their model. Interpretation models use combinations of resistors, capacitors, constant phase elements (CPEs), and Warburg components to represent the complex processes at the electrode-tissue interface, enabling extraction of physical parameters and improvements in stimulation protocols. O'Sullivan et al.[81] created process models for chronic intracranial electrodes, extracting and interpreting CPE

parameters and resistance during long-term implantation. CPE parameters alone are not meaningful and need to be expressed in terms of a capacitance. Many studies report CPE parameters [88], without connecting them to the physical properties such as surface roughness or resistive distribution [89]. Review studies by Vivier and Orazem [76], Hazelgrove et al.[21], Wang et al.[99] highlight best practices for impedance modeling. Impedance analysis for neural electrodes should include complete impedance spectrum measurement, error structure analysis, assessment with Kramers–Kronig -consistent models, proper regression weighting, and fitting to a meaningful physicochemical interpretation model.

2.4 Advancements of EIS in Neural Stimulation

Advanced mathematical models have emerged that better account for the underlying chemistry and physics of electrode-tissue interface. Lutz et al.[70] applied statistical analysis to develop a process model for SIROF microelectrodes incorporating iridium oxidation states and porous electrode behavior, resulting in more accurate fits that enabled extraction of statistically significant parameters of the electrode. Sridhar et al.[100] demonstrated that charge transfer resistant ( ) and the double-layer capacitance ( ) are dependent on the applied potential. Sehlmeyer et al.[101] introduced an improved cochlear implant electrode model that replaces a simple capacitor with a non-linear, frequency-dependent polarization capacitance and resistance in parallel with a Faradaic resistance, capturing frequency-dependent effects that are not captured in common equivalent circuit models. Rejuvenation studies have recently gained significant attention as a method for reducing impedance and maintaining a long-term electrode performance. Otto et al.[36] showed that voltage pulses reduced impedance and increased the signal to noise ratio (SNR) of neural electrodes. O'Sullivan et al.[37] observed that DC and low-frequency AC voltage pulses can be applied repeatedly to improve electrode functionality. Advances in neural systems including electrode miniaturization and development of charge-injection coatings (SIROF, PEDOT, TiN) [57, 45, 102], demand precise impedance characterization of neural electrodes.

2.5 Electrochemical Impedance Spectroscopy

Electrochemical Impedance Spectroscopy (EIS) is a frequency-domain technique used to characterize the electrochemical properties of materials and interfaces. The technique captures time-constants of various interfacial reactions including charge transfer, double-layer formation, and mass transport, making it useful for interpretation of physical and chemical processes [76]. A number of textbooks are available that discusses EIS [1, 103, 104, 105]. EIS have been applied in batteries, [106], fuel cells [96], corrosion [107], quantum dot [108] and glucose sensors [109]. As shown in Figure , EIS involves the application of a small amplitude sinusoidal potential or current perturbation across a system using a potentiostat or galvanostat and measuring the frequency-dependent current or voltage response [110, 1].

The ratio of the input potential to the output current yields the complex impedance spectrum, consisting of real component, Z ( ) and imaginary component, Z ( ). In potentiostatic modulation, the input signal is a sinusoidal potential, expressed as

$$= \bar{} + |\Delta | \cos( ) \quad (2\text{-}1)$$

where $\bar{}$ is the steady-state potential applied, Δ is the small-amplitude perturbation part of the potential, $\bar{}$, represents the angular frequency at which the system is being oscillated by the applied perturbation, and is the time it takes for the input and output signals to oscillate. The resulting sinusoidal current output is given as,

$$= \bar{} + | \Delta | \cos (+) \quad (2\text{-}2)$$

where is the phase angle which represent the phase lag between input potential and output current, Δ is the current amplitude. As shown in Figure 2-3, both the input and output signals are oscillating at the same frequency , however, there a phase lag associated with the output signal. Using a phasor notation, Equations 2-1 and 2-2 may be expressed as

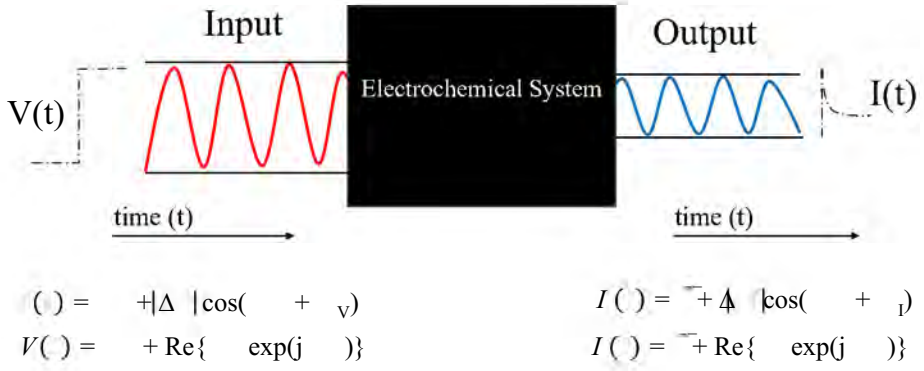

Figure 2-2. A schematic representation of potentiostatic EIS where a sinusoidal potential perturbation is applied to an electrochemical system and the sinusoidal current response is measured.

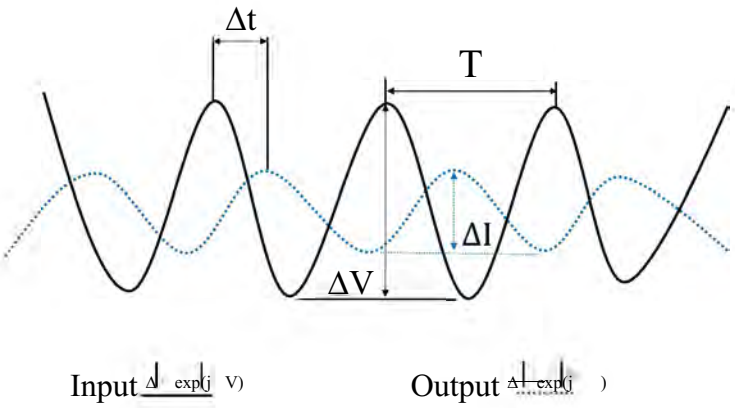

Figure 2-3. Schematic representation of the phase angle, for a sinusoidal input potential perturbation and the phase lag, for the resulting current output at time, T.

$$= \overline{\quad} + \mathrm{Re}\{\tilde{\quad}\exp(j\quad)\} \tag{2-3}$$

and

$$= \bar{\quad} + \mathrm{Re}\{\tilde{\quad}\exp(j\quad)\} \tag{2-4}$$

where $\tilde{\quad}$ and $\tilde{\quad}$ are complex numbers representing potential and current phasors respectively. j is the complex number equal to $\sqrt{-1}$. Both and $\tilde{\quad}$ are independent of time, but frequency-dependent quantities. The impedance is a frequency-dependent complex number expressed as

$$= \frac{\tilde{\quad}(\quad)}{\tilde{\quad}(\quad)} \tag{2-5}$$

The complex form of impedance may be expressed as

$$= {}_{r} + j\ {}_{j} \tag{2-6}$$

where Z_r is the real part represented as

$${}_{r} = |\ (\quad)|\cos(\quad) \tag{2-7}$$

Z_j is the imaginary part expressed as

$${}_{j} = |\ (\quad)|\sin(\quad) \tag{2-8}$$

2.5.1 Graphical Representation

The Nyquist plots shown in Figure 2-4 and Bode plots in Figure 7-4 are used to visualize impedance data. Nyquist plots are drawn with 1:1 aspect ratio, to reveal slopes and loop shapes indicative of underlying physical models [76]. The impedance spectra presented in Figure 2-4 was estimated as

$$= {}_{+}{}^{t}_{e}\ 1 + \frac{R}{\quad\ t\ \ dl} \tag{2-9}$$

with R = 20 Ωcm^2, R = 200 Ωcm^2, and C =20 Fcm^{-2}. Where R is the ohmic resistance, R is the charge-transfer resistance, and C is the double-layer capacitance. The characteristic frequency is obtained from R and C as

$$ c = \frac{1}{2 \quad 1 \quad t \quad dl} = 39.8 \tag{2-10} $$

The magnitude and phase are estimated as

$$ | \quad |= \sqrt{ ^2 + (\quad r)^2} \tag{2-11} $$

$$ = \tan^{-1} \quad \left(\frac{ \quad j}{ \quad r} \right) \tag{2-12} $$

where Z and Z are the real and imaginary components of impedance, respectively. As displayed in Figure 2-5(a), The magnitude asymptotes at high frequencies above the characteristic frequency. The asymptotic feature is attributed to ohmic impedance (non-uniform current and potential distribution at the electrode electrolyte interface) [6]. The phase angle in Figure 2-5(b) tends to zero at low frequencies where the influence of the capacitance is low, and potential and current are in phase. To isolate the influence of ohmic resistance at high frequency, ohmic-resistance-corrected Bode plots displayed in Figure 2-6 are recommended.

The corrected magnitude is estimated as

$$ | \quad |_{adj} = \sqrt{ \quad _j^{\,2} + (\quad r - \quad e)^2} \tag{2-13} $$

and the corresponding phase angle as:

$$ _{adj} = \tan^{-} \quad \left(\frac{ \quad j}{ \quad r - \quad e} \right) \tag{2-14} $$

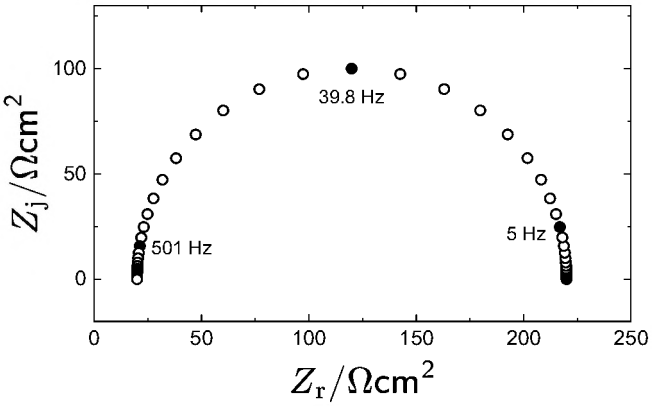

Figure 2-4. Impedance spectra in Nyquist format estimated from equation (6-3) with R = 20 Ωcm^2, R = 200 Ωcm^2, and C =20 Fcm^{-2}

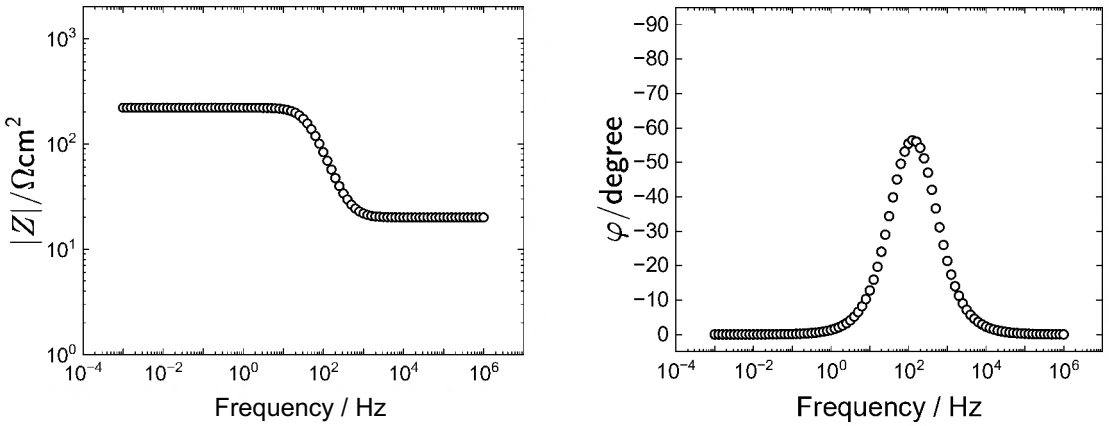

(a) (b)

Figure 2-5. Impedance spectra in Bode representation estimated from equations (2-11) and (2-12) with R = 20 Ωcm^2, R = 200 Ωcm^2, and C =20 Fcm^{-2}: (a) magnitude and (b) phase angle.

where R is the ohmic resistance. As shown in Figures 2-6, the slope of magnitude approaches –1 and phase angle 90 at high frequency. Electrodes often show non-ideal capacitive behavior, modeled using a constant phase element (CPE) [89, 111]:

$$_{CPE} = (j \quad) \frac{1}{} \tag{2-15}$$

where Z is the CPE impedance, Q is the constant-phase-element component of the cable, is the constant-phase-element exponent, j is complex no represented as $\sqrt{-1}$, and is frequency. Graphical representation of EIS data lay the foundation for accurate interpretation and the development of meaningful physical models in neural interface research.

2.5.2 Electrochemical Impedance Spectroscopy Modeling and Interpretation

The effective use of EIS requires not just measurements but regression of mathematical models for accurate data interpretation. Two critical models are required: i) physicochemical or process model which describes the physical and chemical processes occurring in the system under study. The model is not unique, but can be used to extract statistically significant parameters representing the electrochemical system under study. ii) a measurement model with a series of Voigt circuit elements for quantitative analysis of error structure and assessment of data consistency with the Kramers–Kronig relations.

2.5.2.1 Kramers–Kronig Relations

Kramers–Kronig relations are integral functions that correlate the real component of impedance [Z ( )] to the imaginary part [Z ( )] under the assumptions of linearity, stability, and causality. Linearity indicates that the input is linearly combined with the impedance response, and stability implies that the impedance behavior to a sinusoidal perturbation is controlled. At the same time, causality means that the input signal must prompt the response [76].

$$j(\quad) = - \left(\frac{2}{} \right) \int_0^{\infty} \frac{r(\quad) - r(\quad)}{^2 - ^2} \tag{2-16}$$

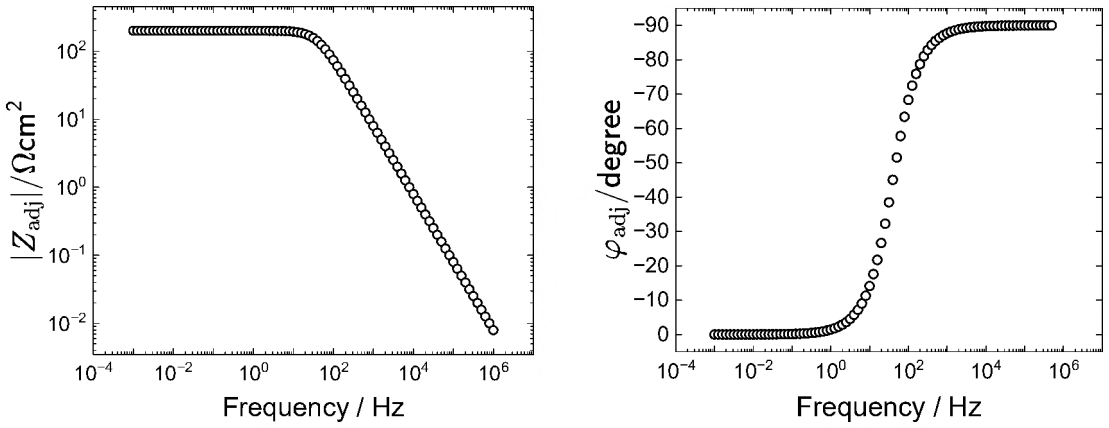

(a) (b)

Figure 2-6. Ohmic-resistance-corrected Bode plots estimated from equation (7-29) and (7-30) with R = 20 $\Omega\mathrm{cm}^2$, R = 200 $\Omega\mathrm{cm}^2$, and C =20 Fcm^{-2}: (a) Ohmic-resistance-corrected magnitude and (b) Ohmic-resistance-corrected phase angle.

$$r(\ ) = r(\infty) + \frac{2}{} \int_{0}^{\infty} \frac{(\ )_j - (\ )_j}{^2 - ^2} \qquad (2\text{-}17)$$

Kramers–Kronig relation is expressed in terms of the real and imaginary parts of impedance in Equation (2-16) and (2-17). The imaginary component of impedance Z can be predicted by integrating the real part over a wide frequency range from 0 to infinity if linearity, stability, and causality conditions are unviolated [112]. Inconsistencies with Kramers–Kronig equation are caused by non-linearity and non-stationarity of impedance measurements. Hence, any system that satisfies Kramers–Kronig equation will provide a good fit for the electrical-circuit model, and such systems are stationary and linear. In practice, impedance measurements are conducted within a finite frequency range. Therefore, data consistency with Kramers–Kronig relations can be determined by extrapolating the parameters for the remaining frequency domain or fitting the data to a Kramers–Kronig -suitable circuit element [112]. Advancements on the application of Kramers–Kronig relations to EIS data has prompted the replacement of Kramers–Kronig integrations with the measurement model developed by Orazem group [3, 4, 113] to regress frequency points of impedance data that are consistent with Kramers–Kronig relations).

2.5.2.2 Error Analysis

Interpretation of impedance data is characterized by quantifying the errors associated with the system under study. Errors in impedance measurements can be expressed as the difference between a modal value Z ( ) and the observed value Z ( )

$$\text{fit}(\ ) + {}_{s}t_{oc}h(\ ) + \text{bi}_{a}(\ ) = {}_{res}(\ ) = {}_{o}b_{s}(\ ) - {}_{mo}d(\ ) \tag{2-18}$$

Where ( ) represents the systematic error attributed to model imperfections, ( ) is the residual error, and $_{h}$( ) is the stochastic error [76]. Error analysis of impedance spectra [96] is required to select appropriate weighting strategy for the process model. Stochastic error structures are heteroscedastic (frequency dependent) and arise from the integration of time-dependent signals. The stochastic error structure is estimated as the standard deviations of the real and imaginary components of impedance as functions of frequency.

2.5.2.3 Measurement Model

The measurement model is a Kramers–Kronig -consistent statistical approach for analyzing impedance data. The measurement model shown in Figure 2-7 was developed by Agarwal et al.[3, 114, 113]. By fitting a series of Voigt-circuit elements (RC circuits) to the impedance spectra, the model represents the impedance without direct use of the Kramers–Kronig integrations (equations (2-16) and (2-17)). The impedance of the measurement model is given by:

$$= + \sum_{k=1}^{K} \frac{k}{1 + j \quad k} \tag{2-19}$$

Where the resistance $_{k}$ is the resistance of the kth element, and has units of [Ω] or [Ωcm^2] and time constant of the kth element, (= $_{k}$ $_{k}$) has units of [s], $_{k}$ is the capacitance of the kth element and has units of [Farads] or [Fcm^{-2}]. The measurement model provides statistically good fit for impedance spectra that are consistent with the Kramers–Kronig relations.

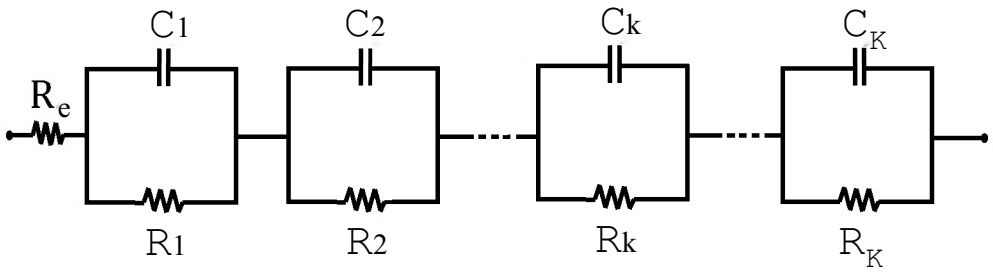

Figure 2-7. A schematic representation of a Voigt circuit used by Agarwal et al.[3, 114, 112] as a measurement model.

2.5.2.4 Characteristic Frequency

The frequency above which electrode geometry may cause frequency dispersion is known as the characteristic frequency f . It is the point of transition from a high-frequency loop to a low-frequency loop. Equation (7-31) is used to estimate characteristics frequency in terms of ohmic resistance R and double-layer capacitance C . R and C values are obtained by regression analysis of impedance data consistent with Kramers–Kronig relations.

$$\cdot \quad \frac{1}{2 = _{e,HF} \ _{dl}} \tag{2-20}$$

$$_{e,LF} \approx _{e,HF} \ 1.08 \ (\Omega) = 1.08 \ \frac{1}{4} \tag{2-21}$$

The characteristic frequency is obtained from the high-frequency ohmic resistance R , . The low-frequency ohmic resistance R , , in Equation (2-21) is 8 percent larger than the high-frequency ohmic resistance R , . At frequencies above the characteristic frequency, the electrode geometry is susceptible to non-uniform currents and potential distribution, and the regressed values are influenced by ohmic impedance. The ohmic impedance is eliminated by truncating the datasets to frequencies below the characteristic frequency.

2.5.2.5 Process Model

Process models provide a mechanistic representation of the electrochemical system under investigation. The model assembles electrical circuit elements (such as resistors (R), capacitors (C), inductors (L), constant phase elements (CPEs), and Warburg components) to represent the physical and chemical processes at the electrode–tissue interface. The interpretation of impedance spectra with electrical circuit model is often limited by the non-uniqueness of the model. Several circuits can equally fit a given impedance dataset, under the assumption that passive elements behave independently. Electrical circuit modeling involves the addition of faradaic and charging currents flowing through the electrode-electrolyte interface, typically by summing charging, faradaic, and diffusion time-constants in series without a physical interdependence between the parameters used, e.g. R, C, the CPE parameters and L. Accurate EIS interpretation requires proper weighting strategies and error structure analysis for process modeling, to derive statistically meaningful parameters. The electrical circuit shown in Figure 2-8 can be used to model impedance data to capture both charging current and cathodic faradaic current flowing through the electrode-electrolyte interface at open-circuit. The total impedance of the circuit is expressed as:

$$= e + \frac{t,c}{1 + t,c(\quad)} \qquad (2\text{-}22)$$

The cathodic impedance R , is the cathodic charge-transfer resistance, is the CPE exponent and Q represents the CPE component.

2.6 Numerical Methods

Impedance studies can provide the basis for understanding the electrochemical properties of microelectrodes and ultramicroelectrodes. The performance of implantable electrodes is time-dependent; therefore, the transient response of current and potential distribution would play a role in determining their pulse stability. Finite element methods are used to validate both experimental findings and impedance analyses of neural electrodes. Multiphysics models offer high accuracy when they incorporate various operating conditions and physical phenomena.

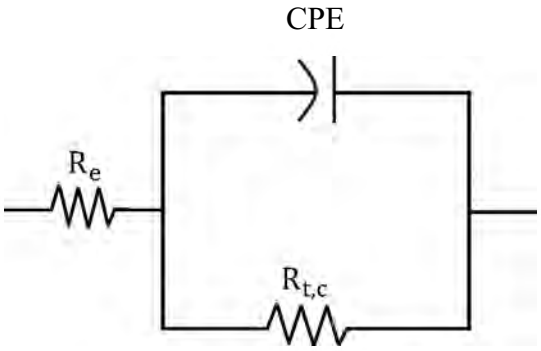

Figure 2-8. Schematic representation of electrical circuit elements for modeling impedance spectra. The ohmic resistance is in series with a parallel combination of a constant-phase element, and charge-transfer resistance.

Consequently, such models can be leveraged to improve the design and performance of devices under optimal operating conditions.

2.6.1 Current and Potential Distributions

The influence of non-uniform current and potential distribution on electrode impedance can be studied using finite-element simulations on disk electrodes. Previous numerical simulations were done using rotating-disk-electrode geometry embedded in an insulating plane. Newman[115, 116] assumed negligible concentration gradients to solve Laplace's Equation for potential using rotational elliptic coordinates. The electrode geometry often limits current density and potential distributions in the electrolyte adjacent to the electrode, which causes non-uniformity. For a disk electrode, the potential distribution is non-uniform when the current density is uniform, and conversely, the current density becomes non-uniform when the solution potential is uniform [116, 117]. Similarly, Parrish and Newman [118, 119] calculated current distributions for planar electrodes under channel flow conditions considering concentration, ohmic potential drops and kinetics and showed that current density calculations can be performed using similar method for both the plane and disk electrode geometries. Newman's [120] numerical simulations for a disk electrode geometry was performed for when the electrode was purely capacitive (J = 0), and when it was influenced by faradaic reactions with J values of 0.1 and

1. J is the dimensionless parameter expressed as [121, 122]

$$= \frac{4 \quad e,HF}{tc} \tag{2-23}$$

where R , is the high-frequency ohmic resistance and R is the charge-transfer resistance for the faradaic reaction. The electrochemical current becomes time-dependent when changes occur in the system. A step-change is applied to the potential, and the current response is recorded. Characterizing the time-constants of the response at both short and long times can provide insight into the system's electrode kinetics and mass transfer properties [116]. Nisancioglu and Newman[123, 124] analyzed the transient response of a disk electrode using a single faradaic reaction associated with a current step-change and a potential step-change.

2.6.2 Influence of Mass Transfer

The rotating disk electrode (RDE) geometry is used to model the influence of mass transport on non-uniform potential and current distribution. The laminar flow at the rotating-disk-electrode surface transports a steady flow of material from the bulk electrolyte to the electrode surface and forms a stagnant layer called the hydrodynamic boundary layer. The electrolyte close to the electrode surface rotates at the speed of the rotating disk electrode. In contrast, the bulk electrolyte far away from the electrode becomes well-mixed and well-stirred by convection-induced rotation. Hence, convection-diffusion concepts can mathematically explain the total motion of materials that forms the bulk electrolyte to the electrode surface. The stirring from the electrode triggers the convectional rotation that causes the mass transport of ions and molecules from the bulk electrolyte into the stagnant layer. Subsequently, as the molecules enter the stagnant layer and get closer to the electrode surface, convection plays a lesser role, and diffusion becomes more significant. The final motion of materials to the electrode surface is dominated by diffusion across a very thin layer of electrolyte adjacent to the electrode called the diffusion layer [125]. The model was solved based on the assumption that species migration was absent due to vital supporting electrolytes and that the reactions were inhomogeneous.

Harding[126] and Cochran[127] developed continuous equations for incompressible fluid flow and used cylindrical coordinates to derive velocity profiles.

2.6.3 Ohmic Impedance

The ohmic impedance is described as a transfer function associated with non-uniform current and potential distribution on the disk electrode surface. Newman [120] proposed that the frequency dispersion of impedance measurements is influenced by the electrode geometry. At high frequencies, the dispersion caused by variations in ohmic resistance and capacitance can be regarded as an ohmic impedance. Gharbi et al.[128] proposed that the Havriliak-Negami equation offers a good fit for the complex ohmic impedance of a disk electrode geometry at high frequency and can obtain the ohmic impedance of different electrode geometries including disk electrodes and electrode systems with complex faradaic reactions. The Havriliak-Negami equation is expressed as

$$= e,HF + (\frac{1 e, LF - e, HF}{+ (\quad)}) \tag{2-24}$$

where is the complex ohmic impedance, e,HF is the high-frequency ohmic resistance, e,LF is the low-frequency ohmic resistance, is the time constant, is the angular frequency, $= \sqrt{-1}$ is the imaginary unit, and are constants. You et al.[6] studied the reversible oxidation of ferrocyanide to ferricyanide on a disk electrode and obtained the relationship for the normalized difference between the low-frequency ohmic resistance and the high-frequency ohmic resistance associated with the dimensionless ohmic impedance in Nyquist format.

CHAPTER 3
ELECTRODE DEVICES

This chapter focuses on the electrode devices analyzed through electrochemical impedance spectroscopy (EIS) with particular emphasis on the structural design, fabrication methods, and coating materials. It details the configuration of a prototypical platinum disk ultramicroelectrode, high-density multi-electrode arrays (HD MEAs), and high-density ultramicroelectrode arrays (HD UMEAs), which were fabricated with various coatings to enhance performance and stability.

3.1 Generation 1 to Generation 3 (G1 to G3) Devices

The study provided insights into how electrode size, design and coating choices impact the impedance behavior of advanced neural-stimulation devices for research and clinical applications. Three generations of electrode arrays (G1 to G3) were tested and analysed using EIS to extract electrochemical properties. A summary of the generation 1 to generation 3 (G1 to G3) devices are presented in Table 3-1. The early designs (G1 and G2) were fabricated at a thickness of 15 m, while the later ultra thin (UT) electrode (G3) was reduced to 5 m, aiming to decrease glial scar formation and tissue encapsulation. Electrode sizes ranged from 5–50 m in microelectrode arrays to 5–25 m in ultramicroerlectrode arrays, with tighter electrode spacing (6–20 m) in UMEAs to enable higher recording density.

The pictorial representation of fabrication procedure for a sample G3 wafer-based SIROF electrode are shown in Figure 3-1. The picture was used with permission from Wu [129]. As shown in the low and high resolution optical image in Figure 3-1(a) and 3-1(b), the G3 electrode has four shanks with different site sizes raging from 20 m^2 to 320 m^2. Each site is a wafer-based test structure coated with SIROF as illustrated in the SEM image in Figure 3-1(d). The wafer-based test structure is composed of a 1 m SiO_2 layer, two 2 m amorphous silicon carbide (a-SiC) layers, a 320 nm Ti–Au–Ti metallization stack, and SIROF coatings, as shown in the cross-sectional SEM images in Figure 3-1(c) and 3-1(e). The fabrication method is the same for all G1 to G3 electrodes evaluated.

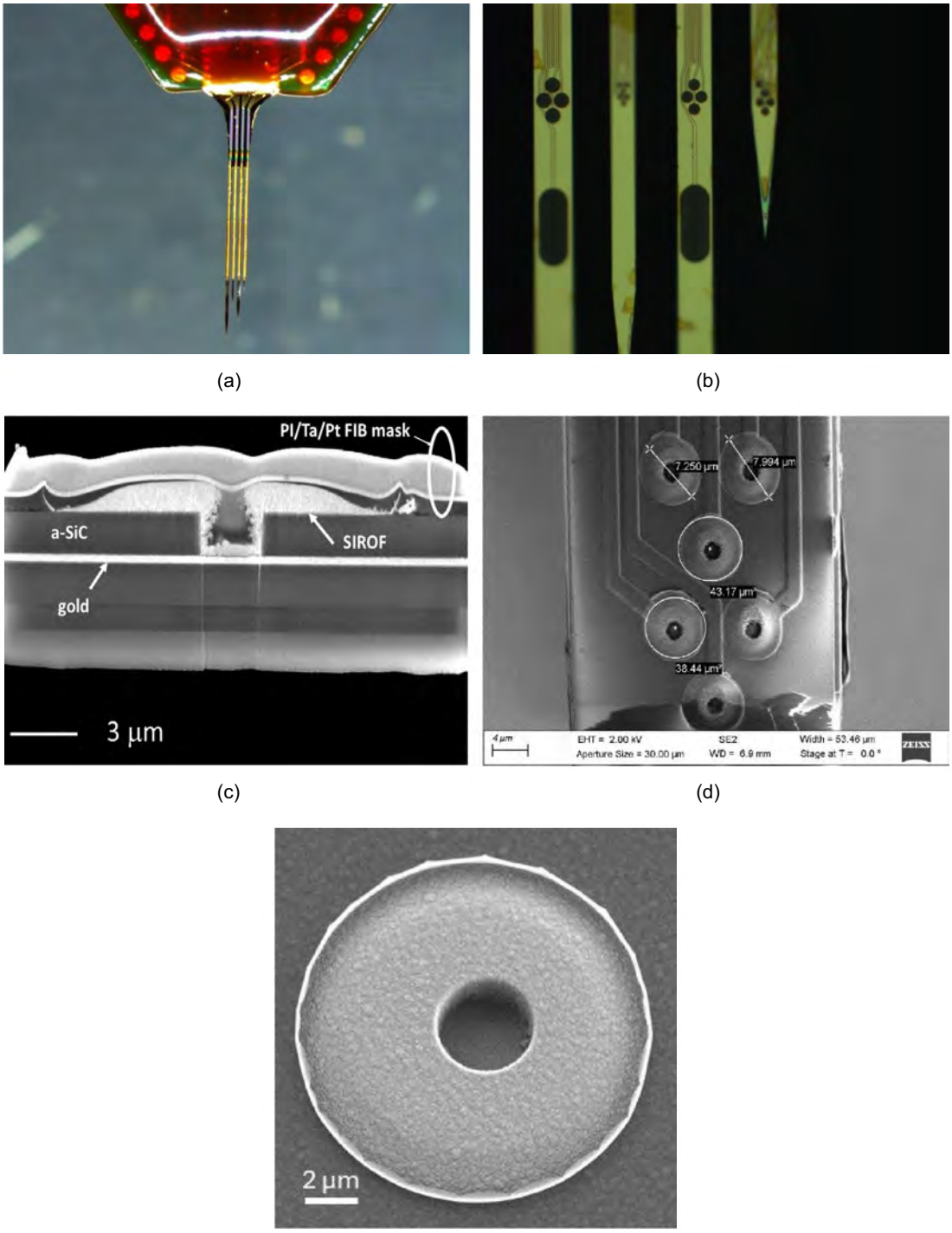

Figure 3-1. Images of SIROF ultramicroelectrode fabrication process used with permission from Wu [129]: a) optical image of a G3 device, b) high-resolution optical image of the G3 device , c) cross-sectional FIB SEM image of 80 m^2 SIROF electrode, d) SEM image of a G3 shank with 80 m^2 electrode, and e) SEM image of 80 m^2 electrode. The wafer-based test structure consist of a 1 m SiO_2 layer, two 2 m amorphous silicon carbide (a-SiC) layers, a 320 nm Ti-Au-Ti metallization layer, and SIROF coatings.

Table 3-1. Summary of the microelectrode and ultramicroelectrode (MAE and UMEA) array designs.

Name	Thickness (m)	Electrode Size (m)	Electrode Spacing (m)
G1 HD MEAs	15	5–50	100
G2 HD UMEAs	15	5–10	6–20
G3 UT HD MEAs	5	5–20	6–20

3.1.1 Generation 1 (G1) Devices

The first generation (G1) is also known as the high-density microelectrode array (HD MEA) devices, which was fabricated during Year 1 (Y1). The primary emphasis in Y1 was on the comprehensive analysis of G1 devices, including detailed interpretation of impedance spectra from measurements conducted in both in vitro and in vivo environments.

3.1.1.1 Design of Generation 1 (G1)

The high-density microelectrode array (HD MEA) devices was designed to explore variations in electrode diameter and spacing. As shown in Figure 3-2, the electrode diameter ranged from 50 m down to 5 m, corresponding to geometric surface areas (GSAs) of approximately 2000 m^2 to 20 m^2. The smallest diameter represented an ultramicroelectrode dimension, while the largest diameter was selected to approximate the surface area of Blackrock Neurotech microelectrodes. Electrode gaps were chosen between 10 m and 40 m, based on prior studies on spatial-dependence of intracortical microstimulation [130].

3.1.1.2 Generation 1 (G1) Fabrication and Coating

The generation 1 electrode arrays is a 4-shank 32-channel devices fabricated using the NeuroNexus commercial microfabrication processes. The arrays consist of amorphous silicon carbide (a-SiC) upper dielectric layer constructed on a 15 m thick silicon substrate to provide insulation and enhance durability. The fabrication method involved a photolithographic patterning on 6-inch wafers to define electrode sites liftoff. The G1 wafers were coated with sputtered iridium oxide films (SIROF), which serve as the electrode coating to improve electrochemical performance, charge-injection capacity, and biocompatibility.

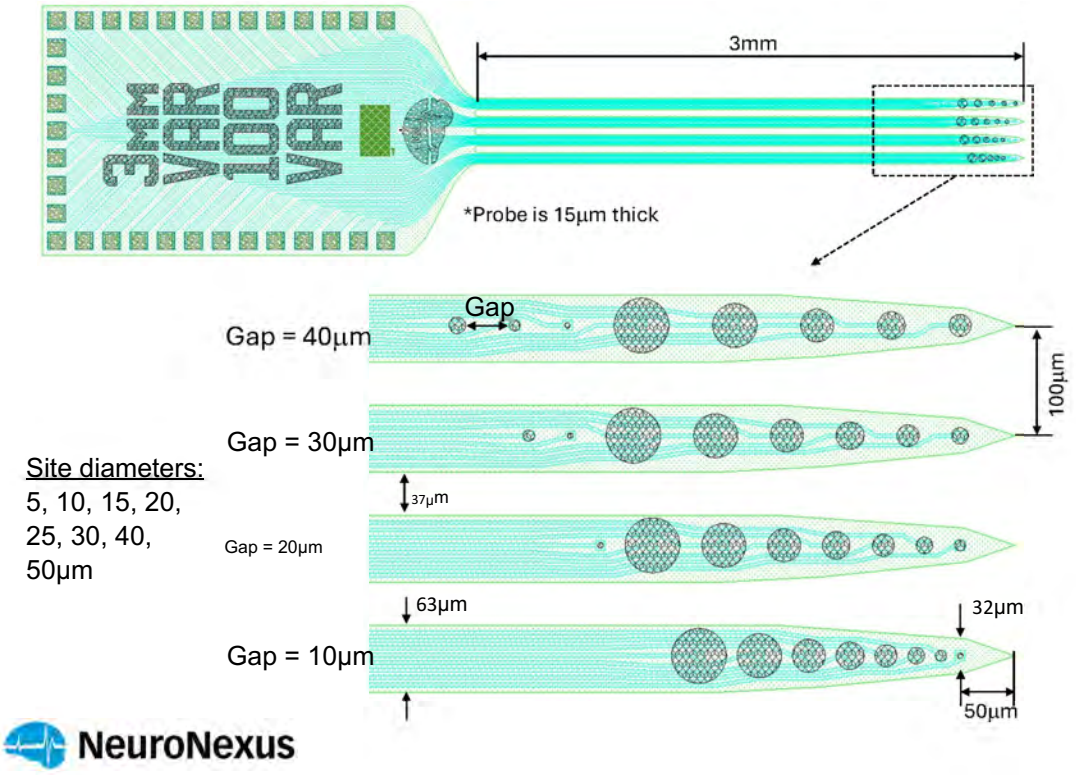

Figure 3-2. Schematics of generation 1 (G1) array device, featuring 4 shanks, and 32-channel microelectrode sites of diameters 50 m down to 5 m. This device was fabricated by NeuroNexus.

3.1.2 Generation 2 (G2) Devices

The second generation (G2) represents high-density ultramicroelectrode arrays (HD UMEAs), which was fabricated during Year 2 (Y2), and improved with more features based on the impedance results and extracted parameters from the generation 1 device. The primary emphasis in Year 2 was to conduct EIS measurements on generation 2 (G2) device in vitro and analyze the impedance spectra.

3.1.2.1 Design of Generation 2 (G2)

The generation 2 (G2) array was developed to evaluate advanced brain stimulation configurations using 5 m and 10 m ultramicroelectrodes, corresponding to geometric surface areas (GSAs) of approximately 20 m^2 to 80 m^2. As illustrated in Figure 3-3, The design consist of two large reference electrodes with geometric surface areas (GSAs) of approximately 4000 m^2, two looped traces for low-impedance assessment, and two terminal traces for high-impedance assessment.

3.1.2.2 Generation 2 (G2) Fabrication and Coating

The high-density ultramicroelectrode arrays consist of 24 recording sites distributed across four shanks, as shown in Figure Figure 3-3. Shanks 2 and 4 contain six electrodes each, with surface areas of 20 m^2 and 80 m^2. Shanks 1 and 3 include a large 4000 m^2 electrode alongside six smaller electrodes measuring 20 m^2 and 80 m^2. The device was fabricated by the NeuroNexus and constructed with a silicon carbide (SiC) upper dielectric layer. The electrode sites were patterned on the wafer through a photolithographic process and coated with sputtered iridium oxide film (SIROF) via a thin-film deposition process reported by Maeng et al.[102]. The SIROF coating offers high charge-injection capacity while minimizing the risk of tissue or material damage. The device has gold traces in looped and terminated configurations to enable closed-circuit and open-circuit EIS measurements, respectively. The ultramicroelectrode design supports accuracy contour evaluation and detailed analysis of electrochemical behavior as a function of electrode size and layout.

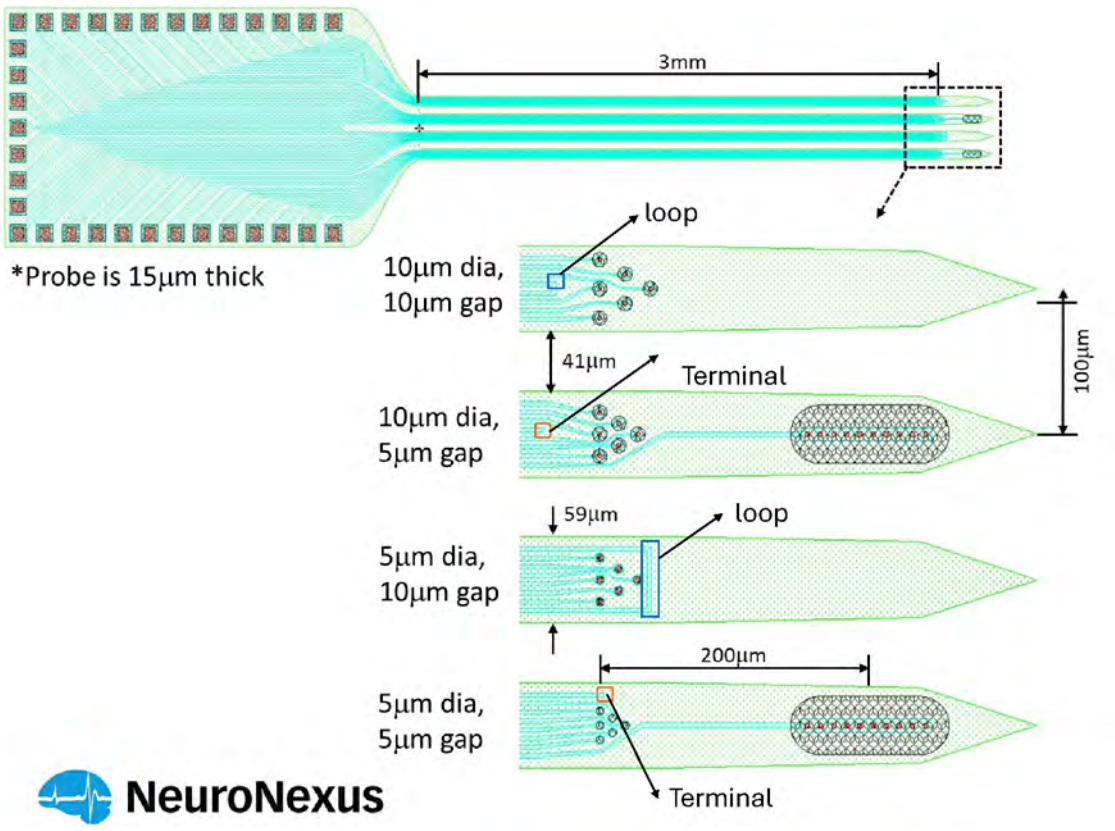

Figure 3-3. Schematics representation of generation 2 (G2) array device featuring 4 shanks. G2 electrode array differs from G1. The G2 electrode is limited to 24-channel ultramicroelectrode sites of diameters 5 m and 10 m, and two large reference electrodes with geometric surface areas (GSAs) of approximately 4000 m^2. Two looped traces for low-impedance assessment, and two terminal traces for high-impedance assessment, were added to facilitate the construction of accuracy contour plots. The device was manufactured by NeuroNexus.

3.1.3 Generation 3 (G3) Devices

The third generation (G3), designated as ultra-thin high-density microelectrode arrays (HD MEAs), was fabricated in Year 3 (Y3) and enhanced with additional features informed by impedance data and parameters obtained from the generation 2 devices. Year 3 primarily focused on performing electrochemical impedance spectroscopy (EIS) measurements on the G3 arrays in vitro and analyzing their impedance spectra.

3.1.3.1 Design of Generation 3 (G3)

The G3 electrode array was developed to evaluate stimulation through ultramicroelectrodes with diameters of 5 m, 10 m, 15 m, and 20 m, patterned onto ultrathin substrates. As shown in Figure 3-4, the design includes two large reference electrodes, four looped traces for assessing low-impedance limits, and three terminal traces intended for high-impedance measurements.

3.1.3.2 Generation 3 (G3) Fabrication and Coating

The G3 electrode arrays were built using NeuroNexus fabrication methods to produce a 19 recording sites. A 6-inch wafer was processed through a photolithographic technique to define the electrode sites. Each array was 5.5 m thick, made up of a 4.4 m silicon layer and a 1.1 m amorphous silicon carbide (a-SiC) layer. The electrode sites ranged in size from 20 m^2 to 320 m^2, with spacing between sites (pitch) varying from 6 m to 20 m depending on the layout. These dimensions were confirmed using optical and scanning electron microscopy (SEM). The metal traces showed only small deviations (±2 m), and the total thickness stayed within 10% of the 5 m design target, matching fabrication standards. To improve charge storage capacity, the electrodes were coated with sputtered iridium oxide film (SIROF) in thicknesses of either 300 nm or 800 nm. Finally, the arrays' performance was validated using electrochemical impedance spectroscopy (EIS) in phosphate-buffered saline (PBS).

3.2 Platinum Disk Ultramicroelectrode

Two platinum disk electrodes with diameters 10 m and 25 m diameter were fabricated and used as prototype to study the impedance response of ultramicroelectrodes. The electrodes were evaluated as a function of potential in phosphate-buffered saline (PBS) and the impedance data

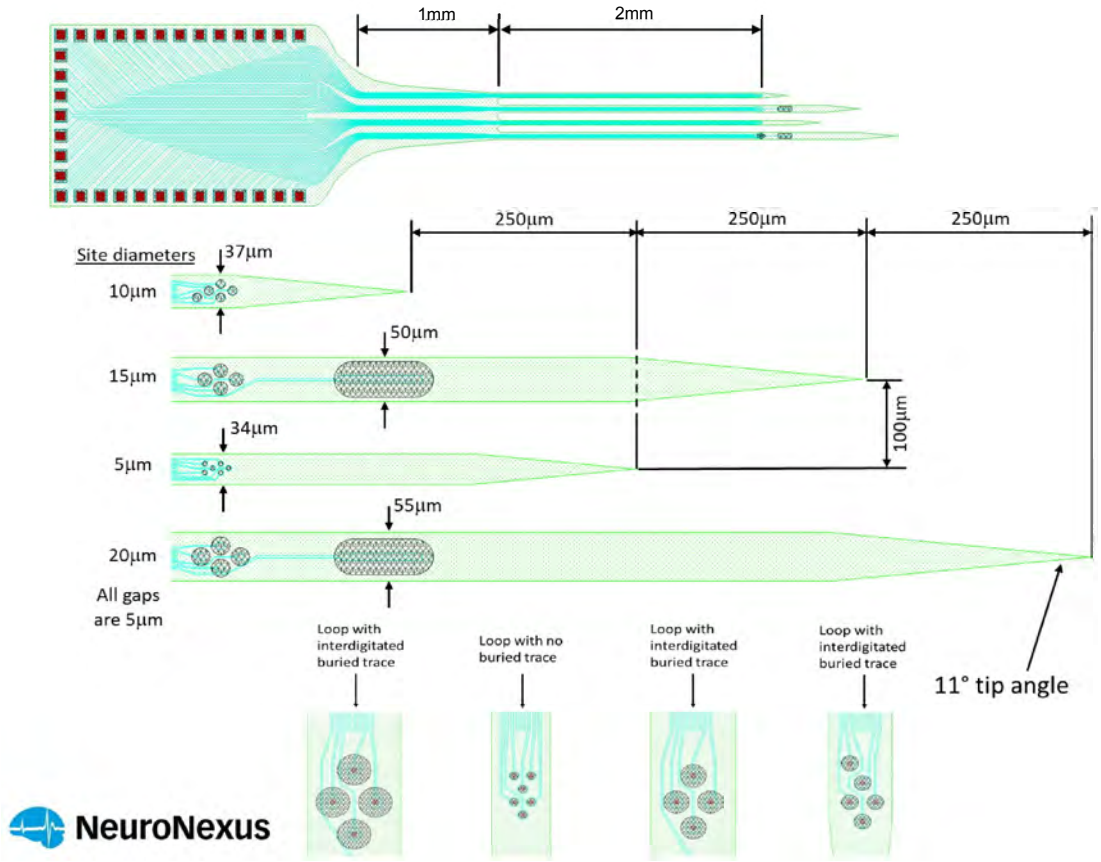

Figure 3-4. Schematics representation of generation 3 (G3) array device featuring 4 shanks. G3 electrode array differs from G1 and G2. The G3 is designed with 19-channel ultra-thin high-density microelectrode sites of diameters 5 m, 10 m, 15 m, and 20 m, and two large reference electrodes with geometric surface areas (GSAs) of approximately 4000 m^2. Four looped traces for low-impedance assessment, and three terminal traces for high-impedance assessment were added to measure the accuracy contour plot. The device was provided by NeuroNexus.

were analysed and interpreted using the measurement model. The extracted parameters provided insights into the general impedance characteristics of ultramicroelectrodes.

Platinum Disk Design and Fabrication: The fabrication procedure was identical for the 10 m and 25 m platinum-disk ultramicroelectrodes evaluated in this study. Each platinum disk was mounted onto a stainless-steel wire using an adhesive carbon fiber, and then embedded within a 7 cm glass tube, as depicted in Figure 3-5. To seal the platinum to the glass, the assembly was heated at elevated temperatures (200–300^{0}C). An optical microscope was employed to inspect the seal at the wire-glass interface and to confirm the absence of air bubbles near the metal tip. The end of the capillary containing the platinum disk was then polished with progressively finer grit sandpaper to achieve a smooth, flat surface. The platinum-disk electrode configuration served as a prototype for impedance analysis of ultramicroelectrodes. The device was provided by Professor Won Tae Choi at the University of Florida.

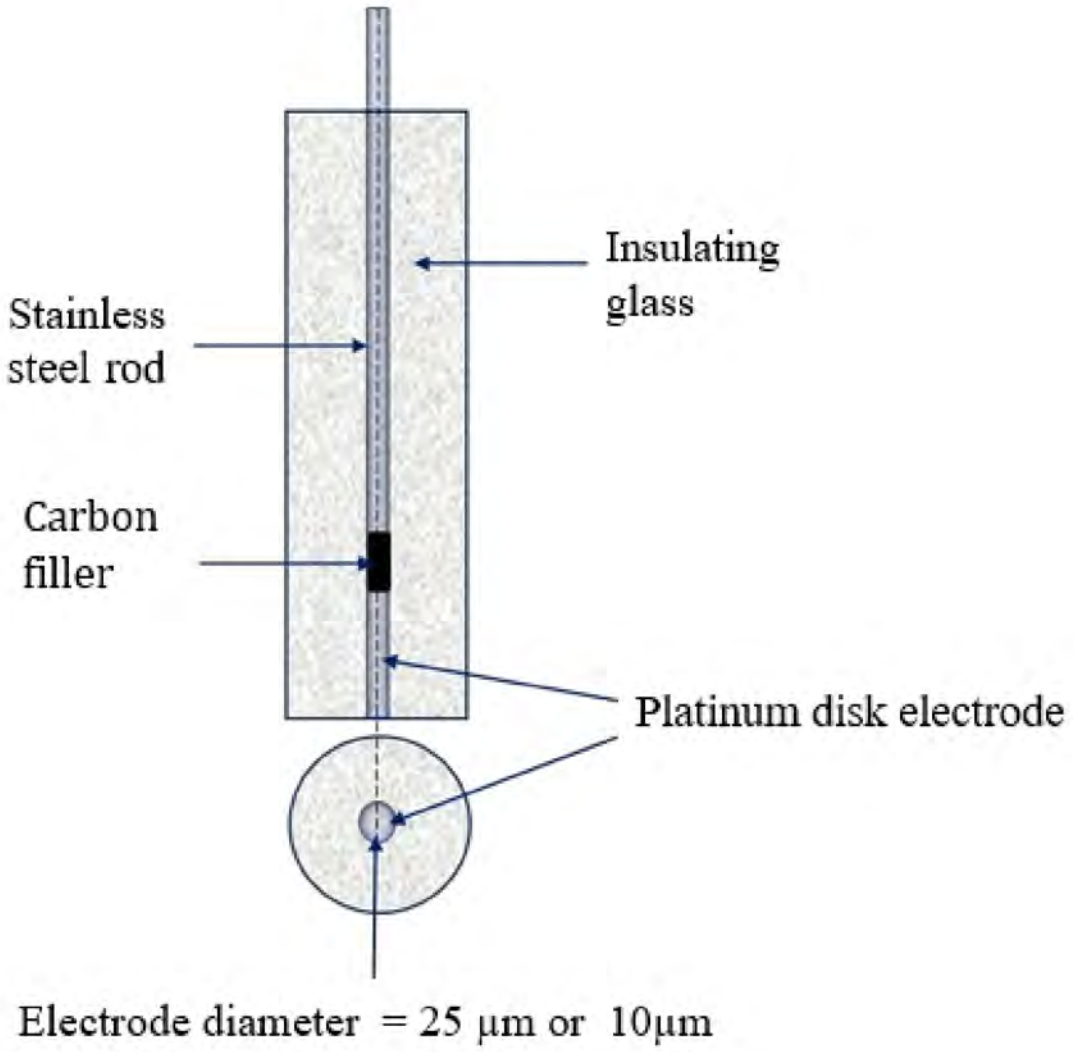

Figure 3-5. Schematics representation of platinum disk ultramicroelectrodes. The platinum disk ultramicroelectrodes has diameters of 10 m and 25 m, each embedded on a stainless-steel rod with an adhesive carbon fiber and placed in an insulating glass. The electrode served as a prototype for impedance analysis of ultramicroelectrodes. The device was provided by Prof. Won Tae Choi at the University of Florida.

CHAPTER 4
SYSTEM SPECIFIC ACCURACY CONTOUR PLOTS

The usable frequency range of impedance spectroscopy measurements were evaluated by plotting the accuracy contour plots for Gamry Reference 600+ potentiostat alone, and when connected to the neural-stimulation devices via different cables and connectors. The accuracy contour limits of the potentiostat were evaluated by performing impedance measurements under open-circuit and closed-circuit conditions. The loop and terminal traces integrated into the generation 2 and generation 3 electrode devices were used to perform the low-impedance and high-impedance measurements, respectively. The accuracy contour plots showed the frequency range where accurate impedance spectra can be obtained for both the potentiostat by itself and when connected to the electrode devices. Measurement model analysis of EIS data confirmed consistency with Kramers–Kronig relations, with differences observed in high-frequency points attributed to geometry-induced ohmic resistance for the microelectrodes and parasitic capacitance for the ultramicroelectrodes. The results obtained from accuracy contour plots were used to gain insights into the frequency and impedance spectrums affected by the cable capacitance.

4.1 Overview of Accuracy Contour Plots

Impedance spectroscopy measurements depends on the experimental conditions, electrochemical system under study and hardware limitations, such as cables, and connectors. In practice, cables and connectors can add capacitive or inductive effects to the measurements, that obscure the true impedance response of the electrodes and complicate data interpretation. The best practice is to ensure that the impedance spectra analysed is not affected by cables and connection hardware. Accuracy contour plots provide a powerful approach for assessing the precision of EIS measurements by visualizing the usable impedance and frequency range of a given system [131]. The accuracy contour plots [1], serve as effective tool to determine the limits of a specific potentiostat and experimental setup. The plot represents the impedance magnitude versus frequency on a log-log scale, showing the reliable frequency points where the low and high impedance limits could be obtained for a given potentiostat and electrode device [99].

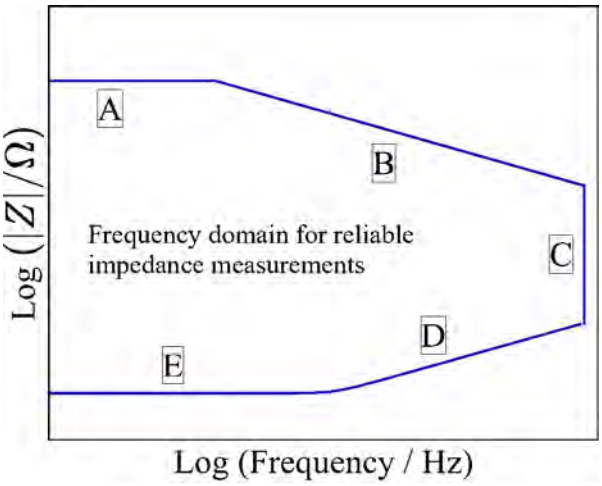

Figure 4-1. Schematic representation of accuracy contour plot: (A) maximum measurable impedance; (B) lead capacitance; (C) maximum measurable frequency capability of the instrument; (D) lead inductance; (E) lowest measurable impedance.

A generic form of accuracy contour plot is shown in Figure 4-1. The region of reliable impedance spectra is highlighted [131]. The boundaries of the plot include: (A) the maximum measurable impedance and (E) the lowest measurable impedance, both determined by open-lead and shorted-lead EIS measurements. The upper-frequency limit of the instrument is represented by (C), while (B) and (D) correspond to the lead's capacitance and inductance, respectively. By leveraging accuracy contour plots, researchers can investigate the origins of high-frequency capacitive loops associated with various electrode configurations [109]. Previous studies [131] have outlined methods for generating accuracy contour plots for Gamry instruments. Hazelgrove et al.[21] highlighted the importance of measuring accuracy contour plots for of a given electrochemical system under investigation. Dong et al.[59] plotted the accuracy contour plots for the Autolab PGSTAT12 (Metrohm, Utrecht, The Netherlands) by itself and when connected to a neural implant via a connection hardware. Hence, relying solely on the accuracy contour plot provided by the vendor is not sufficient.

4.2 Methods

The impedance measurements were performed with a Gamry Reference 600+ with Framework version 7.10.3. The instrument has a 60 cm cable and is capable of functioning as a

potentiostat or galvanostat. The accuracy contour plots of the potentiostat were obtained in air using open-lead and shorted-lead configurations that enabled high-impedance and low-impedance measurements, respectively. The generation 2 (G2) and generation 3 (G3) electrode devices presented in section 3.1.2 and section 3.1.3 are designed with built-in terminal and looped traces that was used to construct the accuracy contour plot. The electrodes were connected to the potentiostat via different configurations: (i) A custom-designed junction box with Zif-clip connector and (ii) the NeuroNexus connector. The accuracy contour plots were measured in air and phosphate-buffered saline (PBS) conditions. The impedance data was analysed with the measurement model program [97] to obtain stochastic error structure and asses consistency with the Kramers–Kronig relations.

4.2.1 Accuracy Contour Measurements for Gamry Reference 600+

The performance of the Gamry Reference 600+ were evaluated following established guidelines [131]. Depending on the electrochemical setup, impedance measurements were conducted under open-circuit or closed-circuit conditions using potentiostatic EIS (potential control) or galvanostatic EIS (current control) techniques.

4.2.1.1 Open-lead Measurements

The open-lead measurements were performed at open-circuit conditions to obtain the high-impedance limits of the potentiostat. As shown in Figure 4-2, the working electrode (WE) and working sense (WS) leads were joined together, while the reference (RE) and counter (CE) leads were connected separately. A 2 cm air gap was maintained between the two lead pairs, following the procedure described in [131]. Both pairs of cables were placed inside a grounded Faraday cage to minimize noise. Potentiostatic EIS measurements were then performed across a frequency range from 1 MHz to 10 mHz, using a 50 mV rms perturbation amplitude.

4.2.1.2 Shorted-lead Measurements

The shorted-lead measurements were conducted at a closed-circuit using the galvanostatic EIS technique. The low-impedance measurement was performed at a frequency range from 1 MHz to 10 mHz with zero DC current and an AC current of 424 mA rms [131]. As illustrated in

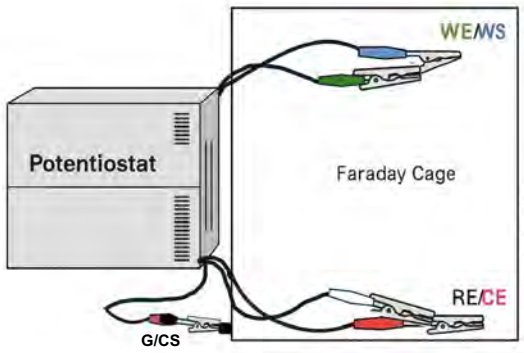

Figure 4-2. Schematics representation of electrochemical cell set-up for Gamry reference 600+ open-lead measurement. The impedance measurement was conducted at open-circuit in a grounded faradaic cage. The WE/WS and CE/RE pairs were separated by 2cm air gap. The configuration was used to obtain the high-impedance limits of the accuracy contour plot.

Figure 4-3, the WE/CE and WS/RE twisted lead pairs were clipped to a copper rod, forming a closed-circuit connection between the leads. The electrochemical set-up was placed in a Faraday cage to shield the electrical noise from the environment. The Faraday cage was grounded to keep the potential at the same level as the ground reference.

4.2.2 Accuracy Contour Measurements for Brain-stimulation Devices

The generation 2 (G2) device shown in Figure 3-3, and generation 3 (G3) electrode shown in Figure 3-4, has gold traces in form of loops and terminated lines that can be used for low-impedance and high-impedance measurements, respectively. The generation 2 device was evaluated when connected to the Gamry Reference 600+ using either a custom junction box with a TDT ZIF-Clip connector or a NeuroNexus connector. The generation 3 device was only interfaced with the Gamry Reference 600+ through the custom junction box with a TDT ZIF-Clip connector, as shown in Figure 4-4.

The accuracy contour measurements for each device (G2 or G3) was performed separately using similar approach at open-circuit condition. The electrochemical set-up was a three-electrode configuration that consist of the working electrode (G3 or G2), an Ag/AgCl reference, and a

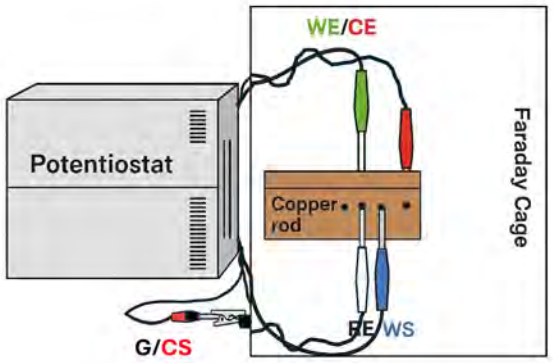

Figure 4-3. Schematics representation of electrochemical cell set-up for Gamry reference 600+ shorted-lead measurement. The impedance measurement was conducted at closed-circuit in a grounded faradaic cage. The WE/CE and WS/RE pairs were shorted together using a copper rod. The configuration was used to obtain the low-impedance limits of the accuracy contour plot.

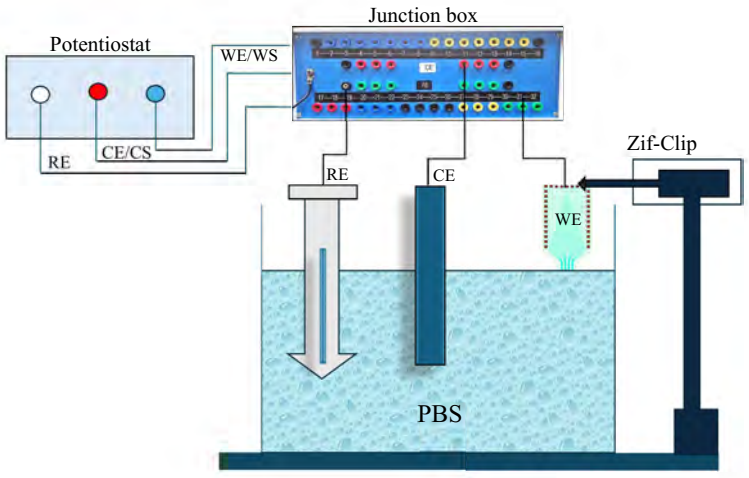

Figure 4-4. Schematics representation of electrochemical cell set-up for accuracy contour measurement in PBS with the custom Junction box with TDT Zif-clip connector. The impedance measurements were performed at open-circuit on the G2 device, in a grounded faradaic cage. The G2 device is integrated with terminal and looped traces used to evaluate the high and low-impedance limits of the accuracy contour plot.

platinum-mesh counter electrode. The low- and high-impedance measurements were performed both in air and phosphate-buffered saline. Both measurements in air and PBS, were conducted at a perturbation amplitude of 25 mV rms, with a frequency sweep from 1 MHz to 10 mHz at 10 points per decade. The PBS solution used in these experiments contained 0.01M phosphate buffer, 0.0027M KCl, and 0.137M NaCl to simulate physiological conditions. A summary of the impedance measurements at different perturbation amplitudes is compiled in Table 4-1.

4.2.2.1 High-impedance Measurements

The high-impedance (open-lead) measurements were performed by connecting the terminated sites (channels) of the G2 or G3 devices as working electrode. The measurement was made when the working electrode (G2 or G3) was immersed in phosphate buffered saline and when the working electrode was exposed to air. For both measurements in air and PBS, the Ag/AgCl reference and platinum-mesh counter electrodes remained in the PBS solution. The measurements were made using the Potentiostatic EIS approach as shown in Table 4-1

4.2.2.2 Low-impedance Measurements

The low-impedance (shorted-lead) measurements were performed by connecting the loop channels of the G2 or G3 devices as the working and counter electrodes. The measurement was made when the working electrode (G2 or G3) was immersed in phosphate buffered saline (PBS) and when the working electrode was exposed to air. For both measurements in air and PBS, the Ag/AgCl reference remained in the PBS solution. Potentiostatic EIS measurement was difficult to perform with the NeuroNexus connector in air, hence the Hybrid EIS option was used as summarized in Table 4-1.

Table 4-1. Impedance measurements recorded at different perturbation amplitudes for the Gamry Reference 600+ Potentiostat, both independently and when connected to the ultramicroelectrode device via a junction box or NeuroNexus cable.

Connector	Feature	Impedance measurement		Perturbation amplitude	
		Air	PBS	Air	PBS
Gamry Ref. 600+	Open-lead (WE/WS CE/RE)	Potentiostatic	-	50 mV rms	-
Gamry Ref. 600+	Shorted-lead (WE/CE RE/WS)	Galvanostatic	-	424 mA rms	-
Jbox/TDT ZIF-Clip	Open-lead (Terminal)	Potentiostatic	Potentiostatic	25 mV rms	25 mV rms
Jbox/TDT ZIF-Clip	Shorted-lead (Loop)	Potentiostatic	Potentiostatic	25 mV rms	25 mV rms
NeuroNexus	Open-lead (Terminal)	Potentiostatic	Potentiostatic	50 mV rms	25 mV rms
NeuroNexus	Shorted-lead (Loop)	Hybrid	Potentiostatic	25 mV rms	25 mV rms

4.2.3 Measurement Model Regression

The impedance spectra of Gamry Reference 600+ and brain stimulation device were analyzed using the measurement model software developed by Waston and Orazem [97]. The program fits a series of Voigt circuit elements formulated by Agarwal et al.[3, 114, 113] to the impedance data. As shown if Figure 2-7, the measurement model represented as Voigt circuit consist of time constants in series with the ohmic resistance e.

To achieve an optimal fit within a 95.4% confidence interval (±2), the number of Voigt circuit elements was sequentially increased up to a maximum value of K. A Monte Carlo simulation was performed to calculate the 95.4% confidence interval for the predicted impedance values, following the method outlined by Orazem [132]. To quantify the noise level of the impedance measurements, replicates of impedance data for measurements made at open-circuit and closed-circuit conditions were uploaded to the measurement model program for error weighting by the stochastic error structures [133]. The stochastic error contribution of each replicated data sets was estimated by the real and imaginary standard deviation of impedance as functions of frequency. An empirical model fitted to the standard deviation of the impedance spectra is given by

$$_{error} = \quad < | \ _j | > + \quad < | \ _r | > + \quad < | \ \cdot | >^2 + \qquad (4\text{-}1)$$

where is the standard deviation of errors, $|\ _r|$ is the absolute value of the real impedance, $|\ _j|$ is the absolute value of the imaginary impedance, and $|\ |$ is the magnitude of impedance [132]. The error parameters , , , and are constants determined by weighting the standard deviation with the variance on a 5-point moving average. The consistency of the EIS data with the Kramers–Kronig [134, 135] were assessed with the measurement model by fitting the data to the Voigt circuit elements at frequency ranges that are linear and stationary. Agarwal et al.[3] showed that the measurement model based on equation (2-19) is a Kramers–Kronig consistent model for evaluating the impedance of typical stationary electrochemical systems.

4.3 Results

The results of accuracy contour measurements in air and PBS for the Gamry Reference 600+ and the ultramicroelectrode arrays (G2 and G3) are presented in this section. Regression of impedance spectra, assessment of data consistency with Kramers–Kronig relations, and evaluation of stochastic error structure was done using version 1.8 of Watson and Orazem's [97] measurement model program . The analysis produced insightful figures, including accuracy contour plots, Nyquist plots, real and imaginary residuals, and stochastic error structure plots. These figures play a crucial role in interpreting the accuracy and reliability of the impedance measurements.

4.3.1 Accuracy Contour Plots

Electrochemical impedance spectroscopy measurements were performed at a frequency sweep from 1 MHz to 10 mHz. The accuracy contour plots for the Gamry Reference 600+ potentiostat alone and when connected to the custom junction box with the TDT ZIF-Clip connector or the NeuroNexus connector are discussed.

4.3.1.1 Gamry Reference 600+

The accuracy contour plots are presented in Figure 4-5 for open-lead (open-circuit) and shorted-lead (closed-circuit) EIS measurements performed in air with the Gamry Reference 600+ alone. The frequency range was varied from 10 mHz to 1 MHz. The lowest measurable impedance for the Gamry Reference 600+ was 1 Ω and the maximum impedance limit was above 1 TΩ. For open-circuit measurements, the estimated errors, represented as the standard deviation of impedance magnitude, were found to be at an order of magnitude smaller than the upper impedance limit across all frequencies. Conversely, for shorted-lead measurements, the error approached the low-impedance limit at low frequency points below 1 Hz.

4.3.1.2 Generation 2 (G2) Array

Accuracy contour plots (ACPs) measured for the generation 2 device are presented in Figure 4-6. The measurements were performed with the custom junction box with a TDT ZIF-Clip connector and the NeuroNexus connector. The maximum and minimum impedance limits signifies open-lead and shorted-lead measurements. The region within the maximum and

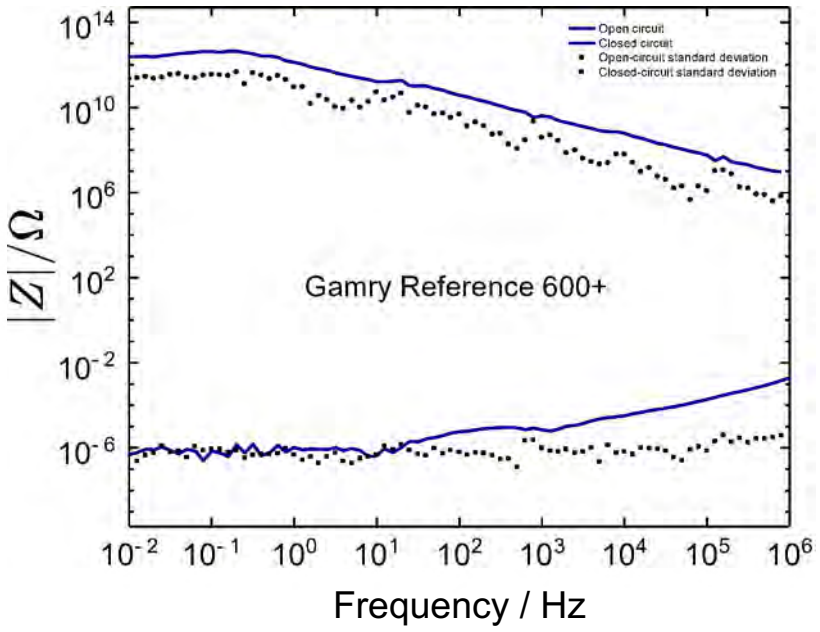

Figure 4-5. Accuracy contour plots measured at open circuit and closed circuit for the Gamry Reference 600+ potentiostat with 0.6 m cables. The stochastic errors associated with the open-circuit and closed-circuit measurements are presented as black circles and black squares respectively.

minimum impedance limits for air and PBS, represents the areas where reliable impedance spectra can be obtained. As shown in Figure 4-6(a) and 4-6(b), the region for accurate impedance data became much smaller when the devices were immersed in phosphate-buffered saline electrolyte. The usable range in PBS is an indication of the interaction between the gold traces and the electrolyte. The upper-impedance limits of the custom junction box with the TDT ZIF-Clip connector was an order of magnitude larger than that of the NeuroNexus connector in PBS, whereas the low-impedance limits of the was one order of magnitude lower than the NeuroNexus. For measurements made in air, the custom junction box with a TDT ZIF-Clip connector and the NeuroNexus connector have similar low-impedance limits that are much larger than for the potentiostat by itself in Figure 4-5. The upper limits (open-circuit) for the NeuroNexus connector were two orders of magnitude larger than that of the custom junction box with the TDT ZIF-Clip connector. The results showed the variations in conducting impedance measurements with

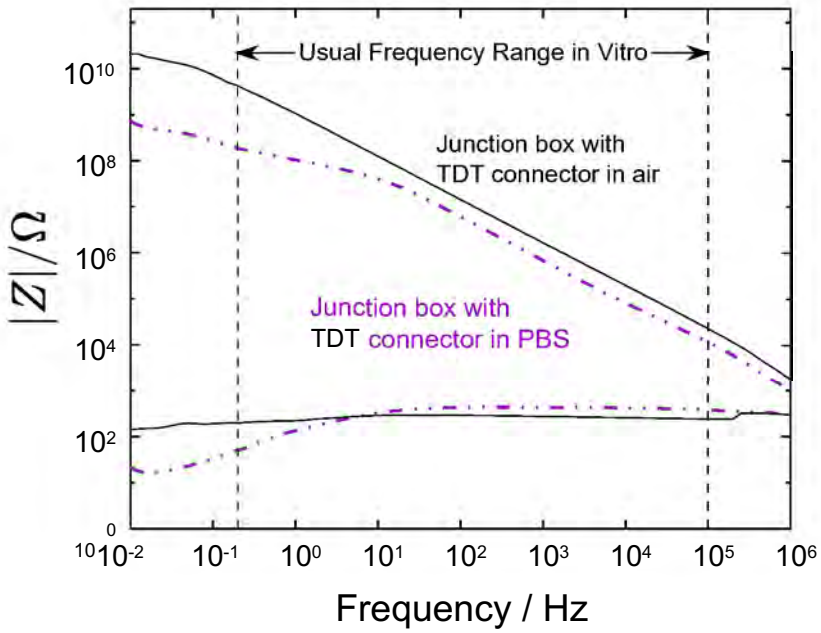

(a)

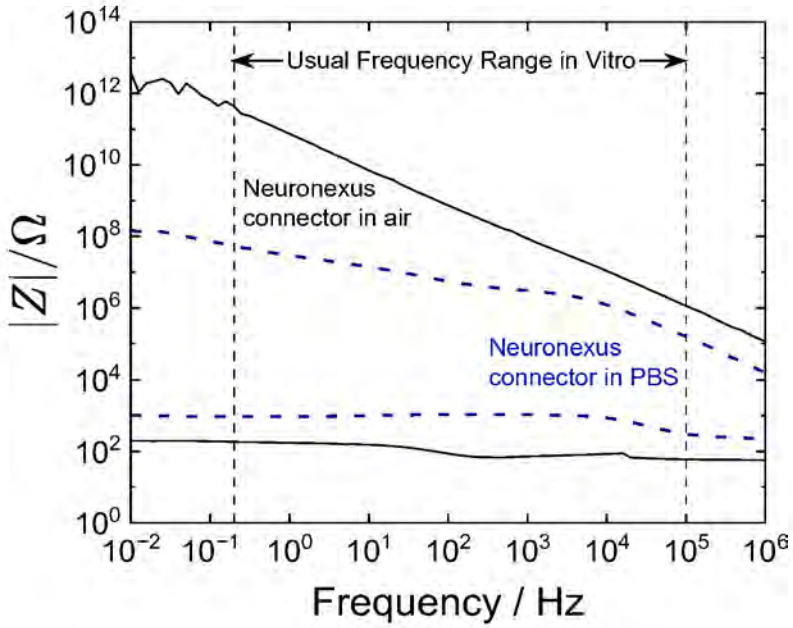

(b)

Figure 4-6. Accuracy contour plots for impedance measurements performed at open circuit with generation 2 device: a) for custom junction box with a TDT ZIF-Clip connector and b) for NeuroNexus connector. The usable impedance range became much smaller when the devices were immersed in PBS. The boundaries for the maximum and minimum impedance represent measurements made with the device's terminal and looped traces, respectively.

different configurations of external cables and connectors, emphasizing the need to measure the accuracy contour plot for each electrochemical set-up studied.

4.3.1.3 Generation 3 (G3) Array

Accuracy contour plots (ACPs) for the generation 3 (G3) device are displayed in Figure 4-7. The measurements were carried out using a custom junction box with a TDT ZIF-Clip connector, both in air and in phosphate-buffered saline (PBS). As shown in Figure 3-4, the G3 device incorporates four shanks with four looped traces designed for low-impedance evaluation and three terminal traces intended for high-impedance assessment. Impedance limits recorded in air using the terminal and looped traces are depicted as straight lines, while the dotted lines illustrate the corresponding high- and low-impedance measurements performed in PBS, as presented in Figure 4-7.

The enclosed region between the maximum and minimum impedance limits in air and PBS delineates where usable impedance spectra can be obtained. Notably, Figure 4-7 reveals that when the device is immersed in PBS, the area permitting accurate impedance data becomes smaller compared to air, reflecting the increased interaction between the gold traces and the electrolyte. The accuracy contour plots generated for the G3 device closely align with that of G2 device, highlighting consistency and guiding the interpretation of usable measurement ranges.

4.3.2 Analysis of Impedance Spectra for Generation 2 Device

The impedance data recorded at different perturbation amplitudes are presented in Table 4-1. Three sets of replicated impedance spectra were obtained for the Gamry Reference 600+ Potentiostat, both independently and when connected to the ultramicroelectrode device via a junction box or NeuroNexus cable. Each replicated datasets required 115 minutes for experiments conducted in air or PBS. A voltage-stabilization period of five minutes was performed before the EIS measurement. The impedance datasets for the Gamry Reference 600+ and the brain-stimulation electrodes were evaluated using the measurement model. The model fits the data across the frequency range that are linear and assesses the data consistency with the Kramers–Kronig relations.

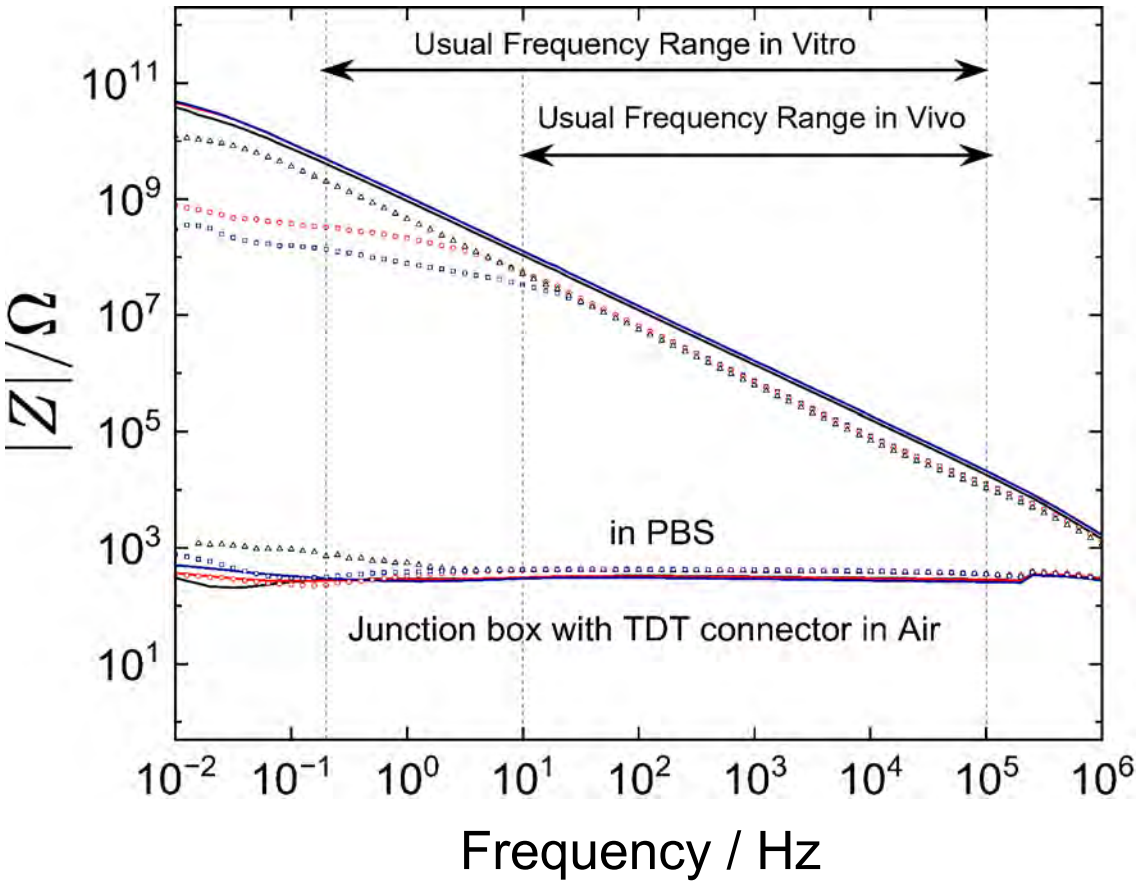

Figure 4-7. Accuracy contour plots measured in air and PBS with the G3 device using custom junction box with a TDT ZIF-Clip connector. The G3 device has four shanks with four looped traces designed for low-impedance evaluation and three terminal traces intended for high-impedance assessment. The high and low-impedance measurements performed in air are shown as straight lines and the corresponding measurements in PBS are depicted as dotted lines. The usable impedance limit reduced when the devices were immersed in PBS.

4.3.2.1 Measurements in Air

The Gamry Reference 600+ accuracy contour measurements were performed in air at open-circuit and closed-circuit conditions. The resulting impedance spectra for open and closed circuit EIS measurements are presented in Figure 4-8. The Nyquist plot for the high-impedance spectra obtained at open-circuit conditions are presented in Figure 4-8(a). The high-impedance data showed capacitive and inductive loops at low frequency points. The data were influenced by noise at low frequency. The measurement model fits the high-impedance data across the entire frequency range consistent with the Kramers–Kronig relations. The low-impedance spectra for the Gamry Reference 600+ obtained at closed-circuit conditions were regressed with the measurement model. The resulting Nyquist plot is shown in 4-8(b). The model fits the impedance data across the entire frequency range which implies that the data is consistent with the Kramers–Kronig relations.

The impedance spectra obtained for the G2 device connected to the custom junction box with a TDT ZIF-Clip are shown in Figure 4-9. The G2 device was integrated with terminal and looped traces for assessing high and low-impedance limits respectively. The Nyquist plot for the high-impedance spectra obtained with the custom junction box are presented in Figure 4-9(a). The measurement model could not capture the impedance behavior at low frequency which implies that the data at low frequency is inconsistent with the Kramers–Kronig relations. The Nyquist plot for the low-impedance data obtained with the custom junction box are presented in Figure 4-9(b), corresponding to measurements on the looped features of the G2 electrodes. The data showed an inductive loop feature across all frequency points. The measurement model captured the experimental impedance response at frequency ranges consistent with the Kramers–Kronig relations.

4.3.2.2 Measurements in Phosphate-buffered Saline

Nyquist plots of the low-impedance and high-impedance measurements conducted in PBS are shown in Figure 4-10. The experimental data was analysed with the measurement model. The high-impedance data obtained with the custom junction box featuring a TDT ZIF-Clip connector

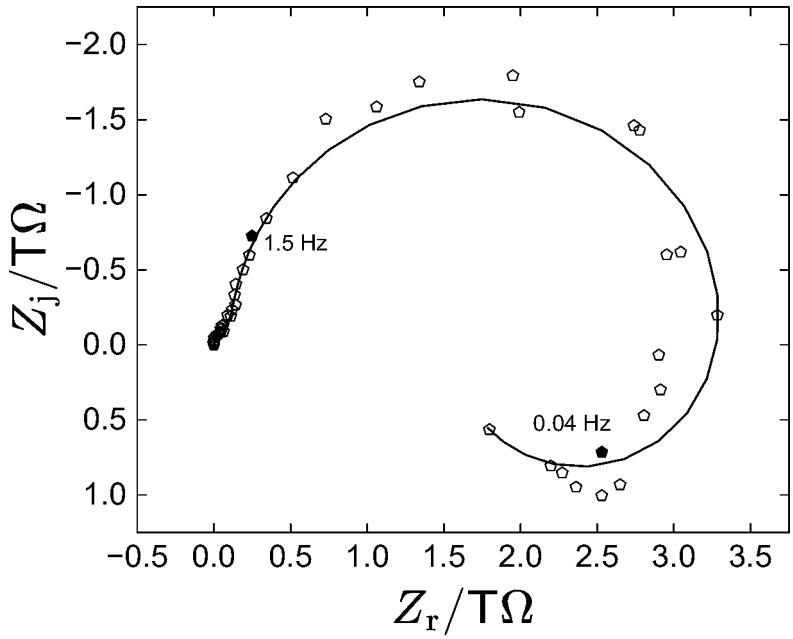

(a)

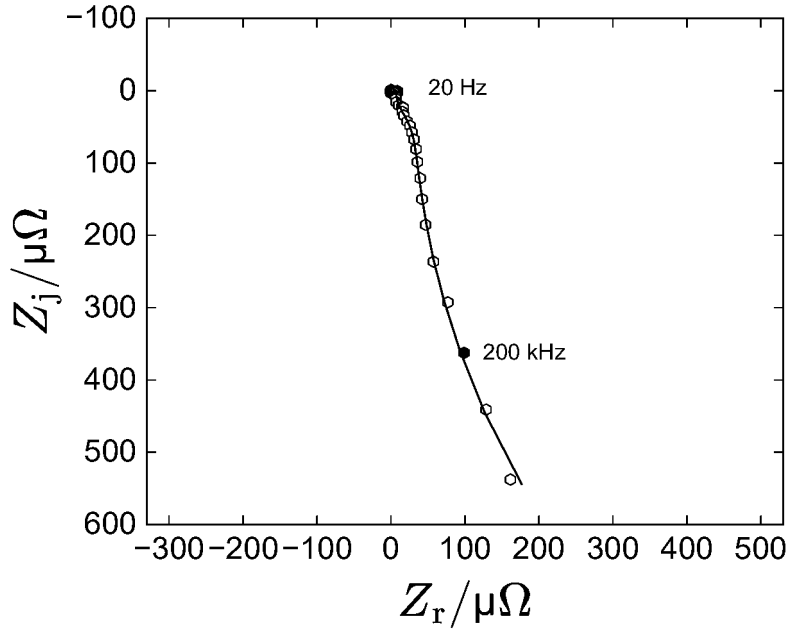

(b)

Figure 4-8. Measurement model regression results in Nyquist format for impedance measurements performed in air for the Gamry Reference 600+ potentiostat alone: a) high-impedance data recorded at open-circuit and b) how-impedance data recorded at closed-circuit. The black circles represent the experimental data and the line represent the fit of the measurement model.

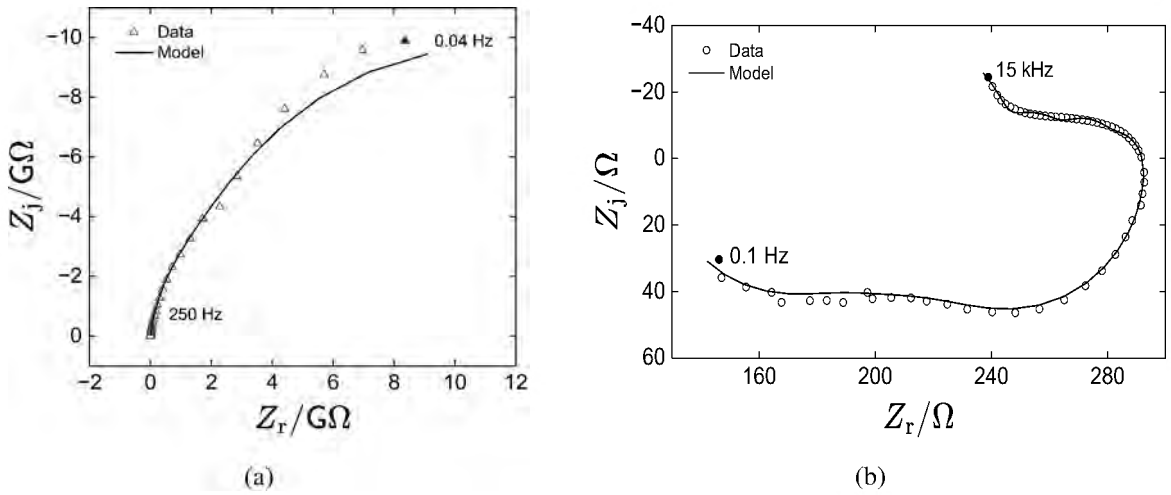

Figure 4-9. Measurement model regression results in Nyquist format for EIS measurements conducted in air and at open circuit with the custom junction box and a TDT ZIF-Clip connector for G2 device: a) high-impedance spectra obtained with terminal features, and b) low-impedance spectra obtained with looped features. The line represents the fit of the measurement model obtained with error structure weighting.

and the NeuroNexus connector are shown in Figures 4-10(a) and 4-10(c) respectively. The measurement model successfully accounted for the high-frequency distortions caused by cable and connection effects. The low-impedance data obtained via the custom junction box with a TDT ZIF-Clip connector and the NeuroNexus connector, are presented in Figures 4-10(b) and 4-10(d), respectively. The model accurately captured the inductive and capacitive behavior observed at low frequencies. The strong agreement between measured and modeled data confirms consistency with the Kramers–Kronig relations.

4.3.3 Stochastic Error Structure Analysis

The stochastic error structure analysis enabled filtering of errors introduced by instrument artifacts during impedance measurements. The stochastic error structures of the real and imaginary standard deviation of impedance spectra were estimated by weighting the impedance data with a Levenberg–Marquardt regression [97]. Replicated EIS datasets for the Gamry Reference 600+, the custom junction box with a TDT ZIF-Clip connector, and NeuroNexus connector were fitted to the measurement model. An unique number of Voigt circuit elements and frequency range were maintained across each replicated datasets. For each replicates, the standard

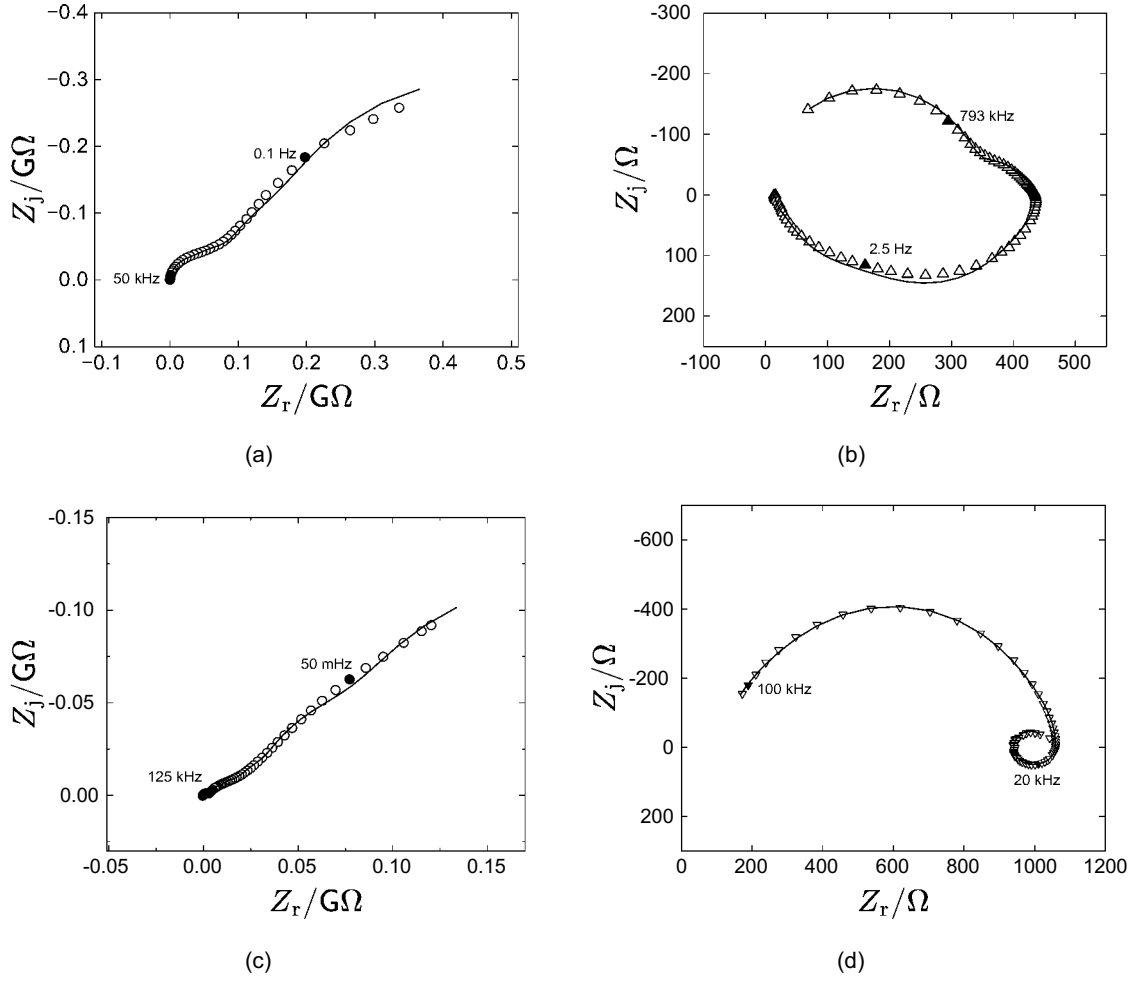

Figure 4-10. Measurement model regression results in Nyquist format for high and low EIS measurements conducted in PBS and at open circuit with the G2 device built-in terminals and loops: a) and b) high and low-impedance spectra obtained with the custom junction box and ZIF-Clip connector, c) and d) high and low-impedance spectra obtained with NeuroNexus connector. The line represents the fit of the measurement model obtained with error structure weighting.

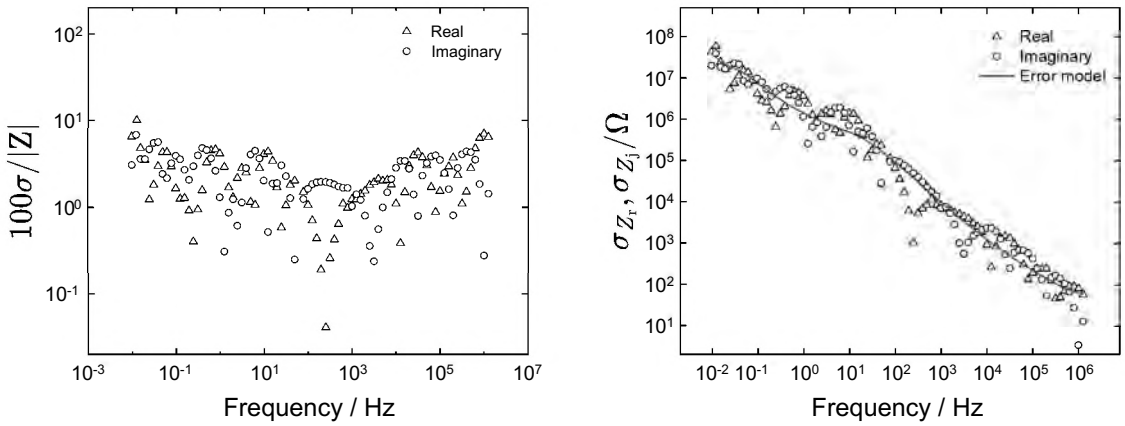

Figure 4-11. Error structure plots for high-impedance measurement performed for the terminal traces of the G2 device in phosphate buffered saline when connected via the custom junction box with a TDT ZIF-Clip connector: a) normalized error structure and b) non-normalized error structure. The line represents the fit of equation (5-1), circles represent the standard deviation for the imaginary part of the impedance and triangles represents the standard deviation for the real part of the impedance.

deviation of the residual errors were computed as a function of frequency. The error structures for the high-impedance measurements conducted in PBS using the custom junction box with a TDT ZIF-Clip connector, are presented in Figure 4-11, as functions of frequency. The standard deviation normalized by the impedance magnitude is shown in Figure 4-11(a). The errors are on the order of 10% of the impedance magnitude at low frequency. The non-normalized standard deviations are presented in Figure 4-11(b). The standard deviations of the real and imaginary components closely overlap as expected for datasets consistent with the Kramers–Kronig relations. The dashed line in both figures represents the fit of equation (5-1). The error model parameters are listed in Table 7-1. However, a statistically significant value for could not be determined.

4.3.4 Assessment of Consistency with Kramers–Kronig Relations

The Kramers–Kronig [134, 135] relations offer a robust consistency check for impedance spectroscopy measurements under the assumption of system stationarity. Discussion about the Kramers–Kronig relation can be found in section 2.5.2.1. The measurement model, defined in Equation (2-19), was used to regress the impedance data, as it adheres to Kramers–Kronig

Table 4-2. Stochastic error structure parameters for impedance measurements via the custom junction box with a TDT ZIF-Clip connector in PBS. the error parameters were estimated form equation (5-1).

Parameter	Value ± St. Dev.
	$0.01466 \pm 5.669 \times 10^{-25}$
	–
	$7.945 \times 10^{-11} \pm 3.484 \times 10^{-16}$
	45.6944 ± 14.21

consistency. To ensure the model accurately captured the complete impedance response, the number of Voigt elements, as illustrated in Figure 2-7 was systematically increased until all fitted parameters were enclosed within the 95.4% confidence interval and excluded zero. The resulting residual errors for the Gamry Reference 600+ are shown in Figure 7-5 as a function of frequency. The real and imaginary residuals for the high-impedance data are further detailed in Figures 4-12(a) and 4-12(b), respectively. In each plot, the residuals are represented by blue circles, and the ±2 (95.4%) confidence intervals are indicated by dashed black lines. The real and imaginary residual errors predominantly fall within the 95.4% confidence interval, indicating that the impedance data are consistent with the Kramers–Kronig relations. The residuals associated with the low-impedance (shorted-lead) measurements are presented in Figures 4-12(c) and 4-12(d) for the real and imaginary components, respectively. The real residual errors falls within the 95.4% confidence interval across the entire frequency range. In contrast, the residual errors for the imaginary component exceeded the confidence interval at certain frequency ranges.

The residual errors for the high-impedance measurements conducted in phosphate-buffered saline (PBS) with the custom junction box with a TDT ZIF-Clip connector are shown in Figures 4-13(a) and 4-13(b). The regression analysis was weighted by the stochastic error model described by Equation (5-1), with the associated error parameters summarized in Table 7-1. The residual errors for the predicted real part of the impedance remained within the 95.4% (±2) confidence interval across the measured frequency range. However, the residuals for the imaginary component exceeded the confidence interval at very low frequencies, specifically below 0.1 Hz. The real and imaginary residual errors for low-impedance (loop) data recorded in PBS with the

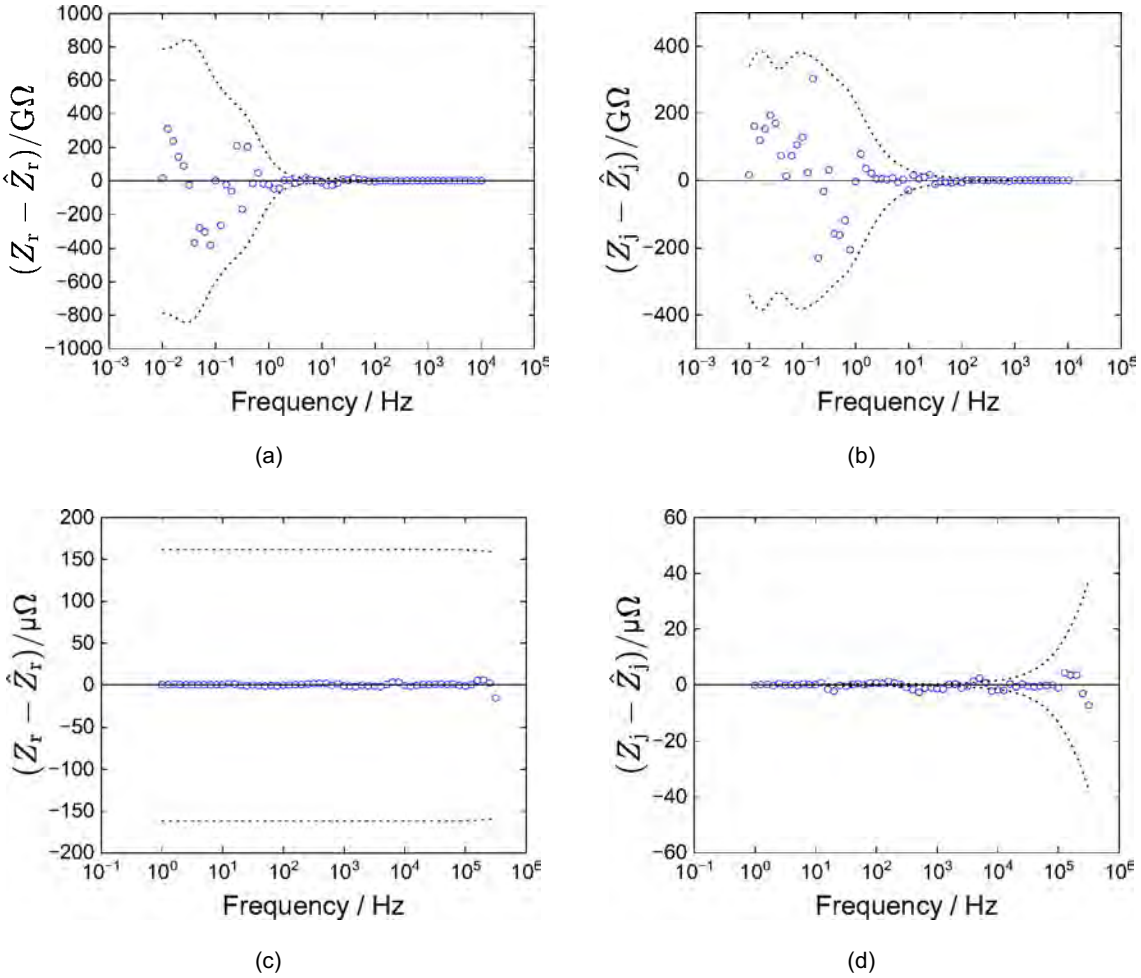

Figure 4-12. Residual errors for regression of the measurement model to the Gamry Reference 600+ impedance data under error structure weighting: a) real residuals for open circuit, b) imaginary residuals for open circuit, c) real residuals for closed-circuit, d) imaginary residuals for closed-circuit. The dashed lines represent the 95.4% (±2) confidence interval.

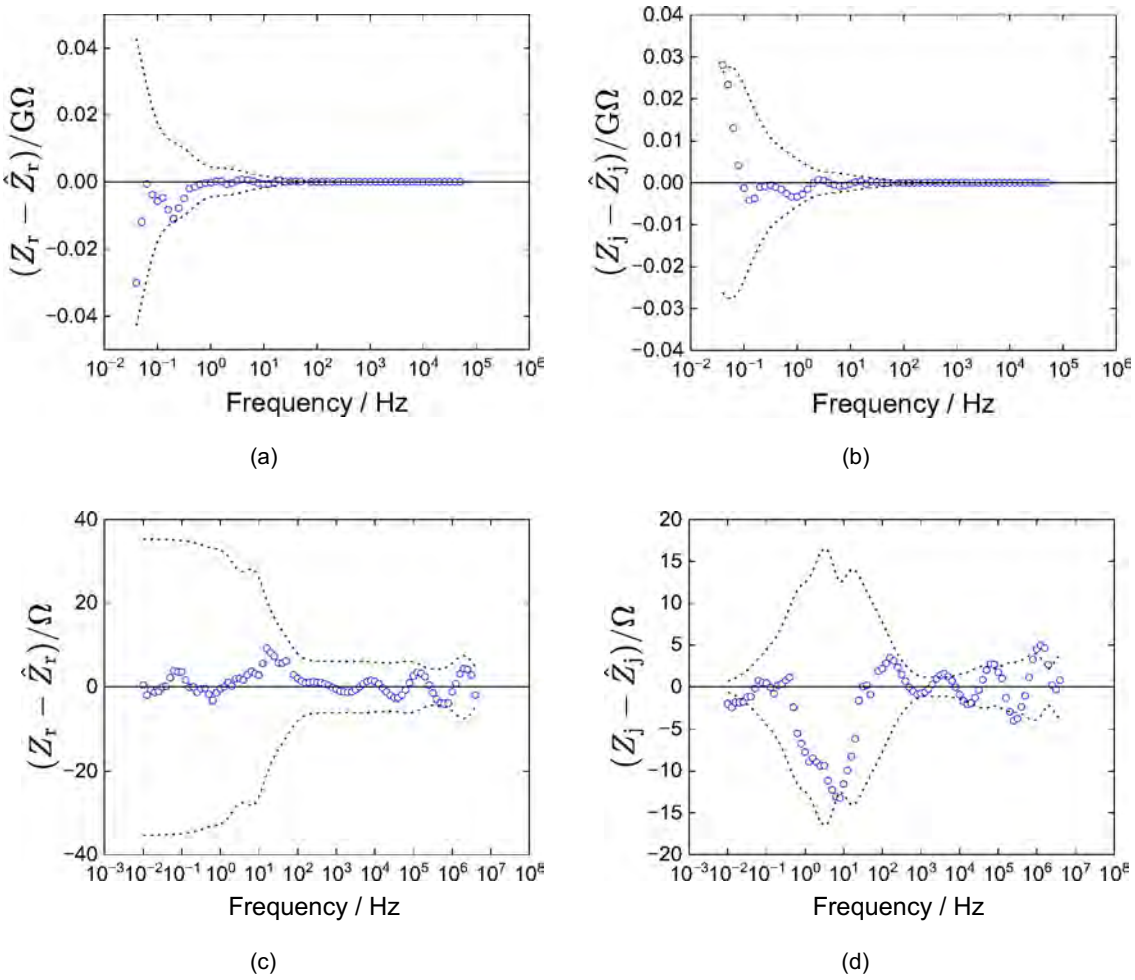

Figure 4-13. Residual errors for complex regression of the measurement model to open-circuit EIS measurements conducted in phosphate buffered saline with the custom junction box with a TDT ZIF-Clip connector: a) real residuals for open-lead (high-impedance) measurement b) imaginary residuals for open-lead (high-impedance) measurement c) real residuals for shorted-lead (low-impedance) measurement d) imaginary residuals for shorted-lead (low-impedance) measurement. The dashed lines represent the 95.4% (±2) confidence interval.

custom junction box are presented in Figures 4-13(c) and 4-13(d). The oscillations observed in the residual errors are attributed to the number of Voigt elements used in the model. The residual errors of the real part falls within the ±2 confidence interval. The errors for the estimation of the imaginary part exceeded the 95.4% (±2) confidence interval at very low and high frequency points, suggesting that the data was affected by non-stationarity in the experimental setup. The ability to fit the majority of the impedance data within the 95.4% (±2) confidence interval using the measurement model indicates that the data is consistent with the Kramers–Kronig relations.

4.4 Parasitic Capacitance

The impact of stray capacitance from capacitive coupling through cables and instrumentation, are observed at the high frequency points of impedance spectra. This effect was quantified across electrode sites of 20 m^2, 80 m^2, and 4,000 m^2 using accuracy contour plots (ACPs) and capacitance-frequency plots shown in Figure 4-14. The high-impedance limits of the accuracy contour plots reflects the leads capacitance at high frequency. As shown in Figure 4-14(a), the impedance magnitude of the smaller electrodes (20 m^2 and 80 m^2) aligned with the high-impedance limit at high-frequency points above 10 kHz. This implies that the impedance response of the smaller electrodes is heavily influenced by the cable high frequency.

Conversely, the larger electrode (4000 m^2) exhibits a distinct flat feature in its high-frequency impedance spectrum. This behavior has been previously attributed to non-uniform current and potential distribution at the electrode–electrolyte interface or ohmic impedance by Gharbi et al.[128] and You et al.[6]. The ohmic-impedance behavior tends to dominate the impedance response in larger electrodes at high frequency. The ohmic impedance is discussed in Section 2.6.3.

The capacitance of the high-impedance limits for the terminal feature of the G2 device, and the capacitance for the 20 m^2, 80 m^2 and 4000 m^2 electrodes were estimated from the imaginary part of the impedance Z [122] as

$$_{OL} = \frac{1}{j} \tag{4-2}$$

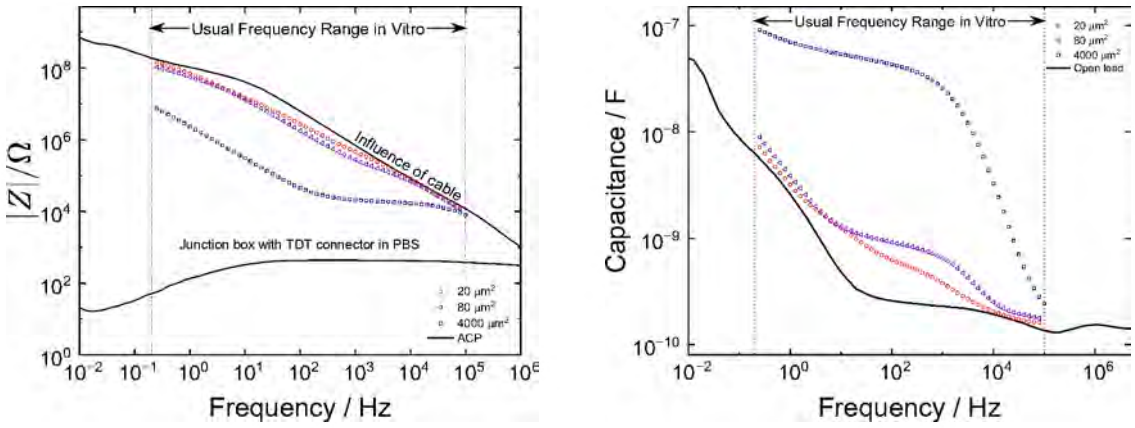

(a) (b)

Figure 4-14. Influence of parasitic capacitance on the impedance spectra of G2 microelectrodes for measurements performed at open-circuit in phosphate-buffered saline: a) impedance magnitudes showing the high and low-impedance spectra for custom junction box with a TDT ZIF-Clip connector in PBS, and impedance data for the 5 m (20 m^2), 10 m (80 m^2) and REF (4000 m^2) diameter electrodes; b) capacitance calculated from equation (4-2) and plotted as a function of frequency for the 5 m (20 m^2), 10 m (80 m^2) and REF (4000 m^2) electrodes and terminal feature of the G2 devices. The measurements were performed at open circuit.

where is the frequency of impedance measurements. The resulting values are presented in Figure 4-14(b) on a log-log-scale to show the frequency points at which the electrode sites are affected by parasitic capacitance. As shown in Figure 4-14(b), the capacitance calculated for the large electrode (4000 m^2) was relatively higher than the values estimated for the high-impedance limit of the accuracy contour plot, the 20 m^2 electrode and the 80 m^2 electrode across all frequency ranges.

The high frequency range illustrates the influence of parasitic capacitance on the impedance spectra. At high frequency points, the capacitance values that approaches the high-impedance limits of the accuracy contour plots are largely influenced by the parasitic capacitance. As shown in Figure 4-14(b), the capacitance estimated for the 20 m^2 and 80 m^2 electrodes aligned with the leads capacitance of 0.2 nF at 10 kHz. However at this frequency point, the calculated capacitance for the 4000 m^2 electrode did not approach this value. The trends for the larger electrode reaffirms its minimal susceptibility to parasitic capacitance. Additionally, equation (7-3)

was used to estimate the cable capacitance contribution for all three electrode sizes. The resulting values of 0.27 ± 0.02 nF for the 20 m^2, 0.24 ± 0.01 nF for the 80 m^2, and 0.18 ± 0.02 nF for the 4000 m^2 electrodes, closely align with the estimates obtained from the trends observed in the capacitance plots shown in Figure 4-14(b).

CHAPTER 5
EXPERIMENTAL METHODS

The neural-stimulation electrodes evaluated are discussed in Chapter 3. Three generations (G1 to G3) of the Neuronexus electrodes were analyzed. The impedance spectroscopy experiments were designed to characterize the electrochemical system and extract the physical parameters of the electrodes. The characterization of electrochemical systems was performed through the ”in-vitro” methods and ”in-vivo” methods, depending on the test environment. ”In-vitro” methods were carried out to asses the electrode behaviour in a phosphate-buffered saline solution and extract parameters that would inform the impedance modeling of electrodes in-vivo. ”In-vivo” methods were performed in brains of animals and used to evaluate the bulk transport and kinetic processes at the electrode-tissue interface. The complexity of the electrochemical system resulted to current-range issues on the impedance measurements.

The methods validates the consistency of the impedance data with the Kramers–Kronig [134, 135] relations using the measurement model approach proposed by Argawal et al.[3, 114]. This chapter describes several experimental methods, discusses challenges encountered during impedance measurements, and presents strategies to address these issues.

5.1 In Vitro Methods

The in-vitro impedance measurements were performed using the Gamry Reference 600+ Potentiostat with Framework version 7.10.3. The experiment was conducted in phosphate buffered saline (PBS) at open-circuit conditions, as shown in Figure 5-1. The saline solution was a mixture of 20 mL of phosphate-buffered saline containing 0.01 M phosphate buffer, 0.0027 M KCl, and 0.137 M, NaCl and 80mL of de-ionized water to simulate physiological conditions. A three-electrode configuration was employed, consisting of the working electrode, an Ag/AgCl reference electrode, and a platinum-foil or Platinum-mesh counter electrode, as shown in Figure 5-1(b). The in vitro measurement approach was same for all the brain-stimulation devices (G1 to G3) tested.

For each brain-stimulation devices tested (G1 to G3 (see Chapter 3)), the electrodes were connected to the Gamry reference 600+ Potentiostat via a custom-junction box with TDT Zif-Clip

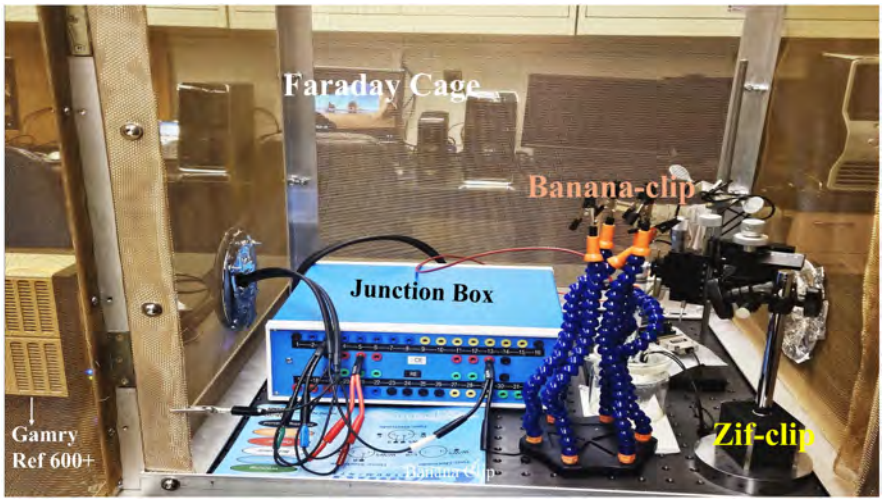

(a)

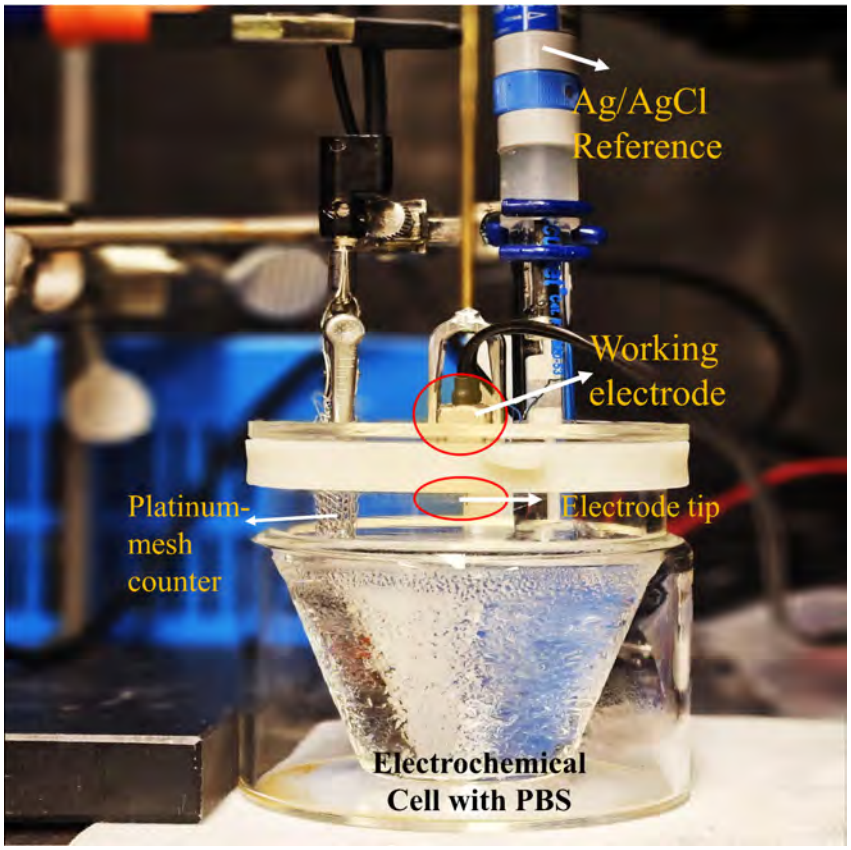

(b)

Figure 5-1. Pictorial representation of electrochemical cell set-up for impedance measurement in phosphate-buffered saline: a) Image showing connection between the Gamry Ref. 600+, custom Junction box with TDT Zif-clip connector, and the device. b) Zoomed image of the electrochemical cell. The in-vitro experiment was performed at open-circuit for all the electrode devices (G1 to G3) analyzed. Photo courtesy of author.

connector as illustrated in Figure 5-1(a). The junction box allowed switching between electrode sites (channels) to designate the working electrode during measurements. A five-minutes stabilization period was applied for each impedance spectra recorded at an applied perturbation of 25 mV rms, with a frequency sweep from 100 kHz to 0.2 Hz at 10 points per decade. The experimental set-up was placed in a grounded Faraday cage to prevent interference with the electrical noise in the environment.

5.2 In Vivo Methods

The study characterized the in vivo impedance spectra obtained with the Generation 1 (G1) electrodes. The in vivo experiments were performed by Elizbeth Olivo with an Autolab PGSTAT12 (Metrohm, Utrecht, The Netherlands) in Professor Kevin Otto lab at the University of Florida. The experimental procedure was published by Dong et al.[59]. As shown in Figure 2-1 taken from Dong et al.[59], a two-electrode configuration was employed, wherein the working electrode was implanted into the somatosensory cortex of anesthetized Sprague-Dawley rats. The counter and reference electrodes were shorted together. All animal procedures and surgeries adhered to protocols approved by the Institutional Animal Care and Use Committee (IACUC) at the University of Florida (Gainesville, FL, USA). During the procedure, anesthetized rats were stimulated through electrodes of varying diameters, and impedance measurements were conducted before, during, and after surgical implantation to evaluate the impact of stimulation and implantation on device performance. The electrode arrays were connected to a multiplexer via a ZIF-clip holder and implanted such that the electrode tips were positioned 1600 m below the cortical surface. Electrical stimulation was delivered immediately using an IZ2 Electrical Stimulator and an RZ5D Base Processor system (Tucker-Davis Technologies, Alachua, FL), as illustrated in Figure 2-1d [59].

5.3 Measurement Modeling Approach

The background on measurement model is presented in section 2.5.2.3 of Chapter 2. The measurement model published by Agarwal et al.[3, 114] serves as a framework to separate the true electrochemical response from artifacts introduced by the measurement system. This approach

systematically accounts for both bias and stochastic errors (see section 2.5.2.2 of Chapter 2) associated with impedance measurements and ensures that the impedance data is consistent with fundamental physical principles, like the Kramers–Kronig [134, 135] (see section 2.5.2.1 of Chapter 2). Following Agarwal's previous work on the measurement model, Orazem and Watson created a measurement modeling program with the Python code for analysing impedance spectra and extracting physical parameters of the electrode that are statistically significant. The impedance spectra of all the electrode devices used in this study (see Chapter 3), were analysed with the version 1.8 of the python-based measurement model program established by Watson and Orazem [97, 132]. The software regresses the measurement model proposed by Agarwal et al.[3] to the impedance data. For each dataset, the highest frequency point affected by external phenomena was removed, and the number of Voigt elements K was increased sequentially such that the 95.4% (±2) confidence interval for each regressed parameter does not include zero. The same value for K can be obtained by minimization of the Akaike information criterion, which penalizes each additional parameter [136].

5.3.1 Impedance Data Conversion

Before analyzing the impedance spectrum, the data file was converted into a format compatible with the measurement model software. As shown in Figure 5-2, the experimental data was imported to the program as a *.txt file extension and the data at line frequencies of 60 Hz ± 3 and 120 Hz ± 3 were deleted to eliminate noise or interference from the fundamental and first harmonic frequencies of the electrical power supply in US and Canada.

The impedance spectra was scaled by the electrode's area and viewed as Nyquist plot during the data loading process. The file was then saved as a *.mmfile extension organized into three separate columns consisting of frequency, real component of impedance, and imaginary component of impedance, and loaded into the next tab of the measurement modeling software for further analysis.

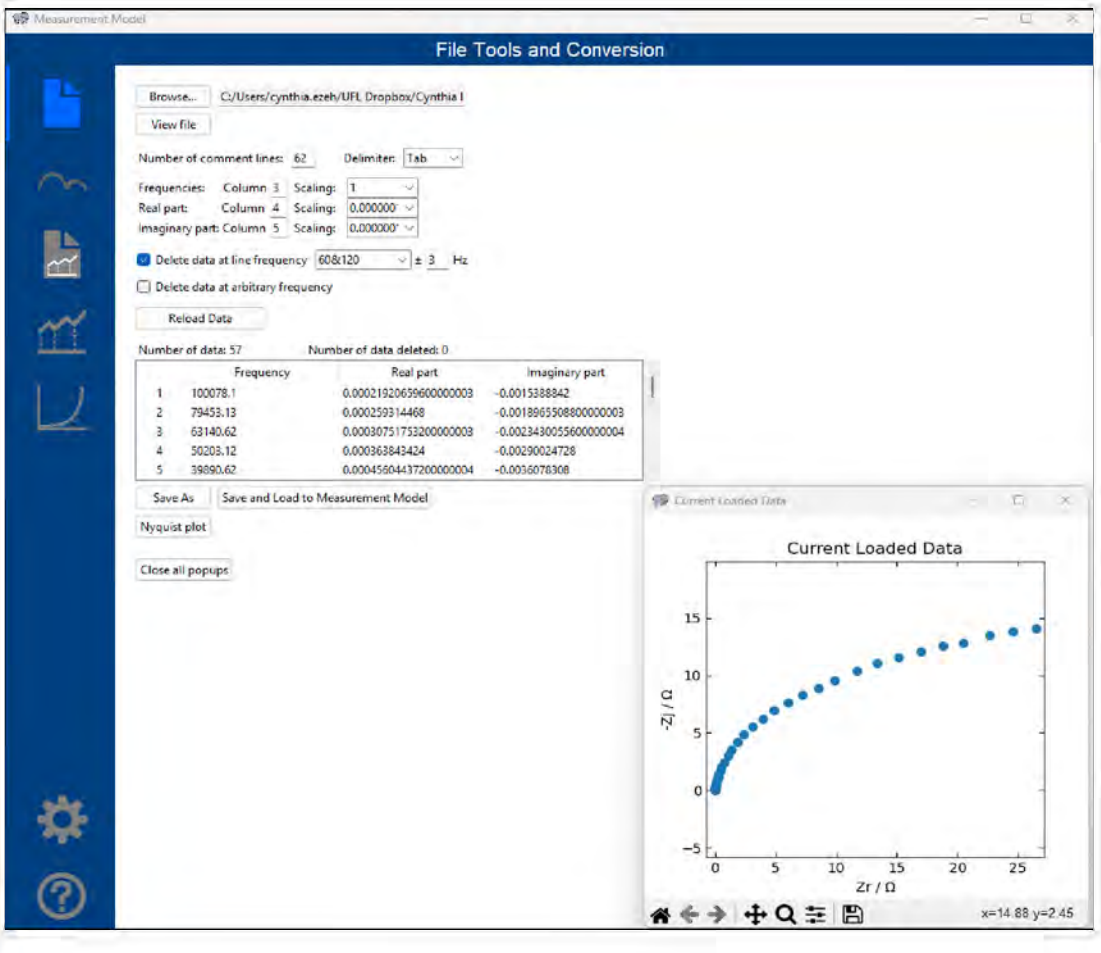

Figure 5-2. Picture showing the conversion of impedance spectra from *.txt file extension to *.mmfle format compatible with the measurement model program. Impedance data at line frequencies of 60 Hz ± 3 and 120 Hz ± 3 were deleted.

5.3.2 Measurement Model Analysis

The *.mmfile extension was loaded to the measurement model tab for impedance data regression. As shown in Figure 5-3, The initial step in the regression was to delete the first frequency point, due to noise from impedance measurement transient generated while switching between frequencies. Subsequently, the measurement model was regressed to the impedance spectra through a sequential procedure. As illustrated in Figure 5-4. The no of line shape describes the no of Voigt circuit elements (or time constants) fitted to the impedance spectra. The program is capable of generating accurate initial guess for the first Voigt element, then the number of Voigt elements are iteratively added such that the 95.4% (±2) confidence interval for each regressed

parameter does not include zero. A modulus weighting approach was chosen for the first stage of measurement model analysis, as it provides a reliable estimate of the error structure of impedance spectra obtained under potentiostatic EIS measurements. After the error structure is characterized, error model weighting was applied to re-model the impedance spectra. A complex regression approach was employed to fit both the real and imaginary components of the impedance data.

The regression analysis shown in Figure 5-5, yielded Nyquist and Bode plots (with and without ohmic resistance correction), logarithmic plots of real and imaginary impedance, the derivative of log of imaginary impedance with respect to log of frequency, and normalized residual errors. The 95.4% confidence intervals, indicated by red dashed lines, were obtained via Monte Carlo simulations using parameter estimates and standard deviations from the Levenberg–Marquardt regression. All real and imaginary error residuals remained within these bounds, demonstrating consistency with the Kramers–Kronig relations. The *.mmresiduals file was saved for subsequent error structure analysis.

5.3.3 Preparation of Error File

For each impedance measurement, the spectra were obtained in triplicate. The replicated datasets, saved with a *.mmresiduals file extension, were imported into the error file preparation tab shown in Figure 5-6. This tab operates based on the number of frequency points and line shapes, ensuring that each replicated dataset contains matching frequency points and is analyzed with the same number of Voigt elements in the measurement model. As illustrated in Figure 5-6, the standard deviations of the real and imaginary impedance components were calculated as functions of frequency. The overlap between these standard deviations indicates that the datasets conform to the Kramers–Kronig relations. Finally, the prepared error file was saved for subsequent error structure analysis.

5.3.4 Error Structure Analysis

The prepared error file was imported for error structure analysis. Error analysis provides a statistical means of quantifying experimental noise present in the impedance spectra. In potentiostatic EIS measurements, impedance spectra exhibit a strong frequency dependence. The

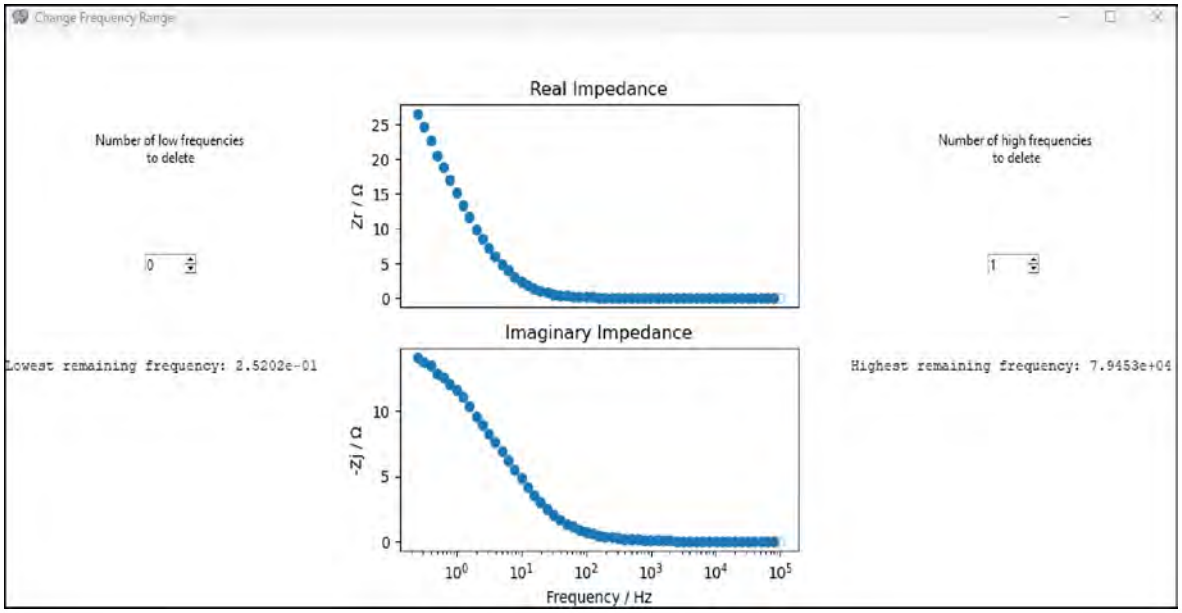

Figure 5-3. The first step in the measurement model regression was to delete the first frequency point, affected by noise from measurement transient generated while switching between frequencies.

stochastic error structure was determined from the standard deviation of the real and imaginary components of impedance. As illustrated in Figure 5-7, the standard deviations of the residual errors are empirically modeled using:

$$= <| \quad | > + \ <| \quad | > + \ <| \ | >^2 + \qquad (5\text{-}1)$$

where | r | is the absolute value of the real impedance, | j | is the absolute value of the imaginary impedance, and | | is the magnitude of impedance [132]. The error parameters , , , and are constants empirically estimated from replicated impedance measurements under the same conditions. Accurate parameters for each replicated datasets are selected through an iterative trial-and-error procedure. For example, the error model shown in Figure 5-7 does not include , and because statistically significant values could not be obtained with , and . For all analyzed impedance data, variance weighting and a five-point moving average were applied, while detrend

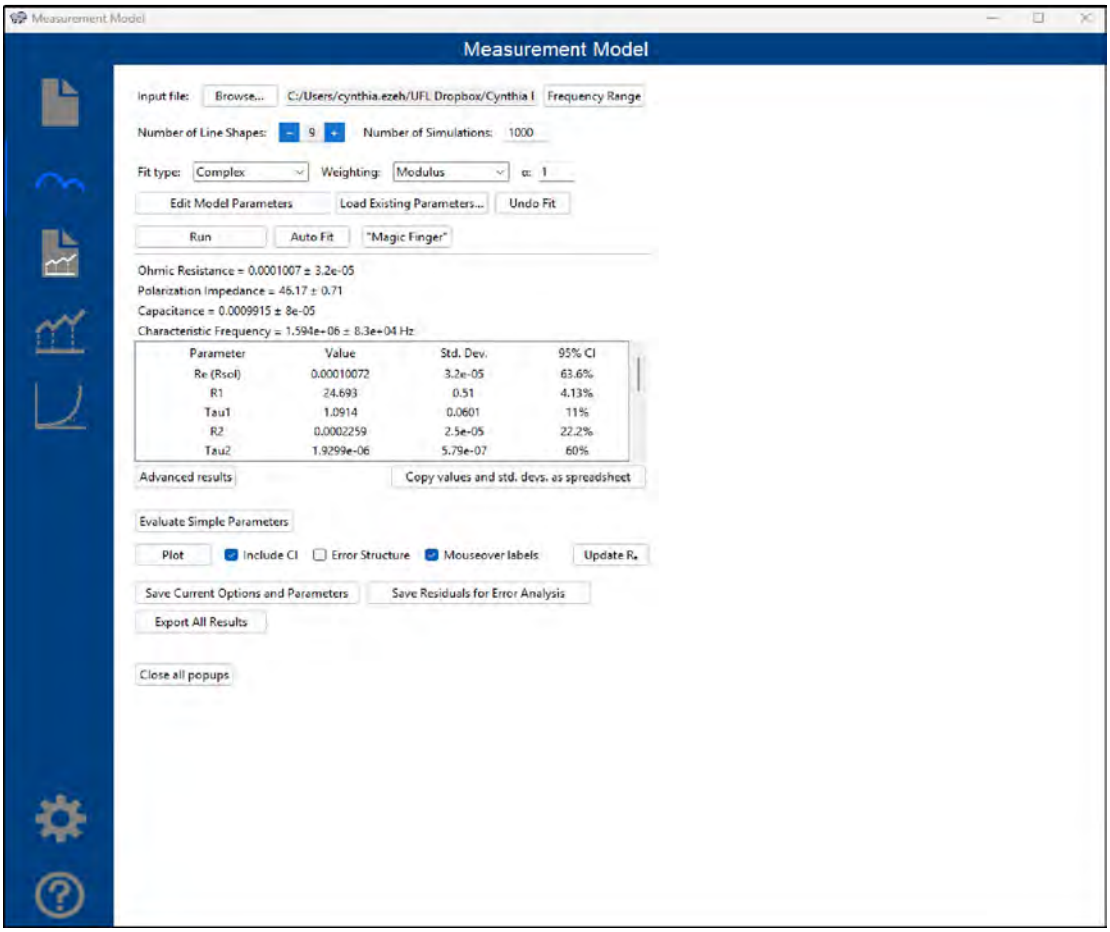

Figure 5-4. Regression of impedance spectra with the measurement model program after removal of the first high frequency point. The data was sequentially regressed with nine Voigt circuit elements.

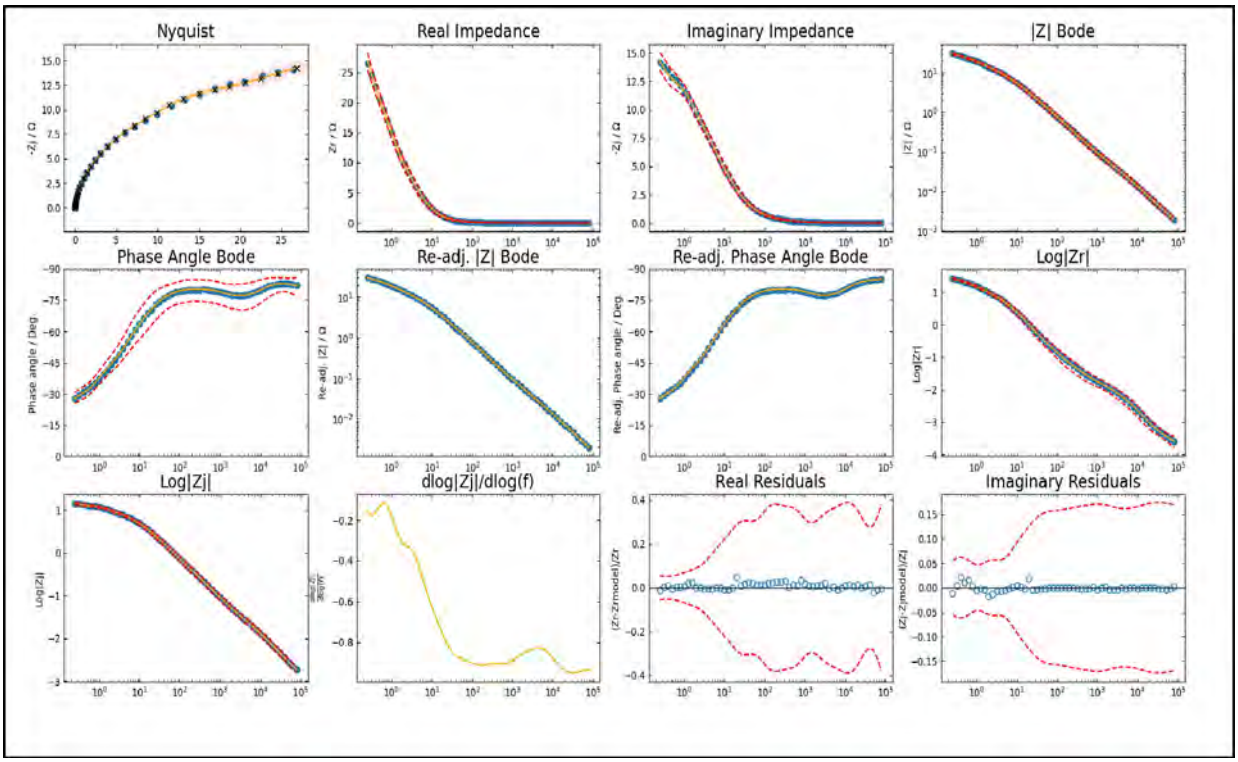

Figure 5-5. Picture of the measurement model regression result showing Nyquist and Bode plots (with and without ohmic resistance correction), logarithmic plots of real and imaginary impedance, the derivative of log of imaginary impedance with respect to log of frequency, and normalized residual errors.

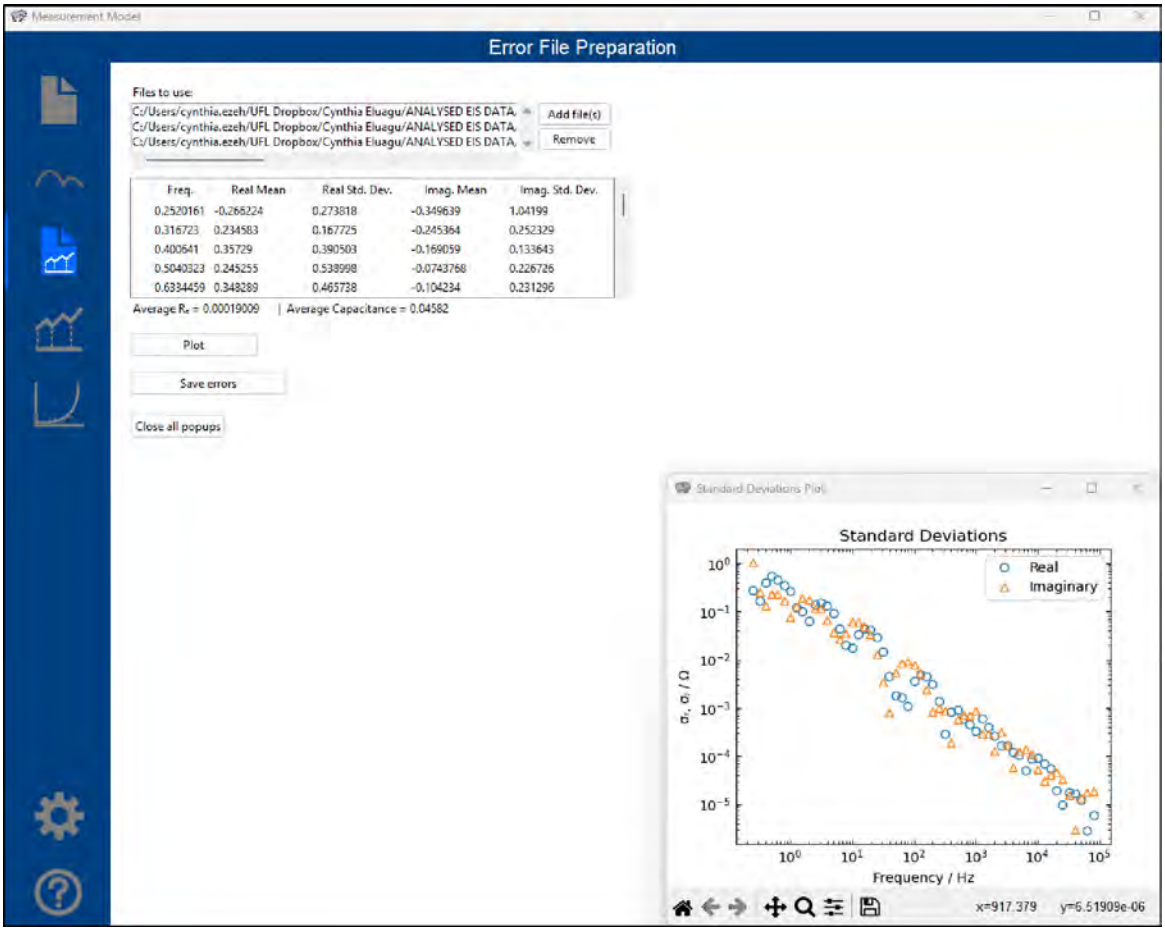

Figure 5-6. Image of error preparation file tab for measurement model regression. Error structure of replicated impedance spectra at open circuit are functions of frequency. Orange triangles and blue circles represent the imaginary and real standard deviations of impedance.

was disabled. The resulting error structure file, containing the error parameters, was saved and subsequently used for process model regression and additional measurement model analysis.

5.3.5 Process Model Fitting

Process models are used to reveal the physical and chemical properties of impedance measurements. Process models are represented as electrical circuits and are fitted to the impedance spectra to evaluate faradaic and charging reactions occurring at the electrode/electrolyte interface. As shown in Figure 5-8, process modeling was executed using the *.mmfile extension. The mathematical formula for electrical circuit model, was coded in python and fitted to the impedance spectra. The regression was performed with a complex fit and weighted by the error model shown in Figure 5-8. The fitting parameters were given an initial guess before the regression. The final values of the regressed parameters are statistically significant such that the 95.4% confidence intervals do not include zero. The regressed values were used to estimate capacitance. The detailed results for the electrode devices tested, are discussed in the next chapters.

5.4 Impedance Measurement Limitations

The major contribution to the impedance measurement challenges are the external cables and connectors added to the Gamry Reference 600+ potentiostat. In general, cables largely influence the measurement capabilities of the electrochemical systems studied, because they provide connection between the potentiostat and the electrochemical cell. The Gamry Reference 600+ potentiostat used in this study were equipped with a 60 mm cable for connecting to the working, counter and reference electrodes of the electrochemical cell. These cables are twisted and shielded to reduce the effect of mutual inductance and external electrical noise from other electrical appliances in the environment.

As discussed in Chapter 3, the brain-stimulation microelectrodes and ultramicroelectrodes used in this research are designed as arrays rather than single electrodes to enable simultaneous recording and stimulation at multiple discrete sites within neural tissue, providing much greater spatial and temporal resolution of brain activity [137, 138]. Due to these electrode configurations,

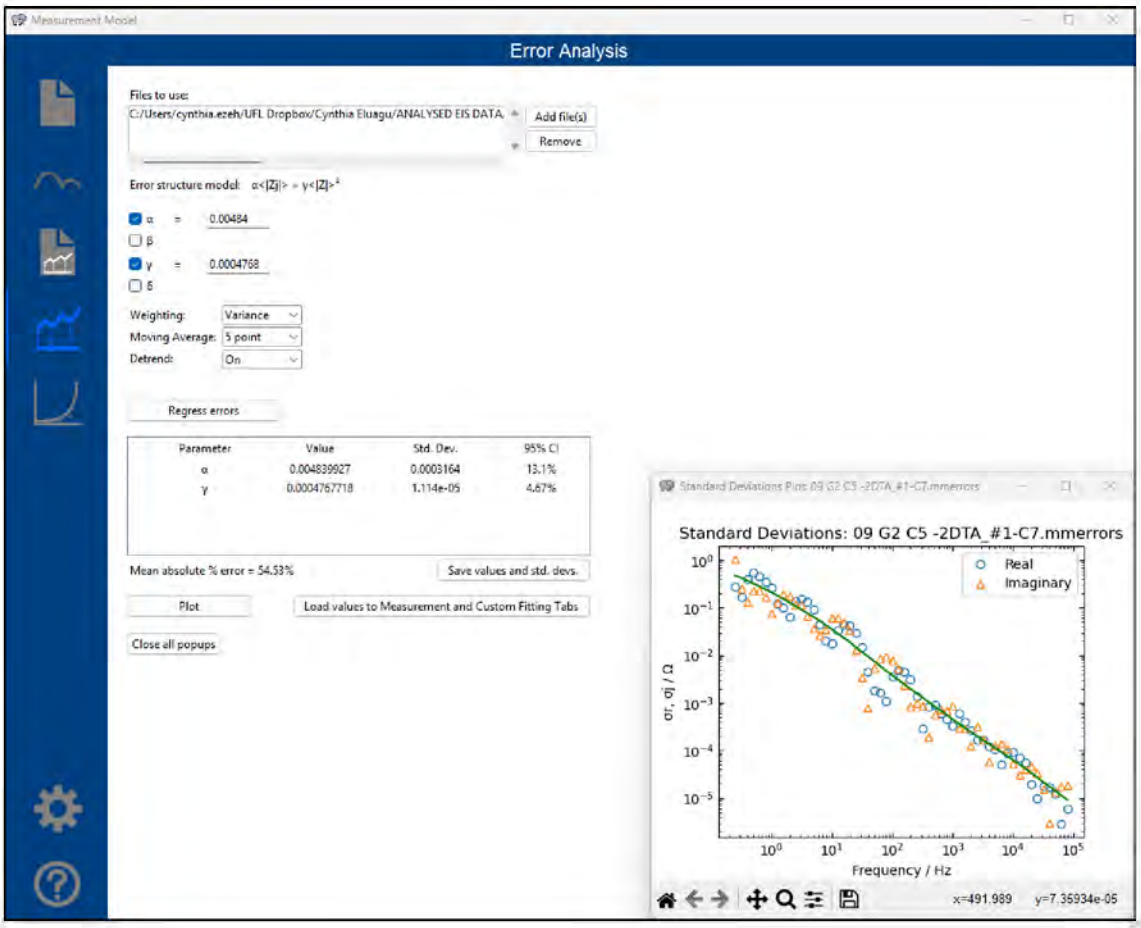

Figure 5-7. Picture showing the regression of Equation 5-1 to stochastic error structure.
statistically significant is not achievable with , and

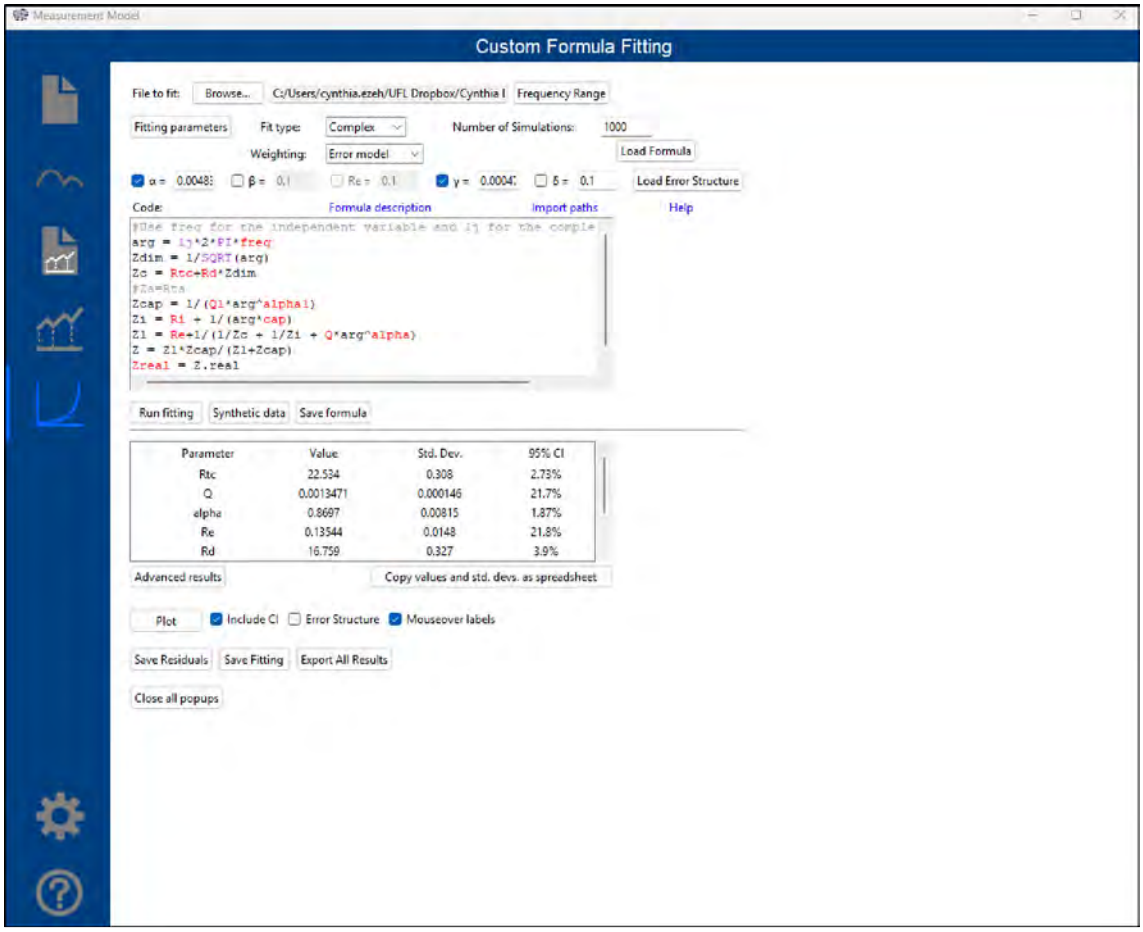

Figure 5-8. Process model analysis tab for the measurement model program. The process model regression was performed with error structure weighting. The python code represent the mathematical formula for the electrical circuit that was fitted to the data.

the external cables and custom-designed junction box with the Zif-clip connector; shown in Figure 5-1(a), were attached to the ends of the Gamry Reference 600+ cell cable to perform the impedance measurement. These cables were unshielded and can act like antennas for ambient electromagnetic noise (such as from nearby electronics), causing apparent current range issues, increasing interference from the leads capacitance at high frequency points, and degrading the system's effective capabilities during impedance measurements.

Accuracy contour plots are used to asses the true response of impedance measurements. If the impedance spectra falls within the accuracy contour plot, then the data is reliable and can be characterized. Detailed discussion about the effects of cable capacitance can be found in section 4.4 of chapter 4.

5.5 Current Range Issues

The current range problems in Gamry Reference 600+ potentiostat originated from external cables, connection hardware and experimental setup (autoranging, range selection). The Gamry instrument automatically switches current ranges during impedance measurements to keep the signal within the optimal current range. This transition from one current range to another causes discontinuities in impedance spectra at the frequency points where the switch occurs. An example of impedance spectra affected by current range issues is shown in Figure 5-9. Discontinuities in the impedance spectra were observed at frequencies where the potentiostat switched to a different current range. As shown in the magnitude and phase plots in Figure 5-9, the jump from 628 Hz to 797 Hz depicts a transition from a current range of 4 A to 5 A, respectively. These challenges significantly complicate the analysis and interpretation of impedance spectra. The impedance measurement is constantly repeated until a good data is obtained.

The Gamry Reference 600 + is extremely sensitive at low-current ranges, so measuring at low currents (picoampere range) is prone to substantial errors because input currents from the reference and counter sense cables can become a significant fraction of the measured signal, causing current ranges and noise [139]. Selecting a fixed current range forces the potentiostat to stay on a constant current range during the impedance measurements. While fixing to the precise

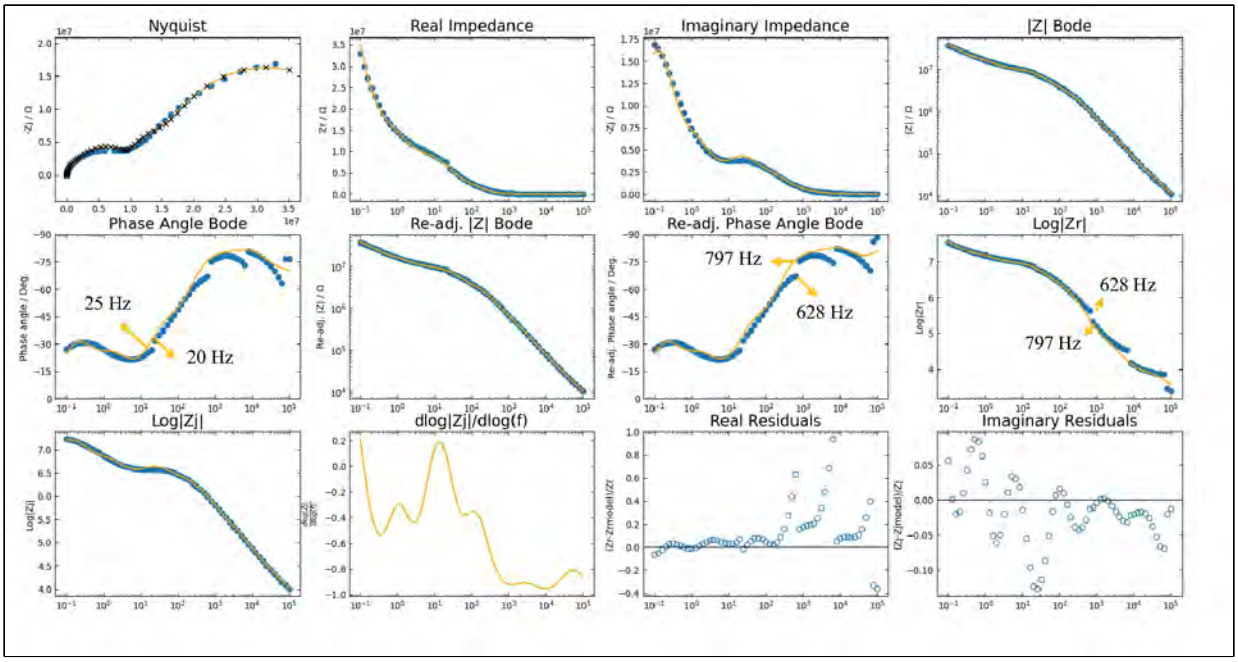

Figure 5-9. Impedance spectra affected by current range at different frequency points. The data exhibited discontinuities at frequencies where the instrument switched between current ranges.

current range reduces noise, a less sensitive range increases noise, while overly sensitive ranges can overload with high currents, triggering current overload warnings.

5.6 Proposed Solutions to Current Range Challenges

Current range issues are common when extending cables or modifying standard impedance measurement setups. The best practice recommended is to use the standard shielded cell cables supplied by Gamry. These cables have been specifically designed for optimal low-noise performance during impedance measurements. However, in situations where extra cables must be added, different approaches can be used to reduce or eliminate current range issue.

The effective approach is to select well-shielded, low-resistance coaxial cables, and calibrate any new or extension cables prior to use. It is essential to ensure that all cable shielding is continuous and properly grounded to minimize noise and interference. Cable extensions should be kept as short as possible to reduce parasitic effects, resistance and noise. Before conducting real experiments, a dummy cell should be used to test the impact of cable extensions and identify measurement artifacts. All electrode connections should be carefully inspected to confirm they are secure and free from bubbles or poor contact. Regular calibration of the potentiostat and its associated cables should be performed. Dummy cell tests are necessary to detect hardware faults or configuration errors. Additionally, placing the entire experimental setup inside a grounded Faraday cage reduces electromagnetic interference, and enhances measurement stability and accuracy. In cases where the instrument becomes overloaded, selecting a less sensitive current range or applying range-file corrections through software may restore measurement stability.

CHAPTER 6
IMPEDANCE SPECTROSCOPY OF G1 ULTRAMICROELECTRODE ARRAYS

The electrochemical properties of the generation 1 (G1) devices were characterized using impedance spectroscopy in vitro and in vivo. The G1 ultramicroelectrode arrays represents the first-generation design in this study aimed at understanding the impedance response of SIROF-coated high-density (HD) microelectrode and ultramicroelectrode arrays for neural stimulation. As illustrated in Figure 3-2, the electrode diameters varied from 50 m down to 5 m, corresponding to geometric surface areas (GSAs) of approximately 2000 m^2 to 20 m^2. The G1 array was used to explore variations in impedance performance as function of electrode diameter and spacing. Fabrication and design of G1 arrays are summarized in section 3.1.1.2.

The impedance spectra of the G1 device were provided by Elizabeth Olivo at the University of Florida. The in vitro experiments was performed with a three-electrode setup consisting of reference, counter, and working electrodes immersed in phosphate-buffered saline (PBS) solution. The frequency sweeps ranged from 10 kHz to 0.1 Hz using a the Autolab PGSTAT12 (Metrohm, Utrecht, The Netherlands). The in vivo experiments, a two-electrode set up was used where the working electrode was implanted into the somatosensory cortex of anesthetized Sprague-Dawley rats and the counter and reference electrodes were shorted together. The experimental procedure for the in vivo experiment is detailed in section 3.1.1.2. The measurement model program created by Watson and Orazem [97] were used to compute the error structure of the impedance data and developed a custom interpretation model with fitting parameters representing the device-electrolyte/tissue interface. The measurement modeling approach is provided in section 5.3

This chapter detail the interpretation model for G1 arrays, the experimental results in vitro and in vivo, parameter extraction through process modeling, as well as the assessment of capacitance across G1 varying electrode diameters. The findings from G1 analysis establish a comparative framework for evaluating the impedance spectra of subsequent designs (G2 and G3) and for optimizing electrode architecture for neural stimulation and recording applications.

6.1 Process Model for G1 Impedance Spectra

Impedance measurements were obtained for G1 microelectrodes and ultramicroelectrodes in phosphate-buffered saline under open-circuit conditions. The impedance spectra were analyzed using a process model to determine key physical parameters of the electrodes. The electrical circuit used for regression and data interpretation are shown in Figure 6-1. The model includes the ohmic resistance, R_e in series with a parallel network representing the electrode's constant-phase-element behavior and faradaic processes associated with mass-transfer influenced oxygen reduction.

Assuming that the reaction mechanism in the electrochemical system studied is oxygen-reduction reaction,

$$4OH^- \quad O2 + 2H_2O + 4e^- \tag{6-1}$$

at open-circuit potential (OCP), the sum of the anodic faradaic current i_a and the cathodic faradaic current $-i_c$ is expressed as

$$_a + \ _c = 0 \tag{6-2}$$

meaning there is no net current flow in the electrochemical system. The anodic and cathodic faradaic processes are balanced at this equilibrium potential, and both the anodic and cathodic faradaic impedances influence the overall impedance response of the system at OCP. If a faradaic impedance is much larger than the other, the bigger faradaic impedance may not be observed in the process [132]. Hence, the anodic faradaic impedance, Z_a can be neglected from the process model in Figure 6-1 because $Z_a \quad Z_c$. The electrode interface is well approximated by the parallel combination of the CPE and cathodic faradaic impedance Z_c.

The overall impedance of the electrical circuit shown in Figure 6-1 is expressed as

$$= \ _e + \frac{_t + \ _D}{1 + (\quad) \quad (\ _t + \ _D)} \tag{6-3}$$

where R_e is the ohmic resistance, R_t is the charge-transfer resistance, Z_D is the diffusion impedance, is the frequency, j is the complex number, $\sqrt{-1}$, and is the

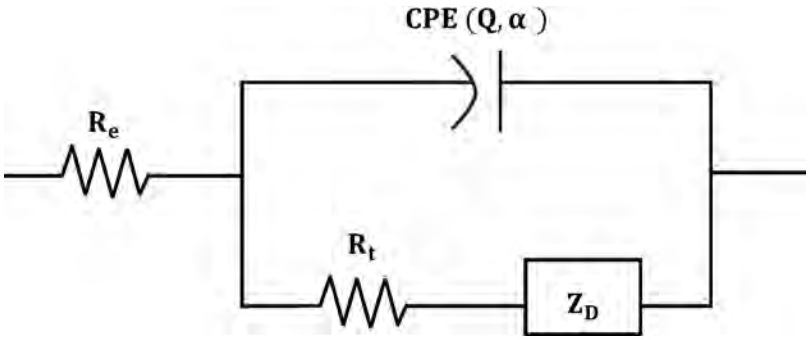

Figure 6-1. Electrical circuit representation of the process model (equation (6-3)) for G1 device. The model accounted for the electrode's constant-phase-element behavior, and mass-transfer-influenced oxygen reduction reaction.

constant-phase-element exponent and component, respectively. The cathodic impedance, Z_c can be expressed in terms of the charge-transfer resistance $R_{t,c}$ and the diffusion impedance Z_d as

$$c = t + D \tag{6-4}$$

where Z_D is the diffusion impedance for an infinite film attributed to Warburg element [78, 140]. The expression for Z_D is

$$D = \frac{}{\sqrt{\ }} \qquad d \tag{6-5}$$

where R_d is a modified parameter expressed as

$$d = \frac{d}{\sqrt{\ d}} \tag{6-6}$$

R_d represents the diffusion resistance and $_d$ is the time-constant for diffusion. The derivation for R_d has been published by Orazem [132].

6.2 Experimental Results for G1

The impedance spectra of G1 ultramicroelectrodes were regressed through a series of Voigt circuit elements satisfying the Kramers–Kronig relation. Error analysis of repeated impedance measurements yielded stochastic error structures and error parameters for fitting the data within the 95.4% confidence interval. Eliminating geometry-induced frequencies above the characteristic

frequency resulted in a fit devoid of non-stationary behaviors. The process model accounts for the electrode's constant-phase-element behavior, ohmic resistance, oxygen-reduction, and diffusion, fitting well for large and small electrodes while satisfying the Kramers–Kronig relation. The capacitance derived from regression analysis was consistent with that from Brug's formula. The analysis revealed diffusion control at low frequencies and a constant-phase element behavior at high frequencies for all site sizes. Overall, the in vitro EIS method facilitated electrode property characterization before testing in a realistic biological setting.

6.2.1 G1 Impedance Spectra

The impedance spectra of G1 ultramicroelectrodes were obtained under open-circuit conditions. A total of 32 sets of triplicate impedance spectra were collected for ultramicroelectrodes with diameters between 5 m and 50 m. The measurement model was used to estimate the frequency above which the ohmic impedance associated with the electrode geometry affects the impedance measurement.

6.2.1.1 In Vitro Data

The Nyquist plots for impedance spectra for electrodes of various sizes, ranging from 5 m to 50 m are summarized in Figure 6-2(a). The result does not show the expected relationship between impedance and electrode size under open-circuit conditions. As electrode size increases, both real and imaginary components of impedance vary substantially, reflecting variations in interfacial impedance, kinetics and time-constant distributions across the electrode surfaces. The measurement was made in phosphate-buffered saline after implantation in rat. The trends in Figure 6-2(a) suggest that smaller electrodes facilitated more electrochemical processes in PBS consistent with ultramicroelectrode theory where edge effects and enhanced mass transport reduce impedance.

6.2.1.2 In Vivo Data

The impedance spectra obtained in vivo for microelectrodes and ultramicroelectrodes ranging from 5 m to 50 m are presented in Figure 6-2(b) . As electrode diameter decreases, both real and imaginary impedance values increases. This trend is suggests reduced double-layer

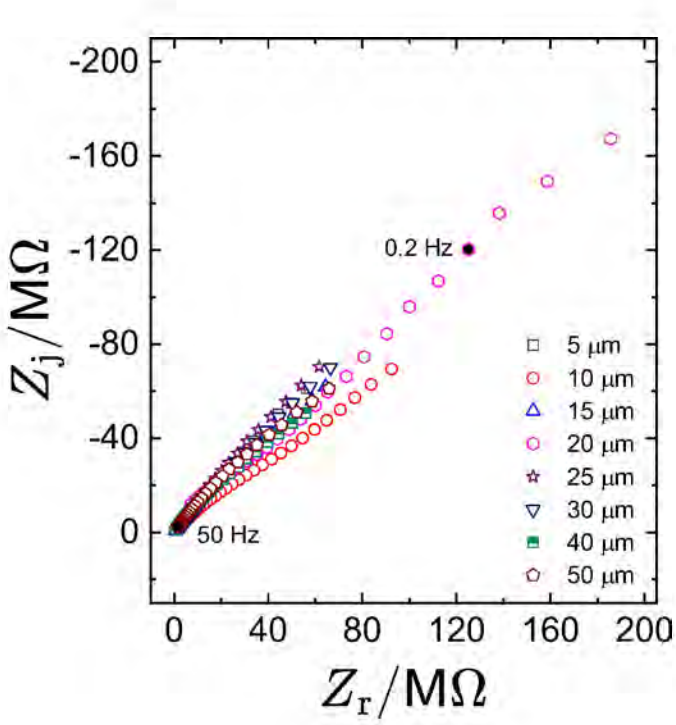

(a)

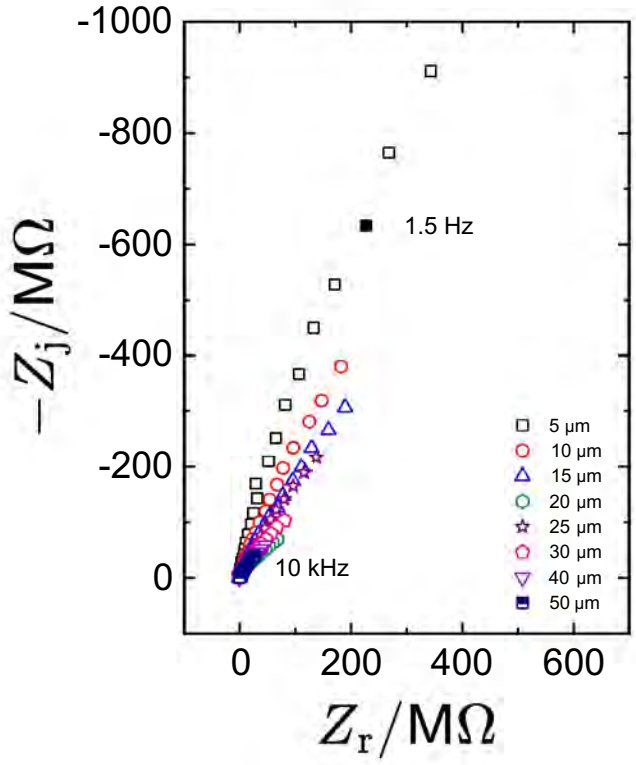

(b)

Figure 6-2. Impedance spectra in Nyquist format with electrode diameter as a parameter: a) in vitro impedance measurements, and b) in vivo impedance measurements. The measurement was performed at open circuit at frequency range from 1 Hz to 100 kHz

capacitance and increased charge-transfer resistance with smaller electrodes. The smaller electrodes (5 m and 10 m) exhibit much larger impedance response than their larger counterparts. The low-frequency impedance behavior across various electrode sizes indicate capacitive effects presumed to be the distribution of time constants and the occurrence of faradaic processes at the at the electrode/tissue interface.

6.2.2 Error Model for G1

Thirty-two sets of impedance spectra, each measured in triplicate, were obtained from both in vivo and in vitro experiments. The error structure of the replicated datasets were analyzed with the measurement model approach provided in section 5.3 to estimate the standard deviations for the stochastic error structure. The stochastic error structure analysis for in vitro and in vivo EIS data was computed using a Levenberg–Marquardt regression.

6.2.2.1 In Vitro Error Structure

The resulting error structure for the replicated datasets obtained in vitro are shown in Figure 6-3(a). The black triangles and red circles represent the real and imaginary standard deviations of impedance, respectively, as shown in Figure 6-3(a). The standard deviations of the real and imaginary components of impedance are heteroscedastic and are overlapping at all frequency points, suggesting that data are consistent with the Kramers–Kronig relations. The line fitted to the error structures in Figure 6-3(a) is the empirical error model described by equation (5-1). The error model parameters for the in vitro impedance spectra are summarized in Table 6-1. The normalized error structure of in vitro datasets obtained by dividing the real and imaginary standard deviations of impedance by the impedance modulus is presented in Figure 6-3(b). The errors are on the order of 1 % at low frequency points and on the order of 0.1 % at high frequency. These values suggests the noise levels typical of measurements obtained using the Autolab potentiostat.

6.2.2.2 In Vivo Error Structure

The stochastic error structure for the in vivo impedance spectra are shown in Figure 6-4(a). The real and imaginary standard deviations of impedance are represented as blue triangles and red circles, respectively, as shown in Figure 6-4(a). The standard deviations of the real and imaginary

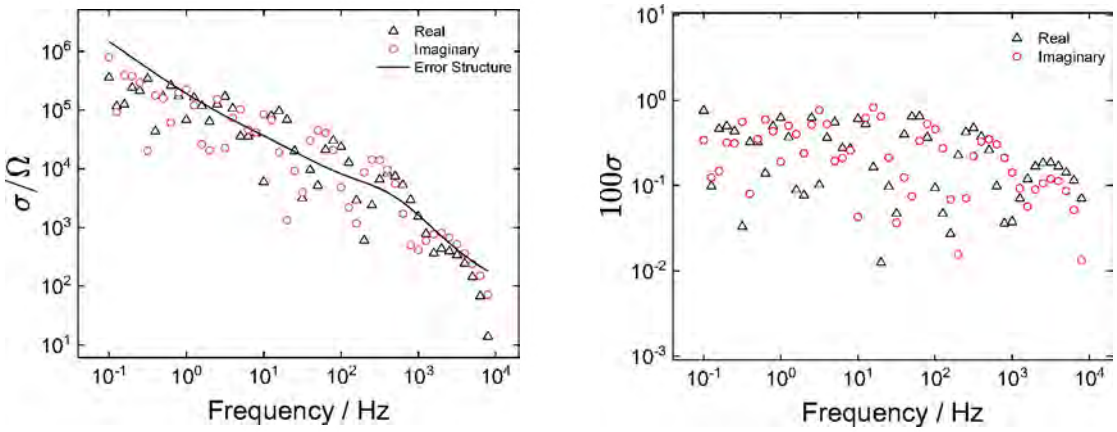

(a) (b)

Figure 6-3. Stochastic error structure for in vitro impedance spectra of G1 device at open circuit: a) error structure, b) normalized error structure. The solid line represents the error model given by equation (5-1). The regressed error parameters are summarized in Table 6-1.

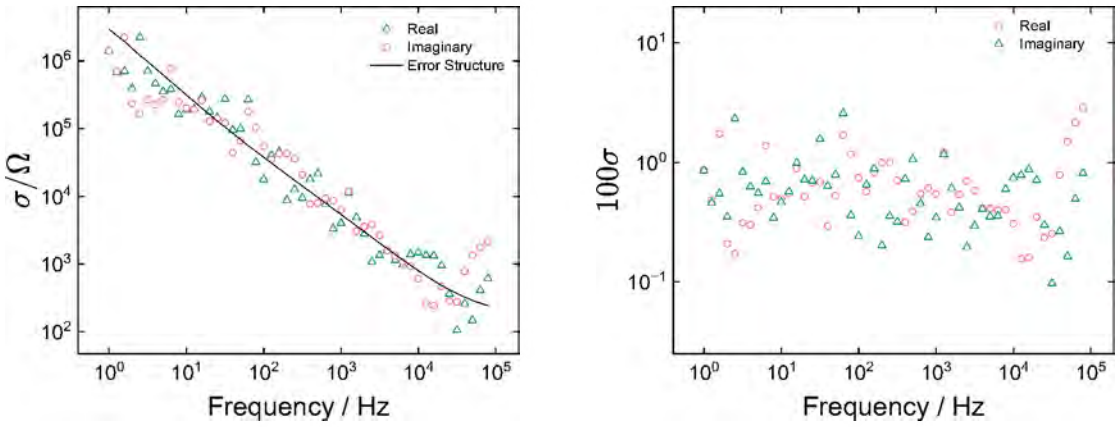

(a) (b)

Figure 6-4. Stochastic error structure for in vivo impedance spectra of G1 device at open circuit: a) error structure, b) normalized error structure. The solid line represents the error model given by equation (5-1). The regressed error parameters are summarized in Table 6-2.

Table 6-1. Error parameters obtained by regressing equation (5-1) to the in vitro impedance spectra of G1 ultramicroelectrodes.

Parameter	Value	Standard deviation
	0.007738023	1.78×10^{-22}
	–	–
	1.06×10^{-10}	2.19×10^{-14}
	–	–

components of impedance are strong functions of frequency and are similar, which implies that the impedance spectra are consistent with the Kramers–Kronig relations. The line regressed to the standard deviations shown in Figure 6-4(a) is the empirical error model described by equation (5-1). The error model parameters for the G1 impedance spectra obtained in vivo are summarized in Table 6-2

The normalized error structure of G1 impedance spectra obtained in vivo is shown in Figure 6-4(b). The plot was computed by dividing the real and imaginary standard deviations of impedance by the modulus. as illustrated in Figure 6-4(b), the errors are on the order of 1 % at the lowest frequency point, indicating the noise levels typical of measurements obtained using the Autolab potentiostat.

6.2.3 Process Model Regression for G1

The impedance response of G1 ultramicroelectrodes was evaluated in vitro and in vivo at open-circuit conditions. The process model shown in equation (6-3) was regressed to the in vitro and in vivo data to interpret the electrochemical reactions in the systems and extract electrode parameters. At open-circuit, the model accounted for the faradaic reactions presumed to be mass-transfer influenced oxygen reduction reactions, and the capacitive behavior of the electrode consistent with the distribution of time constants along the electrode surfaces.

6.2.3.1 In Vitro Regression

The process model regression results for the impedance spectra of a 50 m diameter electrode obtained in vitro are shown in Figure 6-5. The 50 m electrode site is shown here as a representative example of the datasets analyzed. The impedance data and the fitted interpretation model exhibit excellent agreement over the entire frequency range as shown in the resulting

Table 6-2. Error parameters obtained by regressing equation (5-1) to the in vivo impedance spectra of G1 ultramicroelectrodes.

Parameter	Value	Standard deviation
	0.001314706	1.021×10^{-22}
	–	–
	1.254057×10^{-10}	1.042×10^{-14}
	42.96346	12.91

Nyquist, Magnitude and Phase-angle plots presented as Figures 6-5(a),6-5(b) and 6-5(c), respectively. The residual errors of the real and imaginary components normalized by impedance are shown in Figures 6-5(d) and 6-5(e), respectively. The real residuals fall within the ±2 confidence intervals indicated by dashed lines in the real as shown in Figure 6-5(d). The imaginary residual errors suggest show a systematic deviation from the ±2 confidence intervals at high frequency points. The ability to fit the residual errors within the confidence intervals confirms the adequacy of the regressed process model.

6.2.3.2 In Vivo Regression

The fit of the process model given by equation (6-3) to the impedance spectra of a 5 m G1 obtained in vivo is illustrated in Figure 6-6. The impedance spectra presented as Nyquist, magnitude, and phase angle plots in Figures 6-6(a), 6-6(b) and 6-6(c) respectively, show that the process model is in good agreement with the impedance spectra over the full frequency spectrum. Additionally, the normalized error residuals for both real and imaginary components depicted in Figures 6-6(d) and 6-6(e) remain within the ±2 confidence intervals represented as dashed lines.

6.2.4 Kramers–Kronig Consistency Assessment for G1

The measurement model developed by Agarwal et al.[3] was used to regress the impedance spectra of G1 devices obtained for in vivo and in vitro measurements. The regression approach involved a systematic increase in the number of Voigt-circuit (RC) elements, K until the 95.4% confidence interval (±2) for each estimated parameters does not include zero. A parameter estimate is excluded from the final model and considered insignificant if it's confidence interval included zero. The confidence intervals were computed using Monte-Carlo simulation, which allowed for robust estimation of uncertainty under the assumed error structure. The measurement model meets the linearity and stationarity criteria implicit in the Kramers–Kronig . The residuals estimated from the regression was used to assess the consistency of the data with the Kramers–Kronig [134, 135]. Frequency points affected by geometry-induced nonuniform current and potential distributions regarded as ohmic impedance Gharbi et al.[128], were eliminated during the measurement model regression.

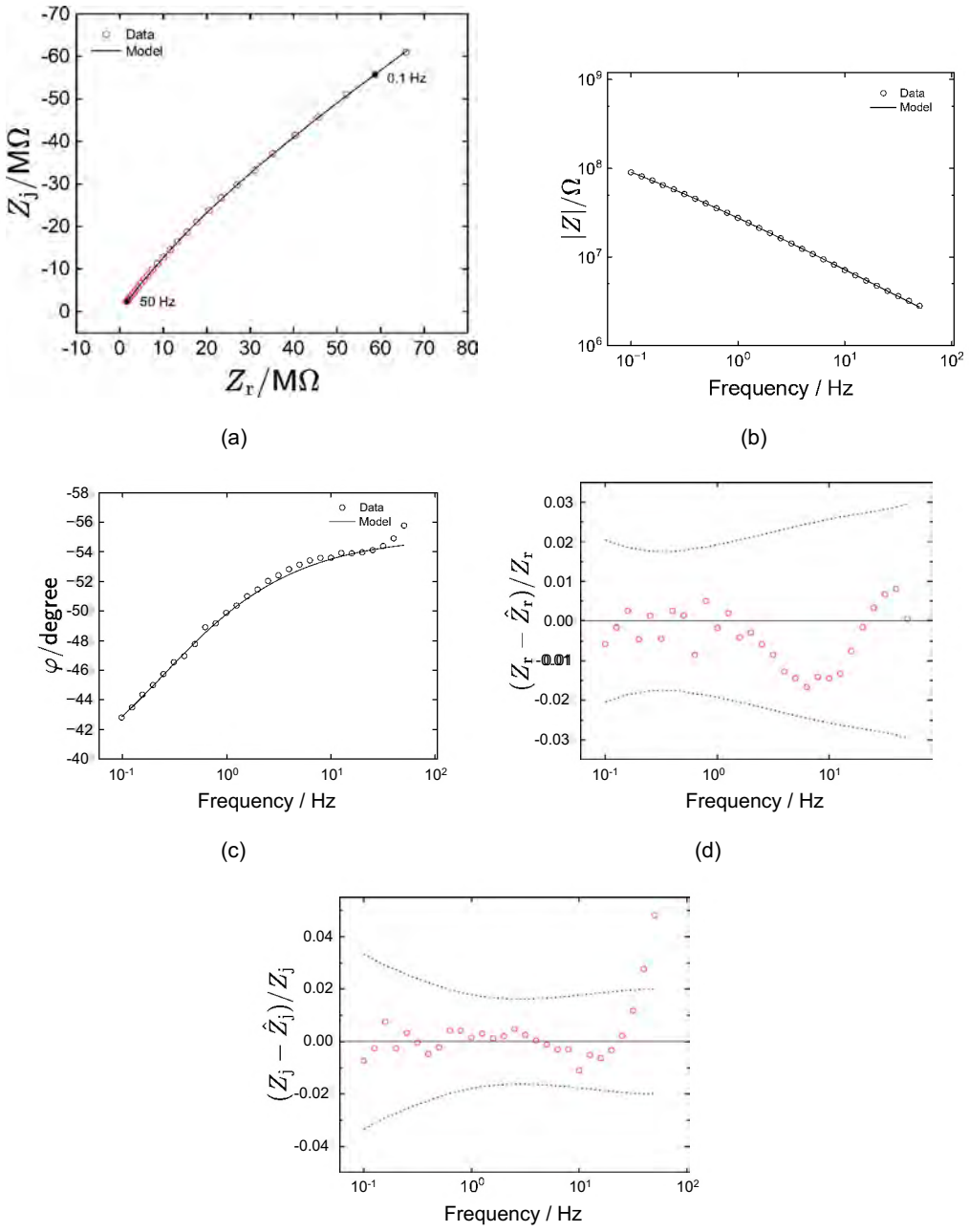

Figure 6-5. Process model regression results for the in vitro impedance spectra of a 5 m electrode at open circuit: a) Nyquist plot, b) impedance magnitude as a function of frequency, c) phase angle as a function of frequency, d) real normalized residuals, and e) imaginary normalized residuals. The lines represent the fit of the process model given as equation (6-3). The dashed lines represents the 95.4% (±2) confidence interval.

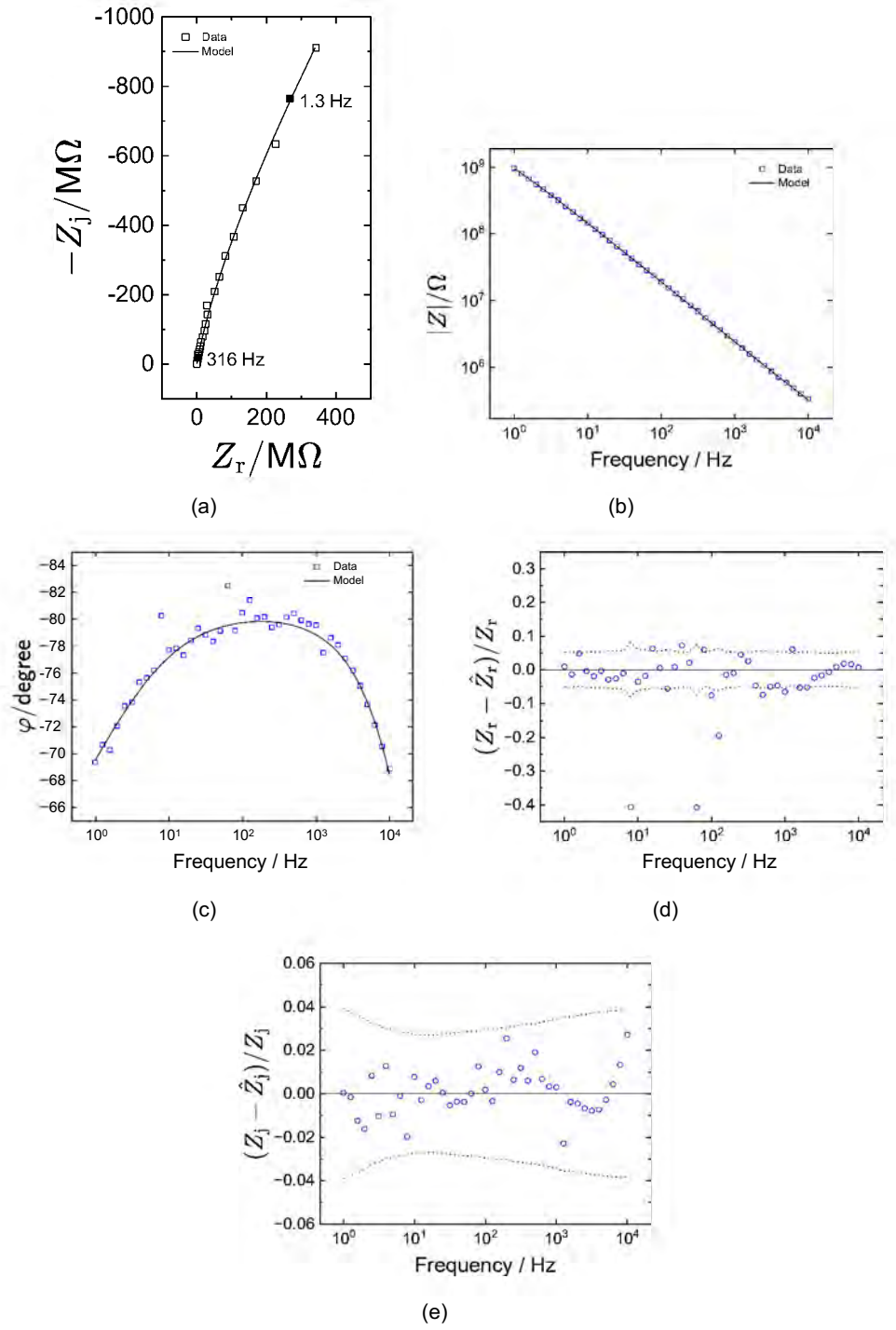

Figure 6-6. Process model regression results for a 50 m electrode in vivo EIS data: a) Nyquist plot, b) impedance magnitude, c) phase angle, d) real normalized residuals, and e) imaginary normalized residuals. The lines represent the fit of the process model given as equation (6-3). The dashed lines represents the 95.4% (±2) confidence interval.

6.2.4.1 In Vitro Impedance Spectra

The normalized real and imaginary residuals are shown in Figures 6-7(a) through 6-7(f) for the in vitro impedance spectra of a 5 m, 25 m, and 50 m diameter electrodes, respectively. Each plot illustrates the residuals as a function of frequency. The real and imaginary residuals were normalized by the real and imaginary component of the impedance respectively. For all diameters, most residual errors across the frequency range fall within the ±2 bounds (95.4% confidence interval), confirming that the impedance data from all electrode sizes are consistent with the Kramers–Kronig relation. The close agreement between measured and modelled data affirms that the system under investigation is linear, and stationary over the frequency range analyzed. The spread of residuals demonstrates how well the measurement model matches the experimental data at each frequency. If the residuals stay within the 95.4% confidence interval for all frequencies, the model is highly reliable for that condition. Broader intervals or outliers at particular frequencies suggest locations where the measurement model fit is weaker.

6.2.4.2 In Vivo Impedance Spectra

The normalized real and imaginary residuals for the in vivo impedance spectra of the representative 5 m, 25 m, and 50 m diameter electrodes are presented in Figure 6-8. Each plot illustrates the residuals errors as a function of frequency. The real and imaginary residuals represented as orange circles were scaled by the real and imaginary component of the impedance respectively. All residuals lie within the ±2 bounds (95.4% confidence interval) indicated by dashed lines in Figures 6-8(a) through 6-8(f), confirming that the impedance data for all electrode sizes are consistent with the Kramers–Kronig relations. The alignment between measured and modeled data suggests that the system is linear and stationary across the analyzed frequency range.

6.3 G1 Discussion

The dependence of regressed process model parameters on the electrode size was evaluated for G1 impedance measurements in vitro and in vivo. The capacitance values estimated from the measurement model regression were compared with those obtained using CPE parameters

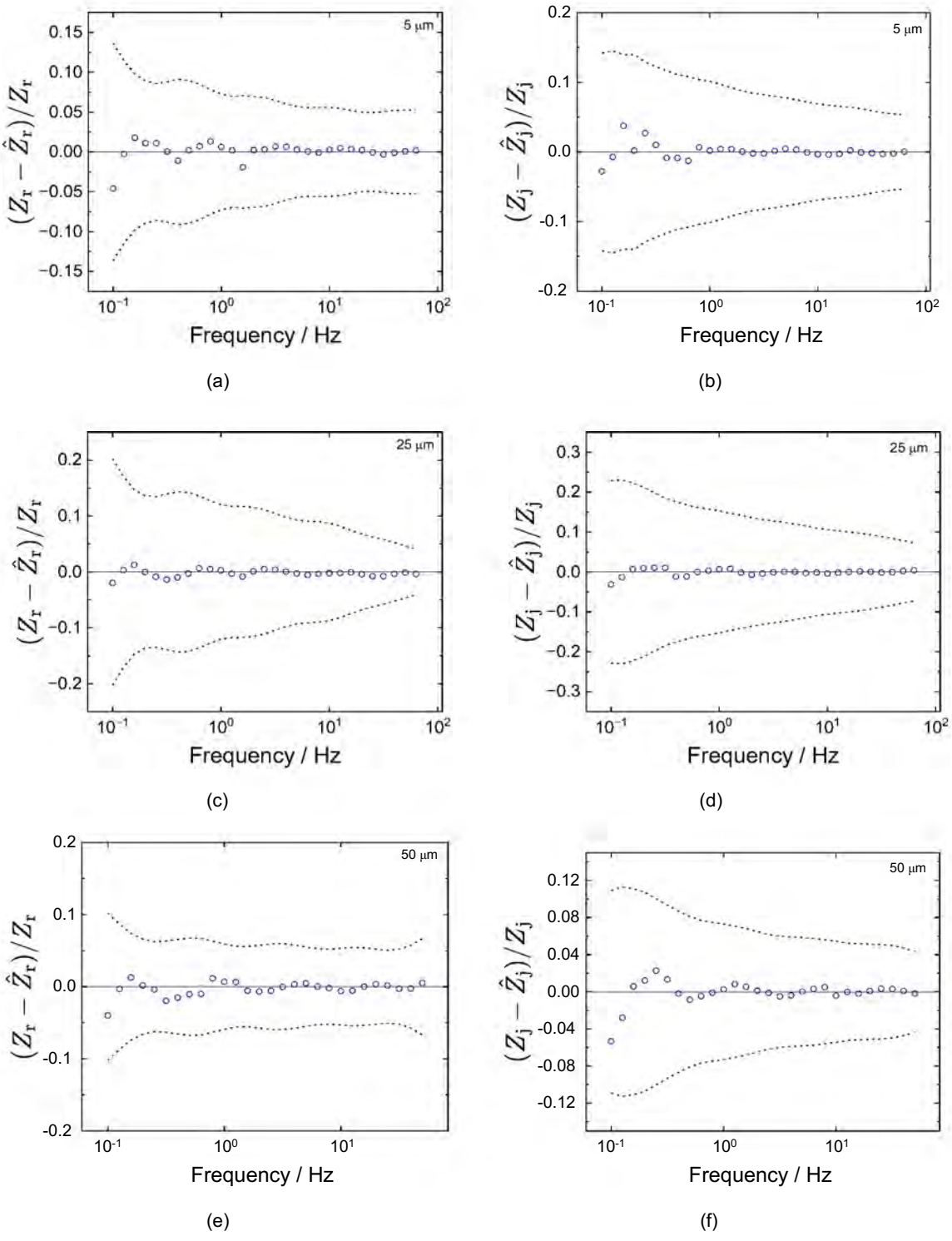

Figure 6-7. Residual errors for regression of the measurement model to the in vitro impedance data under error structure weighting: a) and b) real and imaginary residuals for the 5 m electrode, respectively, c) and d) real and imaginary residuals for the 25 m electrode, respectively, e) and f) real and imaginary residuals for the 50 m electrode, respectively. The dashed lines represents the 95.4% (±2) confidence interval.

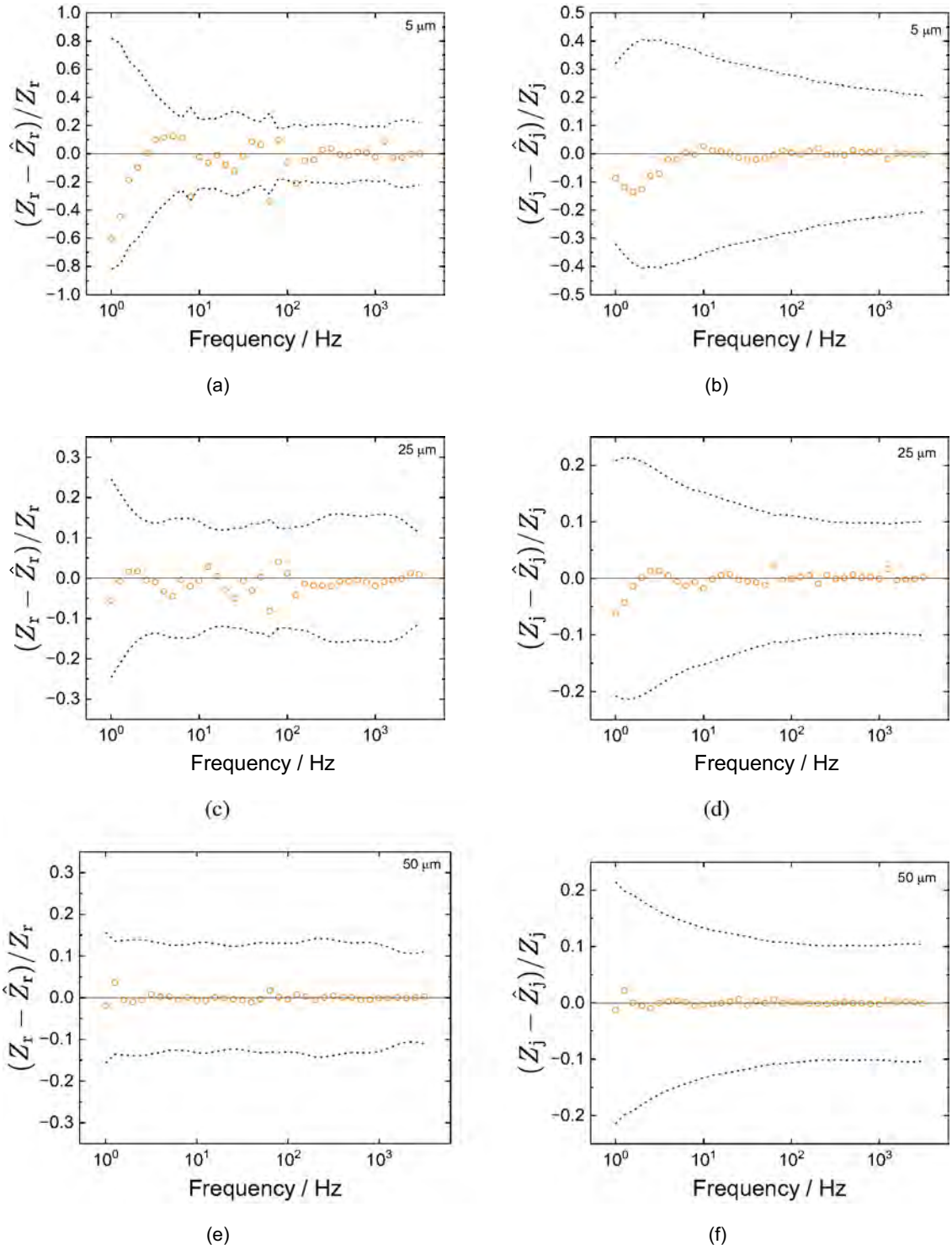

Figure 6-8. Residual errors for regression of the measurement model to the in vivo impedance data under error structure weighting: a) and b) real and imaginary residuals for the 5 m electrode, respectively, c) and d) real and imaginary residuals for the 25 m electrode, respectively, e) and f) real and imaginary residuals for the 50 m electrode, respectively. The dashed lines represents the 95.4% (±2) confidence interval.

extracted from the process model. The measurement model capacitances for impedance measurements in vitro and in vivo show clear dependence on electrode size.

6.3.1 Regressed Parameters In Vivo as a Function of Electrode Size

The regressed model parameters were examined as a function of electrode diameter to determine how electrode size. The process model analysis reveals the consistency of key electrochemical properties such as resistance and capacitance with electrode sizes. The variation of the regressed constant-phase element (CPE) parameters with electrode size are summarized in Figure 6-9 for in vivo impedance spectra. Distinct trends are observed across electrodes of different sizes. The error bars represent ± 1 standard deviation. The constant-phase-element (CPE) coefficient, Q for in vivo impedance response are summarized in Figure 6-9(a). The data points indicate a strong dependence of Q on electrode size, showing a downward trend for larger electrode diameters, meaning that smaller electrodes exhibit higher values of Q. The CPE exponent, fluctuates within a narrow range between 0.75 and 0.95 as diameter increases, as shown in Figure 6-9(b). No clear systematic rise or fall of was observed with increasing electrode diameter.

The ohmic resistance, R_e generally increases with increasing electrode diameter. This trend is observed by the upward slope shown in Figure 6-10(a), with smaller diameters having lower R_e and larger diameters showing higher values. The charge-transfer resistance, R_{tc} displays significant scatter with no clear monotonic increase or decrease with electrode diameter, as shown in Figure 6-10(b). The highest outlier is observed at an intermediate electrode diameter of 30 m. The scatter plots for the diffusion resistance, R_d are illustrated in Figure 6-10(c). The R_d values slightly increases and remains relatively constant above a diameter of 25 m, with greater scatter for small electrodes.

6.3.2 G1 Capacitance as a Function of Electrode Size

The electrochemical impedance spectroscopy of the G1 device was analysed in vivo and in vitro and the dependence of capacitance on electrode geometry were evaluated. The effective double-layer capacitance was obtained by fitting the measurement model (equation (2-19)) to the

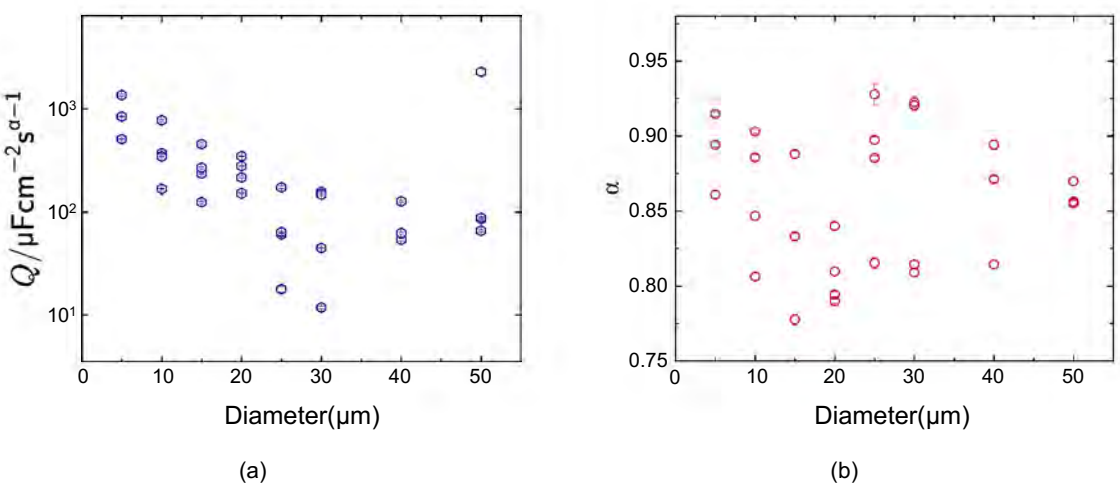

Figure 6-9. Parameter values for the regression of the process model described by equation (6-3) to G1 electrodes in vivo: a) CPE coefficient of pore, Q; b) CPE exponent of pore, ;. Error bars represent one standard deviation.

impedance spectra of G1 devices. The capacitance derived from this model-based regression is defined in equation (7-32). Alternatively, the capacitance was also estimated by converting the constant-phase element (CPE) parameters into an effective double-layer capacitance using the Brug relation [141], which accounts for surface distributions of time constants, as expressed in equation (7-34). For in vitro measurements, the ohmic resistance, R_e could not be obtained from the process model regression, therefore capacitance was only estimated using the measurement model approach.

The effective double-layer capacitance, dl from the regression of process model to in vivo impedance spectra are shown in Figure 6-11(a). The double-layer capacitance (black triangles) are in good agreement with the measurement model capacitance (red circles). As illustrated in Figure 6-11(a), both capacitances decreases as electrode diameter increases with the highest double-layer capacitance of 236 ± 10 F/cm^2 observed for the 5 m diameter electrodes. The capacitance extracted from the regression of the measurement model regression to the in vitro impedance spectra, dl,mm are summarized in Figure 6-11(b). The values of dl,mm also decreases as electrode diameter increases. Small diameters exhibit much larger dl,mm values, while larger diameters show lower and relatively consistent capacitance. The measurement model capacitance

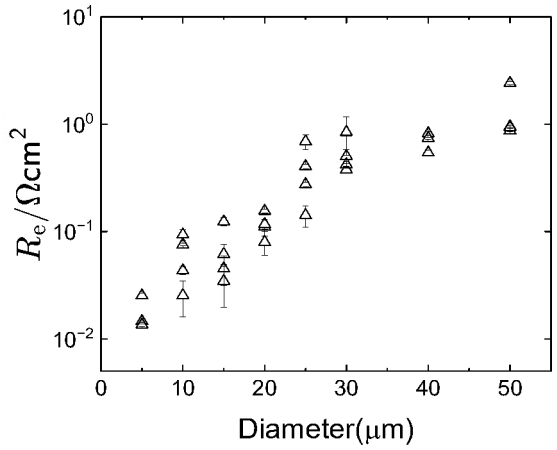

(a)

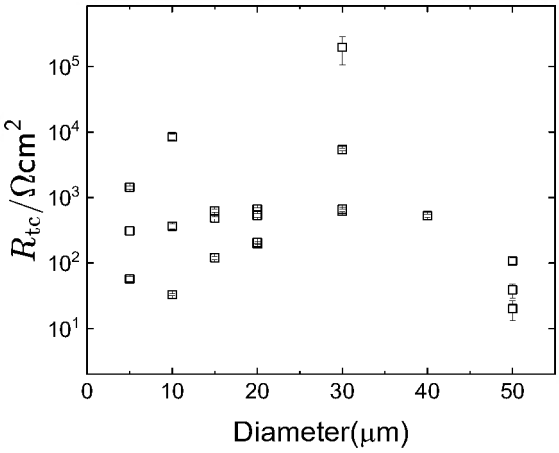

(b)

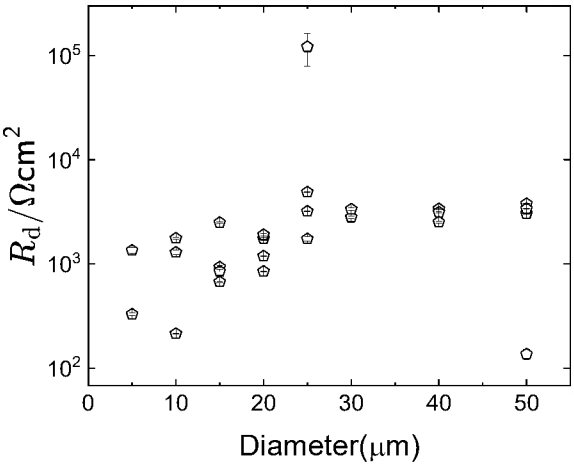

(c)

Figure 6-10. Parameter estimates for the regression of the process model given as equation (6-3) to G1 electrodes in vivo: a) ohmic resistance R_e, b) charge-transfer resistance R_{tc,O_2}, c) Warburg-like diffusion resistance R_{d,O_2}. Error bars represent one standard deviation.

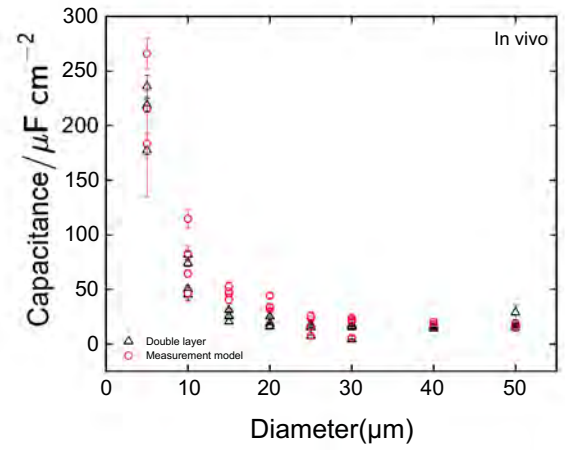

(a)

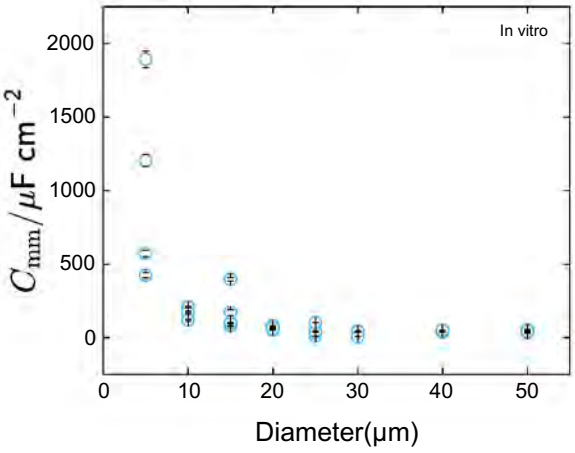

(b)

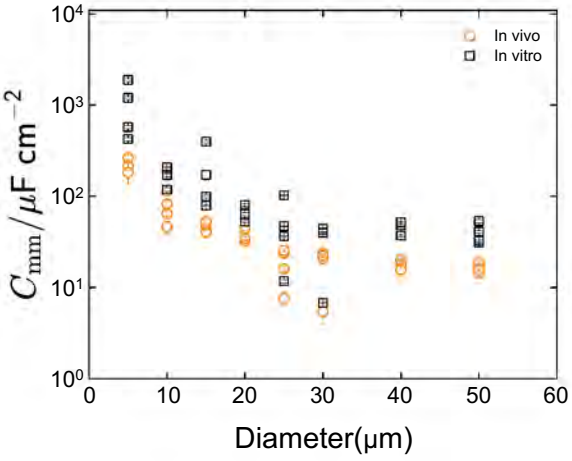

(c)

Figure 6-11. Capacitance as a function of electrode size for G1 electrodes: a) measurement model, C_{mm} and double-layer capacitance, C_{dl} for in vivo data; b) measurement model capacitance, C_{mm} for in vitro data; c) measurement model capacitance, C_{mm} for in vitro and in vivo datasets. Error bars represent one standard deviation.

was compared for in vivo and in vitro impedance measurements in Figure 6-11. Both in vivo (orange circles) and in vitro (black squares) $_{dl,mm}$ capacitance values show a similar trend. $_{dl,mm}$ decreases with increasing diameter. However, the in vitro values (black squares) generally occupy higher resistance values compared to the in vivo capacitance (orange circles) at matching diameters. The trend suggests that smaller electrodes have significantly higher double-layer capacitance per unit area, in both conditions.

6.3.3 Statistical Results for G1

The double-layer capacitance $_{dl}$ was calculated for the impedance spectra of G1 microelectrodes and ultramicroelectrodes ranging in diameter from 5 m to 50 m. The capacitive behavior observed for both in vitro and in vivo measurements were consistent with the distribution of time constant long the electrode surface. Therefore, the capacitances of the G1 electrode were estimated using the Brug's formula (equation 2(7-34)) for surface distribution of time constants. The means and standard deviations of the constant-phase-element parameters, , and , and the ohmic resistance, extracted from the process model regression were used for the calculation. These estimates were obtained via a Monte Carlo simulation.

The resulting normal distributions of the double-layer capacitance for a 5 m ultramicroelectrodes in vivo are shown in Figure 6-12(a). The mean value of capacitance was 236 F/cm^2, and the standard deviation was 10.32 F/cm^2. The statistical distribution of the double-layer capacitance ($_{dl}$) for a 10 m ultramicroelectrode is presented in Figure 6-12(b). The Gaussian fit to the data is represented as a solid blue curve. The double-layer capacitance values for the 10 m sites were normally distributed around 74.19 F/cm^2 with a standard deviation of 3.19 F/cm^2, indicating good reproducibility of the regressed parameters. The mean value and standard deviation of the double-layer capacitance, $_{dl}$ for a 15 m^2 electrode in vivo was 25 ± 1.58 F/cm^2 as illustrated in Figure 6-12(c).

The Guassian curve of the double-layer capacitance values for a 20 m microelectrode are normally distributed around 25.26 F/cm^2 with a standard deviation of 0.67 F/cm^2, as depicted in Figure 6-12(d). The narrow histogram implies a smaller standard deviation for the double-layer

capacitance of the 20 m microelectrode consistent with a uniform time constant distribution along the electrode surface. The statistical results of the double-layer capacitance for a 50 m electrode in vivo is shown in Figure 6-12(e). The mean and standard deviations are normally distributed around 29.04 F/cm^2 and 6.50 F/cm^2 respectively. This result aligns with the distribution of the double-layer capacitance, $_{dl}$ observed across all 50 m^2 electrodes shown in Figure 6-11(a).

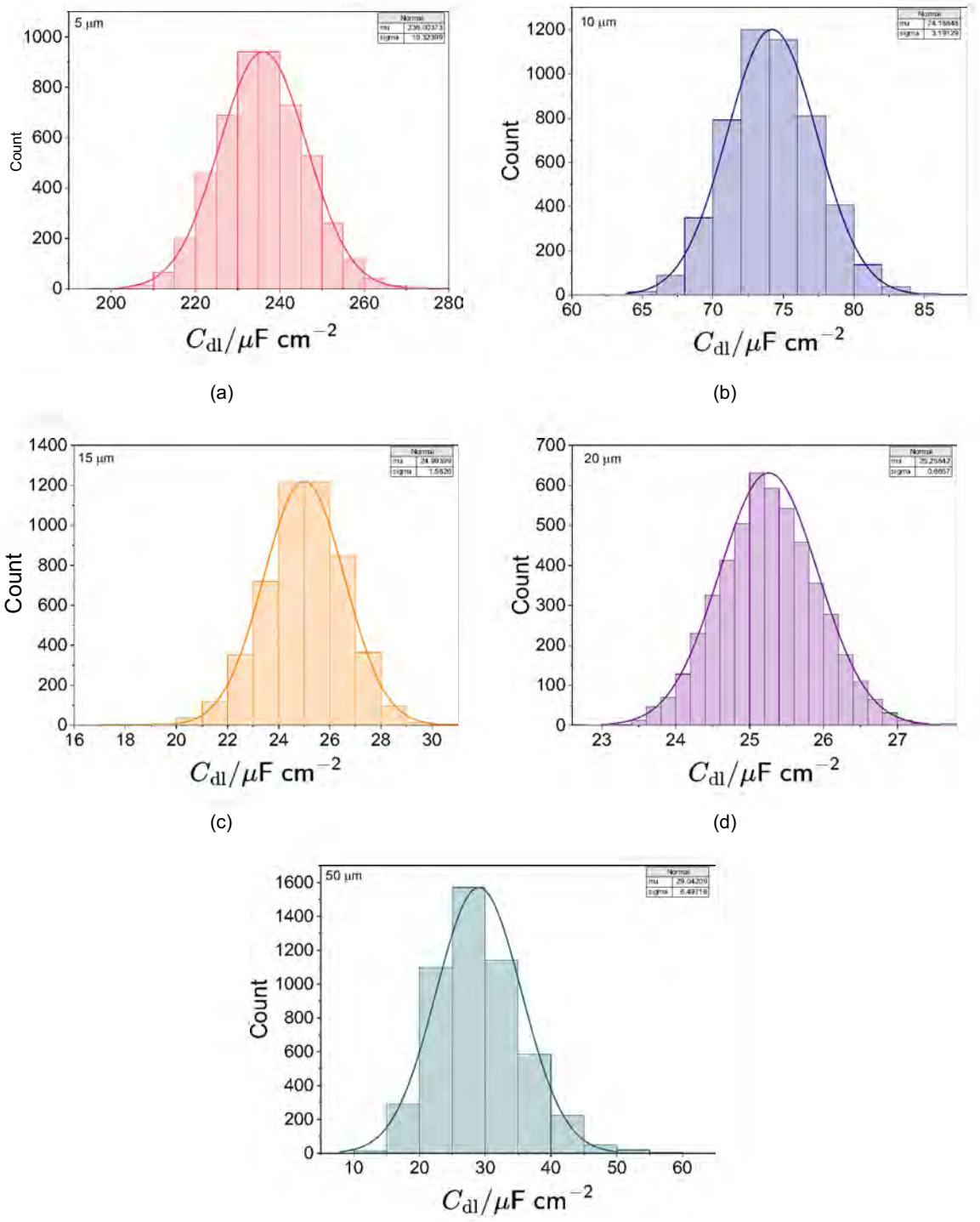

Figure 6-12. Process model regression results showing the normal distribution of the double-layer capacitance calculated from equation (7-34) for the G1 electrodes in Vivo: a) 5 m electrode, b) 10 m electrode, c) 15 m electrode, d) 20 m electrode, and e) 50 m electrode.

CHAPTER 7
IMPEDANCE RESPONSE OF G2 ULTRAMICROELECTRODE ARRAYS

The generation 2 (G2) device consist of high-density ultramicroelectrode arrays (HD UMEAs) featuring geometric surface areas (GSAs) of approximately 20 m^2 to 80 m^2. As shown in Figure 3-3, the electrode design includes two large reference electrodes, each with a geometric surface areas (GSAs) of 4000 m^2, alongside two looped traces and two terminal traces for evaluating both low- and high-impedance limits in the accuracy contour plots. The electrode surface is fabricated from gold and coated with sputtered iridium oxide film (SIROF) to enhance charge-injection capacity. The design and fabrication method for the G2 devices is discussed in section 3.1.2.

The impedance measurement were performed in phosphate-buffered saline at open circuit condition. The details of the experimental procedure can be found in section 5.1. The device was connected to a Gamry Reference 600+ potentiostat via a custom junction box, and the usable frequency range was evaluated through the accuracy contour plots. The methods for plotting the accuracy contour plot is presented in Chapter 4. The impedance data was analyzed with the measurement model to quantify the stochastic error structure and extract physically meaningful parameters. The measurement model theory is discussed in section 2.5.2.3 and the measurement modeling approach is provided in section 5.3.

This chapter details the process modeling and in vitro experimental results that support the interpretation of impedance spectra for the G2 devices. Parameters extracted from process model regression were used to estimate the capacitance of the electrode.

7.1 Process Model for G2 Impedance Spectra

The comprehensive model presented in Figure 7-1 was developed to analyze the impedance spectra of G2 device. The model captured the parallel contributions of the redox-active iridium oxide (IrOx) coating, the constant-phase-element behavior of the flat surface, the influence of the potentiostat cable, and connection interfaces and the faradaic processes including reversible oxygen reduction, and mass-transfer of reacting species. The ohmic resistance (R_e) which represents the resistance to current flow through the electrolyte, is placed in series with the

parallel network of elements representing the electrode interface, as shown in Figure 7-1. The total impedance of the circuit is expressed as

$$\text{total} = \frac{\text{wire} \quad \text{system}}{Z_{\text{wire}} + \quad \text{system}} \tag{7-1}$$

where Z_{wire} is the impedance of the cable accounting for the influence of parasitic capacitance at high frequency. Z_{system} is the impedance of the system given by

$$\text{system} = \quad e + \quad \left(\frac{1}{\text{flat}} + \frac{1}{\text{t,c}} + \frac{1}{\text{t,eff}} \right)^{-1} \tag{7-2}$$

Z_{flat} is the impedance of the flat surface, $Z_{t,c}$ is the cathodic impedance representing the oxygen-reduction reactions influenced by mass transfer, and $Z_{t,eff}$ is the impedance of iridium oxide redox behavior.

7.1.1 Influence of Cables and Connections

The influence of the potentiostat cable and connection interfaces on high-frequency impedance data was modeled using a constant phase element (CPE) [142] whose impedance was expressed as

$$\text{wire} = \frac{1}{(j \quad)^{\quad w} \quad _w} \tag{7-3}$$

where Z_{wire} is the impedance of the cable, Q_w is the constant-phase-element component of the cable, $_w$ is the constant-phase-element exponent of the cable, j is complex number represented as $\sqrt{-1}$, and is frequency. These components replicate the parasitic capacitance introduced by the cable at high frequency.

7.1.2 Flat Substrate Contribution

The behavior of the flat gold substrate was captured using an additional constant-phase element (CPE) in parallel with the electrode–electrolyte interface. The impedance of the flat surface is represented as

$$\text{flat} = \frac{1}{(j \quad)^{\quad f} \quad _f} \tag{7-4}$$

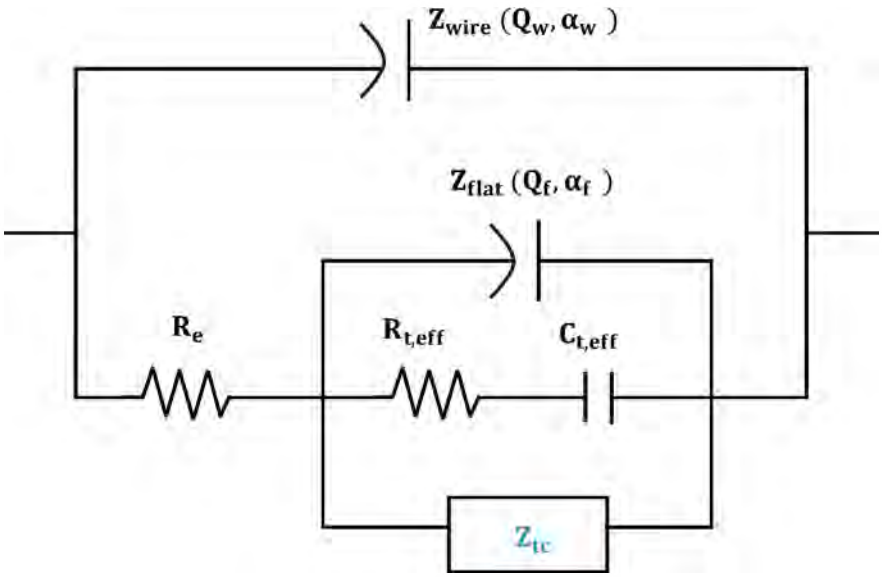

Figure 7-1. Electrical circuit representation of the process model (Equation (7-1)) for G2 device. The model accounted for the rough electrode behavior, cable capacitance, changes in iridium oxidation states, and mass-transfer-influenced oxygen reduction reaction.

where Q_f is the constant-phase-element component of the flat surface and $_f$ is the constant-phase-element exponent of the flat surface, j is complex number represented as $\sqrt{-1}$, and ω is frequency. The CPE accounts for the distributed nature of the interfacial capacitance due to the flat geometry and inhomogeneous current distribution across the surface. The faradaic processes were modelled with a charge-transfer resistance R_{tc}, connected in series to a Warburg impedance. The impedance is given by

$$_{tc} = _{tc} + _{D} \tag{7-5}$$

Where: Z_{tc} is the cathodic impedance, R_{tc} is the charge-transfer resistance, Z_D is the diffusion impedance for an infinite film attributed to Warburg [78, 140].

$$_{D} = \frac{_{d}}{\sqrt{j}} \tag{7-6}$$

R_d is the diffusion resistance, j is complex number represented as $\sqrt{-1}$, and ω is frequency. This sub-circuit captures the impedance behavior typical of mass-transfer influenced oxygen-reduction reactions derived in previous publication [132].

7.1.3 Iridium Oxide Redox Behavior

Given the redox behavior of sputtered iridium oxide films (SIROF), an additional circuit was introduced to simulate the reversible transitions between Ir(III) and Ir(IV) oxidation states. This was modeled using a series combination of an effective capacitance and resistance, as shown in Figure 7-1. The reversible iridium oxidation and reduction reaction may be expressed as:

$$Ir^{3+} \quad Ir^{4+} + e^- \tag{7-7}$$

The interpretation model detailed below was developed by Lutz et al.[70]. The total concentration of electrode sites is

$$\text{total} = \quad 3 + \quad 4 \tag{7-8}$$

where c_3 is the concentration of Ir^{3+} and c_4 is the concentration of Ir^{4+}. The associated surface concentration can be represented as

$$\Gamma_{tot} = \int_0^{} \quad \text{tot} \tag{7-9}$$

A corresponding integration can be obtained for $\quad 3$ and $\quad 4$ resulting in Γ_3 and Γ_4, respectively. The fractional occupation of electrode site by Ir^{3+} is given as

$$\frac{\text{site}}{\text{site}} = \frac{\Gamma_3}{\Gamma_{total}} \tag{7-10}$$

where Γ_3 is the surface concentration of Ir^{3+}, and Γ_{total} is the total surface concentration. The fractional occupation of a electrode site by Ir^{4+}, Γ_4 is expressed as

$$1 - \quad \text{site} = \quad \frac{\Gamma_4}{\Gamma_{total}} \tag{7-11}$$

The oxidation current is given by

$$ _3 = \quad _3 \quad _{site} \quad \quad (\quad _3 \;) \tag{7-12} $$

where K_3 denotes a rate constant expressed in units of current density, while the coefficient b_3 is related to the apparent charge transfer coefficient. The term $V = \quad _m - \quad _0$ represents the local electrochemical driving force. The equilibrium potential is implicitly included in the definition of K_3. The reduction current is given as

$$ _4 = - \quad _4(\; 1 - \quad _{site}) \quad \quad (- \quad _4 \;) \tag{7-13} $$

In this expression, K_4 is a rate constant with units of current density, and b_4 is a coefficient proportional to the apparent charge transfer coefficient. A conservation relationship can be formulated to describe the fractional occupancy of sites by Ir^{3+} as follows

$$ F\Gamma_{total} \overline{\overline{\quad _{site} \quad}} = -(\quad _3 + \quad)_4 \tag{7-14} $$

where F denotes Faraday's constant (F = 96,487 C/equiv.). At equilibrium, the condition $_3 + \quad _4 = 0$ holds, and the fractional occupancy of sites by Ir^{3+} can be expressed as

$$ \overline{\quad}_{site} = \frac{\quad _4 \quad \quad (- \quad _4 \; \overline{\quad})}{\quad _4 \quad \quad (- \quad _4 \; \overline{\quad}) + \quad _3 \quad \quad (\quad _3 \; \overline{\quad})} \tag{7-15} $$

The equilibrium fractional occupation of sites by Ir^{3+} approaches unity at negative potentials and approaches zero at positive potentials. At $\quad = 0$, $_{s}i_{te} = \quad _{site} \quad \frac{\quad _4}{\quad _3 + \quad _4}$, which reflects that the equilibrium potential is inherently incorporated into the definitions of $\quad _3$ and $\quad _4$.

The impedance contribution arising from reaction can be written as

$$ \quad _F = \frac{\tilde{\quad}}{\quad _F} \tag{7-16} $$

where $\tilde{}$ represents the potential phasor and is given as

$$= \bar{} + e\{ \tilde{} ( ) \} \tag{7-17}$$

For sufficiently small perturbation amplitudes, the current density phasors can be expressed as

$$\tilde{} 3 = 3 \; 3\bar{}_{site} \quad (3) \bar{} \tilde{} + 3 \quad (3) \bar{} esite \tag{7-18}$$

and

$$\tilde{} 4 = 4 \; 4(1 - \bar{}_{site}) \quad (4) \bar{} + \tilde{} 4 \quad (- 4)e \; site \bar{} \tag{7-19}$$

The conservation relation in equation (7-14) gives

$$F\Gamma_{tota}le \; s\bar{i}_{te} = -(3 \tilde{} + 4) \tilde{} \tag{7-20}$$

or

$$F\Gamma total \; \tilde{site} = \left(\frac{11}{t,3} + \frac{}{t,4} \right) \tilde{} - \left(3 \exp(3) + \bar{} 4 \exp(- 4) \; site \bar{} \right) \tilde{} \tag{7-21}$$

where the charge-transfer resistances for the oxidation and reduction reactions are expressed as

$$t,3 = \frac{1}{3 \; 3\bar{}_{site} \quad (3) \bar{}} \tag{7-22}$$

and

$$t,4 = \frac{1}{4 \; 4(1 - \bar{}_{site}) \quad (- 4) \bar{}} \tag{7-23}$$

respectively. As the total faradaic current is

$$F = 3 + 4 \tag{7-24}$$

The faradaic impedance is given as

$$_{t,eff} = _{t,eff} \left(\frac{j \quad \Gamma_{total} + \quad 3 \qquad (\quad 3 \ ) + \quad 4 \qquad (- \quad 4 \qquad \quad}{j \quad F\Gamma_{total}} \right) \tag{7-25}$$

where $_{t,eff}$ is the effective resistance, expressed as

$$_{t,eff} = \frac{_{t,3} \quad _{t,4}}{_{t,3} + \quad _{t,4}} \tag{7-26}$$

An alternative form of Equation (7-25) is

$$_{t,eff} = _{t,eff} + \frac{1}{j \quad _{t,eff}} \tag{7-27}$$

where $C_{t,eff}$ is the effective capacitance expressed as a function of potential, the concentration of oxidized and reduced sites, and the associated rate constants as follows

$$_{t,eff} = \frac{F\Gamma_{total}}{_{t,eff}\left(\quad 3 \qquad (\quad 3 \ ) + \quad 4 \qquad (- \quad 4 \quad \right)} \tag{7-28}$$

The inclusion of this element allowed the model to account for the double-layer charging current and the faradaic reaction associated with the changes from Ir^{3+} to Ir^{4+}.

7.2 Experimental Results

The electrochemical impedance spectroscopy measurements for the G2 ultramicroelectrode array was performed at open circuit conditions. The accuracy contour plots was used to defined the operational limits of the Gamry Reference 600+ potentiostat in conjunction with the electrode arrays. The resulting Nyquist and Bode plots were used to examine the frequency-dependent impedance responses of electrodes with different site areas. The measurement error associated with the impedance spectra of the electrode sites was quantified using a stochastic error structure. A process model was used to interpret the impedance spectra and extract the parameters of the

electrode arrays. The measurement modeling and data interpretation were performed with version 1.8 of Watson and Orazem's [97] measurement model program.

7.2.1 Impedance Data

Impedance spectra was recorded for ultramicroelectrode sites with nominal areas of 20 m^2, 80 m^2, and large electrode of 4000 m^2. Measurements were conducted under open-circuit conditions following a stabilization period of 300 seconds. Each potentiostatic EIS experiment spanned 20 minutes, and a total of 32 spectra were collected, i.e. 24 from the electrode sites and 8 from looped and terminated features for accuracy contour evaluations.

Nyquist plots for the representative sets of three electrode sizes are presented in Figure 7-2(a). The result shows distinct impedance profiles without overlap. The impedance values were normalized by electrode area. The scaling resulted to a reduction in both real and imaginary components at low frequencies for the 20 m^2, and 80 m^2 electrodes. However, the larger electrode site (4000 m^2) exhibited significantly higher impedance magnitude at low frequency. While the general trend is that impedance increases as electrode area decreases, deviations from the ideal inverse scaling have been observed for ultramicroelectrodes (UMEs) and may be influenced by various factors related to transport of electroactive species to the electrode through hemispherical rather than linear diffusion, surface roughness, porosity, and enhanced edge effects, leading to non-ideal scaling [143, 71, 144].

The low-frequency trend for all electrode sites suggests constant-phase-element (CPE) behavior and faradaic reactions at the electrode-electrolyte interface. The zoomed-in Nyquist plots shown in Figure 7-2(b), highlight deviations at high frequencies, possibly arising from parasitic capacitance associated with the cables and complexity of the electrode connections. To ensure precise data analysis, initial frequency points exhibiting non-stationary behavior were excluded, and the remaining data were fitted using the measurement model. All subsequent modeling and parameter extraction were performed on the area-normalized impedance data following the procedure described by Orazem [132].

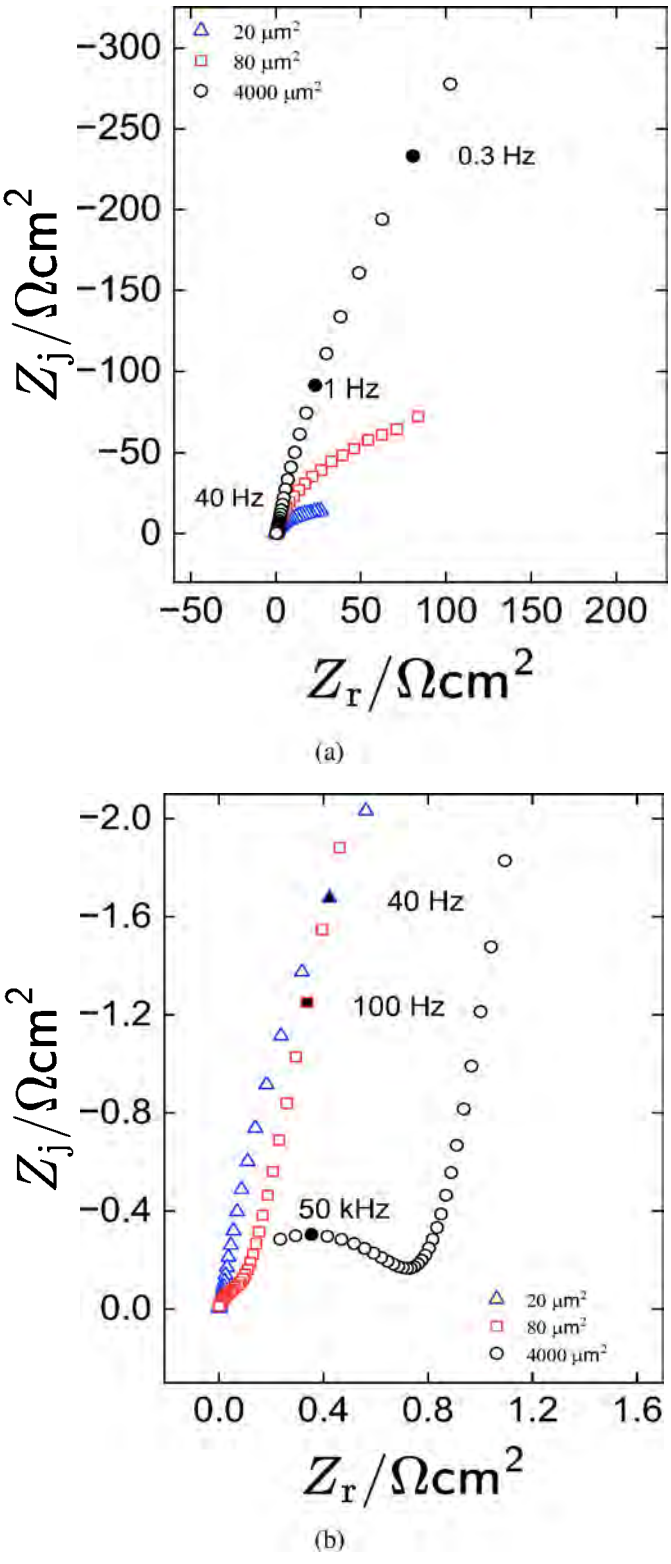

Figure 7-2. Impedance spectra in Nyquist format with electrode area as a parameter: a) complete frequency spectrum and b) zoomed in plot at high-frequency points. The measurement was performed at open circuit at frequency range from 0.2 Hz to 100 kHz

7.2.2 Error Model

The measurement model described by equation (2-19) was used to regress the impedance data for the 20 m^2, 80 m^2, and 4000 m^2 electrode sites. The stochastic error structure analysis was performed to quantify experimental noise level, assess the effects of ohmic impedance and parasitic capacitance, and evaluate consistency of the data with the Kramers–Kronig relations. For each electrode size, three replicates of impedance spectra were obtained, enabling estimation of the stochastic error structure. The standard deviations of the real and imaginary components of impedance are presented in Figure 7-3(a) for the 20 m^2 and 80 m^2 electrodes and in Figure 7-3(b) for the large electrode (4000 m^2). For each electrode sites, the observed error distributions are heteroscedastic, and exhibit overlap across the frequency spectrum, as expected for Kramers–Kronig [134, 135] consistent EIS data. As displayed in Figures 7-3(a), and 7-3(b), the solid lines represent fits to the empirically derived error model (equation (5-1)) for each electrode sites. A total of 24 distinct error models were generated, accounting for differences in electrode geometry.

The error model parameters for the selected electrode sites are summarized in Table 7-1. Parameters and were extracted for the 20 m^2, while, parameters and was extracted for the 80 m^2, and 4000 m^2. Normalized error structure plots, shown in Figure 7-3(c), display the standard deviation divided by impedance magnitude for the 20 m^2, 80 m^2, and 4000 m^2 electrodes. At low frequencies, the normalized error for the smaller electrodes (2%) is approximately an order of magnitude greater than that of the 4000 m^2 site (0.3%). At high frequencies, the normalized error drops to 0.3% for the smaller electrodes and 0.04% for the

Table 7-1. Error parameters across electrode site sizes obtained by regressing equation (5-1) to the impedance spectra of G2 electrodes.

Parameter	20 m^2	80 m^2	4000 m^2
	–	$2.47 \times 10^{-3} \pm 1.98 \times 10^{-4}$	$4.61 \times 10^{-4} \pm 6.98 \times 10^{-5}$
	$1.28 \times 10^{-2} \pm 1.16 \times 10^{-3}$	–	–
	$3.11 \times 10^{-4} \pm 6.83 \times 10^{-5}$	$1.78 \times 10^{-4} \pm 3.32 \times 10^{-6}$	$4.48 \times 10^{-6} \pm 4.00 \times 10^{-7}$
	–	–	–

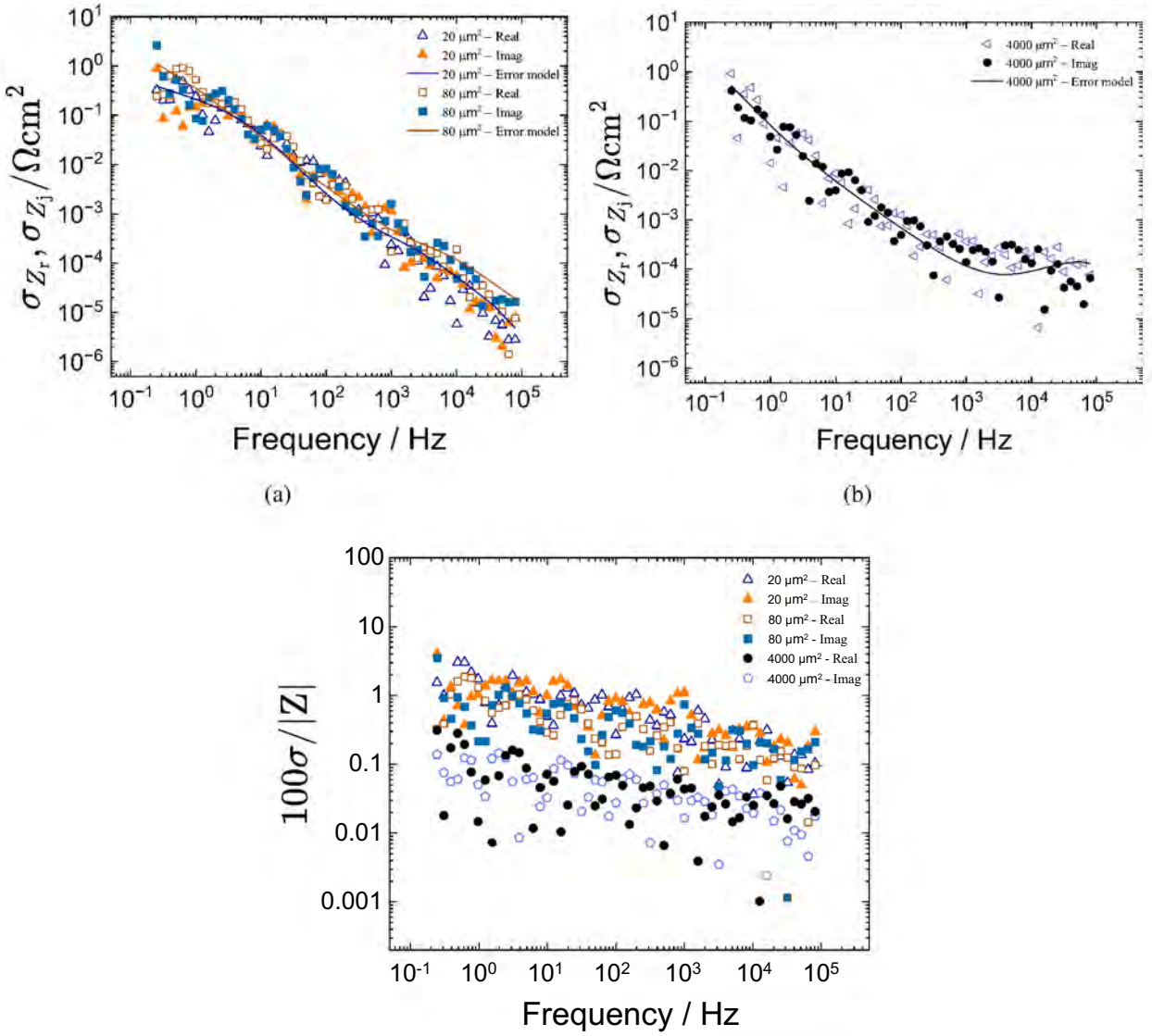

Figure 7-3. Stochastic error structure for impedance spectra of G2 device at open circuit: a) error structure 20 m^2 and 80 m^2 electrodes, b) error structure for 4000 m^2 electrode, c) non-normalized error structure. The solid line represents the error model given by equation (5-1). The regressed error parameters are summarized in Table 7-1. The error structure is a strong function of frequency.

larger site. These noise levels are characteristic of measurements obtained using the Gamry Reference 600+.

7.2.3 Regression with Measurement Model

The Bode magnitude and phase-angle was plotted on a logarithmic scale to visualize the impedance behavior for the 20 m^2, 80 m^2, and 4000 m^2 electrode sites, as a function of frequency. These plots, shown in Figure 7-4 captured the frequency-dependent dispersion at both low and high ends of the impedance spectra. To improve interpretation, the ohmic resistance was removed from the real component of the impedance yielding the ohmic-resistance-corrected magnitude and phase angle plots. The corrected magnitude of impedance was calculated as:

$$|\ |_{adj} = \sqrt{\sqrt{_j^2 + (\ _r - \ _e)^2}} \qquad (7\text{-}29)$$

and the corresponding phase angle as:

$$_{adj} = \tan^{-1}\left(\frac{_j}{_r - \ _e}\right) \qquad (7\text{-}30)$$

where Z_r and Z_j are the real and imaginary components of impedance, respectively, and R_e is the ohmic resistance. Figures 7-4(a) and 7-4(b) present the ohmic-resistance-corrected-Bode magnitude and phase-angle plots, respectively, for all three electrode sizes. The solid lines indicate the fit to the measurement model (equation (2-19)), performed using error-structure weighting. The model aligns closely with experimental data, satisfying the Kramers-Kronig relations. As illustrated in Figure 7-4(a), the 20 m^2 and 80 m^2 electrodes showed a slope of approximately -1 on the log-log magnitude plot, indicative of ideal capacitive behavior at high frequencies. However, the 4000 m^2 electrode displayed a transition to a flat region, suggesting the onset of ohmic effects. This asymptotic feature, observed above the characteristic frequency, arises due to geometry-induced non-uniform current and potential distributions also referred to as ohmic

impedance [6]. The characteristic frequency varies across electrode sizes, and is expressed as

$$\omega_c = \frac{1}{2 R_e C_{dl}} \tag{7-31}$$

The regression of equation (2-19) to the experimental data provided estimates for the characteristic frequency as a function of ohmic resistance, R_e and capacitance, C_{dl} of the system. The capacitance estimated from the regression of (2-19) (measurement model) to the impedance spectra is given as

$$\frac{1}{C_{dl,mm}} = \sum_{k=1}^{k=n} \frac{1}{C_k} = \frac{1}{C_1} + \frac{1}{C_2} + \cdots + \frac{1}{C_n} \tag{7-32}$$

where C_n capacitance of k = nth element and has units of [Farads] or [Fcm^{-2}]. The characteristic frequency for the 20 m^2, 80 m^2, and 4000 m^2 electrodes yielded large values of 940±12 kHz, 900±9 kHz, and 1250±9 kHz, respectively. These large values are the result of an iterative estimation process [70] from the measurement model resulting to lower values of 0.2068±0.007 nF, 0.2067±0.009 nF, and 0.1794±0.003 nF for the 20 m^2, 80 m^2, and 4000 m^2 electrodes, respectively. These low values reflect the combined influence of both interfacial capacitance and parasitic capacitance from lead effects, particularly prominent in the smallest electrodes. Figure 7-4(b) presents the ohmic-resistance-corrected phase-angle plots for all electrode sizes. At high frequencies, the phase angle for the 20 m^2 and 80 m^2 approaches -90^0, indicative of constant-phase-element (CPE) behavior, whereas at low frequencies, the phases shift toward 0^0, signifying an in-phase relationship between current and voltage [1]. Deviations in the phase response of the 4000 m^2 site at high frequencies suggest increased influence from electrolyte resistance, which affects the impedance characteristic.

7.2.4 Kramers–Kronig Consistency Assessment

The real and imaginary components of the measured impedance were regressed using the measurement model (equation (2-19)). The model satisfies the linearity and stationarity criteria implicit in the Kramers–Kronig . The residuals estimated from the regression was used to assess the consistency of the data with the Kramers–Kronig [134, 135]. The measurement model

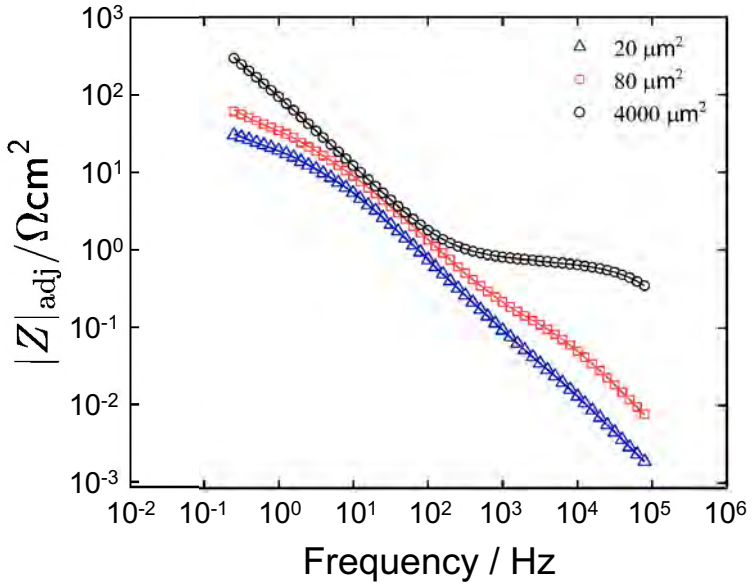

(a)

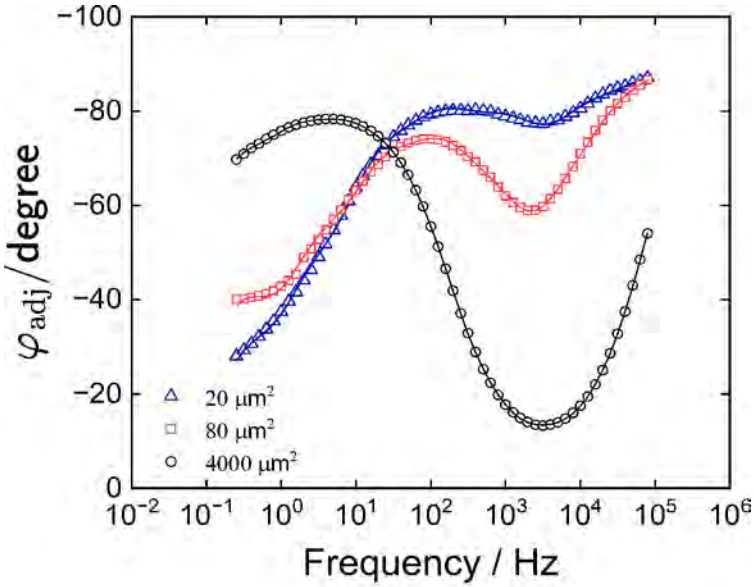

(b)

Figure 7-4. Measurement model (equation (2-19)) regression results for impedance measurements performed at open circuit as functions of frequency with electrode area as a parameter: a) ohmic-resistance-corrected magnitude and b) ohmic-resistance-corrected phase angle. The line represents the fit of the model.

analysis [3] required that the number of Voigt-circuit elements, K was sequentially increased until the 95.4% confidence interval (±2) for each estimated parameter does not include zero. Importantly, any parameter estimate whose confidence interval included zero was considered non-significant and excluded from the final model. Confidence intervals were computed using Monte-Carlo simulation, which allowed for robust estimation of uncertainty under the assumed error structure. The normalized real and imaginary residuals are presented in Figures 7-5(a) through 7-5(f) for the 20 m^2, 80 m^2, and 4000 m^2 electrodes, respectively. Each plot illustrates the residuals as a function of frequency. The real and imaginary residuals were normalized by the real and imaginary component of the impedance respectively. All residuals across the frequency range fall within the ±2 bounds (95.4% confidence interval), confirming that the impedance data from all electrode sizes are consistent with the Kramers–Kronig relation. The close agreement between measured and modelled data affirms that the system under investigation is linear, and stationary over the frequency range analyzed.

7.2.5 Regression with Process Model

To interpret the impedance behavior of the ultramicroelectrodes, the process model (equation (7-1)) was fitted to the impedance spectra. The 20 m^2 electrode site is presented here as a representative example of all the datasets analyzed. The model captured two distinct faradaic processes occurring at the electrode-electrolyte interface. One of these is attributed to the reversible reduction of oxygen, likely enhanced by the aerated conditions under which the measurements were performed. The second process is attributed to a redox reaction involving a change in the oxidation state of iridium, which was modeled using a resistor in series with a capacitor, as expressed in equation (7-27). The fit of the process model (equation (7-1)) to the impedance data for the 20 m^2 electrode is illustrated in Figures 7-6. The Nyquist, magnitude, and phase angle plots (Figures 7-6(a), 7-6(b),and 7-6(c)) demonstrate strong agreement between the measured data and the model fits across the full frequency range. Furthermore, the normalized residual plots for both the real and imaginary components (Figures 7-6(d) and 7-6(e)) show that

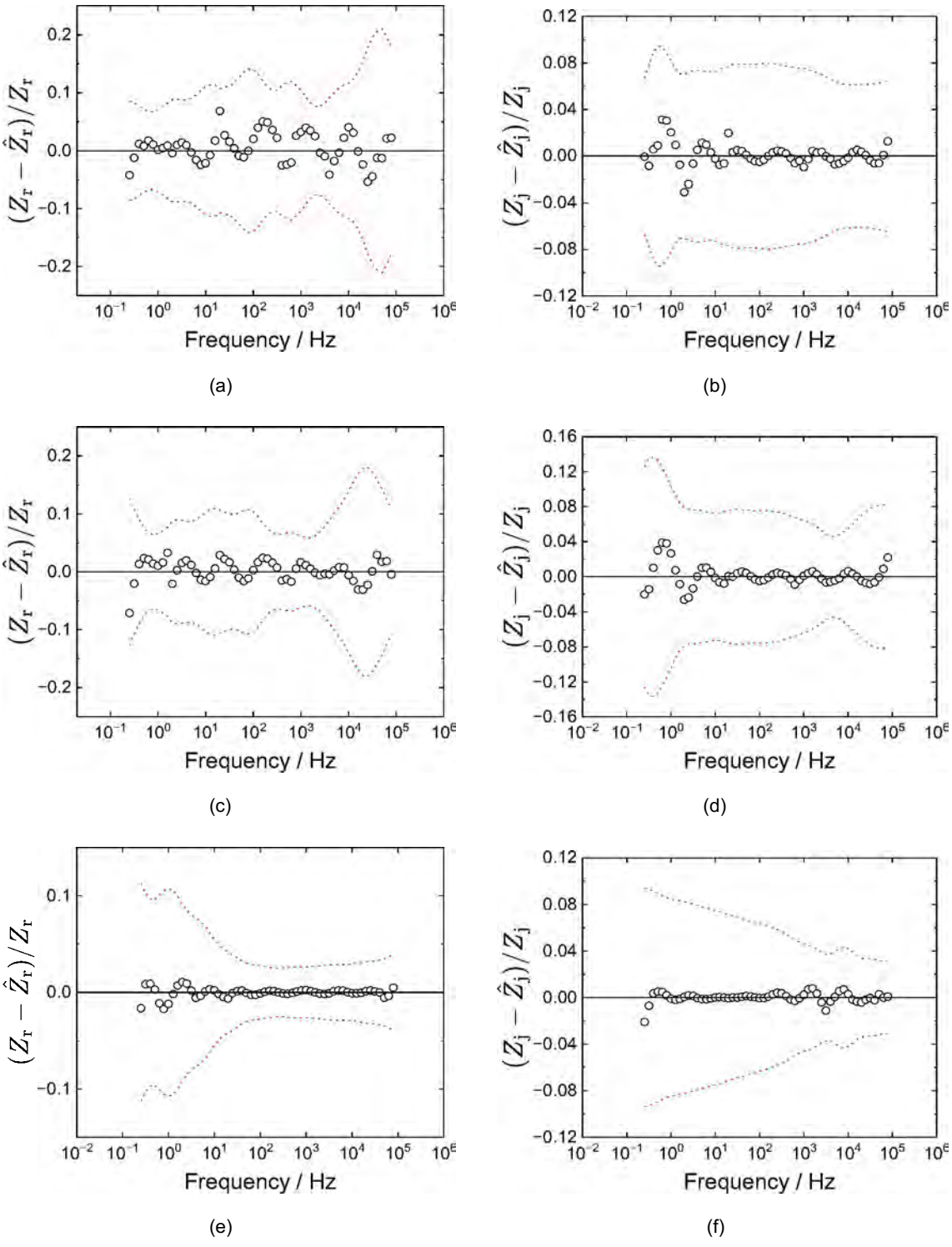

Figure 7-5. Residual errors for regression of the measurement model to the impedance data under error structure weighting: a) and b) real and imaginary residuals for the 20 m^2 electrode, respectively, c) and d) real and imaginary residuals for the 80 m^2 electrode, respectively, e) and f) real and imaginary residuals for the 4000 m^2 electrode, respectively. The dashed lines represents the 95.4% (±2) confidence interval.

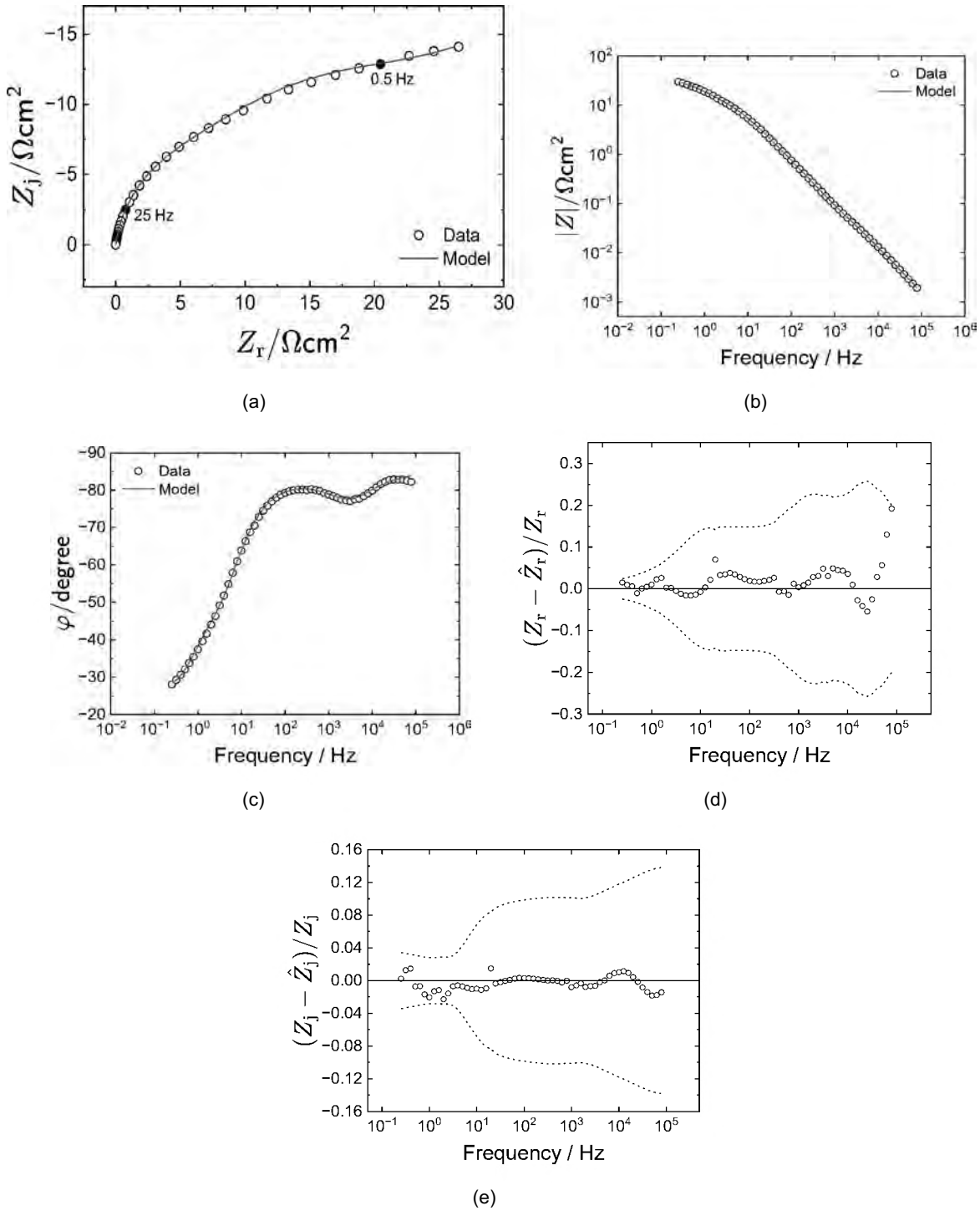

Figure 7-6. Process model regression results for the 5 m (20 m^2) electrode at open circuit: a) Nyquist plot, b) impedance magnitude as a function of frequency, c) phase angle as a function of frequency, d) real normalized residuals, and e) imaginary normalized residuals. The lines represent the fit of the process model given as equation (7-1). The dashed lines represents the 95.4% (±2) confidence interval.

the residuals lie within the ±2 bounds, indicated by dashed lines in each plot. These residuals suggest no systematic deviation, and confirms the adequacy of the regressed model.

The parameters extracted from fitting the 20 m^2 dataset are provided in Table 7-2. These values were evaluated for statistical significance using the ^{2} / criterion, where denotes the degrees of freedom and ^{2} is the chi-square error. For a statistically valid model fit, ^{2} / approaches 1. The values reported in Table 7-2 all fall within the ±2 confidence interval and do not include zero, indicating statistical significance. The obtained ^{2} / values ranged from 1 to 100 across the 14 datasets analyzed, consistent with previously reported results by [70, 6]. These values reflect the variability in electrode behavior while confirming the reliability of the model across different electrode sizes and experimental conditions. The interpretation model accounted for the interfacial redox processes contributing to the overall system response and the influence of the cable.

Table 7-2. Parameter estimates for the regression of the process model given as equation (7-1)) to the impedance data of 20 m^2 site shown in Figure 7-6. Confidence intervals reported are ±1 .

Parameter	Unit	Value
R_t	Ωcm^2	22.53 ± 0.31
Q_f	$mF/s(1-)cm^2$	1.35 ± 0.15
$_e$	–	0.8697 ± 0.0082
R_e	Ωcm^2	0.135 ± 0.015
R_d	Ωcm^2	16.76 ± 0.33
$_w$	–	0.9398 ± 0.0038
$R_{t,eff}$	Ωcm^2	49.76 ± 1.90
$C_{t,eff}$	$mFcm^{-2}$	1.380 ± 0.062
Q_w	$mF/s(1-)cm^2$	2.27 ± 0.11
^{2}/	–	6
Calculated values		
C_{flat} (equation (7-34))	$mFcm^{-2}$	0.372 ± 0.058
C_{total} (equation (7-36))	$mFcm^{-2}$	1.75 ± 0.12
C_{wire} (equation (7-35))	nF	0.266 ± 0.016

7.3 G2 Discussion

The dependence of the extracted parameters on electrode sites reveals a consistent trend across all electrode geometries. The total capacitance exhibit clear dependence on electrode size. The capacitance estimated from the measurement model was compared to the values estimated for the influence of cables on the impedance spectra. The observed trends provides an understanding of the equivalent circuit model used in this study.

7.3.1 Regressed Parameters as a Function of Electrode Size

The interpretation of impedance spectra with equation (7-1) yielded seven parameters that are statistically significant. The dependence of the regressed parameters on the electrode area is summarized in Figure 7-7 and 7-8. Clear trends emerged across geometries with the error bars indicating ± 1 standard deviation. The constant-phase-element (CPE) coefficient for the wire component, Q_w showed a consistent decrease with increasing electrode size, dropping from 2.27 ± 1.9 mF/cm^{2}S $^{-1}$ for the 20 m^2 sites to 0.0275 ± 0.0018 mF/cm^2 S $^{-1}$ for the 4000 m^2 sites, as shown in Figure 7-7(a). A similar decreasing trend was observed for the CPE coefficient of the flat surface Q_f in Figure 7-7(b), The values declined from 5.869 ± 0.315 mF/cm^2 S $^{-1}$ at 20 m^2 to 1.614 ± 0.026 mF/cm^{2}S $^{-1}$ at 4000 m^2.

The CPE exponent associated with the wire (w) given in Figure 7-7(c), decreased with increasing electrode area, reducing from 0.9614 ± 0.00393 for 20 m^2 to 0.7611 ± 0.0037 for 4000 m^2. Conversely, f, the exponent associated with the flat surface in Figure 7-7(d), exhibited an increasing trend with area. The values varied from 0.799 ± 0.00463 to 0.90 ± 0.00286, for the 20 m^2 and 4000 m^2 respectively. The ohmic resistance, R_e increased with electrode size, ranging from 0.0739 ± 0.00367 Ωcm^2 for the 20 m^2 to 0.852 ± 0.004 Ωcm^2 for the 4000 m^2, as shown in Figure 7-8(a). Similarly, both charge-transfer resistance, R_{t,O_2} and Warburg-like diffusion resistance, R_{d,O_2} increased with electrode size as presented in Figures 7-8(b) and 7-8(c) respectively.

For electrodes coated with sputtered iridium oxide (SIROF), the redox activity was characterized by an effective charge-transfer resistance, t,eff , and capacitance, t,eff, derived from

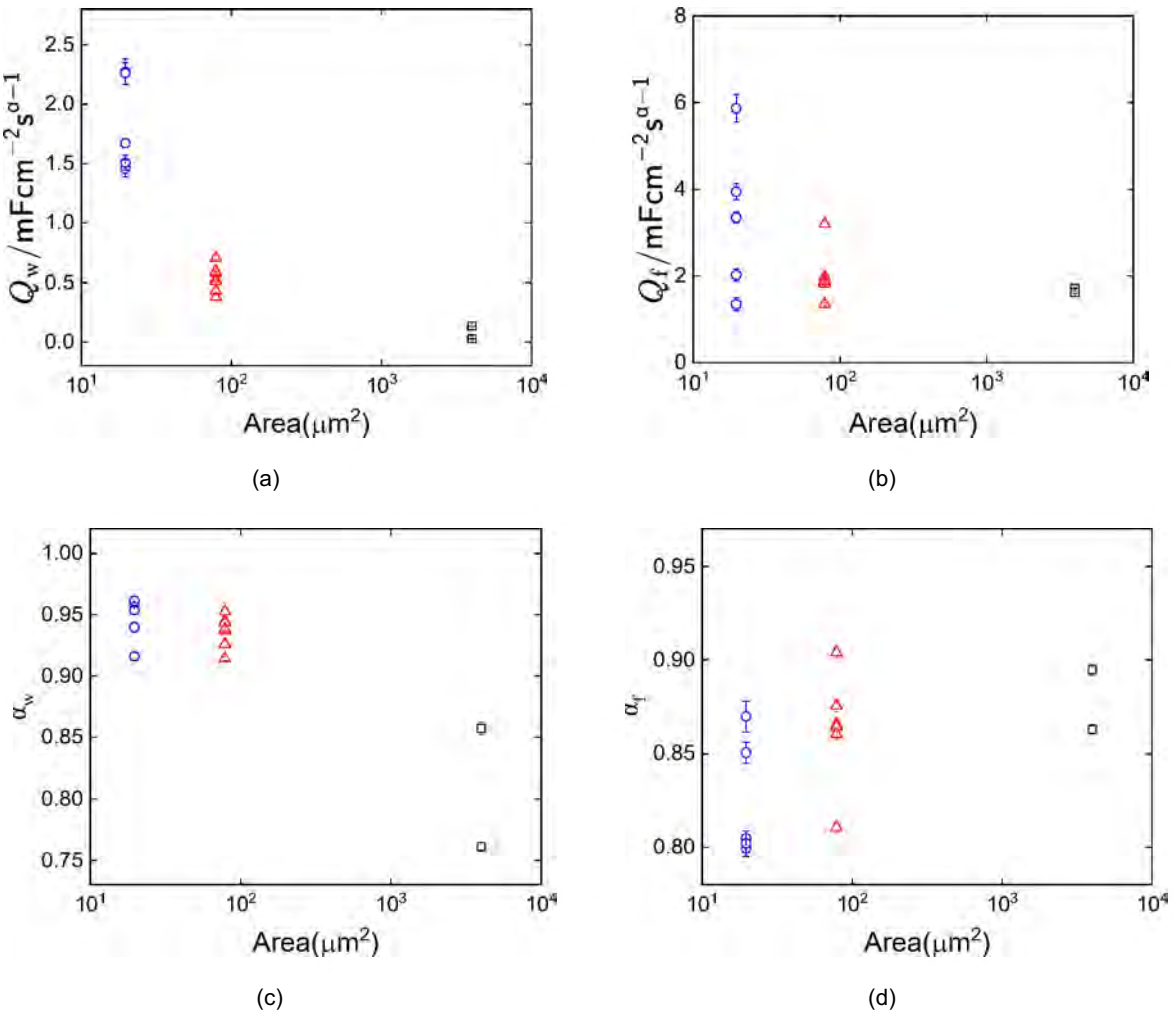

Figure 7-7. Parameter estimates for the regression of the process model given as equation (7-1) to G2 electrodes: a) CPE coefficient of wire, Q_w; b) CPE coefficient of flat surface, Q_f; c) CPE exponent of wire, α_w; d) CPE exponent of flat surface, α_f. Error bars represent one standard deviation.

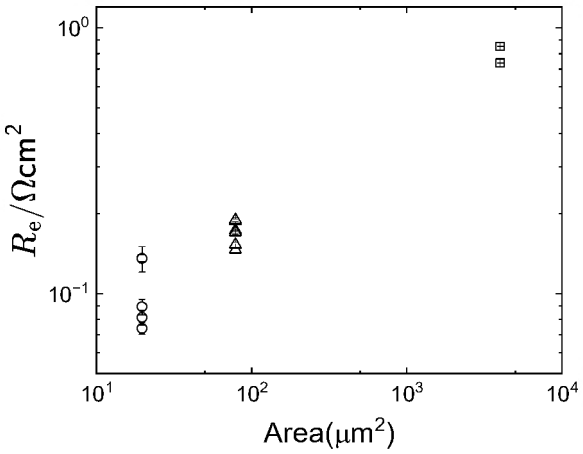

(a)

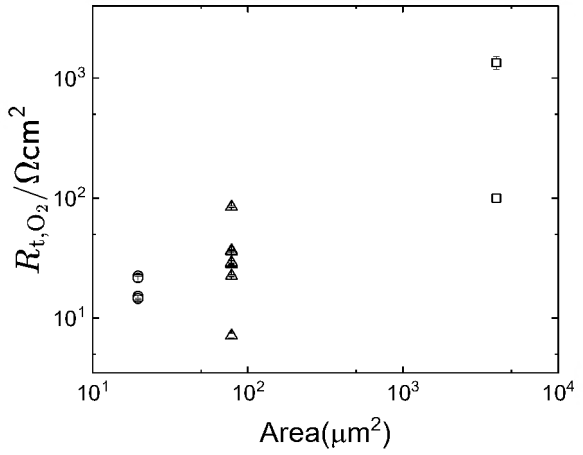

(b)

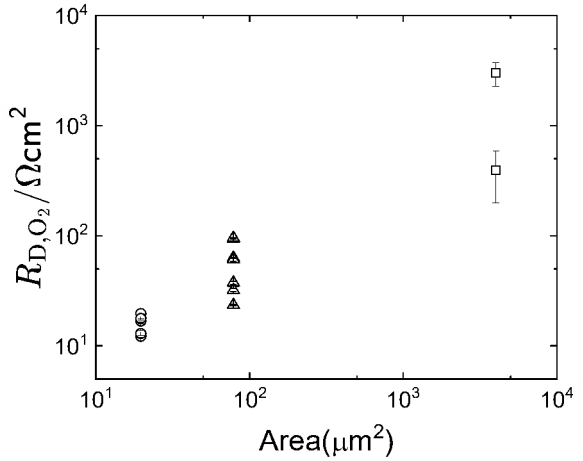

(c)

Figure 7-8. Parameter estimates for the regression of the process model given as equation (7-1) to G2 electrodes: a) ohmic resistance R_e, b) charge-transfer resistance R_{t,O_2}, c) Warburg-like diffusion resistance R_{d,O_2}. Error bars represent one standard deviation.

equations (7-26) and (7-28), respectively. As displayed in Figure 7-9(a), $_{t,eff}$ generally decreased with increasing electrode area, though some deviations were noted for the 80 m^2 electrode sites. $_{t,eff}$ also decreased as a function of electrode size in Figure 7-9(b), consistent with a reduction in the effective redox-active surface area. The calculated time constant (= $_{t,eff}$ $_{t,eff}$) showed strong dependence on the electrode geometry, with values decreasing from 0.06900 ± 0.00012 s for the 20 m^2 electrodes to 0.00025000 ± 0.00000048 s for the 4000 m^2 electrodes in Figure 7-9(c). A single notable outlier was again observed in the 80 m^2 category. Importantly, all values of remained below 60 s, confirming that steady-state conditions were achieved during measurement.

7.3.2 Capacitance as a Function of Electrode Size

The effective double-layer capacitance of the ultramicroelectrode arrays was extracted by fitting the measurement model (equation (2-19)) to the impedance spectra. Another approach was the conversion of the constant-phase-element (CPE) parameters to an effective capacitance using the Brug's [141] formula for the surface distribution of time constant. The expression is given as;

$$_{eff,surface} = 1/ \left(\frac{\quad}{e^{\frac{e}{+}}} \right)^{(1-)/} \tag{7-33}$$

where R is the parallel resistance, Q_f is the constant-phase-element coefficient for the flat surface, $_f$ is the CPE exponent for the flat surface, and R_e is the ohmic resistance. In the limiting case where the total charge-transfer resistance R_t is R_e, the effective capacitance of the electrode surface was approximated by:

$$_{eff,flat} = f1/ _f e(1- f)/ _f \tag{7-34}$$

For the cables not covered by a film, a similar formulation was applied as:

$$_{eff,wire} = {}^{1/ (1- _w) / _w}_{w \quad e} \tag{7-35}$$

where Q_w is the constant-phase-element (CPE) coefficient for the cable, $_w$ is the CPE exponent for the cable. The total effective capacitance of the electrodes was estimated as the sum of the

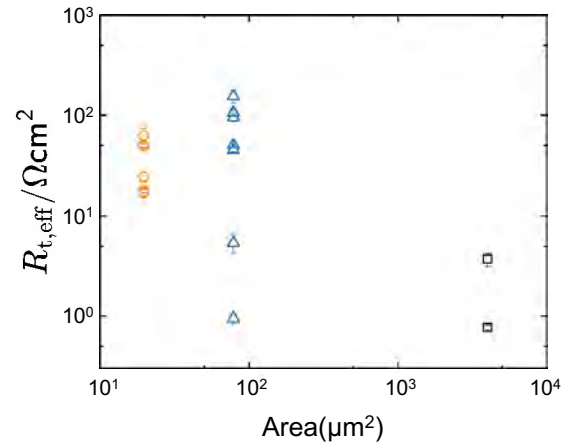

(a)

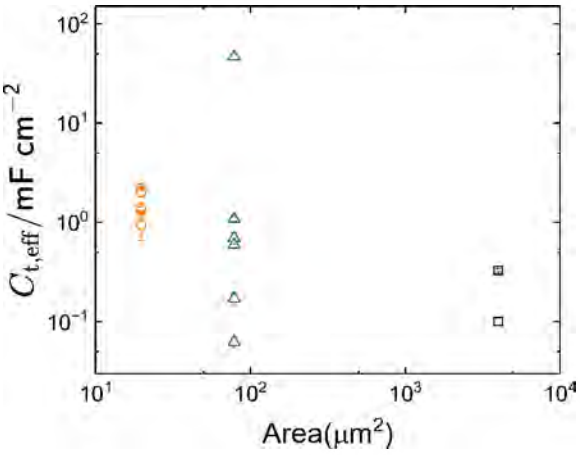

(b)

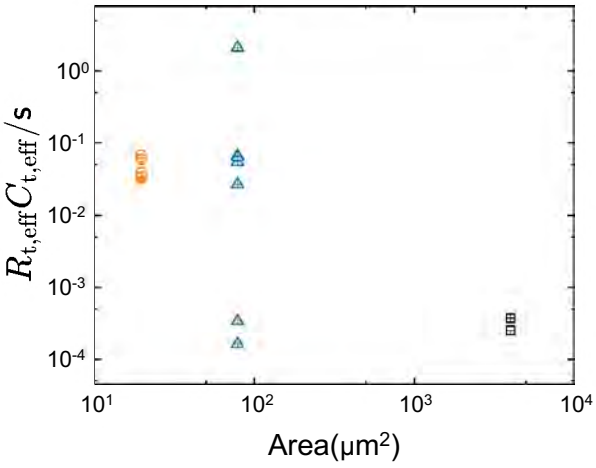

(c)

Figure 7-9. Regressed parameters of the process model given as equation (7-1) associated with changes in the iridium oxidation state as functions of electrode size: a) effective charge-transfer resistance $R_{t,eff}$, b) capacitance $C_{t,eff}$, and c) time constant ($= R_{t,eff} C_{t,eff}$). Error bars represent one standard deviation.

flat-surface effective capacitance and the effective capacitance estimated from the changes in iridium oxidation state (equation (7-28)) as

$$\text{total} = \text{eff,flat} + \text{eff,ir}_{3+}/\text{ir}_{4+} \tag{7-36}$$

The capacitance calculated from the measurement model is given by equation (7-32). The estimated effective capacitances are presented in Figure 9-13 as a function of electrode area (20 m^2, 80 m^2, and 4000 m^2). As shown in Figure 7-10(a), the flat surface capacitance, $_{flat}$, exhibited an increasing trend with increasing electrode area, ranging from 0.372 ± 0.057 mF/cm^2 at 20 m^2 to 0.743 ± 0.022 mF/cm^2 at 4000 m^2, with an outlier observed among the 20 m^2 electrodes. In contrast, the total capacitance $_{total}$, which includes contributions from the flat surface and changes in the oxidation state of the iridium, showed a decreasing trend with increasing electrode size. As illustrated in Figure 7-10(b), $_{total}$ values ranged from 2.87 ± 0.275 mF/cm^2 at 20 m^2 to 0.843 ± 0.031 mF/cm^2 at 4000 m^2. An outlier was observed at 47.161 ± 3.460 m^2 in the 80 m^2 category, which may be attributed to localized hemispherical diffusion effects or variations in the thickness of coating associated with ultramicroelectrodes, as discussed previously in Section 7.2.1.

The capacitance estimated for the influence of cables, $_{eff,wire}$, and the capacitance calculated from the measurement model regression, $_{dl,mm}$, yielded comparable trends across electrode sizes, as shown in Figure 7-10(c). $_{dl,mm}$ varied between 0.142 ± 0.009 and 0.295 ± 0.0357 nF.

A comparison of impedance magnitudes was done with the parameters estimated from equation (7-2), to evaluate the contributions of the flat surface impedance, $_{flat}$, impedance for iridium-redox reactions $_{t,eff}$ (or $_{iridium}$), and mass-transfer-limited oxygen reduction, $_{tc}$, to the total impedance magnitude. The ohmic resistance was excluded as part of the evaluation. As shown in Figure 7-11(a) for the 20 m^2 electrode, the flat surface dominated the impedance magnitude at frequencies above 10 Hz, whereas at lower frequencies, the influence of oxygen

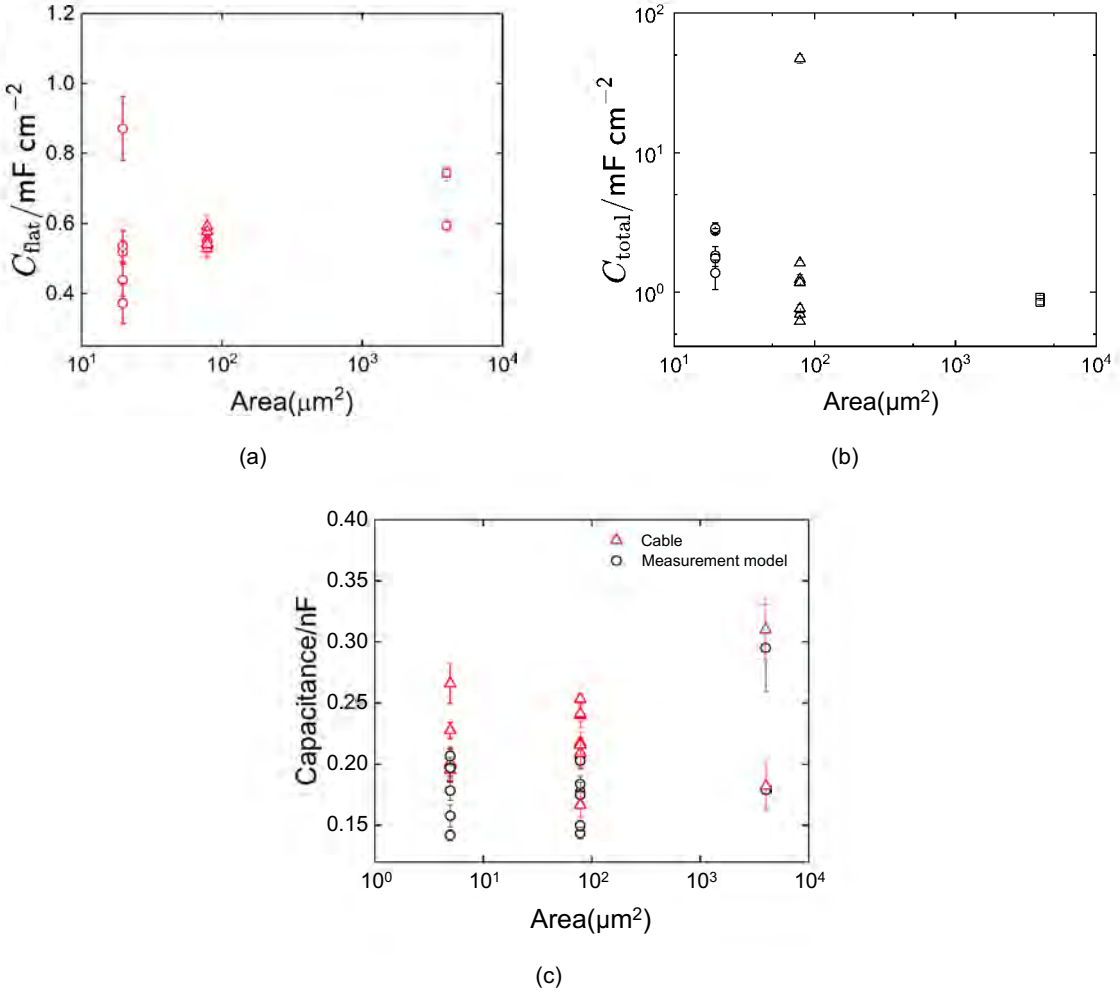

Figure 7-10. Capacitance as a function of electrode size: a) flat-surface capacitance, C_{flat} estimated from equation (7-34); b) total capacitance C_{total} estimated from equation (7-36); c) wire capacitance, C_{wire} estimated from equation (7-34) and measurement model capacitance, $C_{mm,dl}$ calculated from equation (7-32). Error bars represent one standard deviation.

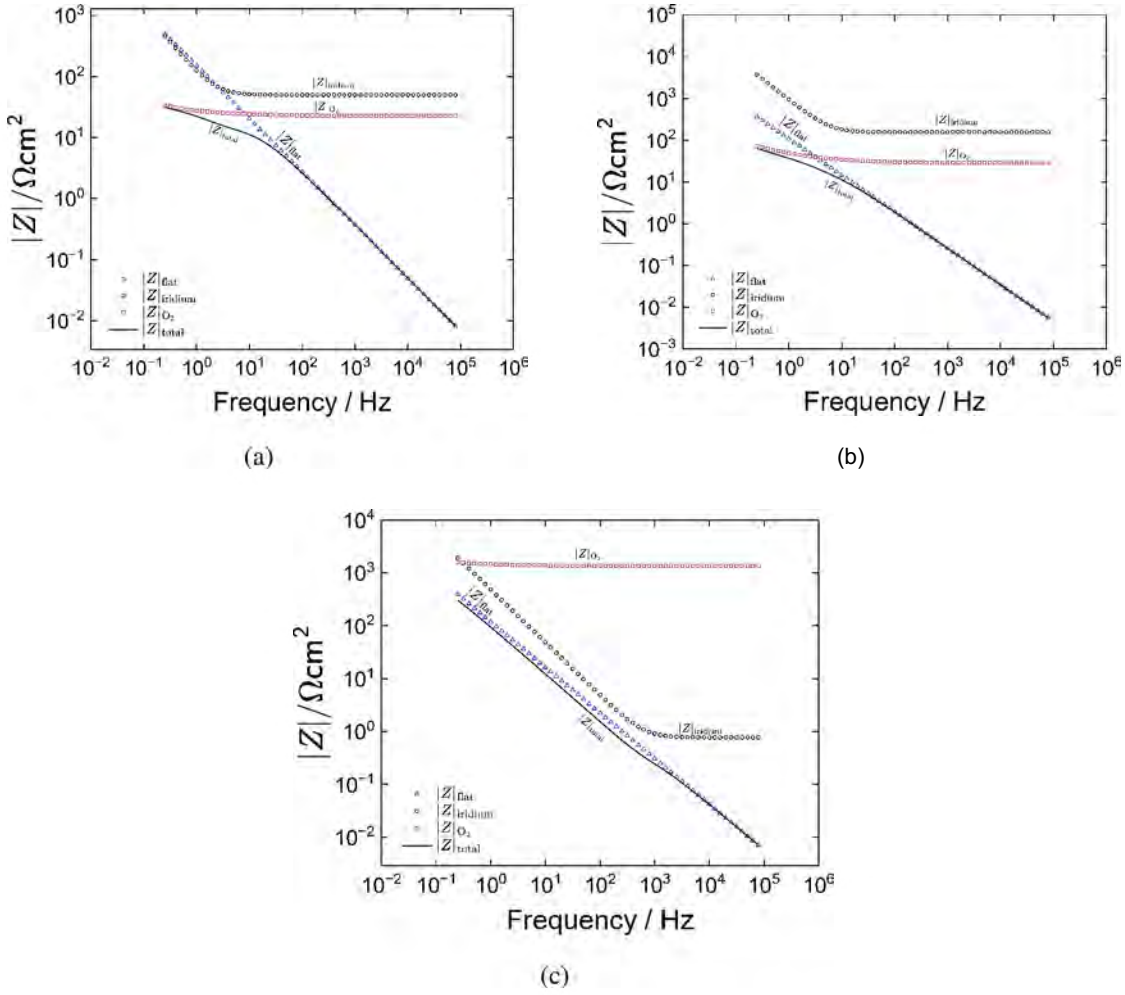

Figure 7-11. Comparison of impedance magnitudes for flat surface, iridium-redox reactions, oxygen reduction, and total impedance magnitude: a) 20 m^2 electrode, b) 80 m^2 electrode, and c) 4000 m^2 electrode site. The parameters were estimated from equation (7-2), without ohmic resistant R_e

reduction became significant. A similar trend was observed in the 80 m^2 electrodes in Figure 7-11(b). In contrast, for the 4000 m^2 electrodes given by Figure 7-10(c), the impedance magnitude was consistently governed by the flat surface across the entire frequency range (0.2 Hz to 100 kHz).

7.3.3 Statistical Results

The parameters extracted from the electrical circuit model (equation (7-1)) were statistically significant because the values fall within the 95.4% confidence interval (±2) and do not include zero. The capacitance for the electrode substrate $_{flat}$, expressed as equation (7-34), incorporates the contributions from the fitted constant-phase-element parameters and the ohmic resistance. For each electrode analyzed, the mean value of the capacitance $_{flat}$ and its associated confidence intervals were estimated from the values and standard deviation of the regressed parameters $_f$, $_f$, and $_e$ using the Monte Carlo simulation. The normal distribution of the estimated capacitance values for the flat surface is shown in Figure 7-12.

The mean value and standard deviation of $_{flat}$ for the 20 m^2 electrode, given in Figure 7-12(a), was 372.1 ± 57.5 F/cm^2. This result aligns with the distribution of capacitance observed across all 20 m^2 electrodes in Figure 7-10(a), demonstrating the consistency of the model parameters within this electrode category. In contrast, a specific 80 m^2 electrode site analyzed in Figure 7-12(b) yielded a higher mean capacitance of 592.46 F/cm^2, with a narrower standard deviation of 26.3 F/cm^2. These values also fall within the range of $_{flat}$ calculated for all the 80 m^2 electrodes. The 4000 m^2 electrodes displayed a mean $_{flat}$ of 594.63 ± 16.77 F/cm^2. The value of $_{flat}$ range between 0.372 ± 0.057 F/cm^2 and 0.871 ± 0.0907 F/cm^2 across the electrode sizes, as shown in Figure 7-10(a). These results confirm the statistical significance of the extracted parameters and validate the use of Brug's model to extract double-layer capacitance across different electrode sizes. The histograms provide visual evidence of the normal distribution of estimated capacitance values, supporting the reproducibility of the interpretation model.

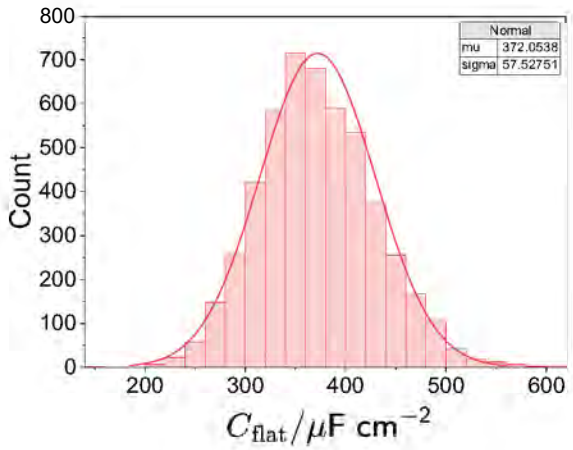

(a)

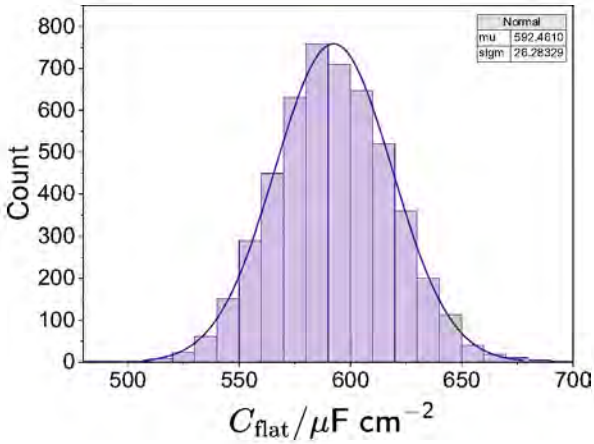

(b)

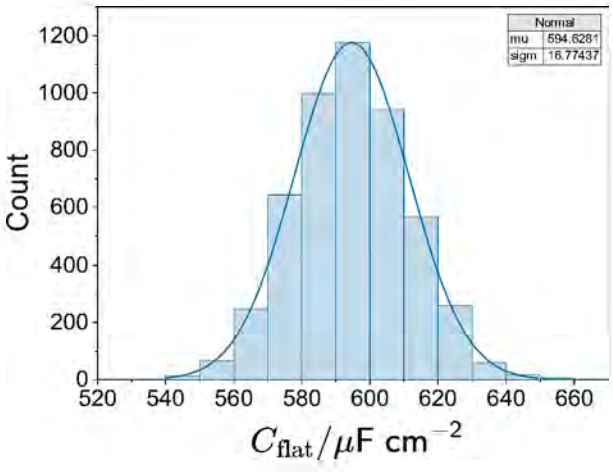

(c)

Figure 7-12. Process model regression results showing the normal distribution of the flat-surface capacitance calculated from equation (7-34): a) 20 m^2 electrode, b) 80 m^2 electrode, c) 4000 m^2 electrode site.

CHAPTER 8
IMPEDANCE BEHAVIOR OF G3 ULTRAMICROELECTRODE ARRAYS

The third-generation (G3) device comprises ultra-thin, high-density microelectrode arrays (HD MEAs) with electrode diameters and geometric surface areas (GSA) ranging from 5 m (20 m^2), 10 m (80 m^2), 15 m (180 m^2) to 20 m (300 m^2). As illustrated in Figure 3-4, the electrode layout includes two large reference electrodes with surface areas of 4000 m^2, along with four looped traces and three terminal traces engineered to assess both low-impedance and high-impedance limits via accuracy contour analysis. Each electrode features a gold substrate coated with sputtered iridium oxide film (SIROF) at thicknesses of 300 nm or 800 nm to enhance charge-injection capacity. Details of the design and fabrication of G3 arrays are presented in section 3.1.3.

Impedance measurements were conducted in phosphate-buffered saline under open-circuit conditions. The experimental methods for the G3 devices are provided in section 5.1. The device was interfaced with a Gamry Reference 600+ potentiostat using a custom-designed junction box, and the precision of impedance measurements were evaluated by measuring the accuracy contour plots of the device using the loop and terminal configurations. The methodology for plotting the accuracy contour plots is described in Chapter 4. Impedance data were evaluated using a measurement model, enabling quantification of stochastic errors and extraction of key physical parameters. The theoretical framework for the measurement model is presented in section 2.5.2.3, and the measurement modeling procedures are detailed in section 5.3.

This chapter presents the process models and the in vitro experimental results that inform the interpretation of impedance spectra taken from G3 devices. Parameters obtained by fitting the process model to experimental data were subsequently used to calculate the electrode's capacitance.

8.1 Process Model for G3 Impedance Spectra

The process models formulated to interpret the impedance spectra of SIROF-coated ultramicroelectrodes with coating thicknesses of 300 nm and 800 nm, are shown in Figure 8-1. The impedance response of the device exhibited characteristics intermediate between porous and

rough electrode behavior. The process model shown in Figure 8-1(a) was used to regress the impedance spectra of electrodes displaying rough-type behavior. The rough-electrode model was similar to the process model regressed to the G2 electrodes. The mathematical development for the rough electrode's process model in Figure 8-1(a), has been discussed in section 7.1. The expression for the total impedance of the rough-electrode model in Figure 8-1(a) is given as equation (7-1). The model captured the contributions of the redox-active iridium oxide (IrOx) coating, the constant-phase-element behavior of the flat surface, the influence of the potentiostat cables and connection interfaces, and the faradaic processes including reversible oxygen reduction and mass-transfer of reacting species.

The distinction between the rough and porous process models arises from differences in the electrochemical interactions between the SIROF coatings and the phosphate-buffered saline. In rough electrodes, cathodic faradaic reactions can be computed in parallel with the flat surface and changes in iridium oxidation states, as depicted in Figure 8-1(a). In contrast, electrodes exhibiting porous impedance behavior may possess a more pronounced pore depth that significantly modulates charge transfer reactions at the electrode–electrolyte interface.

The total impedance for the porous-electrode model in Figure 8-1(b) is given as (7-1). The expression for the system's impedance, Z_{system} is different for both the porous and rough electrode impedance response. For the porous electrode response, the Z_{system} is given by

$$Z_{system} = R_e + \left(\frac{1}{Z_{flat}} + \frac{1}{Z_{pore}} + \frac{1}{Z_{t,eff}} \right)^{-1} \tag{8-1}$$

where R_e is the ohmic impedance, Z_{flat} is the impedance of the flat surface expressed as equation (7-4), $Z_{t,c}$ is the cathodic impedance representing the oxygen-reduction reactions influenced by mass transfer given as equation (7-5), and $Z_{t,eff}$ is the impedance of iridium oxide redox behavior presented as equation (7-27).

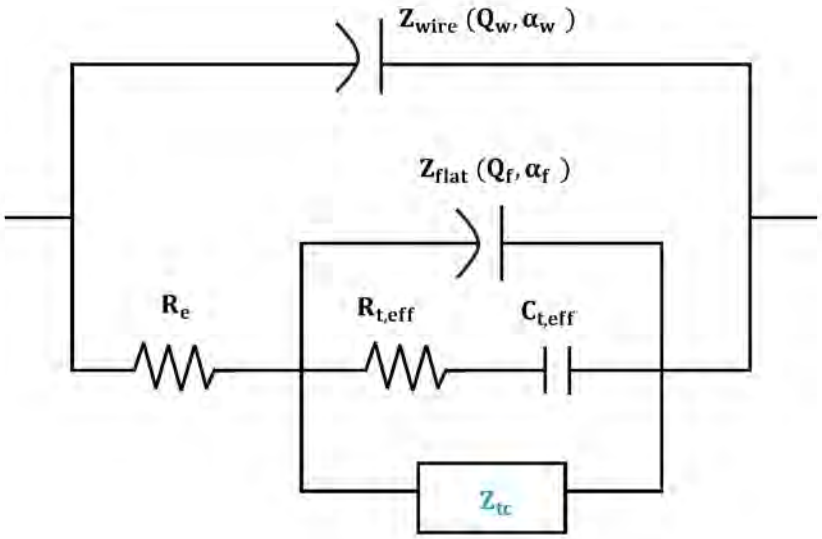

(a)

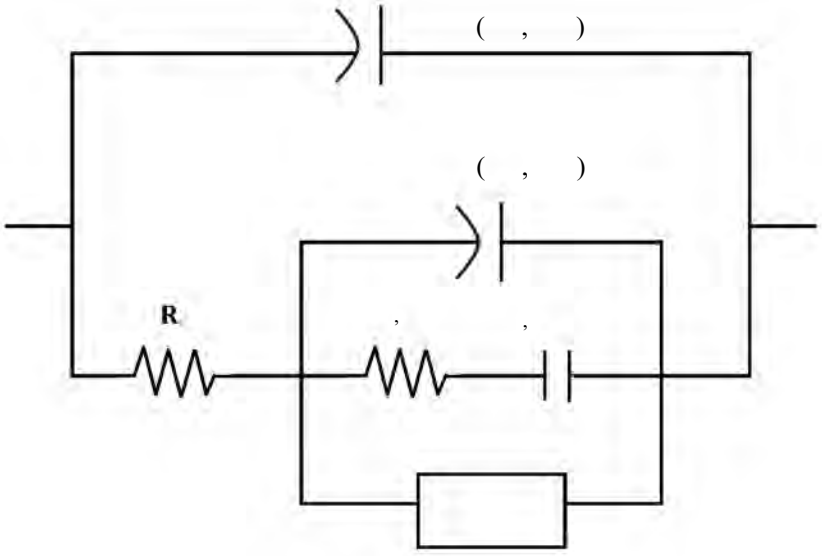

(b)

Figure 8-1. Electrical circuit representation of the process model for G3 impedance spectra: a) rough-electrode behavior expressed as equation (7-1) and b) porous-electrode behavior expressed as equation (8-1)

The porous impedance Z_{pore} shown in Figure 8-1(b) followed the work published by de Levie [98] and Lasia [103] on porous electrodes. The impedance of the porous electrode is expressed as

$$_{porous} = \frac{\__p}{\sqrt{\Lambda}} \coth \Lambda\left(\sqrt{\_}\right) \tag{8-2}$$

where $_p$ is a lumped parameter that includes the number of pores and represents the pore resistance as

$$_p = \frac{s}{2} \tag{8-3}$$

where A is the electrode area, $_s$ is the pore electrolyte resistivity, l is the pore depth and n is the is the total number of pores in the electrode. Λ is the dimensionless admittance given as

$$\Lambda = (\ _{\cdot})^{\ p}\ _p \tag{8-4}$$

is a lumped parameter that includes the depth and size of the pores, $_p$ and $_p$ are parameters of a constant-phase element. The expression for is given as

$$= 2\frac{\__s}{l^2} \tag{8-5}$$

The process model regressed to the porous impedance spectra, captured the contributions of the redox-active iridium oxide (IrOx) coating, the constant-phase-element behavior of the flat surface, the influence of the potentiostat cables and connection interfaces, and the pore contributions on the electrode's impedance.

8.2 Experimental Results for G3

The impedance spectroscopy characterization of the G3 ultramicroelectrode arrays were performed using a combination of experimental measurements and model-based analysis. System performance and measurement reliability were assessed using accuracy contour plots, which delineate the operational limits of the Gamry Reference 600+ potentiostat when used with the electrode arrays. Nyquist and Bode plots were employed to analyze the frequency-dependent

impedance responses of individual electrodes, while stochastic error structure plots were used to quantify measurement uncertainty across spectral data. A physical process model was implemented to interpret the impedance spectra and extract relevant electrode parameters. All measurement modeling and data analysis were conducted using version 1.8 of Watson and Orazem's [97] measurement model program, and the resulting parameters were used to determine the electrode capacitance.

8.2.1 G3 Impedance Spectra

Impedance measurements for the G3 devices were performed under open-circuit conditions after a 300-second stabilization period. Each potentiostatic EIS experiment lasted approximately 1200 seconds (20 minutes). A total of 19 triplicates of impedance spectra were recorded for ultramicroelectrodes ranging from 5 m to 20 m in diameter, along with spectra for two larger electrodes possessing a geometric surface area of 4000 m^2. The impedance responses of the electrodes exhibited characteristics intermediate between porous and rough electrode behavior. Nyquist plots for representative sites exhibiting rough electrode behavior are shown in Figure 8-2. The impedance spectra were normalized by electrode area for different SIROF coating thicknesses. The impedance data for the 300 nm thickness is presented in Figure 8-2(a) with electrode diameter as a parameter. The results reveal distinct impedance profiles characteristic of rough electrode behavior, with no overlap at low-frequency points for the 5 m, 10 m, 15 m, and 20 m electrode sites. These differences in impedance response are attributed to variations in the distribution of time constants across the electrode surfaces.

The Nyquist plot for the 800 nm thickness is presented in Figure 8-2(b) with electrode diameter as a parameter. The impedance profiles are consistent with rough electrode behavior and show no overlap at low-frequency points. The area-normalized spectra reveal reductions in both the real and imaginary components at low frequencies for smaller electrodes, whereas the larger reference site (4000 m^2) exhibits a substantially higher impedance magnitude in the same range. Although impedance generally increases as electrode area decreases, deviations from the ideal inverse-area scaling are evident for ultramicroelectrodes (UMEs). These deviations can arise from

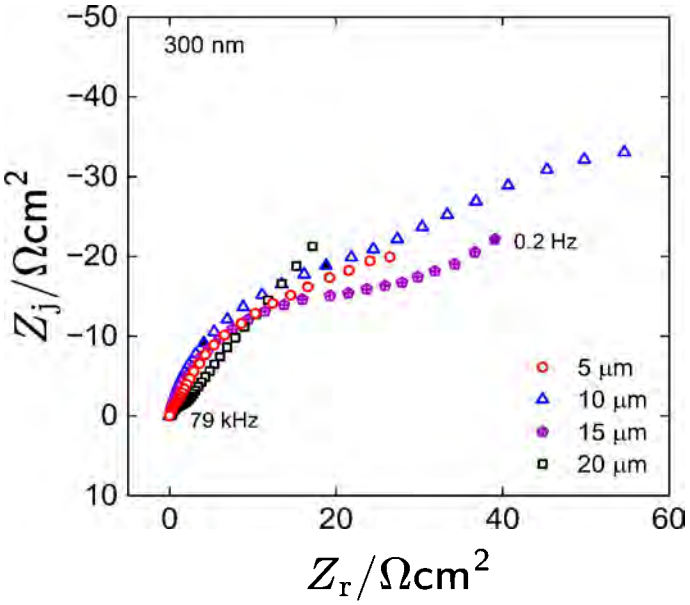

(a)

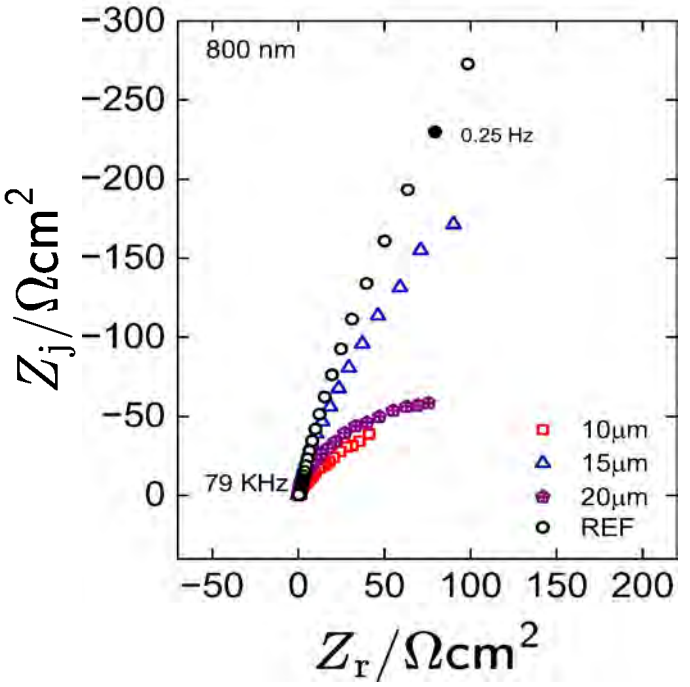

(b)

Figure 8-2. Impedance spectra for rough electrode behavior in Nyquist format with electrode diameter as a parameter: a) for 300 nm SIROF coating, and b) for 800 nm SIROF coating. The measurement was performed at open-circuit at frequency range from 0.2 Hzto 100 kHz.

factors such as hemispherical rather than linear diffusion of electroactive species, surface roughness, porosity, and pronounced edge effects, all contributing to non-ideal scaling behavior [143, 71, 144]. The low-frequency response across all electrode sites indicates constant-phase-element (CPE) behavior and the occurrence of faradaic processes at the electrode–electrolyte interface.

The impedance spectra for the representative electrode sites exhibiting a porous electrode behavior are presented in Figure 8-3 for various coating thicknesses of SIROF. The resulting Nyquist plots for the 300 nm and 800 nm thicknesses are shown in Figures 8-2(a) and 8-2(b), respectively. The impedance profiles for the 5 m diameter ultramicroelectrode at both thicknesses align with the expected characteristics of porous electrode behavior. As reported by Lutz et al.[70], SIROF microelectrodes typically exhibit porous impedance responses, which can be effectively described using a porous-electrode model. The deviations observed at high frequencies may stem from parasitic capacitance associated with the measurement cables and system complexity. All subsequent modeling and parameter extraction were conducted on the area-normalized impedance data, following the procedure outlined by Orazem [132].

8.2.2 Error Model for G3

The measurement model expressed by equation (2-19) was applied to regress the impedance data obtained from the G3 devices with SIROF coating thicknesses of 300 nm and 800 nm, with electrode configurations ranging from 5 m (20 m^2), 10 m (80 m^2), 15 m (180 m^2) to 20 m (300 m^2). The stochastic error structure analysis was conducted to quantify experimental noise levels and assess data consistency with the Kramers–Kronig relations. For each electrode size, three replicate impedance spectra were collected, three replicate impedance spectra were collected, enabling estimation of the stochastic error structure associated with their impedance measurements. The stochastic error structure is represented by the standard deviations of the real and imaginary impedance as a function of frequency.

The stochastic error structures for the 300 nm SIROF coating are presented in Figure 8-4(a), with electrode diameter as the varying parameter. For each electrode site, the observed error

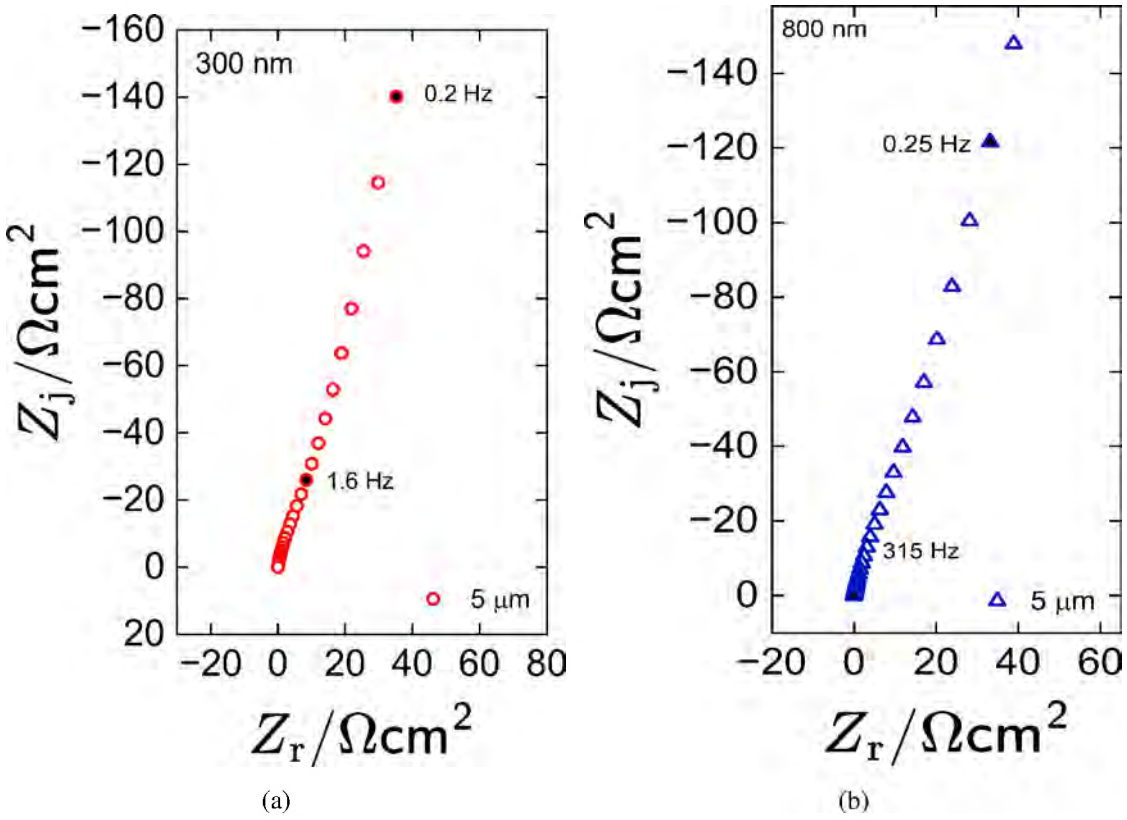

Figure 8-3. Impedance spectra for porous electrode behavior in Nyquist format for 5 diameter electrodes: a) for 300 nm SIROF coating, and b) for 800 nm SIROF coating. The measurement was performed at open-circuit at frequency range from 0.2 Hz to 100 kHz.

Table 8-1. Error parameters across electrode areas obtained by regressing equation (5-1) to the impedance spectra of G3 device coated with 300 nm thickness of SIROF.

Area (m^2)			
20	$1.23 \times 10^{-3} \pm 1.09 \times 10^{-4}$	$4.56 \times 10^{-5} \pm 9.33 \times 10^{-7}$	–
80	$1.01 \times 10^{-3} \pm 5.93 \times 10^{-5}$	$1.18 \times 10^{-4} \pm 1.09 \times 10^{-6}$	–
180	$1.33 \times 10^{-3} \pm 1.11 \times 10^{-4}$	$6.51 \times 10^{-5} \pm 8.94 \times 10^{-7}$	–
300	$1.78 \times 10^{-4} \pm 5.42 \times 10^{-5}$	$1.45 \times 10^{-5} \pm 2.28 \times 10^{-7}$	–
4000	$2.90 \times 10^{-4} \pm 5.01 \times 10^{-5}$	$4.65 \times 10^{-6} \pm 2.50 \times 10^{-7}$	$4.27 \times 10^{-5} \pm 1.16 \times 10^{-5}$

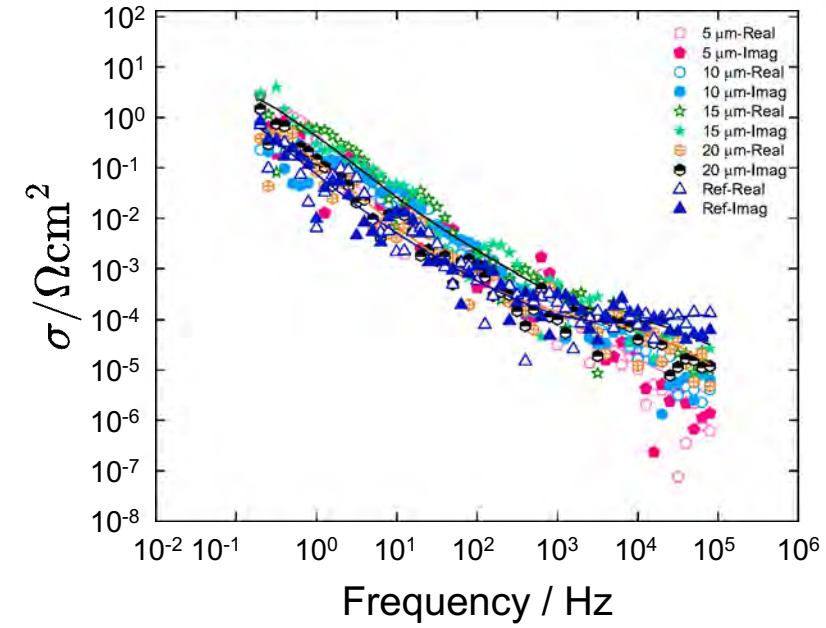

(a)

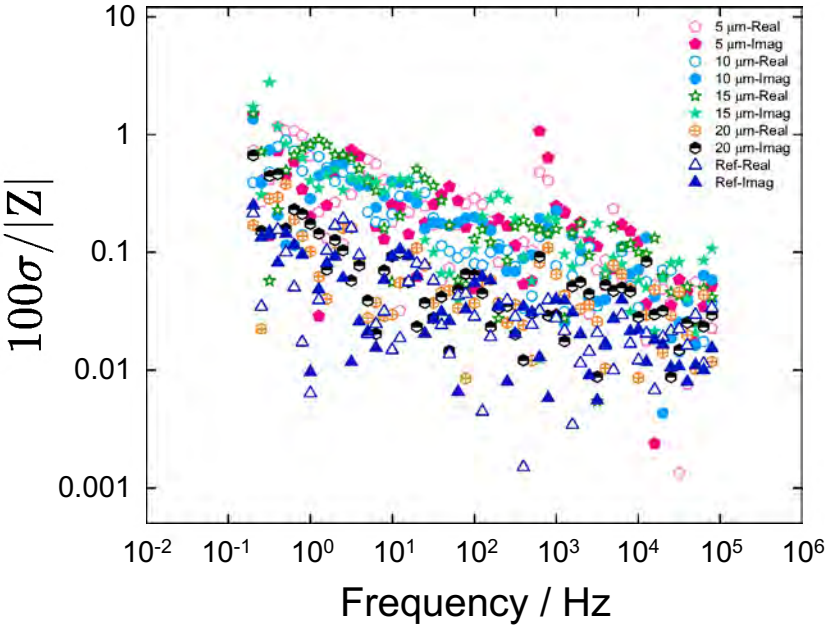

(b)

Figure 8-4. Stochastic error structure for impedance spectra of G3 device at open circuit with electrode diameter as a parameter: a) normalised error structure, b) non-normalized error structure. The solid line represents the error model given by equation (5-1). The regressed error parameters are summarized in Table 8-1.

distributions are heteroscedastic and exhibit overlap across the frequency spectrum, as expected for Kramers–Kronig [134, 135] consistent EIS data. The solid lines in Figure 8-4(a) correspond to fits of the empirically derived error model (equation (5-1)) for each electrode site. In total, nineteen distinct error models were developed to account for variations in electrode behavior. The corresponding error model parameters for the electrode sites shown in Figure 8-4(a) are summarized in Table 8-1. Parameters and were extracted for all the electrode sizes.

The normalized stochastic error structures for the G3 electrode sites are shown in Figure 8-4(b). Each plot represents the standard deviation normalized by the impedance magnitude. At low frequency points, the normalized errors for the smaller electrodes 5 m (20 m^2) to 20 m (300 m^2) are approximately 3%, which is an order of magnitude larger than the 4000 m^2 site (0.3%). These noise levels are typical of measurements obtained using the Gamry Reference 600+ potentiostat.

8.2.3 Measurement Model Analysis for G3

The Bode magnitude and phase-angle was plotted on a logarithmic frequency scale to visualize the impedance behavior for the G3 electrode sites as a function of frequency. As shown in Figure 8-5, the plots capture the frequency-dependent dispersion observed at both the low and high ends of the impedance spectra. The ohmic-resistance-corrected magnitude and phase-angle responses were obtained by subtracting the ohmic resistance from the real part of the impedance, as shown in equation (7-29) and (7-30).

The ohmic-resistance-corrected Bode plots for the G3 device with a 300 nm SIROF coating are presented in Figure 8-5 as function of electrode diameter. The solid lines represent fits obtained from the measurement model (equation (2-19)) using error-structure weighting. The strong agreement between the model and experimental data confirms consistency with the Kramers–Kronig (KK) relations. As illustrated in Figure 8-5(a), the 5 m (20 m^2) and 10 m (80 m^2) electrodes exhibit a distinct negative slope in the log–log magnitude plot at high frequencies above 1 kHz, indicating the impact of parasitic capacitance on the electrode impedance. In contrast, the 15 m (180 m^2), 20 m (300 m^2) and large reference electrode

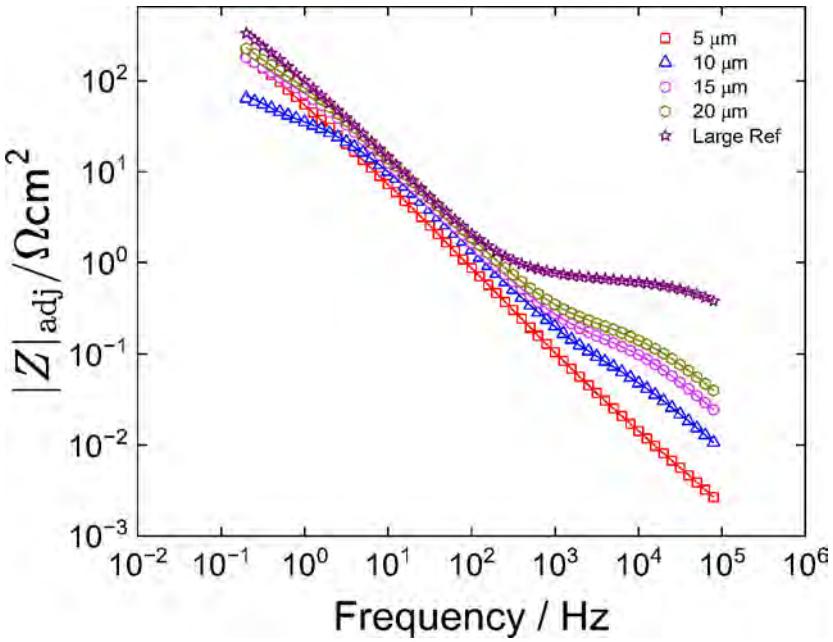

(a)

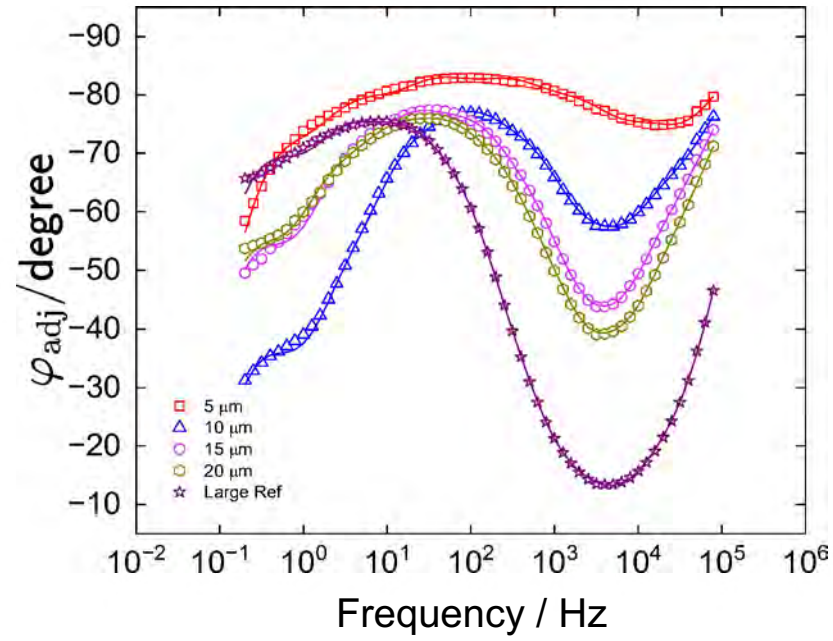

(b)

Figure 8-5. Measurement model (equation (2-19)) regression results for impedance measurements performed at open circuit for the 300 nm SIROF thickness as functions of frequency with electrode diameter as a parameter: a) ohmic-resistance-corrected magnitude, and b) ohmic-resistance-corrected phase angle. The line represents the fit of the model.

(4000 m^2) display a transition toward an asymptotic region that becomes more pronounced with increasing electrode size. This asymptotic behavior is likely attributed to geometry-induced nonuniform current and potential distributions, commonly referred to as ohmic impedance [6].

The ohmic-resistance-corrected phase-angle plots as a function of electrode diameter are shown in Figure 7-4(b). At high frequencies, the phase angles for the smaller electrodes (20 m^2 and 80 m^2) approach -80^0, reflecting combined contributions from constant-phase-element (CPE) behavior and parasitic capacitance effects. In contrast, deviations in the high-frequency phase responses of the 15 m (180 m^2), 20 m (300 m^2), and 4000 m^2 electrodes suggest increased influence from electrolyte resistance, which alters their overall impedance characteristics.

8.2.4 Kramers–Kronig Consistency Assessment for G3

The measurement model (equation (2-19)) was used to regress real and imaginary components of the impedance for various SIROF coating thicknesses. The model satisfies the linearity and stationarity criteria implicit in the Kramers–Kronig relations. Residuals obtained from the regression were used to evaluate the consistency of the experimental data with the Kramers–Kronig relations [134, 135]. Following the procedure outlined by Agarwal et al.[3], the number of Voigt-circuit elements, K in the model was iteratively increased until the 95.4% confidence interval (±2) for all parameter estimates does not include zero. Importantly, Parameters whose confidence intervals included zero were deemed statistically insignificant and excluded from the final model. Confidence intervals were determined using Monte-carlo simulation providing a robust estimation of parameter uncertainty under the assumed error structure.

The normalized real and imaginary residuals for the 300 nm SIROF-coated electrodes are shown in Figure 8-6 for the representative 20 m^2, 180 m^2, and 4000 m^2 electrodes. Each plot illustrates the residuals errors as a function of frequency. The real and imaginary residuals presented as red circles were normalized by the real and imaginary component of the impedance respectively. All residuals lie within the ±2 bounds (95.4% confidence interval) indicated by

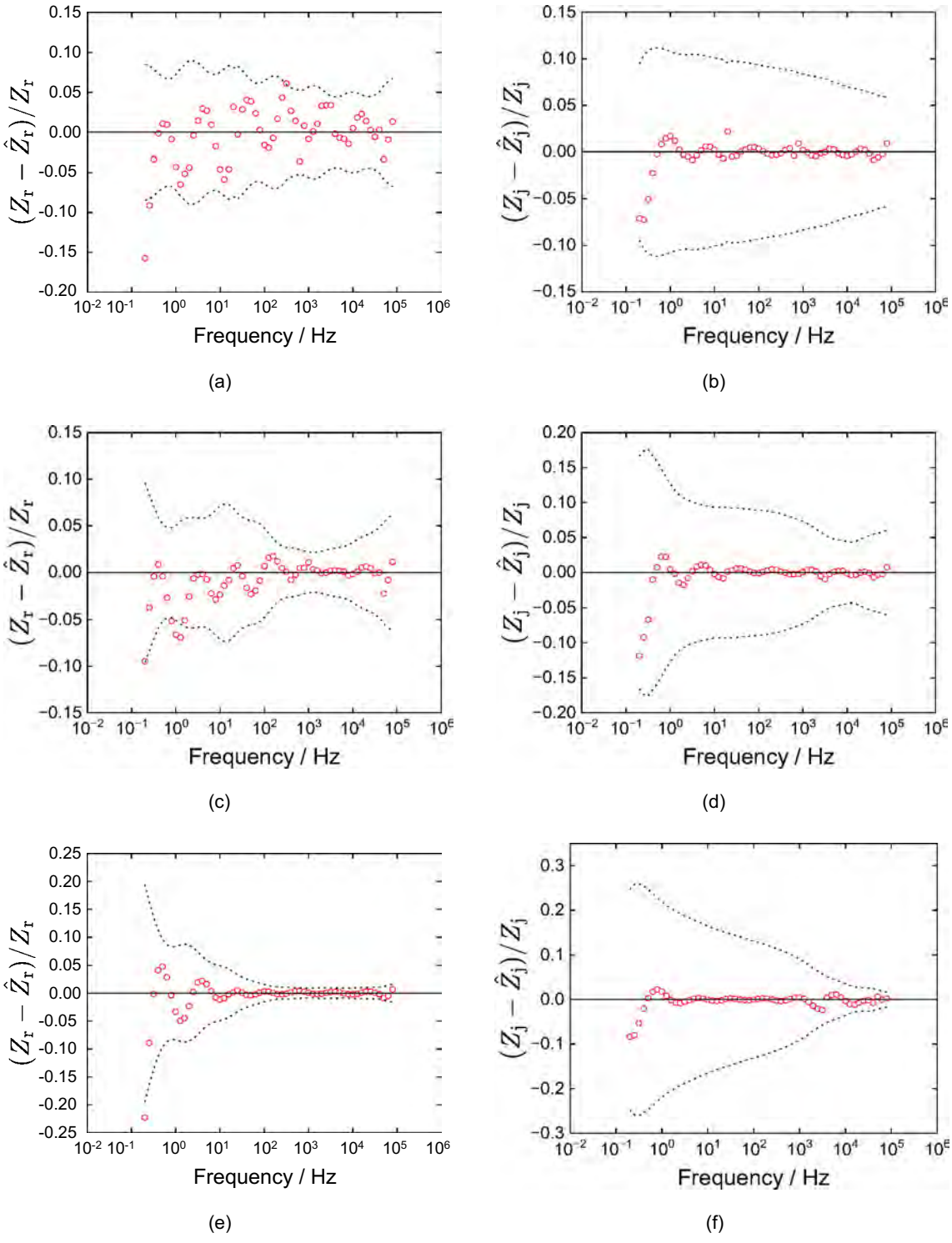

Figure 8-6. Residual errors for regression of the measurement model to the impedance data of the 300 nm thick SIROF electrodes under error structure weighting: a) and b) real and imaginary residuals for the 20 m^2 electrode, respectively, c) and d) real and imaginary residuals for the 180 m^2 electrode, respectively, e) and f) real and imaginary residuals for the 4000 m^2 electrode, respectively. The dashed lines represents the 95.4% (±2) confidence interval.

dashed lines in Figures 8-6(a) through 8-6(f), confirming that the impedance data for all electrode sizes are consistent with the Kramers–Kronig relations. The strong agreement between measured and modeled data further verifies that the system remains linear and stationary across the analyzed frequency range.

8.2.5 Process Model Regression for G3

The process models developed to interpret the impedance spectra of the G3 SIROF ultramicroelectrodes with 300 nm and 800 nm coating thicknesses are presented in Figure 8-1. Under open-circuit conditions, the impedance responses of the G3 ultramicroelectrodes exhibited characteristics intermediate between porous and rough electrode behavior. The porous-electrode model shown in Figure 8-1(b) was applied to impedance spectra consistent with porous-type behavior, while the rough-electrode model illustrated in Figure 8-1(a) was used to analyze spectra displaying rough electrode characteristics. To interpret these responses, the process model (equation (7-1)) was fitted to the experimental impedance data. Representative results for two 20 m^2 electrodes, one from the 300 nm and the other from the 800 nm SIROF datasets are presented here to illustrate typical rough and porous impedance behaviors observed across all measurements.

The rough-electrode model captured two distinct faradaic processes occurring at the electrode–electrolyte interface. The first is attributed to the reversible reduction of oxygen, likely enhanced by the aerated measurement conditions. The second corresponds to a redox process involving changes in the oxidation state of iridium, represented in the model by a resistor in series with a capacitor as expressed in equation (7-27). The fit of the rough-electrode model (equation (7-1)) to the impedance data for a 20 m^2 electrode with a 300 nm SIROF coating is illustrated in Figure 8-7. The Nyquist, magnitude, and phase angle plots presented in Figures 8-7(a), 8-7(b),and 8-7(c) demonstrate excellent agreement between the measured data and the fitted model across the entire frequency range. Moreover, the normalized residuals for the real and imaginary components, shown in Figures 8-7(d) and 8-7(e) lie within the ±2 bounds (dashed lines),

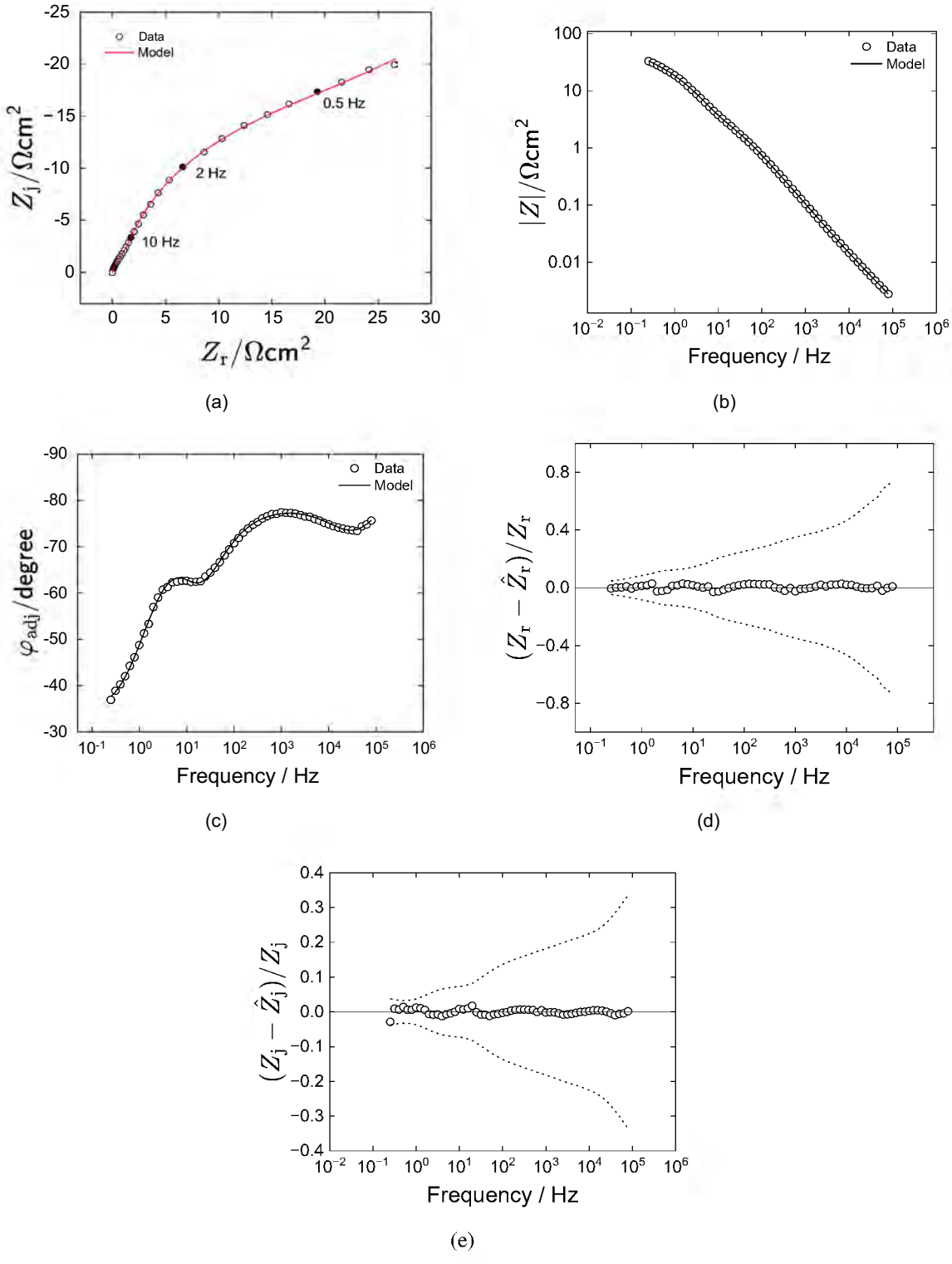

Figure 8-7. Rough electrode process model regression results for the 20 m^2 SIROF electrode with 300 nm thickness at open circuit: a) Nyquist plot, b) impedance magnitude, c) phase angle, d) real normalized residuals, and e) imaginary normalized residuals. The lines represent the fit of the process model given as equation (7-1). The dashed lines represents the 95.4% (±2) confidence interval.

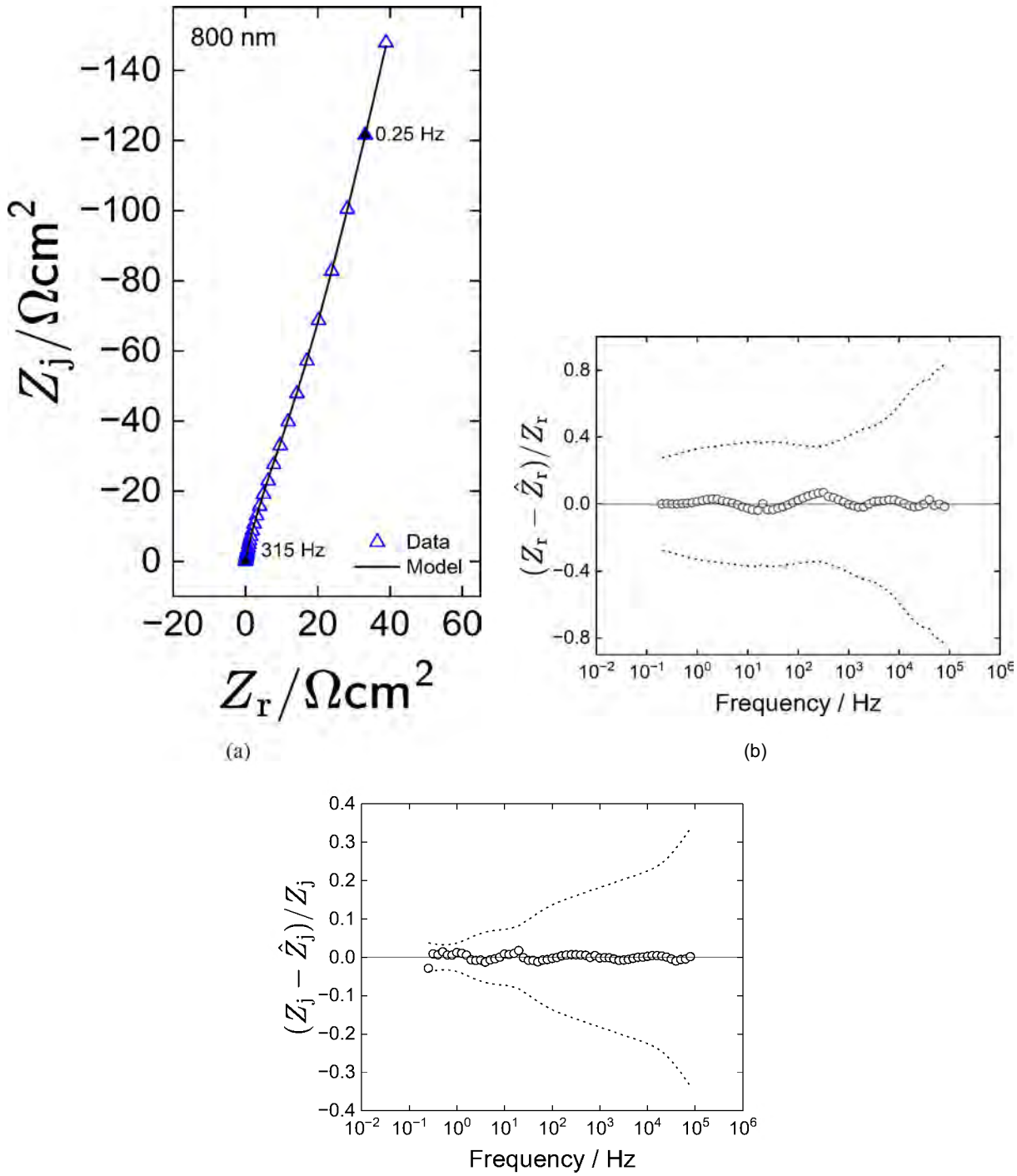

Figure 8-8. Porous electrode process model regression results for the 5 m (20 m^2) SIROF electrode with 800 nm thickness at open circuit: a) Nyquist plot, b) impedance magnitude, c) phase angle, d) real normalized residuals, and e) imaginary normalized residuals. The lines represent the fit of the process model given as equation (8-1). The dashed lines represents the 95.4% (±2) confidence interval.

indicating the absence of systematic deviations and confirming the adequacy of the regression model.

The porous-electrode model includes the parallel contributions of the time-constant distributions associated with the flat surface, the porous component of the impedance, and a redox process involving changes in the oxidation state of iridium. This redox reaction was modeled using a resistor in series with a capacitor as expressed in equation (7-27). The fit of the porous-electrode model given by equation (8-1) to the impedance spectra of a 20 m^2 electrode with 800 nm SIROF coating is illustrated in Figure 8-8. The Nyquist, presented in Figure 8-8(a) demonstrate strong agreement between the measured data and the porous-electrode model across the full frequency range. Furthermore, the normalized residual plots for both the real and imaginary components depicted in Figures 8-8(b) and 8-8(c) remain within the ±2 confidence bounds (dashed lines), indicating no systematic deviations and confirming the adequacy of the fitted porous-electrode model.

The parameters extracted from fitting the rough-electrode model to the 20 m^2 dataset in Figure 8-7 are provided in Table 8-2. The extracted parameters for regressing the porous-electrode model to the 20 m^2 dataset in Figure 8-8 are shown in Table 8-3. The parameters were evaluated for statistical significance using the $^2/$ criterion, where denotes the degrees of freedom and ^{2} is the chi-square error. For a statistically valid model fit, $^2/$ approaches 1. The values reported in Tables 8-2 and 8-3 fall within the ±2 confidence interval and does not include zero, indicating statistical significance. The obtained $^2/$ values reflect the variability in electrode behavior while confirming the reliability of the two models across different electrode sizes and experimental conditions. The interpretation models accounted for the influence of parasitic capacitance on the ultramicroelectrodes.

8.3 G3 Discussion

The variations of the extracted parameters on electrode sizes was evaluated for the G3 electrodes with SIROF coatings of 300 nm and 800 nm. The total capacitance values calculated for both coating thicknesses were comparable, with the overall capacitance strongly influenced by

Table 8-2. Parameter estimates for the regression of the rough-electrode model expressed as equation (7-1) to the impedance data of 20 m^2 electrode coated with 300 nm thickness of SIROF. Confidence intervals reported are ±1 .

Parameter	Unit	Value
R_t	Ωcm^2	25.23 ± 0.55
Q_f	$mF/s^{(1-\ )}cm^2$	4.23 ± 0.29
e	–	0.8040 ± 0.0082
R_e	Ωcm^2	0.01020 ± 0.00087
R_d	Ωcm^2	27.32 ± 0.68
w	–	0.954 ± 0.010
$R_{t,eff}$	Ωcm^2	7.78 ± 0.20
$C_{t,eff}$	$mFcm^{-2}$	1.522 ± 0.031
Q_w	$mF/s^{(1-\ )}cm^2$	1.16 ± 0.17
2/	–	14
Calculated values		
$C_{fl_{at}}$ (equation (7-34))	$mFcm^{-2}$	0.365 ± 0.033
C_{total} (equation (7-36))	$mFcm^{-2}$	1.890 ± 0.066
$C_{wi_{re}}$ (equation (7-35))	nF	0.132 ± 0.027

Table 8-3. Parameter estimates for the regression of the porous-electrode model expressed as equation (8-1) to the impedance data of 20 m^2 electrode coated with 800 nm thickness of SIROF. Confidence intervals reported are ±1 . The parameter B was fixed in the Levenberg–Marquardt regression.

Parameter	Unit	Value
Q_p	$mF/s^{(1-\ )}cm^2$	0.01503 ± 0.00085
p	–	0.832 ± 0.016
R_p	Ωcm^2	380.78 ± 23.50
B	Ωcm^2	46416
R_e	Ωcm^2	0.0237 ± 0.0035
f	–	0.879 ± 0.015
Q_f	$mF/s^{(1-\ )}cm^2$	1.55 ± 0.36
Q_w	$mF/s^{(1-\ )}cm^2$	2.07 ± 0.36
w	–	0.908 ± 0.012
$R_{t,eff}$	Ωcm^2	0.537 ± 0.039
$C_{t,eff}$	$mFcm^{-2}$	0.1830 ± 0.0079
2/	–	34
Calculated values		
C_{flat} (equation (7-34))	$mFcm^{-2}$	0.39 ± 0.13
C_{pore} (equation (8-6))	$mFcm^{-2}$	0.005310 ± 0.000075
C_{total} (equation (8-7))	$mFcm^{-2}$	0.58 ± 0.14
C_{wire} (equation (7-35))	nF	0.150 ± 0.035

the component associated with changes in the oxidation state of iridium. The capacitance estimated from the measurement model also aligned with the values expected from cable-induced effects in the impedance spectra. These observed trends provide insight into the characteristic porous and rough electrode behaviors exhibited by the G3 electrodes.

8.3.1 G3 Regressed Parameters as a Function of Electrode Size

The consistency of the extracted parameters from the regression of process model to the rough and porous electrodes were evaluated and compared for two different thicknesses (800 nm and 300 nm) by plotting the parameters obtained from each regression as a function of electrode areas. The dependence of the regressed constant-phase element (CPE) parameters on the electrode areas are summarized in Figure 8-9. A clear trends emerged across different geometries and thicknesses. The error bars represent ± 1 standard deviation.

The constant-phase-element (CPE) coefficient for the flat surface, Q_f are summarized in Figure 8-9(a). The values presented includes both for rough and porous electrodes. The open circles represent 300 nm thickness, and filled squares denote 800 nm thickness of SIROF. The values of Q_f are fairly consistent across electrode areas, showing no systematic changes with increase in area for each thickness, especially for the 800 nm SIROF coatings. The 300 nm roup has larger variability, particularly for smaller electrode areas, as observed from the error bars shown in Figure 8-9(a). The overlap in values of Q_f between SIROF thicknesses suggest that thickness may not have a substantial effect on electrode capacitances. The CPE exponent associated with the flat surface ($_f$), remains relatively constant across a the electrode areas for both 300 nm and 800 nm SIROF coatings, with values clustering around 0.8 to 1.0 as shown in Figure 8-9(b).

The scatter plots for the CPE coefficient of the wire component, Q_w are illustrated in Figure 8-9(c). The trend showed a clear decrease in the values of Q_w as electrode area increases for both 300 nm (open circles) and 800 nm (filled squares) SIROF coatings. Both 300 nm and 800 nm thick electrodes follow the same downward pattern, but 800 nm electrodes tend to have slightly higher values of Q_w than 300 nm electrodes at corresponding areas, indicating stronger influence

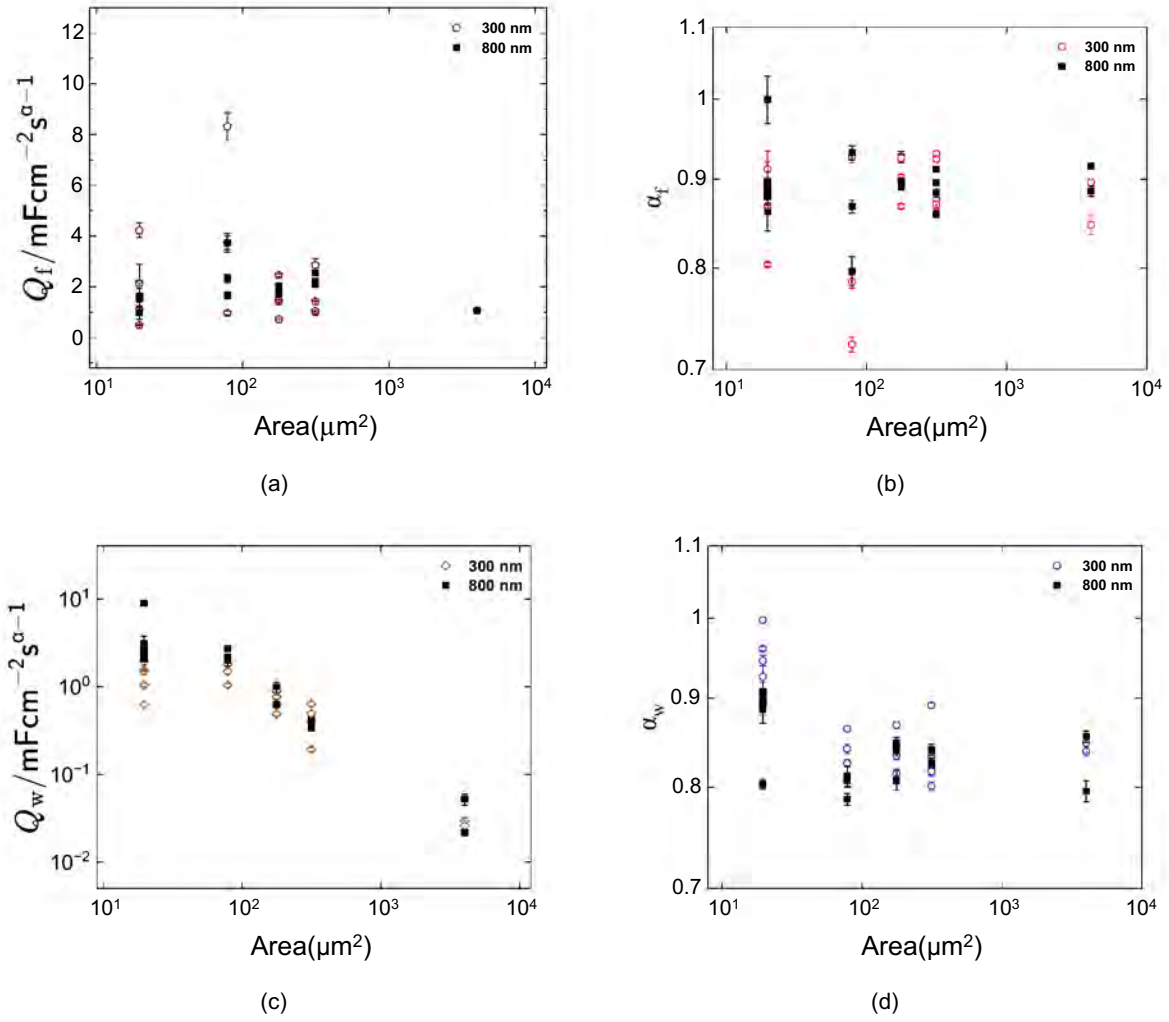

Figure 8-9. Parameter estimates for the regression of the process models shown in Figure 8-1 to G3 electrodes with film thickness as a patrameter: a) CPE coefficient of wire, Q_w; b) CPE coefficient of flat surface, Q_f; c) CPE exponent of wire, α_w; d) CPE exponent of flat surface, α_f. Error bars represent one standard deviation.

of parasitic capacitance on smaller electrodes. The CPE exponent associated with the wire ($_w$) remained fairly stable with increasing electrode area for both 300 nm and 800 nm thicknesses, with values distributed around 0.8 to 1.0 as shown in Figure 8-9(d).

The ohmic resistance, R_e displays dependence on electrode size for both 300 nm and 800 nm thicknesses. The observed trend yielded an increase in R_e with electrode area, as shown by the upward slope in Figure 8-10(a). Both 300 nm and 800 nm thicknesses follow same pattern, with larger electrode areas consistently exhibiting higher values of R_e. The alignment of the two datasets suggests that thickness has no dramatic influence on the overall area normalized R_e. The values of R_{tc} are highly dispersed across the range of electrode areas for both 300 nm and 800 nm electrodes, as shown in Figure 8-10(b). There is no clear monotonic increase or decrease of R_{tc} with increasing electrode area. A cluster of R_{tc} values are found at smaller electrode areas, while higher charge-transfer resistance outliers exist over the entire electrode range. This trend suggest influence of factors other than geometrical surface area, such as surface roughness, local inhomogeneities, or measurement artifacts on the electrode.

As illustrated in Figure 8-10(c), the diffusion resistance, R_d generally increases with area for both 300nm and 800 nm thicknesses. The values of R_d for 800 nm electrodes remains higher with increasing area compared to the 300 nm electrodes, suggesting a thickness-dependent effect on diffusion resistance. The dependence of effective charge-transfer resistance for iridium ($R_{t,eff}$) on electrode areas and thicknesses are summarized in Figure 8-10(d). $R_{t,eff}$ generally decreases as electrode area increases. The datasets for both 300 nm and 800 nm thickness follow a similar downward trend, however, the data for 800 nm-thick electrodes (black squares) generally occupy lower resistance values compared to 300 nm (open circles) at matching areas. This behavior indicate dependence of $R_{t,eff}$ on both electrode thickness and area.

The extracted parameters for the regression of the porous model to electrodes with porous behavior are summarized in Figure 8-11 for both 300 nm and 800 nm thick SIROF coatings. The pore CPE component, Q_p fairly increases as electrode area increases, for both 300 nm and 800 nm thicknesses with higher values of Q_p observed for 300 nm at smaller areas. The values of the pore

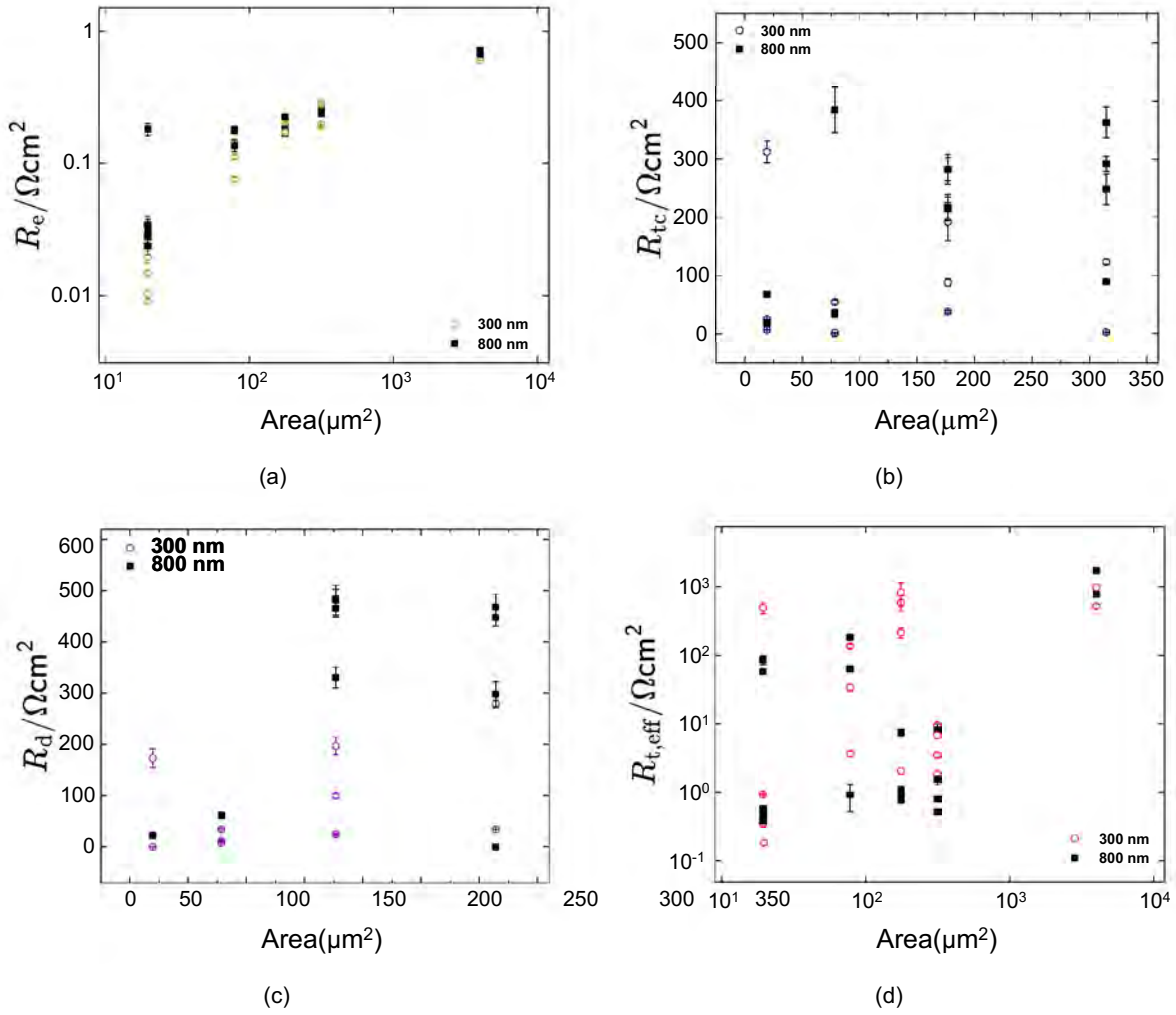

Figure 8-10. Parameter estimates for the regression of the process model shown in Figure 8-1 to G3 electrodes with film thickness as a parameter: a) ohmic resistance R_e, b) charge-transfer resistance R_{t,O_2}, c) Warburg-like diffusion resistance R_{d,O_2}, and d) effective charge-transfer resistance for changes in the iridium oxidation state $R_{t,eff}$. Error bars represent one standard deviation.

CPE exponent, $_p$ remains relatively constant over the electrode area, with most values between 0.8 and 0.9 for both 300 nm and 800 nm thicknesses, as illustrated in Figure 8-11(b). The dependence of the pore resistance, R_p are summarized in Figure 8-11(c). R_p sharply decreases with increasing area for both 300 nm and 800 nm, indicating an inverse relationship between pore resistance and electrode areas. The values of the pore geometry parameter, B generally shows a downward trend with increasing electrode area, although the relationship is less linear and more scattered. The values are similar for both 300 nm and 800 nm thickness.

8.3.2 G3 Capacitance as a Function of Electrode Size

The G3 ultramicroelectrodes exhibited impedance characteristics intermediate between rough and porous electrode behavior under open-circuit conditions. The process models shown in Figures 8-1(a) and 8-1(b) were fitted to the impedance spectra corresponding to rough and porous electrodes, respectively. The parameters extracted from both models were statistically significant and were used to estimate the effective capacitance. Capacitance values were determined using both the measurement model approach (equation (2-19)) and the Brug's [141] formula (equation(7-33)) which derives the double-layer capacitance from the constant-phase-element (CPE) parameters, assuming a normal distribution of time constants along the electrode surface [145, 89, 111]. The G3 ultramicroelectrodes impedance behavior was consistent with the CPE behavior attributed to the surface distribution of time constants.

The effective double-layer capacitance of the flat surface was calculated using equation (7-34). The influence of the parasitic capacitance was evaluated, assuming a surface distribution of time constants on the cables. The CPE parameters of the wires were used to calculate the wire capacitance depicted as equation (7-35). The general expression for estimating the capacitance of the porous surface is given as

$$_{eff,p} = \quad ^{1/}{}_{p} \quad p^{(1-}{}_{p)/}{}_{p} \tag{8-6}$$

where R_p is the pore resistance, Q_p is the constant-phase-element coefficient for the pore surface, and $_p$ is the CPE exponent for the pore surface. The capacitance calculated using the

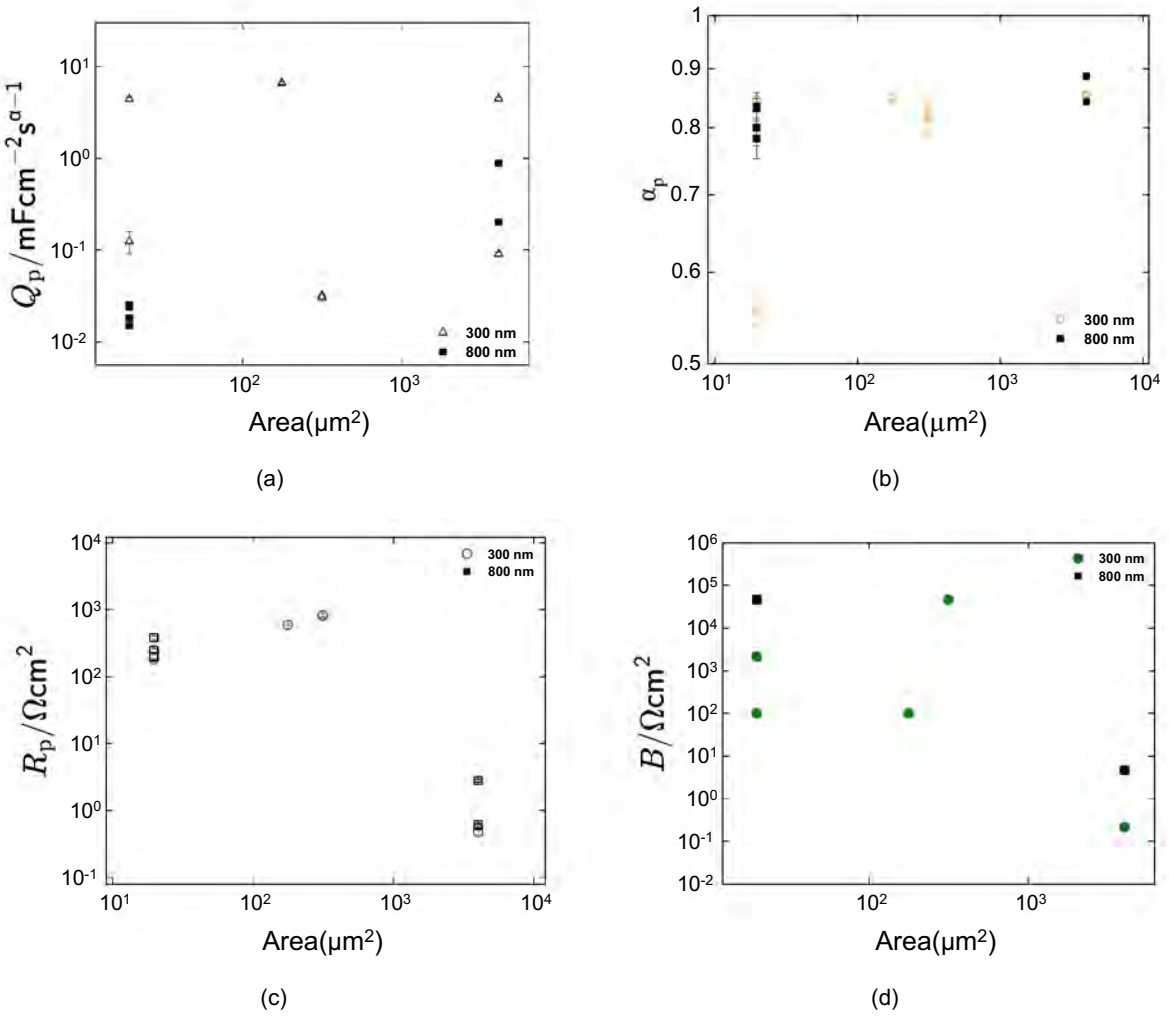

Figure 8-11. Parameter estimates for the regression of the porous model shown in Figure 8-1(b) to G3 electrodes with film thickness as a parameter: a) CPE coefficient of pore, Q_p; b) CPE exponent of pore, α_p; c) pore resistance, R_p; d) pore geometry parameter, B. Error bars represent one standard deviation.

measurement model approach is given by equation (7-32). The effective capacitance for the changes in iridium oxidation state was calculated using equation (7-28).

The difference between the porous and rough process models lies in the electrochemical reactions occurring between the SIROF coatings, the gold substrate and the phosphate-buffered saline. For rough electrodes, the cathodic faradaic reactions could be extracted and modeled in parallel to the flat surface and changes in iridium oxidation states as shown in Figure 8-1(a). However, electrodes with porous impedance behavior may have a pronounced pore structure influencing the charge reactions at the electrode-electrolytes interface. As shown in Figure 8-1(b) the pore impedance was modeled in parallel to the flat surface and changes in iridium oxidation states as shown in Figure 8-1(a). The influence of parasitic capacitance is reflected in the two models. The total effective capacitance of the rough electrodes was estimated using equation (7-36). The expression for calculating the total effective capacitance of the porous electrodes is given as

$$\text{total} = \text{eff,flat} + \text{eff,ir}_{3+/ir4+} + \text{eff,p} \quad (8\text{-}7)$$

where $C_{eff,p}$ is the effective capacitance of the pore surface, $C_{eff,flat}$ is the effective capacitance of the flat surface, and $C_{eff,ir^{3+}/ir^{4+}}$ is the effective capacitance for the changes in iridium oxidation state (equation (7-28)).

The estimated effective capacitances are presented in Figure 8-12 as a function of electrode sizes. The plots were used to assess the influence of SIROF coating thicknesses on the impedance behavior of G3 electrodes. The calculated capacitances for the 300 nm thicknesses of SIROF are shown in Figures 8-12(a) and 8-12(b) for normalized and non-normalized values respectively. The effective capacitances in Figure 8-12(a) were normalized by the electrode areas to allow for meaningful comparison between the G3 ultramicroelectrodes of different sizes and geometries. As illustrated in Figure 8-12(a), the impedance behavior varies between porous and rough electrodes. The flat-surface capacitance, C relatively varies with increasing electrode area, having a lowest value of 0.300 ± 0.032 mF/cm^2 for the 4000 m^2 electrode site and a highest value of 5.545 ± 0.027 mF/cm^2 for the 315 m^2 electrode site, as shown in Figure 8-12(a).

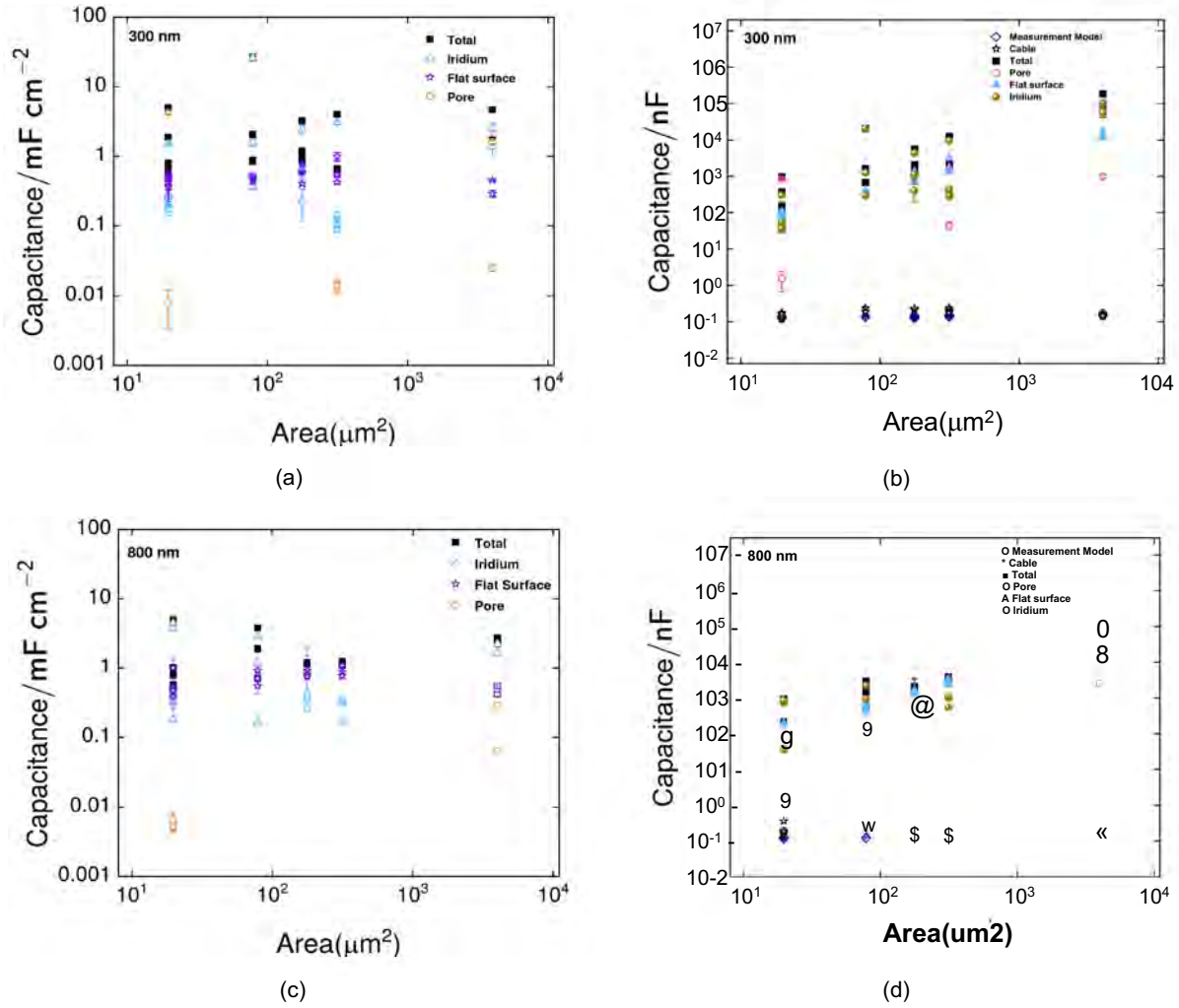

Figure 8-12. Capacitance for G3 as a function of electrode size and SIROF coating thickness: a) and b) 300 nm thickness c) and d) 800 nm thickness. Error bars represent one standard deviation.

The capacitance associated with redox changes in iridium increases with electrode area, as illustrated in Figure 8-12(a). The pore capacitance was estimated for electrodes exhibiting porous behavior using equation (8-6). The relatively high pore capacitance values may indicate electrodes with deep or highly developed pore structures. The total capacitance C which accounts for contributions from the flat surface, pores, and iridium redox transitions, varies with electrode area and reflects dependence on the impedance characteristics of each electrode. As shown in Figure 8-12(a) the overlap between the total capacitance and the iridium redox-related capacitance suggests that the overall charge-storage behavior is largely governed by changes in iridium oxidation state. Conversely, total capacitance values correlating with pore capacitance imply a dominant porous electrode response. The pore capacitance across electrodes displaying porous behavior ranged from 0.0249 ± 0.0023 mF/cm^2 to 4.248 ± 0.234 mF/cm^2, highlighting variability in structural and electrochemical properties among the G3 sites.

The non-normalized capacitance plot for the 300 nm SIROF coating shown in Figure 8-12(b), illustrates the influence of parasitic capacitance on the G3 ultramicroelectrodes. The capacitance attributed to the cables aligns closely with the values estimated using the measurement model. As shown in Figure 8-12(b), both the cable capacitance and the measurement model capacitance are substantially lower than the other calculated capacitances. The cable capacitance ranges from 0.117 ± 0.00784 nF to 0.255 ± 0.01607 nF across the different electrode areas, with the lower values indicating minimal parasitic capacitance contributions to the impedance measurements.

A similar trends for porous and rough electrode impedance responses were observed for the normalized and non-normalized capacitance plots of the 800 nm SIROF coated electrodes as show in Figures 8-12(c) and 8-12(d), respectively. The highest and lowest values of C was recorded as 0.387 ± 0.129 mF/cm^2 and 1.010 ± 0.381 mF/cm^2, as shown in Figure 8-12(c). The capacitance calculated for redox changes in iridium varied between 0.164 ± 0.050 mF/cm^2 and 4.439 ± 0.57 mF/cm^2, as illustrated in Figure 8-12(c). The non-normalized capacitance plots shown in Figure 8-12(d) suggests an increasing trend with the electrode area for the total

capacitance, flat capacitance, and the capacitance for redox changes in iridium, and a decreasing pattern with the electrode sizes for the cable capacitance and the measurement model approach. The measurement model approach and cable capacitance are similar as shown in Figure 8-12(d). Larger values may imply higher parasitic capacitance contributions in the impedance data. The estimated total capacitances for the 300 nm and 800 nm SIROF are compared in Figure as a function of electrode sizes. $_{total}$ for the 300 nm and 800 nm SIROF are in good agreement. The values mostly varied from 0.6 mF/cm^2 to 5 mF/cm^2 across the electrode sizes.

The individual contributions of the magnitude of impedance of the flat surface, $|\ |_{fl_{at}}$, iridium-redox reactions $|\ |_{t,eff}$ (or $|\ |_{iridium}$), pore surface, $|\ |_{pore}$ and mass-transfer-limited oxygen reduction, $|\ |_{O_2}$ (or $|\ |_{tc}$), to the total impedance response were evaluated for both rough and porous electrodes. The magnitude of impedance for the rough and porous electrodes were calculated using equations (7-2) and (8-1), respectively, without ohmic resistant R_e. For both rough and porous-electrode models, the overall impedance response is a parallel combination of the individual impedance responses, which implies that the lower impedance magnitude would contribute more to the total impedance. The resulting impedance magnitude as a function of frequency for a 20 m^2 rough electrode coated with 300 nm-thick SIROF are summarized in Figure 8-14(a). The total impedance magnitude ($|\ |_{total}$) decreased linearly with frequency, at high frequency points above 500 Hz and overlapped with the impedance magnitude of the flat surface. This behavior suggests that the impedance of the bare electrode surface dominates in this regime. The contributions of the oxygen-reduction impedance ($|\ |_{O_2}$) remains nearly flat and higher at the high-frequency region, however, at low frequency points below 1 Hz the impedance response of $|\ |_{O_2}$ dominates.

The impedance magnitude as a function of frequency for a 20 m^2 porous electrode coated with 800 nm-thick SIROF are shown in Figure 8-14(b). The magnitudes of the total impedance ($|\ |_{total}$) and the flat surface ($|\ |_{flat}$) are in good agreement and decreased linearly with a slope of approximately –1 on the logarithmic plot. The iridium redox changes contributes ($|\ |_{i_ridi_{um}}$) more than the porous layer ($|\ |_{pore}$) at high frequency point, however, a transition is observed between

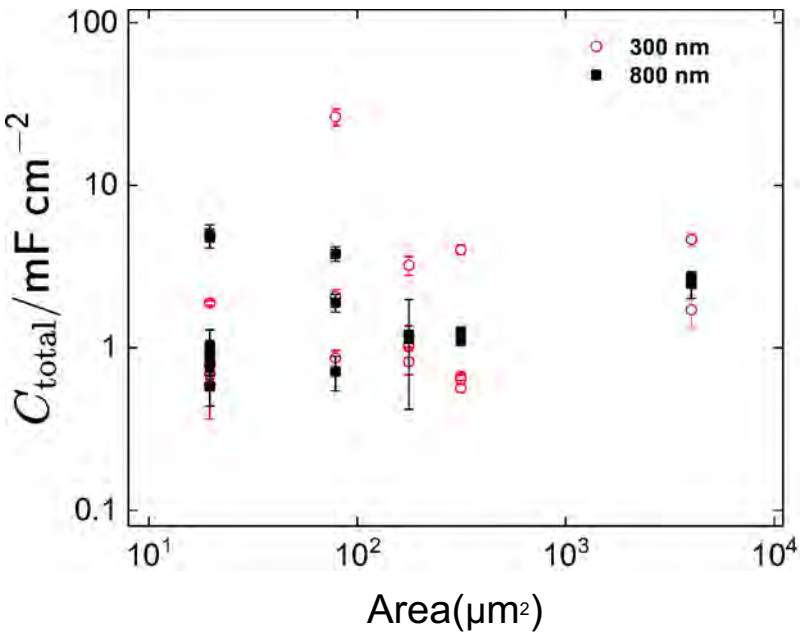

Figure 8-13. Total capacitance for G3 as a function of electrode size with SIROF coating thickness as a parameter.

the two at the low frequency regime, where the influence of the pore surface (| |$_{pore}$) is greater than the impedance due to changes in iridium oxidation state (| |$_{i,idi_{um}}$). The impedance responses shown in Figure 8-14 confirms the intermediate behavior between a rough and porous electrode observed in G3 electrodes.

8.3.3 Statistical Results for G3

The parameters extracted from fitting the process models to the impedance spectra of both porous and rough electrodes were statistically significant, as their values lie within the 95.4% confidence interval (±2) and does not include zero. The capacitance for the electrode substrate $_{fl_{at}}$ defined by equation (7-34) was estimated for both the porous and rough electrode impedance spectra using the constant-phase-element parameters and the ohmic resistance in each case. For each electrode area and coating thickness, the mean and confidence intervals of $_{flat}$ were estimated using Brug's formula, based on the means and standard deviations of the regressed parameters ($_f$, $_f$, and $_e$). These calculations were performed via Monte Carlo simulation. The

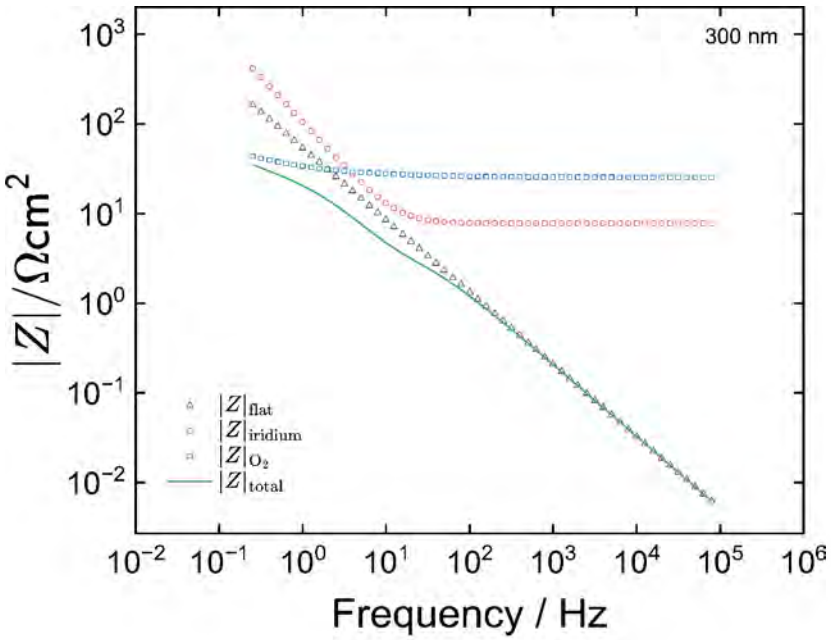

(a)

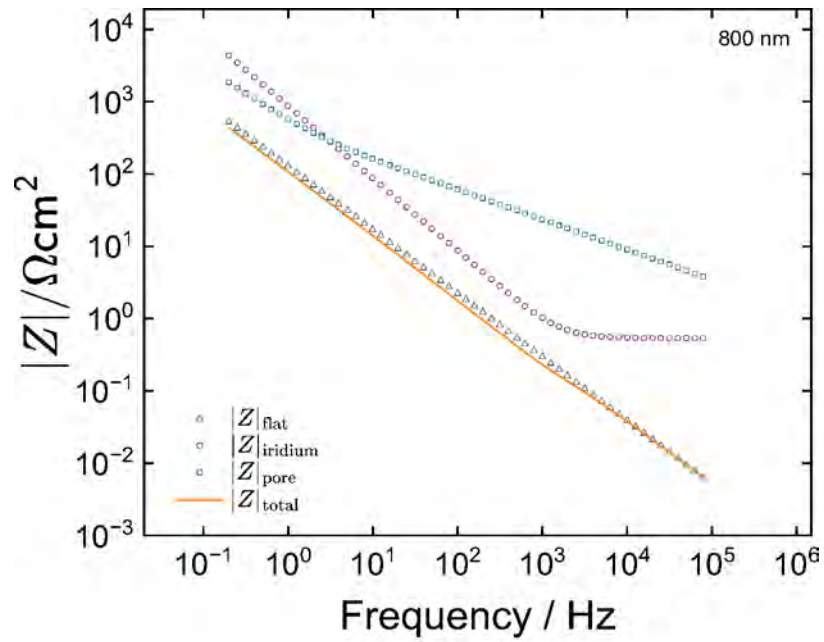

(b)

Figure 8-14. Comparison of impedance magnitudes for 20 m^2 electrodes with different SIROF coatings: a) rough electrode, and b) porous electrode. The magnitudes for the rough and porous electrode were calculated using equations (7-2) and (8-1), without ohmic resistant R_e

normal distributions of the flat capacitance calculated for different electrode areas with 300 nm thicknesses are shown in Figure 8-15.

The mean value and standard deviation of $_{fl_{at}}$ for the 20 m^2 site with a rough electrode behavior is shown in Figure 8-15(a). The estimated value was 364.7 ± 32.6 F/cm^2. This result aligns with the distribution of capacitance observed across all 20 m^2 electrodes in Figure 8-12(a), demonstrating the consistency of the model parameters within this electrode category. Similarly, the analysis of a representative 80 m^2 site displaying rough electrode characteristics, shown in Figure 8-15(b), yielded a mean capacitance of 481.56 F/cm^2, with a standard deviation of 52.5 F/cm^2. These results fall within the range of $_{flat}$ calculated for all the 80 m^2 electrodes presented in Figure 8-12(a).

The $_{fl_{at}}$ estimated for a representative 180 m^2 electrode site with porous impedance response is 360.07 ± 17.20 F/cm^2 as illustrated in Figure 8-15(c). A mean value and standard deviation of 422.78 ± 18.18 F/cm^2 was obtained for a 300 m^2 electrode site with a rough electrode impedance behavior as shown in Figure 8-15(d). The 4000 m^2 site having a porous electrode behavior displayed a $_{fl_{at}}$ of 288.37 ± 31.79 F/cm^2 as shown in Figure 8-15(e). These results confirm the statistical significance of the extracted parameters and validate the use of Brug's model to extract double-layer capacitance across different electrode sizes. The histograms provide visual evidence of the normal distribution of estimated capacitance values, supporting the reproducibility of the interpretation model.

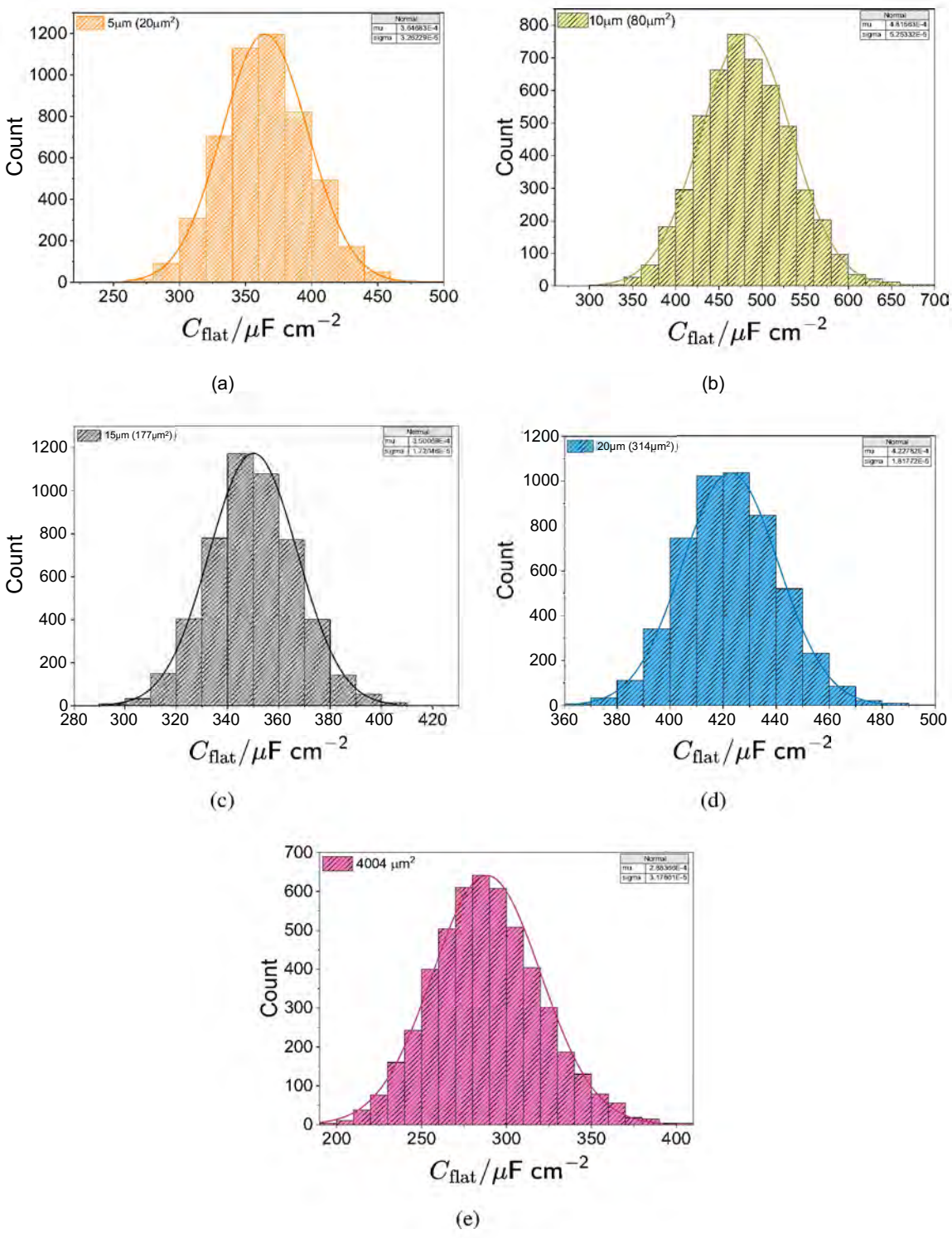

Figure 8-15. Process model regression results showing the normal distribution of the flat-surface capacitance calculated from equation (7-34) for the porous and rough electrodes with 300 nm thickness of SIROF: a) 20 m^2 rough electrode, b) 80 m^2 rough electrode, c) 180 m^2 porous electrode, d) 300 m^2 rough electrode, and e) 4000 m^2 porous electrode.

CHAPTER 9
IMPEDANCE RESPONSE OF PLATINUM ULTRAMICROELECTRODES

The 10 m and 25 m platinum-disk ultramicroelectrodes where provided by Professor Won Tae Choi at the University of Florida. The ultramicroelectrodes shown in Figure 3-5 served as a prototype for understanding the impedance behavior of ultramicroelectrodes in phosphate-buffered saline. The design and fabrication method for the platinum ultramicroelectrodes are discussed in section 3.2. The Impedance data were analyzed with the measurement model to quantify the stochastic error structure and extract physically meaningful parameters. The measurement model theory is discussed in section 2.5.2.3 and the measurement modeling approach is provided in section 5.3.

This chapter presents the experimental procedure, process modeling, and results that support the interpretation of impedance spectra for the 10 m and 25 m platinum-disk ultramicroelectrodes. Parameters obtained from the process model regression were used to estimate the electrode's capacitance as a function of applied potential.

9.1 Impedance Spectroscopy Experiment

Electrochemical examinations were performed for 10 m and 25 m platinum ultramicroelectrodes in phosphate-buffered saline using the Gamry Reference 620+ potentiostat. The saline solution was a mixture of 20 mL of phosphate-buffered saline containing 0.01 M phosphate buffer, 0.0027 M KCl, and 0.137 M, NaCl and 80 mL of de-ionized water to simulate physiological conditions. A three-electrode cell configuration which consist of the working electrode, a platinum-mesh counter electrode and a silver/silver-chloride (Ag/AgCl) reference was used. The measurements were taken under aerated conditions at a temperature of 37^0 C. A 25 mV root means square sinusoidal perturbation was applied to the Gamry equipment at 100 KHz to 0.2 Hz. Before potentiostat impedance measurements, chronoamperometry measurements were used to monitor the transient current response following a step in potential from -0.6 V(Ag/AgCl) to 0.6 V(Ag/AgCl), at a step change of 0.03 V(Ag/AgCl). Each step lasted for 1800 seconds (30 minutes). Polarization curves were plotted at a steady state. The 0.49 V(Ag/AgCl) and 0.39 V(Ag/AgCl) were identified as the open-circuit potential (OCP) for the 10 m and 25 m

platinum electrodes, respectively. The potentiostatic EIS measurements were conducted at potentials of 0.47 V, 0.48 V, 0.50 V, and 0.51 V for the 10 m platinum electrode. While the impedance measurements for the 25 m platinum electrode were performed at 0.37 V, 0.38 V, 0.40 V, and 0.41 V.

9.2 Process Model for Platinum Ultramicroelectrodes

The impedance spectra of the 10 m and 25 m platinum ultramicroelectrodes were collected in phosphate-buffered saline at open-circuit and aerated conditions. The data were carefully regressed with a process model to extract the physical parameters of the electrode. The process model regressed to the impedance spectra is shown in Figure 9-1. The model integrates the ohmic resistance in series with a parallel combination of the constant-phase-element behavior of the electrode, and the faradaic reactions presumed to be oxygen-reduction influenced by mass-transfer of reacting species.

The electrochemical impedance spectroscopy of the 10 m and 25 m platinum ultramicroelectrodes were performed to understand the impedance behavior of ultramicroelectrodes in phosphate-buffered saline. A similar interpretation model was applied to both platinum electrodes and the G1 electrodes presented in Chapter 6. The model was formulated under the assumption that oxygen-reduction reaction (see equation (9-1)) occurred in the system.

$$O_2 + 2H_2O + 4e^- \rightarrow 4OH^- \qquad (9\text{-}1)$$

At open-circuit potential (OCP), the anodic and cathodic faradaic currents are balanced resulting in no net current flow. The total impedance can be described as

$$= + \frac{+}{e\ 1+(\ )\ (\ t+\ D)} \qquad (9\text{-}2)$$

where R_e is the ohmic resistance, R_t is the charge-transfer resistance, Z_D is the diffusion impedance, is the frequency, j is the complex number, -1, and is the

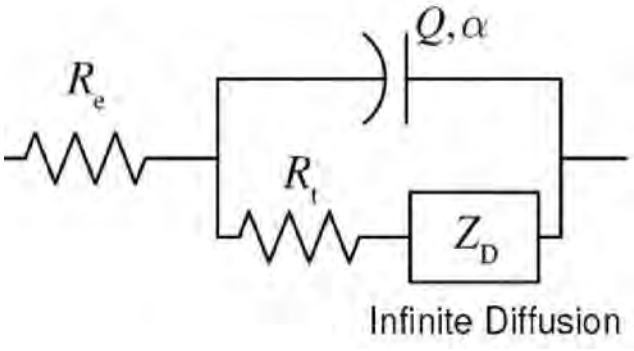

Figure 9-1. Process model for platinum-disk ultramicroelectrodes. Potentials were measured with respect to the Ag/AgCl reference electrode.

constant-phase-element exponent and component, respectively. A detailed derivation of this model and the assumptions behind it are presented in section 6.1 of Chapter 6.

9.3 Experimental Results for Platinum

The impedance spectra obtained at open circuit were analyzed using Watson and Orazem's[97] measurement model program. The nyquist plots, normalized real and imaginary residuals of impedance, and ohmic-resistance corrected bode plots, were plotted as part of the analysis. The process model used to regress the data was guided by polarization in aerated conditions and was expressed in terms of ohmic resistance, diffusion resistance, and an expression for the constant-phase element. Detailed discussions regarding the obtained physical parameters are provided for the 10 m and 25 m platinum-disk ultramicroelectrodes.

9.3.1 Polarization Curve

Polarization measurements for the 10 m and 25 m platinum electrodes were achieved using a sequence of chronoamperometric steps. The experiment was recorded in phosphate-buffered-saline (PBS) versus an Ag/AgCl reference electrode at aerated conditions. The applied potential incrementally varied from 0.6 V (Ag/AgCl) to -0.6 V (Ag/AgCl) in 30 mV intervals. The phosphate-buffered saline solution contained 0.01 M phosphate buffer, 0.0027 M KCl, and 0.137 M, NaCl and 80mL of de-ionized water to simulate physiological conditions. To

achieve steady-state current conditions, each potential was held for 30 minutes before advancing to the subsequent step and each chronoamperometry measurements lasted for 21.5 hours for the 10 m and 25 m platinum electrodes. The non-linear cathodic polarization curves are shown in Figure 9-2.

The resulting steady-state polarization response of the 10 m platinum ultramicroelectrode is presented in Figure 9-2(a). A low cathodic current is observed at more negative potentials between -0.6 V (vs Ag/AgCl) to –0.3 V (vs Ag/AgCl). This region corresponds to the weak reduction of oxygen present in the aerated saline solution. The absence of a mass-transfer plateau at more negative potentials above –0.4 V (vs Ag/AgCl) suggests that the oxygen-reduction reaction proceeds under mixed kinetic and mass-transfer control, with the rate of reaction limited by oxygen transport. As the potential is increased from –0.3 V (vs Ag/AgCl) to +0.4 V (vs Ag/AgCl), a rapid current increase from the cathodic regime to the anodic region is seen. This reflect a shift from cathodic reduction reactions to anodic charge transfer. This intermediate region represents the kinetic region where for the adsorption of hydrogen and hydroxyl intermediates. The steep slope of the polarization curve in this region suggests interfacial electron-transfer kinetic reactions on the 10 m platinum ultramicroelectrode.

The faradaic current approaches a near-steady plateau close to 0 nA, at more positive potentials above +0.3 V (vs Ag/AgCl). This domain correspond to the mass-transfer-limited region where no faradaic processes could be observed. In this regime, the faradaic current response is dominated by double-layer charging. The anodic regime ends at +0.6 V vs Ag/AgCl, prior to the onset of platinum oxide formation (usually initiated above +0.8 V). The absence of the oxide peak confirms that the potential window employed probes only the mass-transfer influenced oxygen reduction reaction and capacitive behavior of the 10 m platinum ultramicroelectrode in PBS.

The polarization curve for the 25 m platinum ultramicroelectrode is shown in Figure 9-2(b). The electrode exhibits a gradual decrease in cathodic faradaic current at negative potentials above –0.4 V (vs. Ag/AgCl), reaching about –30 nA near a potential of –0.6 V(vs. Ag/AgCl). This region corresponds to oxygen-reduction reaction in the aerated PBS solution. The

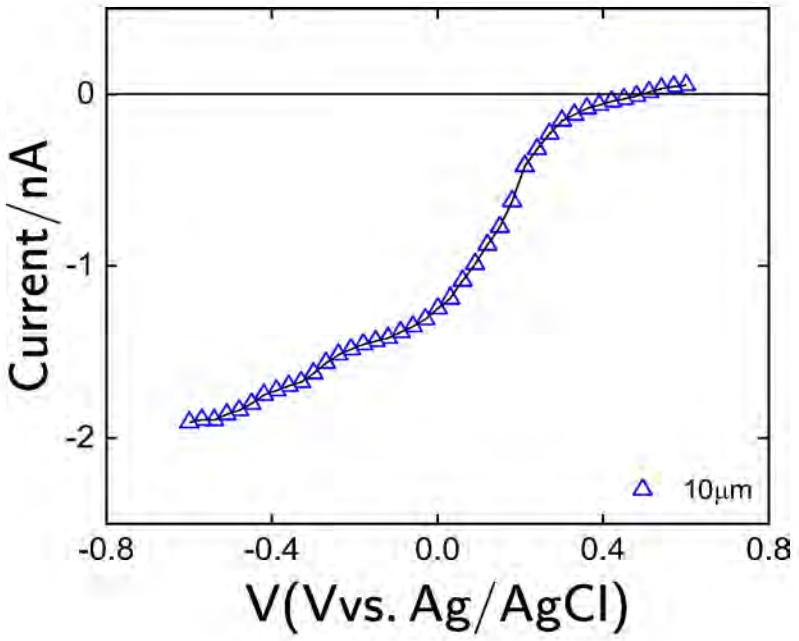

(a)

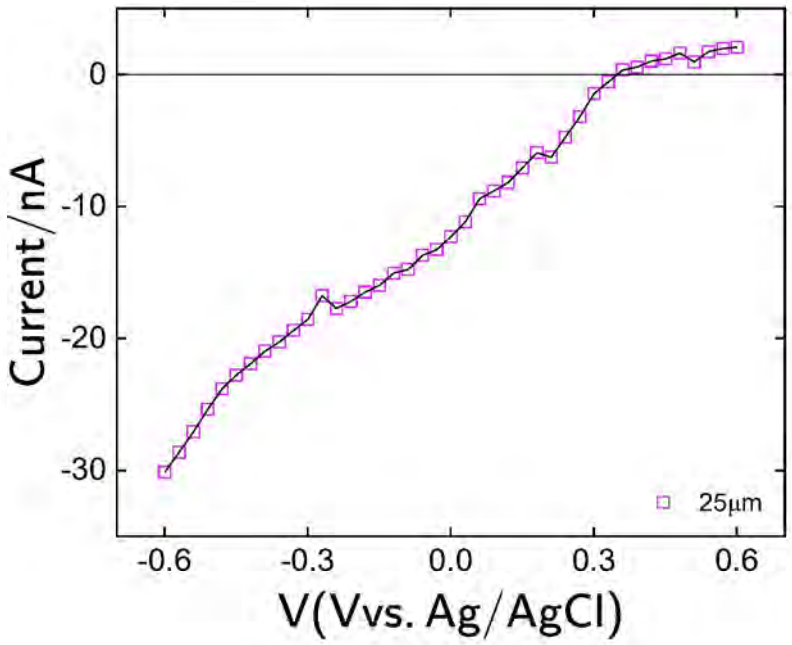

(b)

Figure 9-2. Polarization curves: a) 10 m and b) 25 m. The potential was measured with reference to the Ag/AgCl electrode.

progressive decrease suggests that the system operates under the combination of kinetics and mass-transfer control. A potential increase towards the more positive values from –0.3 V (vs. Ag/AgCl) to +0.3 V (vs. Ag/AgCl) indicates faradaic current transitions to near-zero values. This transition region represents the kinetic domain for depletion of oxygen and the accumulation of hydrogen. The current reaches zero at a potential of +0.39 V (vs. Ag/AgCl). In this domain, no faradaic oxidation reactions were observed as the potential remains below +0.8 V for the onset of platinum oxide formation. The current increased with the applied potential showing cathodic oxygen-reduction within the system.

9.3.2 Linear Sweep Voltammetry (LSV)

Linear sweep voltammetry was performed for the 10 m and 25 m platinum ultramicroelectrodes in an aerated phosphate-buffered saline. The illustration in Figure 9-3 compares the current measured at a sweep rate of 0.1 mV/s and 1 mV/s to the polarization response of the ultramicroelectrodes. The resulting linear sweep voltammograms (LSVs) and steady-state polarization curve for the 10 m platinum ultramicroelectrode in phosphate-buffered saline are shown in Figure 9-3(a). At more negative potentials between –0.6 V (vs Ag/AgCl) and –0.3 V (vs Ag/AgCl) the electrode exhibits a cathodic faradaic current attributable to the reduction of oxygen. The polarization curve (blue line) yields a limiting current that suggest mass-transfer influenced oxygen-reduction reaction on the electrode surface. The linear sweep voltammetry recorded at 0.1 mV/s (black squares) closely approaches the steady-state polarization curve at the more negative region. The faster sweep rate of 1 mV/s represented by red circles showed larger cathodic currents at these negative potentials which may arise from the influence of non-steady diffusion and increased capacitive contribution at higher scan rates.

The linear sweep voltammograms (LSVs) and steady-state polarization curve for the 25 m platinum ultramicroelectrode are compared in Figure 9-3(b). At more positive potentials above +0.3 V (vs Ag/AgCl), the linear sweep voltammogram for the low sweep rate of 0.1 mV/s (blue squares) and fast weep of 1 mV/s (pink circles) closely aligns with the steady-state polarization curve. The consistency suggest that the electrode does not undergo faradaic reaction within this

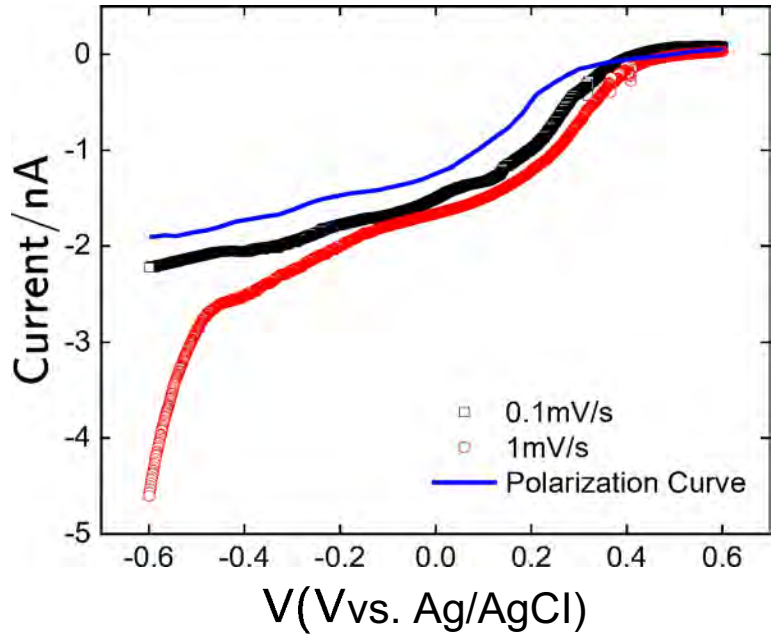

(a)

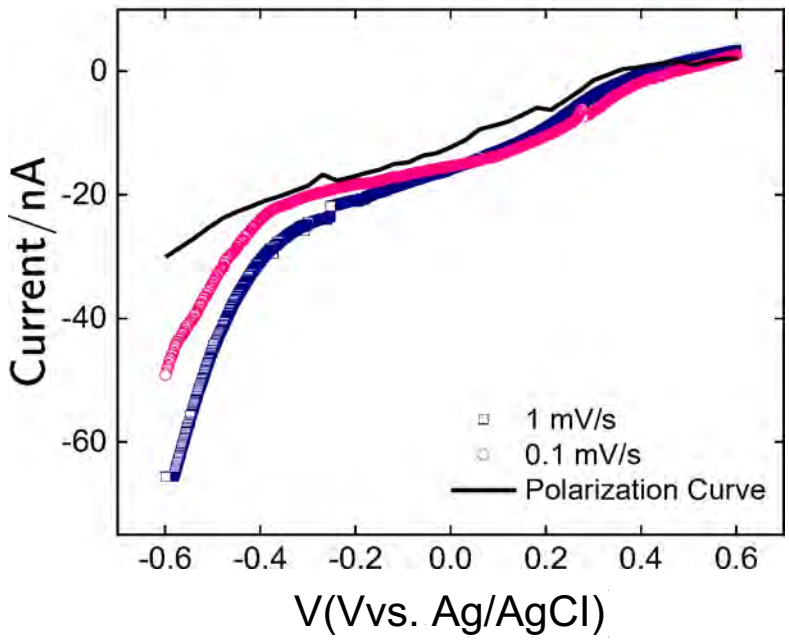

(b)

Figure 9-3. Linear sweep voltammetry and steady-state polarisation curves for platinum ultramicroelectrodes: a) 10 *μm,* and b) 25 pm. Potentials were measured with respect to the Ag/AgCl reference electrode.

region. The electrode showed a cathodic faradaic current attributable to the reduction of oxygen at more negative potentials between –0.6 V (vs Ag/AgCl) and –0.3 V (vs Ag/AgCl) with the cathodic faradaic currents being more pronounced for the sweep rate of 1 mV/s. This behaviour can be attributed to increased capacitive contribution to the electrode surface at larger scan rates.

9.3.3 Impedance Spectra for Platinum

The impedance data for the platinum ultramicroelectrodes were obtained in triplicates at open-circuit conditions. The potentiostatic EIS experiment for each replicated datasets lasted for 1200 seconds (20 minutes). The impedance measurements for the 10 m, and 25 m electrodes was guided by polarizing the current at potentials from -0.6 V(Ag/AgCl) to 0.6 V(Ag/AgCl), at a step change of 0.03 V(Ag/AgCl). The open-circuit potentials for the 10 m, and 25 m electrodes were 0.49 V(Ag/AgCl) and 0.39 V(Ag/AgCl) respectively. Replicated datasets were collected for the 10 m platinum electrode at potentials of 0.47 V, 0.48 V, 0.50 V, and 0.51 V and for the 25 m at 0.37 V, 0.38 V, 0.40 V, and 0.41 V.

The impedance spectra for the 10 m platinum-disk electrode is shown in Nyquist format in Figure 9-4(a). The plot yielded a semi-circular arc with a radius between the initial and final charge-transfer resistance across the measured potentials of 0.47 V to 0.51 V. The Nyquist plot for all potentials overlap at high frequency points. The trends in the figure may suggest mass-transfer influenced faradaic reactions and surface distribution of time constants in the system. Nyquist plots for the 25 m platinum-disk electrode are presented in Figure 9-4(b). The results show similar impedance profiles for potentials spanning from 0.37V to 0.41V. The Nyquist plots for all potentials are overlapped at high-frequency points and separated at low-frequency regions. The impedance profile is consistent with a constant-phase element behavior attributed to the distribution of time constants at the electrode surface.

9.3.4 Error Model for Platinum

The error structure analysis of the impedance spectra of 10 m and 25 m platinum electrodes were computed using the measurement model software developed by Watson and Orazem [97]. The impedance data were collected in three replicates for different potentials at

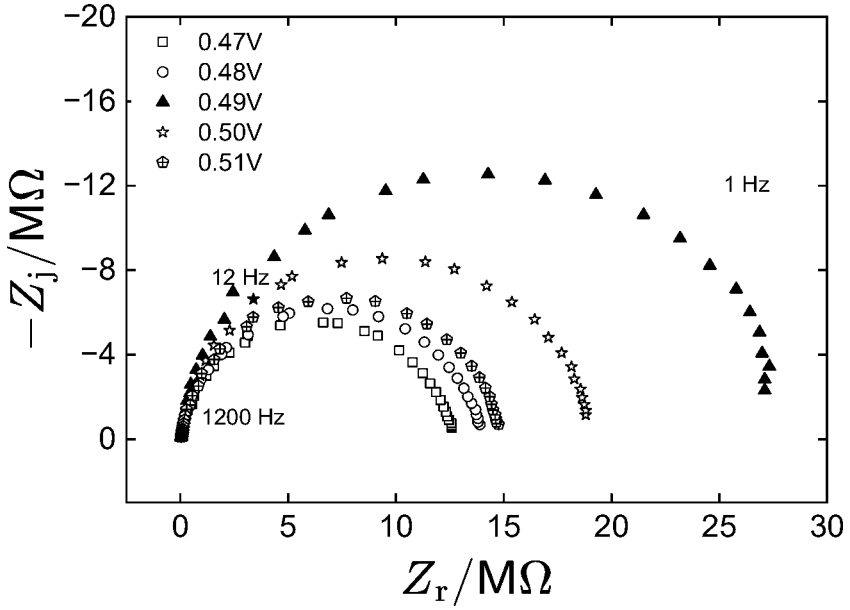

(a)

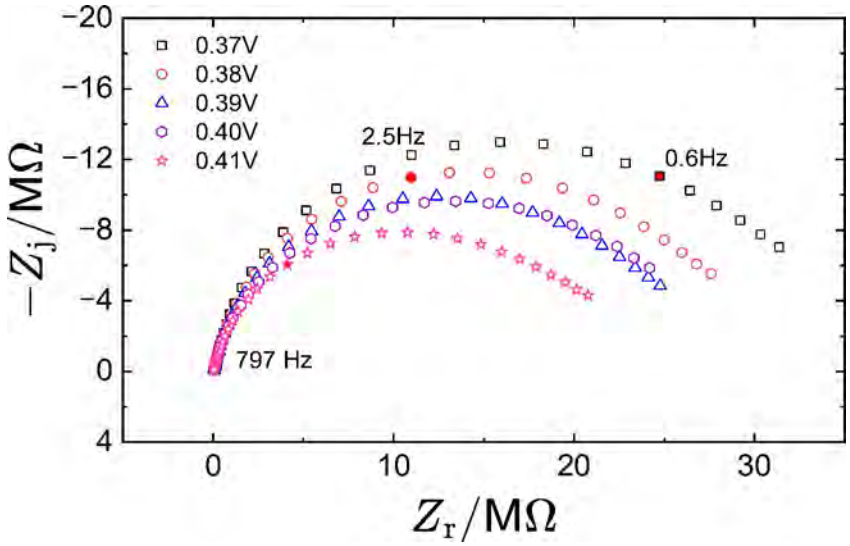

(b)

Figure 9-4. Impedance spectra in Nyquist format for platinum ultramicroelectrodes: a) 10 um, and b) 25 cm. The measurements were performed at open-circuit.

open circuit. The methods for stochastic error structure analysis are presented in section 5.3.4. The error analysis was done to filter bias errors caused by instrument artifacts or time-dependent spectrum of a system. The stochastic error structure is computed from the standard deviations of the real and imaginary components of impedance using a Levenberg–Marquardt regression.

The error structure of sample replicated datasets for the 10 m and 25 m Platinum ultramicroelectrodes are shown in Figure 9-5. The triangles and circles represent the real and imaginary standard deviations of impedance, respectively, as shown in Figures 9-5(a) and 9-5(b). The line fitted to the error structures in Figure 9-5 depicts the empirical error model in equation (5-1). The error model is unique for the 10 m and 25 m Platinum ultramicroelectrodes. The error model parameters for the 10 m and 25 m Platinum electrodes are summarized in Table 9-1. Both standard deviations of the real and imaginary impedance are overlapping and heteroscedastic as shown in Figures 9-5(a) and 9-5(b). The ability to fit the overlap between the real and imaginary standard deviations of impedance implies that the 10 m and 25 m impedance data are consistent with the Kramers–Kronig relation, as shown in Figures 9-5(a) and 9-5(b).

The normalized error structures of the 10 m and 25 m Platinum ultramicroelectrodes are illustrated in Figure . The results display the standard deviation divided by impedance magnitude for the 10 m, and 25 m platinum electrodes. At low frequency points, the normalized errors for the 10 m platinum electrodes are on the order of 0.3% as depicted in Figure 9-6(a). The normalized error structure for the 25 m platinum electrode is presented in Figure 9-6(b). The errors are also on the order of 0.3% at low frequency points. The normalized errors for the 10 m and 25 m Platinum ultramicroelectrodes are similar at low frequency points and depicts the noise levels for measurements obtained using the Gamry Reference 600+.

Table 9-1. Error parameters obtained by regressing equation (5-1) to the impedance spectra of platinum-disk ultramicroelectrodes.

Parameter	10 m	25 m
	$1.692 \times 10^{-2} \pm 1.227 \times 10^{-22}$	$3.05 \times 10^{-3} \pm 3.877 \times 10^{-21}$
	–	–
	$2.206 \times 10^{-11} \pm 4.737 \times 10^{-14}$	$5.902 \times 10^{-11} \pm 1.495 \times 10^{-13}$
	–	–

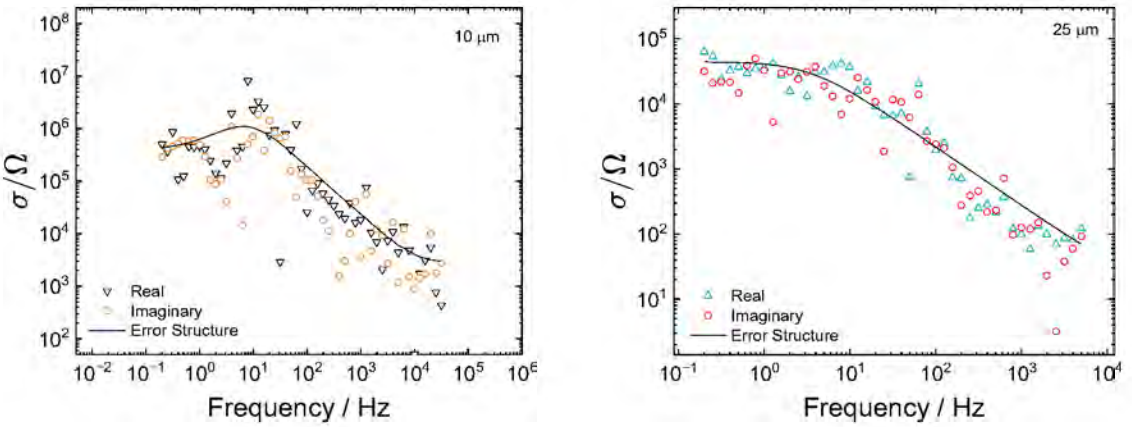

(a) (b)

Figure 9-5. Error structure generated by fitting equation (5-1) to the impedance spectra of 10 m and 25 m Platinum ultramicroelectrodes: a) 10 m, and b) 25 m.

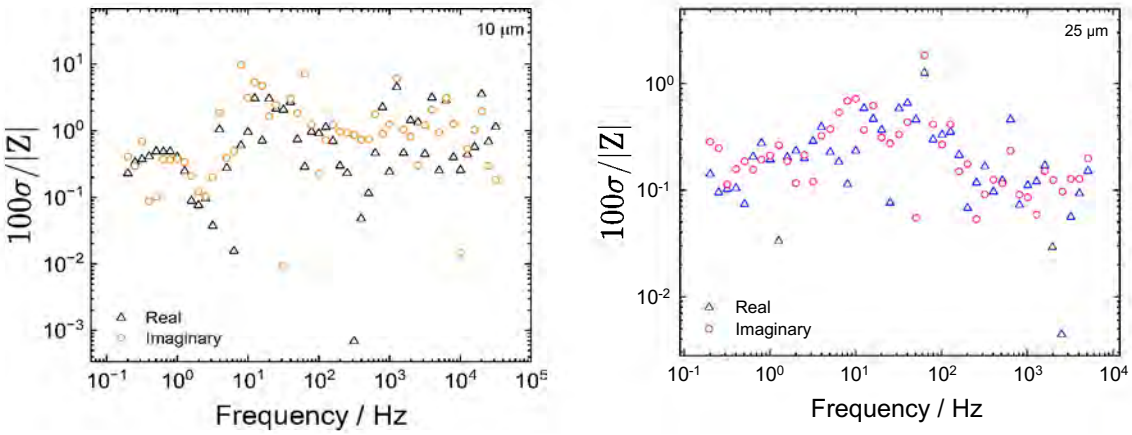

(a) (b)

Figure 9-6. Normalized error structure for Platinum ultramicroelectrodes: a) 10 m, and b) 25 m.

9.3.5 Measurement Model Analysis for Platinum

The measurement model developed by Argawal et al.[3] was regressed to the impedance spectra of the 10 m and 25 m Platinum ultramicroelectrodes. The resulting ohmic-resistance-corrected Bode plots for the platinum electrodes are shown in Figures 9-7 and 9-8. The plot was obtained by subtracting the ohmic resistance from the real component of the impedance as shown in equation (7-29) and (7-30). The corrected Bode plots can be used to explain the kinetic behavior of the electrochemical systems. The plots show characteristic bends or ”break frequencies” in Impedance spectra. The physical parameters of the electrical circuit model in Figure 9-1depend on the slope of the temperate regions of the curve. For example, a zero slope depicts the resistor, while the slope of -1 and -1/2 represents the capacitor and the Warburg diffusion, respectively.

The ohmic-resistance-corrected-magnitude plot for the 10 m Platinum ultramicroelectrodes is shown in Figure 9-7(a) with potential as a parameter. The open-circuit potential (OCP) is 0.49 V. The solid lines indicate the fit to the measurement model (equation (2-19)) performed using error-structure weighting. The model aligns closely with experimental data which implies consistency with the Kramers–Kronig relations. At high frequency points above 10Hz, the open-circuit potential (OCP) and potentials at ± 2 OCP and ± 1 OCP, overlapped and showed an impedance response with a slope of -1. This high-frequency impedance response may be attributed to the surface distribution of time constants at the electrodes. At low frequency points, the open-circuit potential is larger than the other potentials by a factor of two. The corrected magnitude plots for the 25 m electrode presented in 9-7(b). The measurement model fits the data well across different potentials. The impedance response of the open-circuit potential (OCP) and potentials at ± 2 OCP and ± 1 OCP, align closely at both low-frequency and high-frequency points.

The ohmic-resistance-corrected phase angle, $_{Re}$ for the 10 m and 25 m Platinum electrodes are illustrated in Figure 9-8 as functions of potentials. The plot shows the frequency dispersion and constant-phase element behavior of the system. The ohmic-resistance-corrected

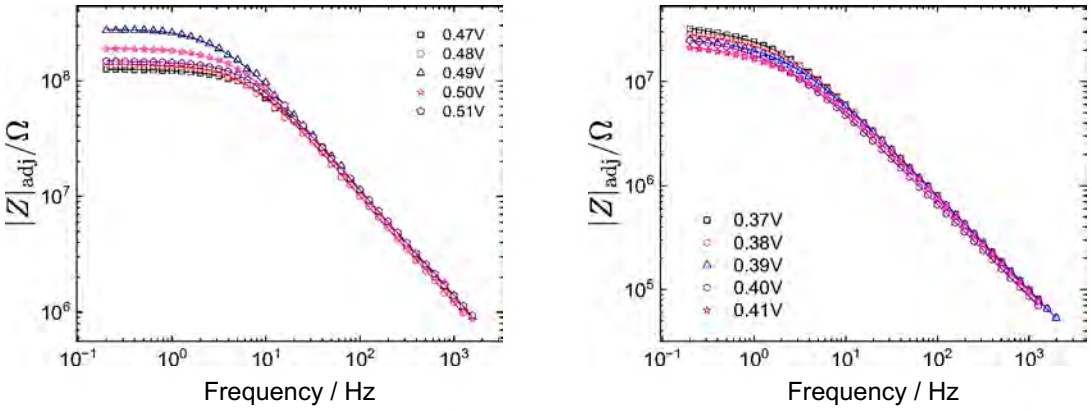

(a) (b)

Figure 9-7. Measurement model (equation (2-19)) regression results for impedance spectra of platinum ultramicroelectrodes with potential as a parameter: a) and b) ohmic-resistance-corrected magnitude for 10 m, and 25 m. Potential measured with reference to the silver/silver chloride (Ag/AgCl) electrode.

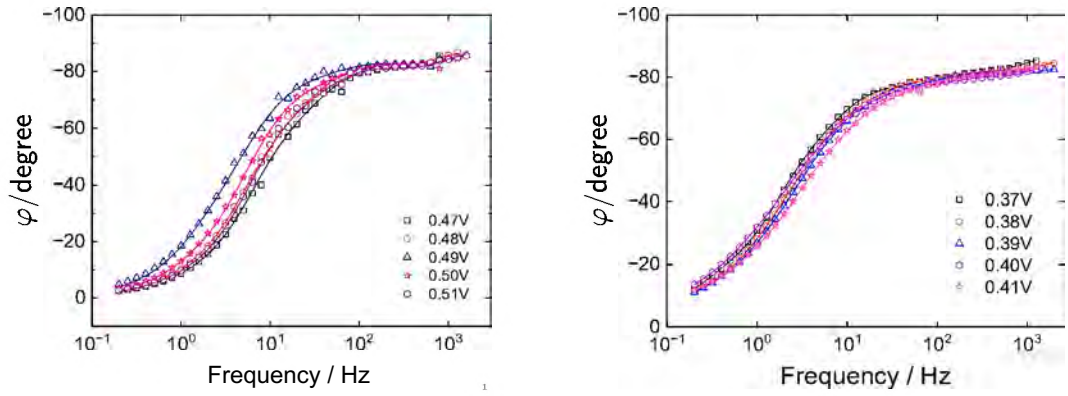

(a) (b)

Figure 9-8. Measurement model (equation (2-19)) regression results for impedance spectra of platinum ultramicroelectrodes with potential as a parameter: a) and b) ohmic-resistance-corrected phase angle for 10 m, and 25 m. Potential measured with reference to the silver/silver chloride (Ag/AgCl) electrode.

phase angle $_{Re}$ is expressed in terms of real and imaginary impedance as

$$_{adj} = \frac{180}{} \quad .1\left(\frac{j}{_{r} - _{e}}\right) \tag{9-3}$$

where the constant-phase element exponent, is related to the phase angle, $_{adj}$ as

$$= \frac{- _{adj}}{90} \tag{9-4}$$

the corrected phase angle for the 10 m Platinum electrode is shown in Figure 9-8(a). The impedance behavior at different potentials have similar trends and approaches -90^0 at high-frequency points. The impedance response at low-frequency points suggest mass-transfer-influenced faradaic reactions. The resulting ohmic-resistance-corrected phase angle plots for the 25 m Platinum electrode is presented in Figure 9-8(b). The impedance response of the open-circuit potential (OCP) and potentials at ± 2 OCP and ± 1 OCP, overlapped at all frequency points. The impedance data for the 10 m and 25 m Platinum electrodes were regressed with values between 0.8 and 0.99, which confirms the constant-phase-element behavior of the electrodes. For a system that behaves like a pure capacitor, the value of is 1.

9.3.6 Process Model Regression for Platinum

The process model described by equation (6-3) provided a good fit within the 94.5% confidence interval for the impedance spectroscopy data of the 10 m and 25 m Platinum-disk ultramicroelectrodes. Sample regression results for the impedance spectra of the 10 m ultramicroelectrodes measured at 0.48 V are shown in Figure 9-9. The Nyquist, magnitude, and phase angle plots in Figures 9-9(a), 9-9(b), and 9-9(c) demonstrate strong agreement between the measured data across the full frequency range. The normalized residual plots for both the real and imaginary components shown in Figures 9-9(d) and 9-9(e) yielded error residuals which fall within the ±2 confidence intervals represented as dashed lines in each plots. The residual errors suggest no systematic deviation, and confirms the adequacy of the regressed model. The model

accounted for the constant-phase-element behavior of the electrode, the ohmic resistance, and oxygen-reduction reaction influenced by mass transfer.

The fit of the process model defined by equation (6-3) to the impedance spectra of the 25 m platinum ultramicroelectrode is shown in Figure 9-10. The resulting Nyquist plot presented in Figure 9-10(a), demonstrates strong agreement between the experimental data (red triangles) and the fitted model (solid line) over the entire frequency range. Figures 9-10(b) and 9-10(c) present the Bode magnitude and phase angle plots, respectively, both of which further highlight the close agreement between measured and modeled impedance responses at all frequency points.

As illustrated inn Figures 9-10(d) and 9-10(e), the normalized residuals for the real and imaginary impedance components are plotted as a function of frequency. The residuals remain within the ±2 confidence interval represented as dashed lines, indicating the regressed parameters are statistically significant. This result confirms both the quality of the fit and the adequacy of the process model in describing the electrode's impedance behavior. The parameters estimated from fitting the impedance spectra of the 10 m and 25 m electrodes measured at 0.48 V and 0.39V are provided in Tables 9-2 and 9-3. These values were evaluated for statistical significance using the ^{2} / criterion, where denotes the degrees of freedom and ^{2} is the chi-square error. For a statistically valid model fit, ^{2} / approaches 1. The values reported in Tables 9-2 and 9-3 lie within the ±2 confidence interval and does not include zero, confirming the statistical significance of the parameters.

Table 9-2. Parameter estimates for the regression of the process model given as equation (6-3) to the impedance data of 10 m platinum ultramicroelectrode. Confidence intervals reported are ±1 .

Parameter	Unit	Value
R_d	MΩ	1.82 ± 0.23
Q	F s$^{(\ -1)}$	0.0002400 ± 0.0000025
	–	0.9294 ± 0.0018
R_e	MΩ	0.329 ± 0.015
R_{tc}	MΩ	13.80 ± 0.18
^{2}/	–	2
Calculated values		
C_{dl} (equation (7-34))	Fcm^{-2}	151.76 ± 3.41

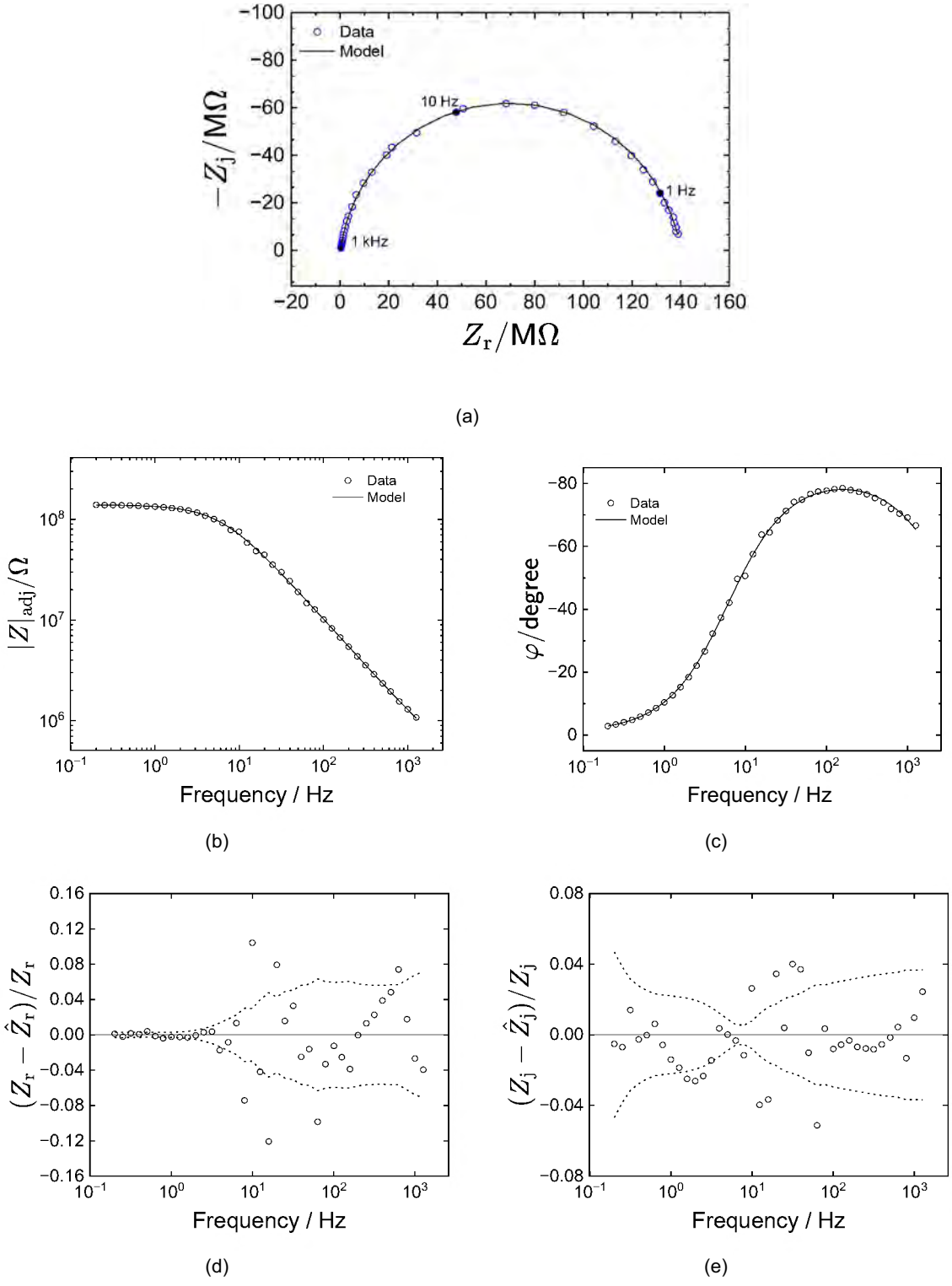

Figure 9-9. Process model regression results for the impedance spectra of 10 m platinum electrode measured at 0.48 V: a) Nyquist plot, b) impedance magnitude, c) phase angle, d) real residuals, and e) imaginary residuals. The lines represent the fit of the process model given as equation (6-3). The dashed lines represents the 95.4% (±2) confidence interval.

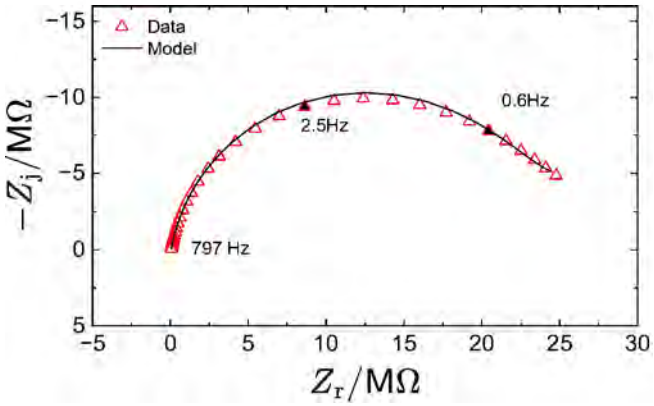

(a)

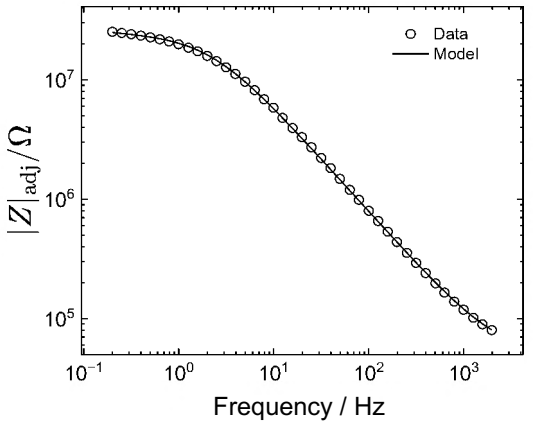

(b)

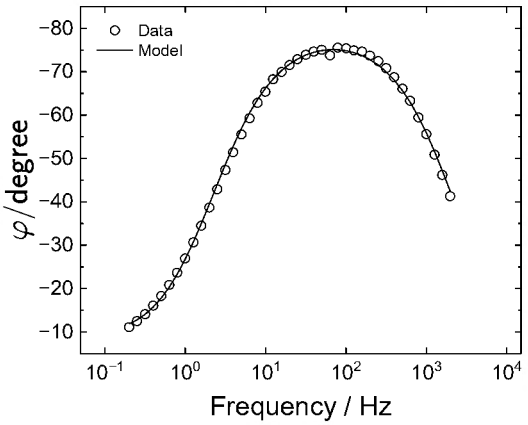

(c)

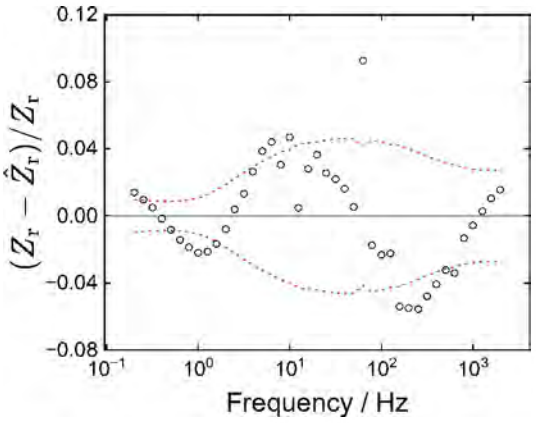

(d)

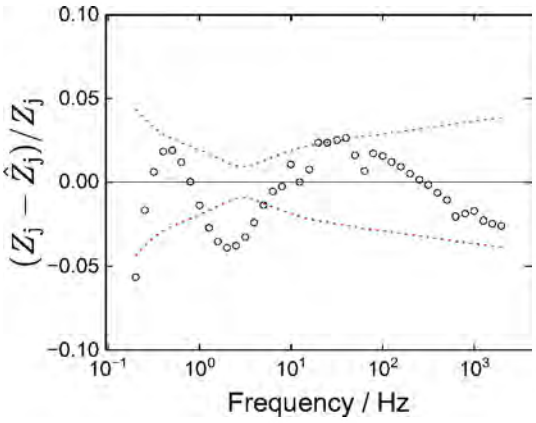

(e)

Figure 9-10. Process model regression results for the impedance spectra of 25 m platinum electrode measured at 0.39 V: a) Nyquist plot, b) impedance magnitude, c) phase angle, d) real residuals, and e) imaginary residuals. The lines represent the fit of the process model given as equation (6-3). The dashed lines represents the 95.4% (±2) confidence interval.

Table 9-3. Parameter estimates for the regression of the process model given as equation (6-3) to the impedance data of 25 m platinum ultramicroelectrode. Confidence intervals reported are ±1 .

Parameter	Unit	Value
R_d	MΩ	3.55 ± 0.14
Q	F s$^{(-1)}$	0.004080 ± 0.000042
	–	0.8915 ± 0.0017
R_e	MΩ	0.04973 ± 0.00077
R_{tc}	MΩ	23.60 ± 0.11
^{2}/	–	54
Calculated values		
C_{dl} (equation (7-34))	Fcm^{-2}	294.81 ± 6.32

9.4 Discussion for Platinum

The parameters extracted from process model regression of the impedance spectra of 10 m and 25 m Platinum-disk ultramicroelectrodes were evaluated as functions of potentials. The capacitance calculated from the measurement model was compared to the values obtained by converting the constant-phase-element parameters to double layer. The results provide an understanding of the properties of the electrode.

9.4.1 Regressed Parameters as a Function of Potential

The parameters extracted from the regression of the process model to the impedance spectra of 10 m platinum ultramicroelectrode are summarized in Figure 9-11 as a function of applied potential. The error bars represent one standard deviation. The resulting ohmic resistant, R_e are shown in Figure 9-11(a). The values remain nearly constant across the potential range from 0.244 ± 0.018 Ωcm^2 to 0.258 ± 0.012 Ωcm^2, indicating stable electrolyte conductivity and negligible change in ohmic drop during measurement. As illustrated in Figure 9-11(b), the CPE coefficient, Q exhibits a slight decrease from 310.79 ± 3.18 F/cm^{2}S $^{-1}$ to 269.88 ± 2.83 F/cm^{2}S $^{-1}$ with increasing potential, suggesting a reduction in the effective double-layer charging capacity. The CPE exponent, presented in Figure 9-11(c) increased from 0.926 ± 0.002 and 0.932 ± 0.002 , reflecting constant element behavior of the electrode across various potentials. The diffusion resistance, R_d plotted in Figure 9-11(d) shows a moderate dependence on potential, with a high value at open-circuit potential of 0.49 V. The variation of the charge-transfer resistance, R_{tc} is

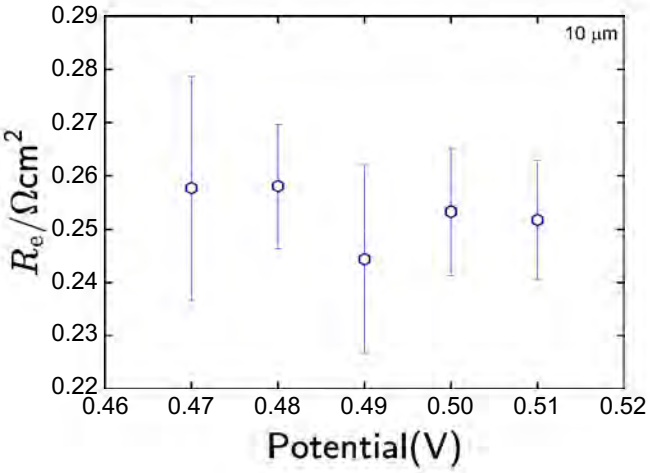

(a)

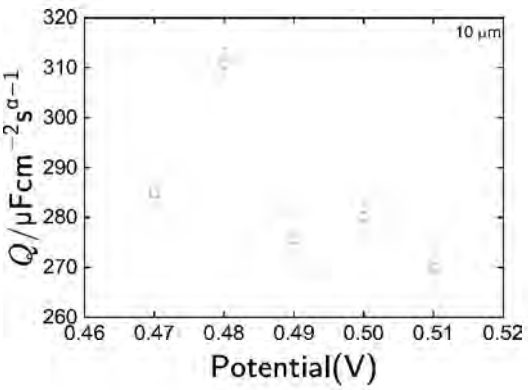

(b)

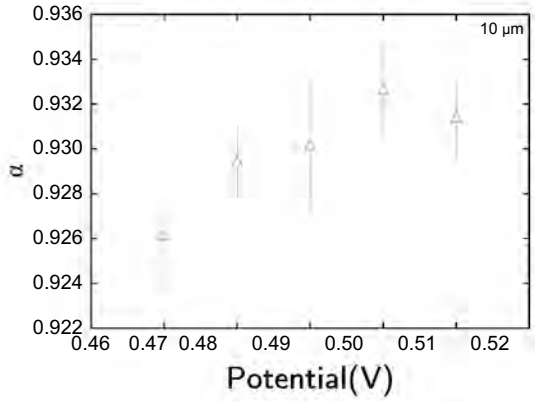

(c)

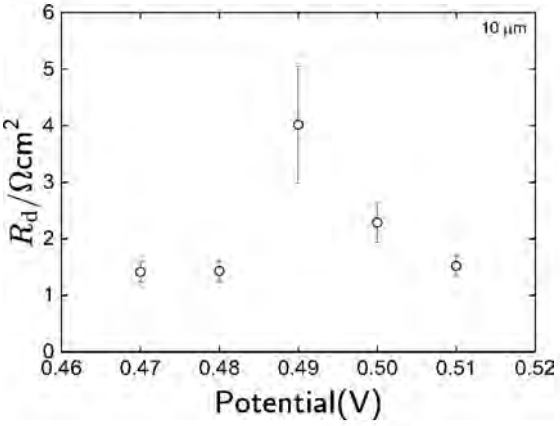

(d)

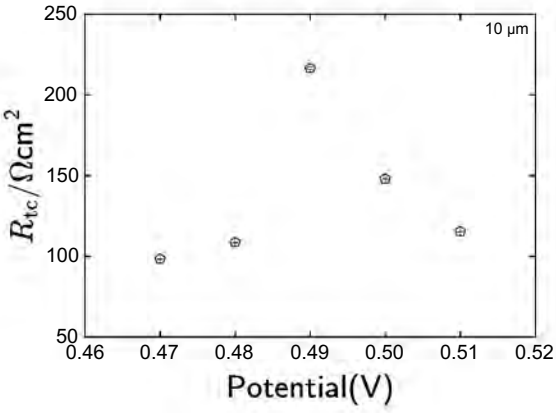

(e)

Figure 9-11. Parameter estimates for the regression of the process model given as equation (6-3) to 10 m platinum ultramicroelectrodes: a) ohmic resistance, R_e; b) CPE coefficient, Q; c) CPE exponent, ; d) diffusion resistance, R_d; e)ohmic resistance, R_{tc}. Error bars represent one standard deviation.

shown in Figure 9-11(e). The values varied with increasing potential from 98.35 ± 0.144 Ωcm^2 to 216.48 ± 0.801 Ωcm^2.

The parameters obtained from the regression of the process model to the impedance spectra of 25 m platinum ultramicroelectrode are shown in Figures 9-12 as a function of applied potential. The variation of ohmic resistance, R_e are illustrated in Figure 9-12(a), which remains relatively constant across the potential range, suggesting stable electrolyte conductivity and negligible potential-dependent effects on the ohmic resistance. The resulting CPE coefficient, Q shown in Figure 9-12(b) exhibits a slight upward trend from 789.29 ± 6.48 F/cm^2S^{-1} to 1142 ± 15.68 F/cm^2S^{-1} with increasing potential. The CPE exponent, plotted in Figure 9-12(c), retains values between 0.867 ± 0.002 and 0.895 ± 0.001, implying that the electrode–electrolyte interface shows constant-phase behavior.

The diffusion resistance, R_d shown in Figure 9-12(d) demonstrates moderate variability, with a mild decrease at higher potentials, suggesting that charge-transfer kinetics become more favorable as the electrode potential increases. As illustrated in Figure 9-12(d) the charge-transfer resistance, R_{tc} generally decreases from 149.15 ± 0.58 Ωcm^2 to 94.54 ± 0.65 Ωcm^2. with increasing potential, consistent with potential-driven acceleration of faradaic processes at the platinum electrode.

9.4.2 Capacitance as a Function of Potential

The impedance data of the 10 m and 25 m Platinum-disk ultramicroelectrodes were obtained at different potentials. The effective double-layer capacitances were determined by regressing the measurement model (equation (2-19)) to the impedance spectra. The resulting capacitance estimated from the measurement model approach is defined by equation (7-32). Another method for estimating capacitance was converting the constant-phase-element (CPE) parameters to an effective double-layer capacitance using the Brug's [141] formula for surface distribution of time constant expressed as equation (7-34). The effective double-layer capacitances for the 10 m electrode as functions of potential are shown in Figure 9-13(a). The capacitance decreased from 151.76 ± 3.41 F/cm^2 to 133 ± 5.06 F/cm^2 with increasing

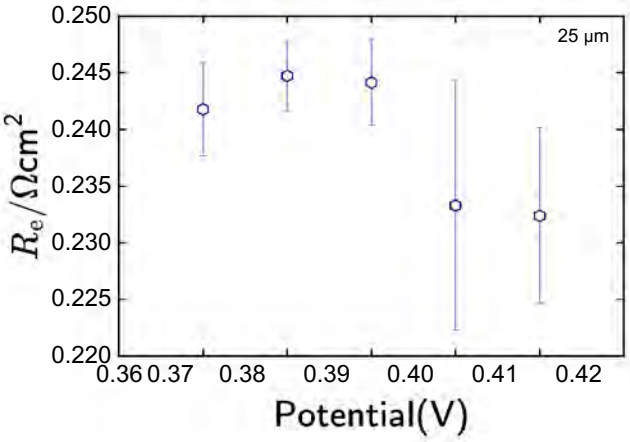

(a)

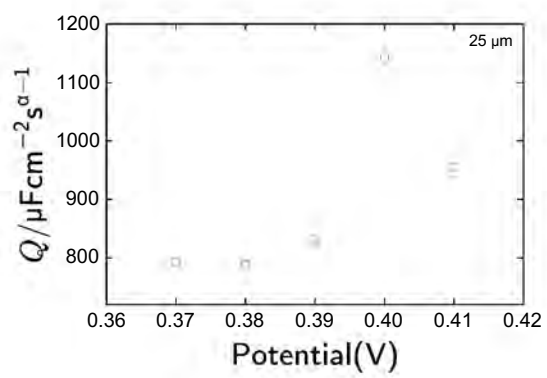

(b)

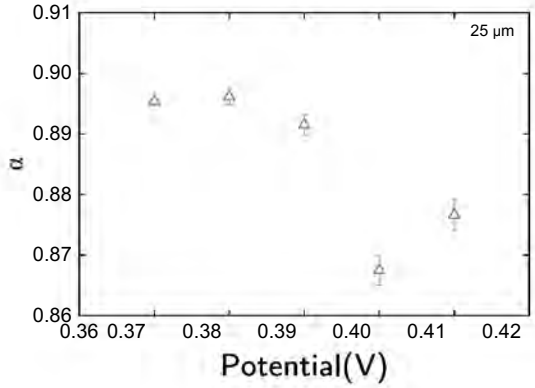

(c)

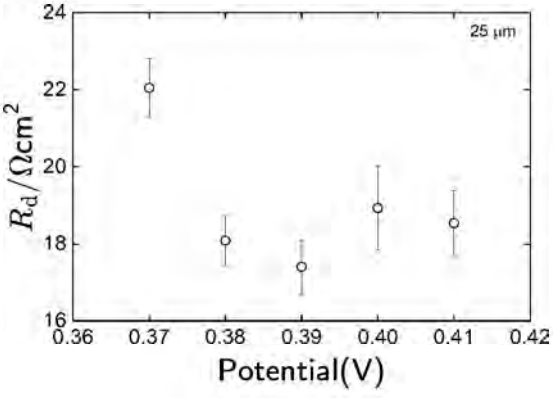

(d)

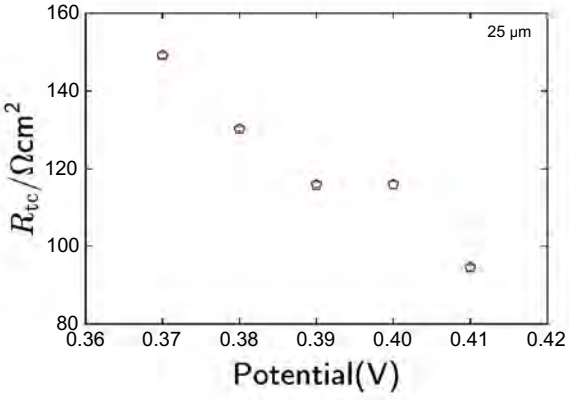

(e)

Figure 9-12. Parameter estimates for the regression of the process model given as equation (6-3) to 25 m platinum ultramicroelectrodes: a) ohmic resistance, R_e; b) CPE coefficient, Q; c) CPE exponent, ; d) diffusion resistance, R_d; e) charge-transfer resistance, R_{tc}. Error bars represent one standard deviation.

potentials. The capacitance extracted from the measurement model regression are similar to the double-layer values at different potentials, as shown in Figure 9-13(a).

The effective double-layer capacitance obtained for the 25 m platinum electrode at different potentials are presented in Figure 9-13(b). The capacitance values decreased from 343.98 ± 33.12 F/cm^2 to 280.08 ± 27.41 F/cm^2 across various potentials, as shown in Figure 9-13(b). The capacitance extracted from the measurement model correspond to these values at different potentials. For a double-layer capacitance, the nominal range of capacitance is between 10 F/cm^2 and 50 F/cm^2. The capacitance of the 10 m and 25 m platinum ultramicroelectrodes does not fall within the nominal range for double-layer. The values obtained for these electrodes suggest the influence of parasitic capacitance on their impedance spectra.

9.4.3 Statistical Results as a Function of Potential

The parameters extracted from the regression of the process model in equation (6-3) to the impedance spectra of the 10 m and 25 m platinum electrodes are statistically significant because the values lie within the 95.4% confidence interval (±2) and does not include zero. The double-layer capacitance $_{dl}$ was estimated for impedance spectra of 10 m and 25 m platinum electrodes using the constant-phase-element parameters and the ohmic resistance extracted from the process model regression. For each potential analyzed, the mean value of $_{dl}$ and its corresponding confidence intervals were determined using Brug's formula (equation (7-34)), based on the means and standard deviations of the regressed parameters such as , , and . These estimates were obtained through Monte Carlo simulation. The resulting normal distributions of the double-layer capacitance for the 10 m platinum ultramicroelectrodes are shown in Figure 9-14.

The mean value and standard deviation of $_{dl}$ for the impedance spectra of the 10 m platinum electrode obtained at open-circuit potential is shown in Figure 9-14(a). The estimated value was 133.94 ± 95 F/cm^2. The double-layer capacitance, $_{dl}$ for 0.51 V is presented in Figure 9-14(b). The result yielded a mean capacitance of 132.99 F/cm^2, with a standard

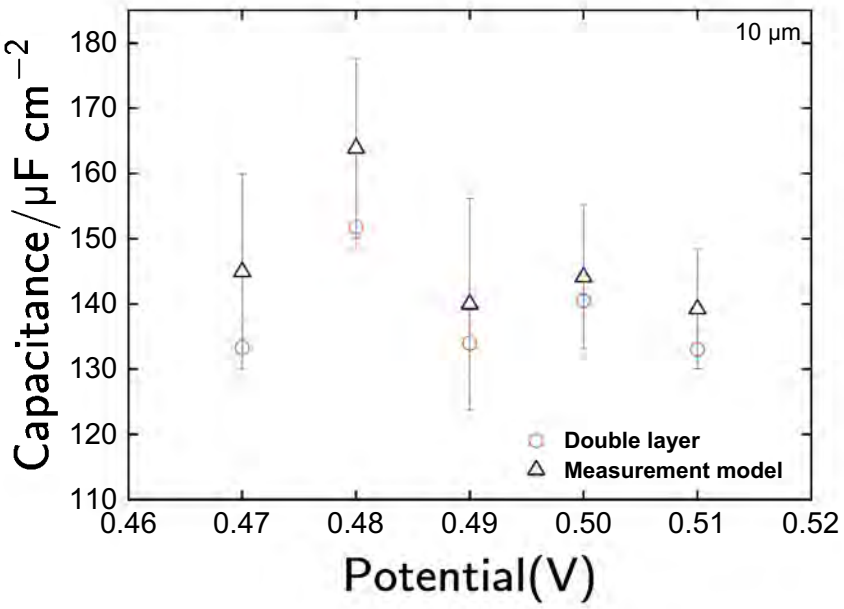

(a)

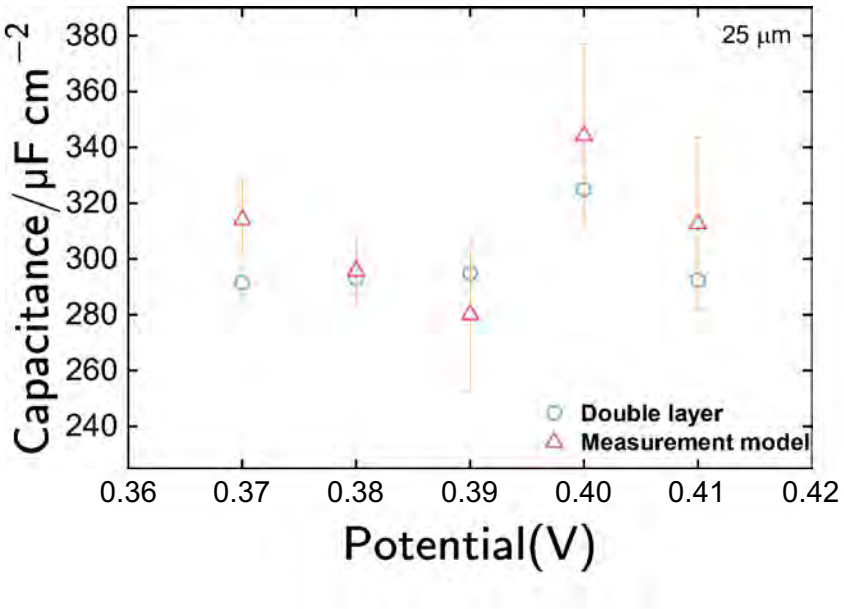

(b)

Figure 9-13. Effective double-layer capacitance as a function of potential: a) 10 m, and b) 25 m. The double-layer capacitance was estimated from equation (7-34). Error bars represent one standard deviation.

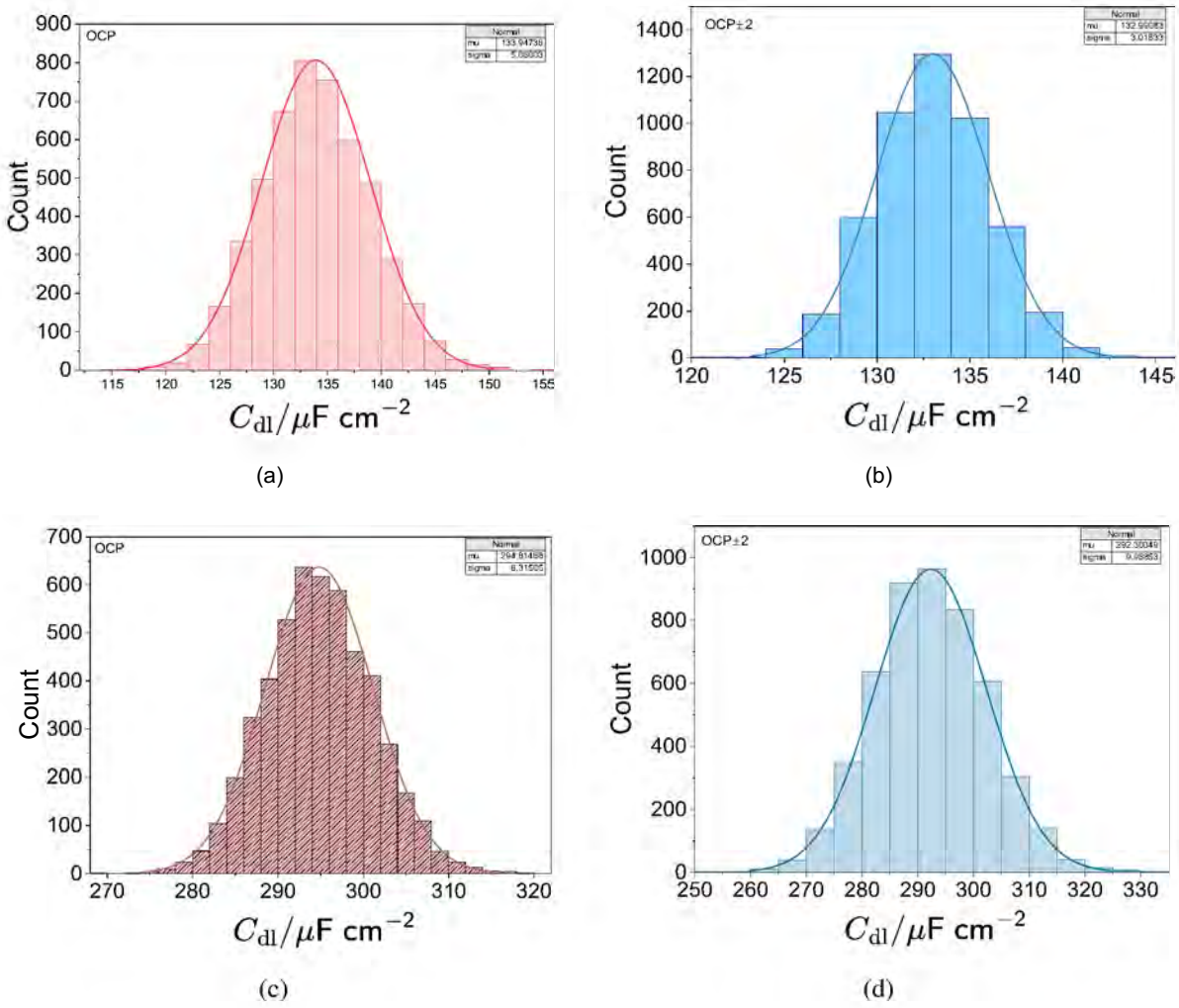

Figure 9-14. Process model regression results showing the normal distribution of the double-layer capacitance calculated from equation (7-34) for the platinum electrodes: a) and b) 0.49 V and 0.51 V for the 10 m^2 platinum electrode, c) and d) 0.39 V and 0.41 V for the 25 m^2 platinum electrode.

deviation of 3.02 F/cm^2. These values also fall within the range of $_{dl}$ calculated for potentials within ± as shown in Figure 9-13(a).

As illustrated in Figure 9-14(c), the $_{dl}$ estimated for the 25 m platinum electrode's impedance spectra collected at open-circuit potential is 294.81 ± 6.32 F/cm^2. A mean value and standard deviation of 292.30 ± 9.97 F/cm^2 was obtained for the impedance spectra measured at 0.41 V as shown in Figure 9-14(d). These results confirm the statistical significance of the extracted parameters at open-circuit potentials and validate the use of Brug's model to extract double-layer capacitance across different potentials. The histograms provide visual evidence of the normal distribution of estimated capacitance values, supporting the reproducibility of the interpretation model.

CHAPTER 10
FINITE-ELEMENT MODELING OF ULTRAMICROELECTRODES

Stimulation by ultramicroelectrodes is envisioned to enable precise control for activation of the target neural population. However, the corresponding large current densities can lead to adverse effects such as tissue damage, neural degeneration, inflammation, and electrode damage. By studying the charging and faradaic reactions of ultramicroelectrodes, we can optimize stimulation parameters to minimize these risks and maximize the effectiveness of neural stimulation. The goal of this chapter is to develop mathematical models that describe current and potential transients, as well as ohmic impedance, using parameters extracted from measurement model analysis.

Finite-element simulations are employed to investigate the ohmic impedance associated with mass-transfer-influenced oxygen reduction reactions and to validate results obtained from measurement model analysis of ultramicroelectrodes. A two-dimensional axisymmetric disk electrode geometry was used to model current and potential distributions under both faradaic and charging conditions. Laplace transforms were applied to formulate numerical models for the time-dependent response of ultramicroelectrodes to current and potential transients. The influence of mass transfer on a rotating disk electrode was simulated using COMSOL Multiphysics.

10.1 Numerical Methods

Numerical models for impedance response of primary and secondary current distributions, transient behaviors of non-uniform current and potential were developed using COMSOL Multiphysics ® 5.2 and 6.3. The hardware used was a 64-bit Dell TM Precision T7500 workstation with dual Intel ® E5620 2.4 GHz processors and 96GB of RAM. The model was built using AC/DC module. Finite-element models were combined with experiments to optimize electrochemical properties of neural-stimulation devices. Numerical models are developed to validate experimental results and impedance analysis. Multiphysics models are accurate when a range of operating conditions and physics are considered. Hence, models can be used to enhance the design and processes of every device in good operating conditions.

10.1.1 Geometry

The 2-dimensional axisymmetric disk electrode geometry shown in Figure 10-1 was used to develop finite-element models describing current and potential distributions. The model was defined in cylindrical coordinates (r, ,y) and consisted of three boundaries, including Γ_{WE} for the disk electrode, Γ_{C_E} for the counter electrode, and Γ_I for insulating surfaces. The working electrode was positioned at the y = 0 axis. The counter-electrode radius was set to be 3000 times larger than that of the working electrode and was sectioned at an angle of 90^0, as displayed in Figure 10-1. The large size difference between the working and counter electrodes was implemented to approximate an infinite separation between the two surfaces, minimizing boundary interaction effects.

10.1.2 Meshing

A non-uniform triangular mesh illustrated in Figure 10-2 was used to perform finite-element simulations. The mesh was coarser at the counter-electrode domain and finer at the working-electrode domain, allowing for accurate simulation of current and potential distributions.

10.2 Mathematical Development

Numerical models were developed to describe both the primary and secondary current distributions on a disk electrode. The time-dependent behavior of ultramicroelectrodes under current and potential transients was simulated using Laplace's equation. The ohmic impedance associated with mass-transfer-influenced oxygen reduction reactions was modeled using a rotating disk electrode geometry, where Laplace's equation was coupled with the convective–diffusion equations to account for simultaneous charge transport and mass-transfer effects.

10.2.1 Steady-state Nonuniform Current and Potential Distributions

Impedance responses are influenced by the distribution of current and potential at the electrode-electrolyte interface. Primary distribution means that electrolyte adjacent to the electrode has a uniform concentration and potential [122]. Assuming that concentration is uniform,

$$\overline{\overline{\nabla}} i = 0 \qquad (10\text{-}1)$$

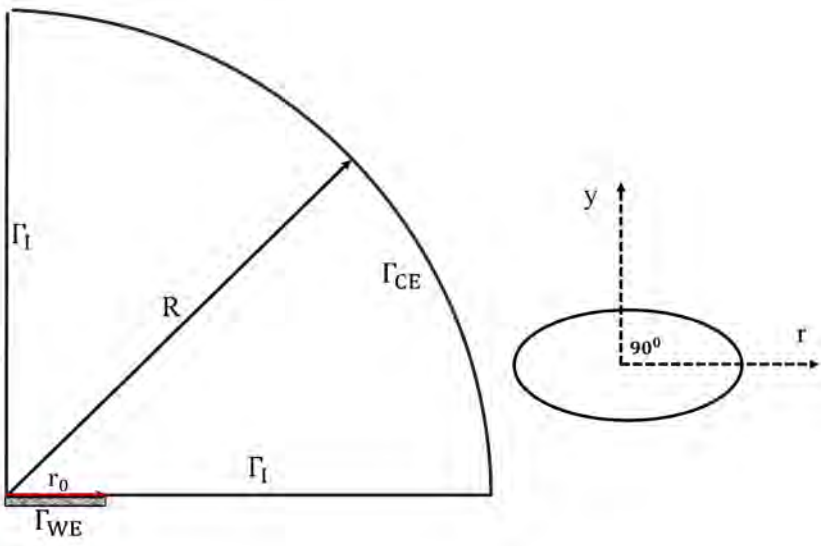

Figure 10-1. Schematic representation of rotating disk electrode geometry with boundaries labeled as Γ for the working electrode, Γ for the counter electrode, and Γ for insulating surfaces. R / $_0$ = 3000, and $_0$ = 1.0 cm.

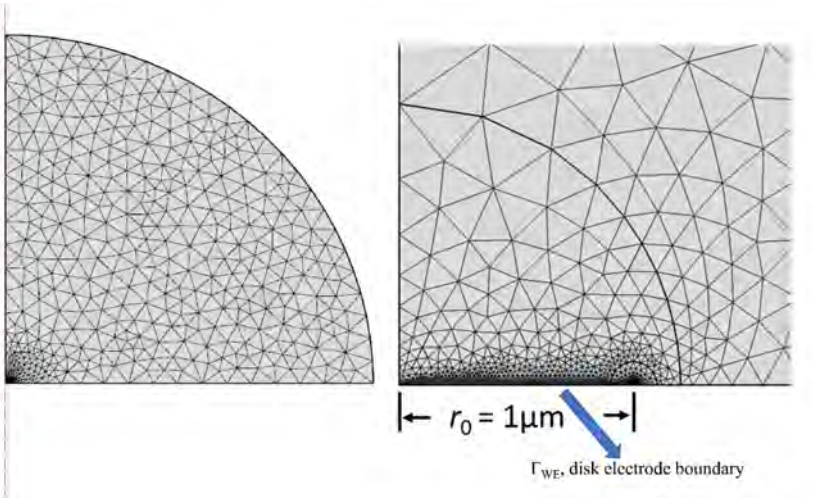

Figure 10-2. Schematic representation of non-uniform triangular meshing of the disk electrode geometry.

Hence, potential is governed by laplace equation

$$^2\Phi = 0 \tag{10-2}$$

current flow in the system is controlled by ohmic resistance $_e$. Primary current and potential distributions therefore occurs when ohmic resistance dominates and kinetic limitations are neglected. Only charging current plays a role in the system. For a disk electrode of radius r_0, embedded in an insulating plane and with a counter electrode infinitely far away, the primary current density is shown by Newman[120] as

$$\frac{}{} = \frac{1}{2\sqrt{1 - (\quad)^2_0}} \tag{10-3}$$

where is the area-averaged current density, and is the normalize current density distribution dependent on geometry. The corresponding primary resistance is the ohmic resistance expressed as

$$_e = \frac{1}{4 \quad 1 \quad 0} \tag{10-4}$$

The equation is modeled by assuming that the resistivity of the electrolyte is 0.1 Ωm.

10.2.2 Secondary Current Distributions

For secondary current distribution, kinetic effects are accounted for, and the potential within the electrolyte adjacent to the electrode is non-uniform $\Phi \neq 0$. In this case, both faradaic and kinetic processes influence the overall current behavior. The current density $_0$ is governed by Butler-Volmer or Tafel equation at the working electrode boundary.

$$_0 = \frac{\tilde{\Phi}}{\quad} \quad |_{y=0} = \quad (\quad) = - \quad \exp(- \quad _c(\quad _m - \quad _0)) \tag{10-5}$$

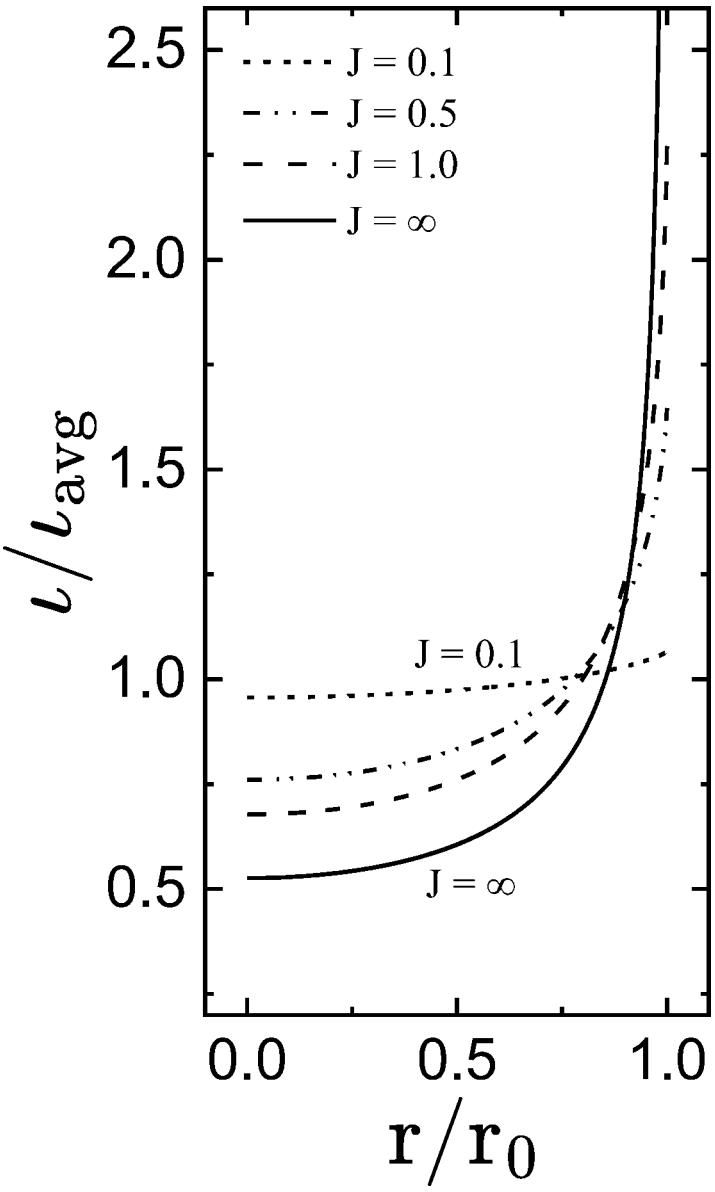

Figure 10-3. Secondary current distribution for linear polarization at a disk electrode with dimensionless current, J as a parameter.

where $_c$ is the kinetic parameter for cathode in the units of inverse potential expressed as

$$= \frac{F}{R} \tag{10-6}$$

where n is the no of electron transfer, F is the Faraday constant, T is the temperature, and R is the molar gas constant. For kinetic control, the current density is defined as

$$= {}_0\{\exp(\ _a \ s) - \exp(- \ _c \ s)\} \tag{10-7}$$

and for anodic and cathodic reaction, the dimensionless current density is described as

$$= \frac{(\ _a + \ _c) \ 0}{} \tag{10-8}$$

where $_a$ is kinetic parameter for anode in the units of inverse potential expressed as

$$= \frac{(1 - \ )}{_a} \tag{10-9}$$

is the conductivity of the electrolyte. l is the characteristic length of the electrode. l = $_0$, for a disk electrode. Hence, J can be expressed in terms of ohmic resistance $_e$ and charge-transfer resistance $_t$ as

$$= \frac{4}{_e \ _t} \tag{10-10}$$

and

$$_t = \frac{1}{\exp(- \ )} \tag{10-11}$$

The results obtained for the normalized current density as a function of the dimensionless radial position for a disk electrode, with dimensionless current, J as a parameter, is shown in Figure 10-3. For low J values of 0.1, the curve is relatively flat, indicating nearly uniform current density across the disk. Decrease in J values results in secondary current distributions. As J increases to 0.5, 1.0, and ∞, the curves shift upward and become more sharply peaked near the disk edge

($\frac{i}{i_0} \rightarrow 1$), with current density increasing rapidly at the periphery. For large J values, current is more concentrated near the disk edge suggesting ohmic resistance dominates and primary current distribution play a role. The present results are consistent with previous results obtained by Newman [116] for J values of 0.1, 0.5, 1.0, and ∞.

10.3 Transient Models

Ultramicroelectrodes offer significant advantages owing to their reduced geometric surface area, leading to lower absolute charge injection requirements and minimized tissue damage, while also benefiting from reduced impedance and improved selectivity for neural stimulation. A time-dependent model of secondary current and potential distribution was developed to evaluate the transient response of ultramicroelectrodes to potential and current step-changes. The numerical modeling approach was used to compliment the experimental investigation of the voltage transients that occur immediately after current pulsing. As reviewed by Cogan [42] potential transient measurements are critical for understanding the maximum charge injection capacity in a current-controlled stimulation pulse as well as the maximum potential that can risk the safety of neural stimulation electrodes.

10.3.1 Time-dependent Response of Current to Potential Step-change

Numerical simulation of current transients to potential step-change was performed on a 2-D axisymmetric disk ultramicroelectrode geometry. The radius of the working electrode was 5 m, and a fine mesh was applied to the electrode boundary of the working electrode for accurate simulation of current response. Voltage transients in form of ramp, and rectangular step change were applied in the simulation and the corresponding faradaic and charging current were determined.

10.3.1.1 Ramp Model

The time-dependent potential step-change simulation was performed using a rapid ramp transient of 10^{-9}s as illustrated in Figure 10-4. The potential was stepped from -0.4V to -0.5V. As time increases, there is a steep rise in potential at a short time of 1 nanoseconds from -0.5V to -0.4V, followed by a new flat plateau where the potential stabilizes. The model was governed by

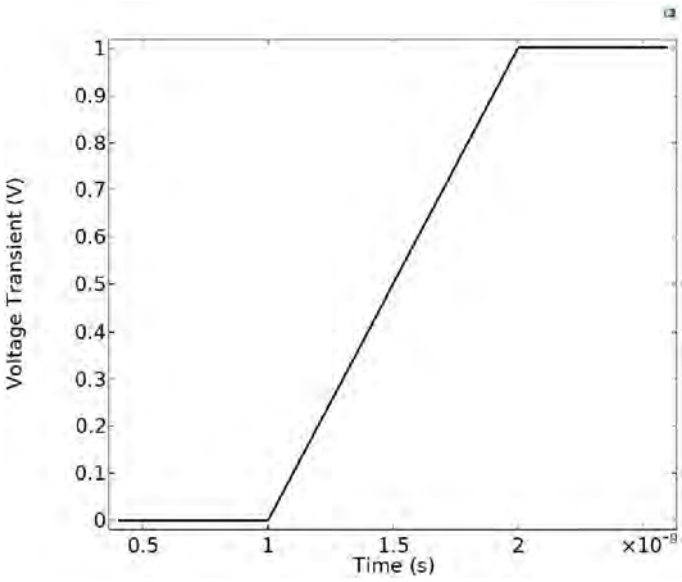

Figure 10-4. Schematic representation of ramp potential step-change from -0.4V to -0.5V for 1 nanoseconds.

nonlinear partial differential equations in the cylindrical coordinates. The conservation equation is described as

$$\frac{\partial c_i}{\partial t} = -\nabla \cdot \mathbf{N}_i + R_i \qquad (10\text{-}12)$$

where c_i is species concentration, t is the time taken for the reaction to occur, $\mathbf{N}_i$ is the flux of the species, and R_i is the homogeneous rate of the reaction. The flux of any given species is defined by

$$\mathbf{N}_i = -z_i F u_i c_i \nabla \Phi - D_i \nabla c_i \qquad (10\text{-}13)$$

where z_i is the number of charge, F is the Faraday constant, Φ is the electrical potential, D_i is the diffusion coefficient, and u_i is the mobility. the current density is expressed as

$$\mathbf{i} = F \sum_i z_i \mathbf{N}_i \qquad (10\text{-}14)$$

under the assumption of electroneutrality and charge conservation,

$$\cdot \mathbf{i} = 0 \tag{10-15}$$

and

$$\sum \quad = 0 \tag{10-16}$$

in the absence of concentration gradient, Laplace equation is expressed as

$$^2\Phi = 0 \tag{10-17}$$

and current density as a function if potential is expressed as

$$= - \quad \Phi \tag{10-18}$$

the total current at the electrode surface is determined by an integral expression, which can be written as

$$\int_0 \quad 2 \quad - \quad = 0 \tag{10-19}$$

a set of non-linear expression were used as the boundary condition for the ramp model. The total current density at the disk electrode boundary Γ_{WE} is given by a combination of faradaic and charging current transient responses, as shown below

$$_{total} = \quad _c(\quad) + \quad _F(\quad) \tag{10-20}$$

where the charging current density as a function of time is expressed as

$$_c(\quad) = \frac{\quad _0 \quad (\Phi_m - \Phi_0 - \quad (\quad))}{} \tag{10-21}$$

furthermore, the transient equation for faradaic current density is

$$F(\ ) = \exp(-\ (\Phi_m-\Phi_0-\ (\ ))) \quad (10\text{-}22)$$

where f(t) is the ramp change in potential given as

$$(\ ) = \Delta \times (10^{-9}) \quad (10\text{-}23)$$

the boundary condition on the counter electrode Γ_{CE} is

$$\Phi = 0 \quad (10\text{-}24)$$

where Φ is the reference potential and for the insulating surface Γ_I, the condition is given as

$$\mathbf{n}\Gamma_I \cdot \Phi_\Gamma \neq 0 \quad (10\text{-}25)$$

the time-constants associated with current transient response to potential step change was evaluated to determine the time to reach the maximum current.

10.3.1.2 Potential Step Model

Time-dependent current response to potential transient was studied using the rectangular step-change shown in Figure 10-5. The curve starts at 0 V, remains flat, and then sharply steps up to a value near 1.0 V at around 0.4 s were it remained stable until just after 0.6 s, and then sharply drops back to 0V, where it stays flat till 10 s. The flat portions before and after the pulse, together with the sharp rise and fall, are characteristic features of a potential step pulse. The model accounted for the cathodic reduction of oxygen on the surface of the ultramicroelectrode and the influence of concentration of dissolved oxygen on both charging and faradaic current transient responses to potential step change. The radius of the working electrode was 5 m. The governing equations are same with the ramp model presented in section 10.3.1.1. The boundary conditions

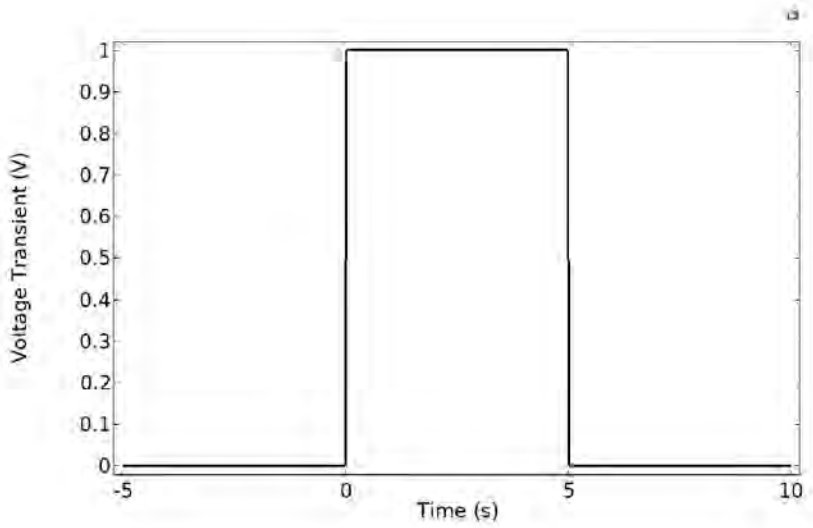

Figure 10-5. Schematic representation of the rectangular potential step-change from 0 V to 1 V for 10 s.

consists of a set of non-linear equations. As shown in Figure 10-1, the counter-electrode, Γ_{CE} boundary conditions is defined by equation 10-26 and

$$\text{Bulk} = \text{O}_2 \tag{10-26}$$

the conditions at the insulating surface, $\Gamma_{}$ is expressed as 10-25. At the working electrode boundary, Γ_{WE} the total current transient response is governed by equation 10-20, the time-dependent charging current is defined by equation 10-21, the transient expression for faradaic current density is expressed as

$$F(\ ) = -\ c\ \text{O}_2(0) \exp(-\ c(\Phi_m - \Phi_0 -\ (\ ))) \tag{10-27}$$

where $c_{O_2}(0)$ is the rate of concentration of Oxygen at the electrode surface. The total flux for reacting species in electrochemical reactions is defined by

$$N_{O_2\Gamma_{WE}} = \frac{i}{nF} \qquad (10\text{-}28)$$

where n is the number of electrons in the electrochemical reactions and F is the Faraday constant.

10.3.2 Simulation Results

Numerical simulation was performed for potential transient to calculate the transient response of charging and faradaic current densities and the total current.

10.3.2.1 Response to Ramp Step-change

The simulation results for current transient responses to the ramp potential step-change plotted in Figure 10-4, are shown in Figure 10-6. The resulting charging current density exhibits an initial rise at 0 seconds followed by an exponential decay toward 0 Acm^{-2}, as shown in Figure 10-6(a). This exponential decay corresponds to the rapid charging of the double layer which stabilizes at equilibrium where no net capacitive current flows, and only the faradaic current is observed. As illustrated in Figure 10-6(b), the potential drops sharply from -0.4 V and then reaches steady state value of -0.5 V as time increases. The faradaic current density initially rose to -5 $mAcm^{-2}$ and then decays toward a steady-state value of -15 $mAcm^{-2}$, as depicted in Figure 10-6(c). This short time suggests very rapid electron transfer or diffusion processes.

The time-constant behavior of current and potential responses shown in Figure 10-6 can be interpreted. The time-constant of potential responses to current density control is characterized by charge-transfer resistance R_t and is independent of disk radius. Potential changes depend on faradaic reactions, and time-constants for the faradaic reaction are expressed as

$$t = 0 \quad t \qquad (10\text{-}29)$$

where R_t is the charge-transfer resistant for linear kinetic on a disk electrode given by

$$_t = \frac{R}{F_{i\,0}} = \frac{1}{\exp(\ -\overline{)}} = \frac{2.303}{} \qquad (10\text{-}30)$$

where K is the rate constant, A is the area of the electrode, — is the potential difference between the electrode, and b is a constant. The time-constant of the current response to potential step-change is characterized by ohmic resistance R_e, which depends on the radius of the disk electrode and the time-constant of charging the electrode surface as

$$_c = \ 0 \ e \qquad (10\text{-}31)$$

where R_e is the ohmic resistance, given for a disk electrode in the unit of ohms

$$_e = 4\frac{0}{} \qquad (10\text{-}32)$$

Where is the electrolyte conductivity. Based on the results, we can interpret the influence of disk size on electrochemical behavior. First, small disk electrodes reduce ohmic resistance and increase charging. Smaller disk electrodes decrease the influence of ohmic impedance by expanding usable frequency.

10.3.2.2 Response to Rectangular Step-change

The electrochemical kinetics and mass-transfer response to a rectangular step-change in electrode potential from 0 V to 1 V are shown in Figure 10-7. The plot suggest the effects of electrode polarization and concentration at the electrode interface. As shown in Figure 10-7(a), the double-layer potential response is a square wave, which initially rose to a value of 0.6 V and then drops to 0.5 V after a steady state period of 5 s. The rate of concentration of Oxygen at the electrode surface, $c_{O_2}(0)$ is illustrated in Figure 10-7(b). The surface concentration show similar response with the potential step, but mass-transfer limitations cause the surface concentration to lag behind the bulk. This lag suggests fast electron transfer in the system. The time-dependent

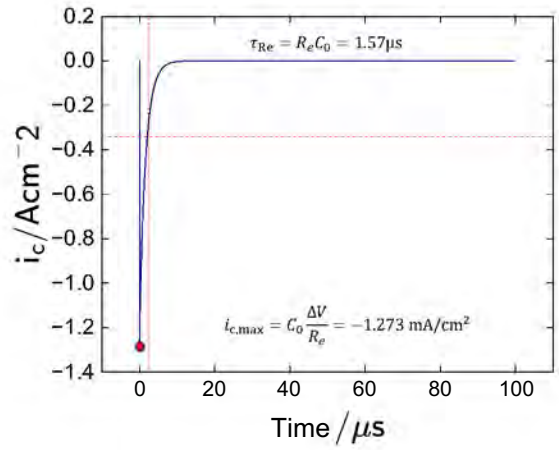

(a)

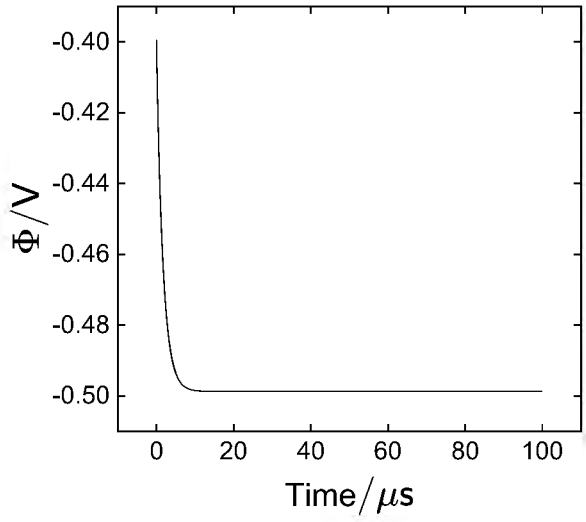

(b)

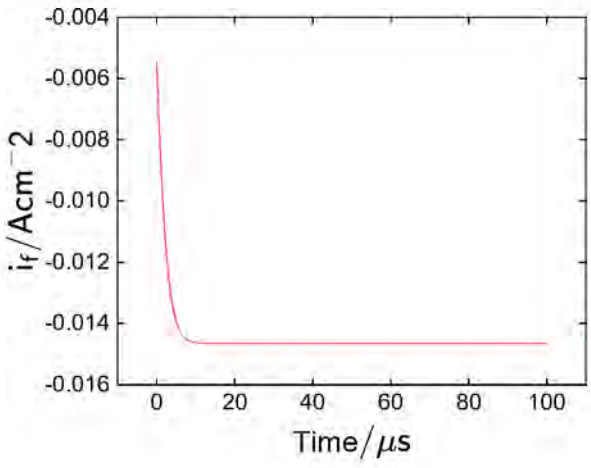

(c)

Figure 10-6. Transient response of charging and faradaic currents to a 0.1 V step-change in potential: a) charging current density, b) double layer potential response, c) faradaic current density response.

response of the normalized surface concentration are shown in Figure 10-7(c). The normalized surface concentration sharply approaches unity, indicating that the surface concentration is rapidly recovered but not instantaneously.

The time-dependent current responses to a rectangular step-change in potential influenced by mass transfer is shown in Figure 10-8. The charging current, I_c presented in Figure 10-8(a) showed a sharp spike which dropped quickly and returned to zero after the electrode surface charges. The sharp, narrow current pulse suggests effective double-layer capacitance and fast system relaxation. The faradaic current presented in Figure 10-8(b), I_F increase rapidly to a quasi-steady value of -0.00025 pA during the potential step and then drops after 5 seconds to a steady value as depicted in Figure 10-8(c), the total current, I_T expressed as the sum of charging and faradaic currents shows sharp initial transients similar to the charging current pulse and a slower plateau.

10.3.3 Transient Response of Potential to Current Step-change

Finite-element simulation of voltage transient response to current was performed to evaluate the safe potential limits for ultramicroelectrodes for neural stimulation. Two approaches were used for current pulsing, including the ramp and the biphasic pulsing. The biphasic current transients were archived with a piecewise function in COMSOL multiphysics.

10.3.3.1 Ramp Current Pulse

The initial and final current response corresponding to the ramp step-change in potential shown in Figure 10-4 were used for the simulation. The final current was 1.7 nA/cm^2, and the initial current was 2.9 nA/cm^2. The disk ultramicroelectrode of radius 1 m was used for the finite-element modeling. The Laplace transform model was simulated such that as time increases, the current exhibits a steady-state behavior after every 10 seconds. The governing equations for current is summarized in section 10.3.1.1. The governing equations for potential transient response to the current step-change at the working electrode boundary Γ_{WE} is given as

$$\Phi_m = \text{total}(t) + \Phi_0 + ( ) \qquad (10\text{-}33)$$

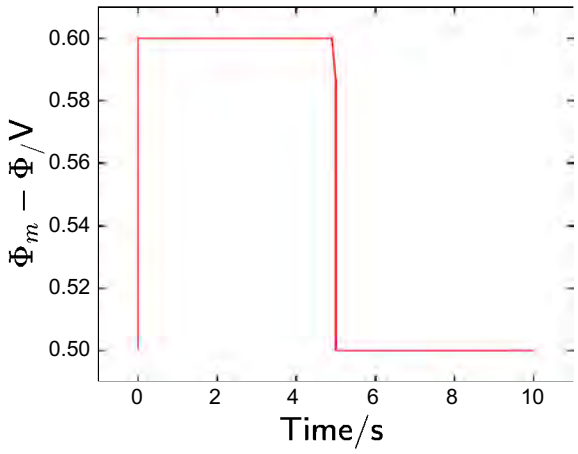

(a)

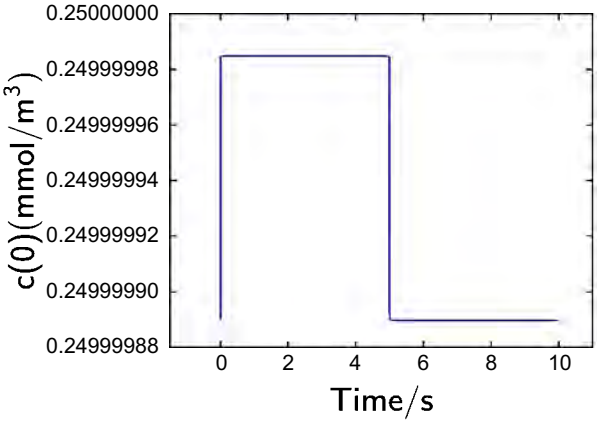

(b)

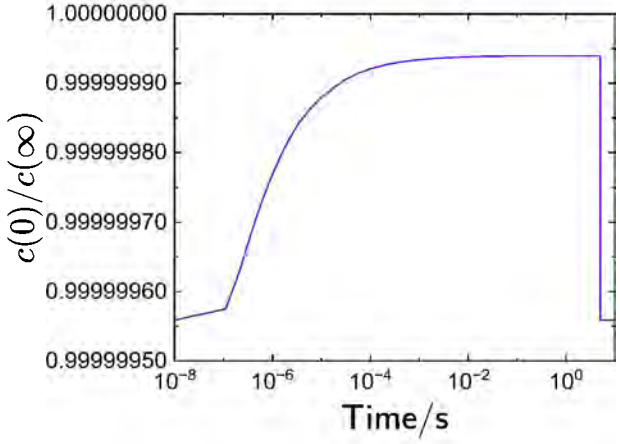

(c)

Figure 10-7. Transient response of potential and concentration to a rectangular step-change in potential. a) double-layer potential, b) rate of surface concentration, c) normalized concentration.

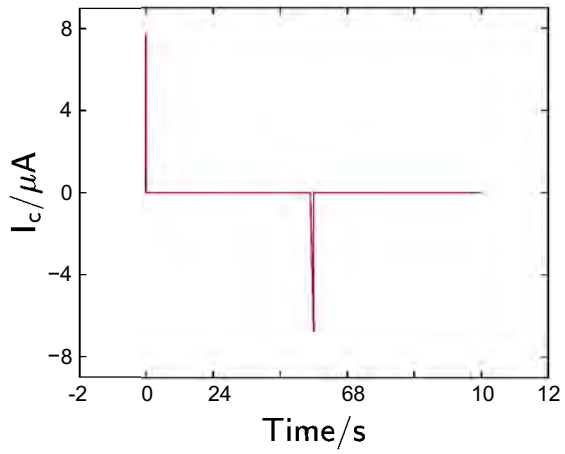

(a)

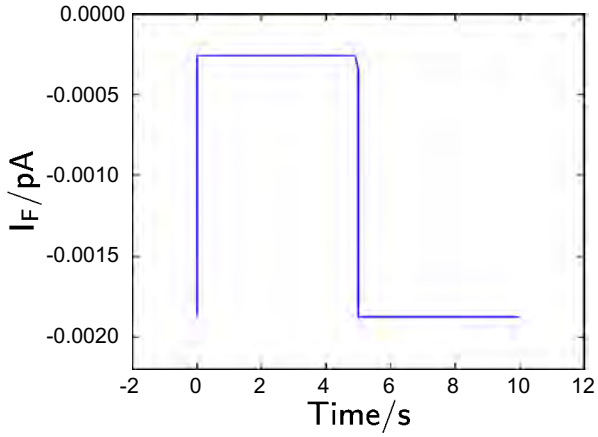

(b)

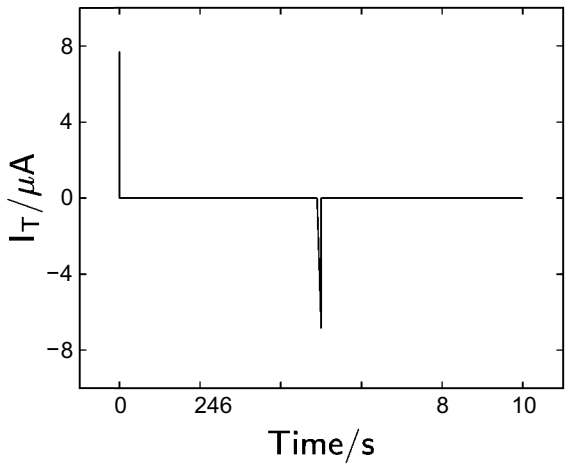

(c)

Figure 10-8. Transient response of charging and faradaic currents to a rectangular step-change in potential. a) charging current, b) faradaic current, c) total current.

where $_{.}(\ )$ is the ramp step-change in current given as $(_{.}) = \Delta$. The boundary condition on the counter electrode Γ_{C_E} is

$$\Phi = 0 \tag{10-34}$$

at the insulating surface Γ is

$$\Gamma_{I}.\ \Phi\Gamma_{I} = 0 \tag{10-35}$$

The results of the voltage transient response to ramp step-change in current is illustrated in Figure 10-9. The charging current density shown in Figure 10-9(a), displays an initial value of 9.09 $mAcm^{-2}$, then rapidly drops to zero. This fast decay suggests the rapid dissipation of the charging current, leaving only the faradaic current as shown in 10-9(a). As illustrated in Figure 10-9(b), the electrode potential showed a step drop from -0.4 V to -0.5 V where it reached an exponential plateau at steady-state overpotential. The faradaic current density initially rose to -5 $mAcm^{-2}$ and then approaches a steady-state value of -15 $mAcm^{-2}$, as depicted in Figure 10-9(c). This short time suggests very rapid electron transfer or diffusion processes.

10.3.3.2 Biphasic Current Pulse

The mathematical models for voltage transient response of ultramicroelectrodes to biphasic symmetric current pulsing was governed by the previous work of Cogan [42]. The voltage transient response are evaluated to identify the maximum positive and negative polarization across the electrode/electrolyte interface. A disk ultramicroelectrode with a radius 10 m was used for the simulation. The biphasic current pulse was performed with a piecewise function from 0 to 2 ms, as shown in Figure 10-10. The input parameters used for the finite-element modeling were extracted from the process model (equation (7-2)) regression to the impedance spectra of a 20 m diameter ultramicroelectrode from the G2 device.

A double-layer capacitance value of 4 $mFcm^{-2}$ estimated for the 20 m diameter electrode was used for the simulation. As illustrated in Figure 10-10, the biphasic current pulse starts at an initial zero-current baseline, and is stepped to a current value of -100 A, then return to zero and back to a positive current pulse of 100 A and finally top 0. The biphasic pulsing is selected for

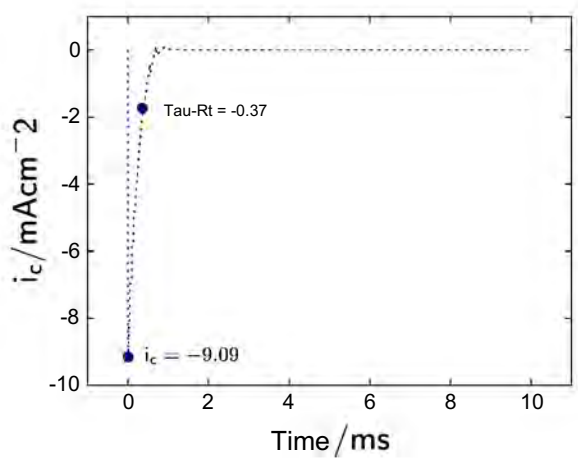

(a)

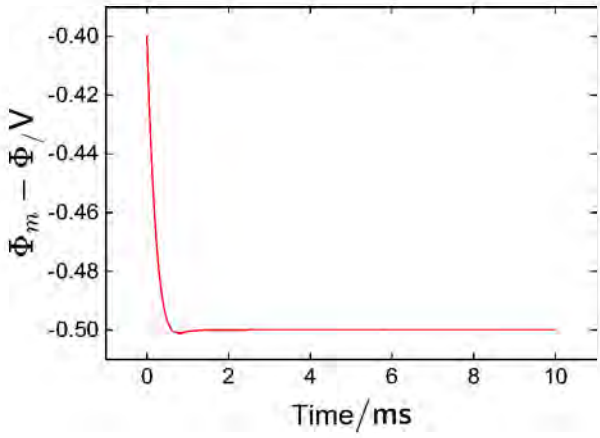

(b)

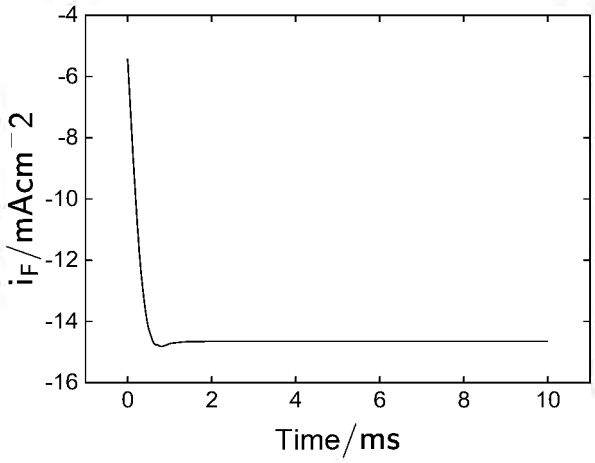

(c)

Figure 10-9. Transient response of current and potential to ramp step-change in current: a) charging current density b) faradaic current density, c) double-layer potential.

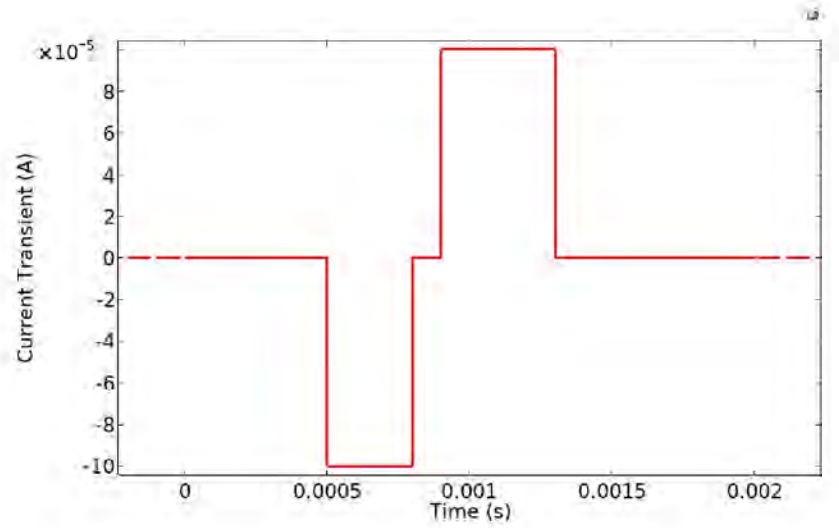

Figure 10-10. Schematic representation of the biphasic current pulsing.

accurate control of the charge delivered per phase. The governing equations for current is summarized in section 10.3.1.1 and the potential transient equations are discussed in section 10.3.3.1.

The detailed electrochemical response of the system to the biphasic current pulse (Figure 10-10), are presented in Figure 10-11. The biphasic waveform consists of a negative current pulse of -100 followed by a positive pulse of equal magnitude. The resulting electrode potential shows a similar biphasic response with negative peak immediately followed by a positive peak, as shown in Figure 10-11(a). The charge transfer resistance, R_{tc} presented in Figure 10-11(b) transiently drops during the negative phase, then stabilizes during the positive pulse, suggesting minor changes in electrochemical kinetics during current pulsing. The faradaic current, I_F dips in the negative direction as expected from the initial cathodic current pulse, then returns back to a positive region in response to the anodic current pulse, as shown in Figure 10-11(c), suggesting slow redox electrochemical kinetics. The charging current, I_c shows a sharp symmetric response to both anodic and cathodic pulsing as depicted in Figure 10-11(d). The resulting rise and fall with each phase suggests double-layer process, with delays after each current reversal. The total

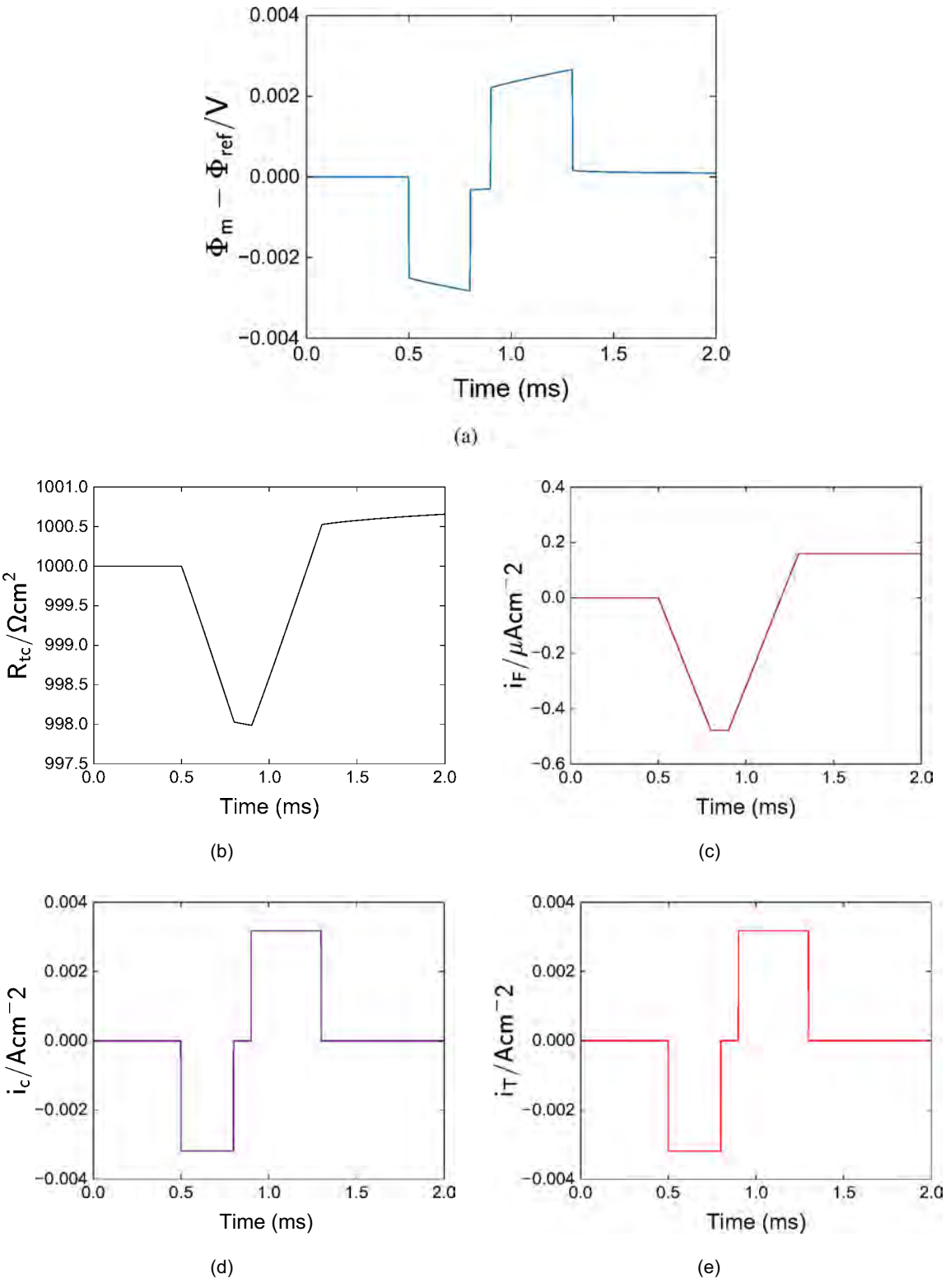

Figure 10-11. Transient response to current biphasic pulsing for 2 ms: a) double-layer potential, b) charge-transfer resistance, c) faradaic current, d) charging current, and e) total current.

current follows a biphasic square wave at both negative and positive current pulsing as illustrated in Figure 10-11(e). The total current is the sum of both faradaic and charging current hence, the response of the total current is dominated by double-layer charging.

10.4 Mass Transfer on Disk Ultramicroelectrodes

Finite-element simulation was used to model the influence of mass transport on non-uniform potential and current distribution. The model was developed with a rotating disk-electrode geometry. The rotating disk has an angular velocity Ω that drags the fluid to its surface. The fluid around the surface of the disk causes a velocity distribution in the radial direction due to the presence of centrifugal force. The domain of the geometry comprised a volume bounded by an area defined by the working electrode Γ_{WE}, the insulator which embeds the electrodes Γ_I, and the hemispherical counter electrode Γ_{CE} [6].

The rotating disk-electrode (RDE) geometry is used for mathematical modeling because laminar flow at the rotating disk-electrode surface transports a steady flow of material from the bulk electrolyte to the electrode surface and forms a stagnant layer called the hydrodynamic boundary layer. The electrolyte close to the electrode surface rotates at the speed of the rotating disk electrode. In contrast, the bulk electrolyte far away from the electrode becomes well-mixed and well-stirred by convection-induced rotation. Hence, convection-diffusion concepts can mathematically explain the total motion of materials that forms the bulk electrolyte to the electrode surface. The stirring from the electrode triggers the convectional rotation that causes the mass transport of ions and molecules from the bulk electrolyte into the stagnant layer. Subsequently, as the molecules enter the stagnant layer and get closer to the electrode surface, convection plays a lesser role, and diffusion becomes more significant. The final motion of materials to the electrode surface is dominated by diffusion across a very thin layer of electrolyte adjacent to the electrode called the diffusion layer [125].

The model was solved based on the assumption that species migration was absent due to vital supporting electrolytes and that the reactions were inhomogeneous. Vonkerman[126] and Cochran[127] developed continuous equations for incompressible fluid flow and used cylindrical

coordinates to derive velocity profiles. The dimensionless distance from the disk is given as

$$= \sqrt{\frac{\Omega}{\quad}} \tag{10-36}$$

where the radial and axial velocity components are:

$$_r = \Omega \ (\ ) \tag{10-37}$$

and

$$_y = \sqrt{\Omega} \ (\ ) \tag{10-38}$$

where is the viscosity of the fluid, Ω is the rotational speed. and are the radial and axial dimensionless velocities expressed in power series with dimensionless distance as

$$_0 = \quad + 2 \frac{1}{2} - 3 \ ^4 - \tag{10-39}$$

and

$$= - \quad ^2 + 1 - ^3 - \frac{^4}{36} \tag{10-40}$$

where a and b are coefficients, a =0.51023, b = -0.616 At distances very far away from the disk,

$$_\infty = \exp(- \quad) - \frac{^2 + ^2}{2 \ ^2} \exp(-2 \quad) + \frac{(\ ^2 + ^2)}{4 \ ^4} \ (-3 \quad) \tag{10-41}$$

$$_\infty = - \quad + \frac{2}{\quad} \exp(- \quad) - \frac{^2 + ^2}{2 \ ^3} \exp(-2 \quad) \tag{10-42}$$

where A, B, and C are coefficients and A =0.934, C = 0.88447, and B = 1.208. The velocity profile expressed below was used to compute mass conservation equations.

$$= (1 - \ ) \quad \rightarrow 0 + \quad \rightarrow \infty \tag{10-43}$$

where f is the in is an interpolation function developed by Wu et al.[146] that is used to weigh the velocity expansions in the inner given by

$$\cdot \quad \overline{1} + \frac{1}{- \ (\ - \ 0)} \tag{10-44}$$

and outer regions of diffusion layer, and $_0$ are constants and have values of = 25 and $_0$ = 1.

10.4.1 Faradaic Reactions

The influence of mass-transfer on frequency-dependent nonuniform current and potential distribution were simulated for oxygen-reduction reaction using a rotating disk-electrode geometry. The resulting ohmic impedance, Z_e, global impedance, Z and interfacial impedance, Z_0, were evaluated for the steady-state nonlinear equations. Synthetic impedance spectra were subsequently computed through a direct linear solver. The computational domain consisted of a 2-dimensional axisymmetric disk electrode geometry enclosed by the boundaries corresponding to the working electrode, Γ_{WE}, the insulator, Γ_I which embeds the electrodes and the hemispherical counter electrode, Γ_{CE} as shown in Figure 10-1. The complex ohmic impedance of a disk electrode geometry at high frequency points could be modeled using the Havriliak-Negami equation (2-24) [128]. You et al.[6] proposed a Havriliak-Negami model for the ohmic impedance associated with reversible oxidation of ferrocyanide to ferricyanide on a disk electrode. The aim of this present work is to identify potentials where Havriliak-Negami could be obtained for electrode systems with complex faradaic reactions.

Consider a reaction mechanism in the electrochemical system presumed as oxygen-reduction reaction

$$O_2 + 2H_2O + 4e^- \rightarrow 4OH^- \tag{10-45}$$

a uniform concentration may be assumed in the region adjacent to the diffusion layer. Potential may be expressed as Laplace equation

$$-\frac{1}{}\left(\ \frac{\overline{\Phi}}{} \right) + \frac{-\overline{\Phi}}{^2} \ = 0 \tag{10-46}$$

At the surface of the working electrode, Γ_{WE}, the steady-state faradaic current can be expressed as

$$\bar{} \quad {}_{O_2} = - \left. \frac{\partial \bar{\Phi}}{\partial} \right|_{y=0} = - \bar{} {}_{O_2} \bar{C}_{O_2}(0) \exp\left(- {}_{O_2} (\bar{\Phi}_m - \Phi_0) \bar{} \right) \tag{10-47}$$

where ${}_{O_2}$ is the reaction rate constants, ${}_{O_2}$ is the lumped parameter related to the apparent transfer coefficients, and $\bar{C}_{O_2}(0)$ is the steady-state concentration of Oxygen on the electrode surface. Φ_m is the electrode potential and Φ_0 is the solution potential adjacent to the electrode. Only the cathodic faradaic reaction is considered in equation (10-47). The flux of ionic species associated with the faradaic current could be expressed as

$$O_2 = {}_{O_2} \left. \frac{\partial \bar{C}_{O_2}}{\partial} \right|_{y=0} = - \frac{{}_{O_2}}{} F \tag{10-48}$$

where ${}_{O_2}$ is the stoichiometric coefficient of Oxygen = - 1, and n = 4 is the number of electrons transferred in the reaction. The stoichiometric coefficient has a negative value for a cathodic element. The steady-state charging current may be defined as

$$\bar{} \quad {}_c = (j \quad) \quad (\bar{\Phi}_m - \Phi_0) \bar{} \tag{10-49}$$

where Q is the constant-phase element component, is the constant-phase element exponent, and is the frequency. From equation (10-47), the faradaic current phasor can be written as

$$\tilde{} {}_{O_2} = {}_{O_2} \bar{C}_{O_2}(0) \quad {}_{O_2} \exp\left(- {}_{O_2} \left(\bar{\Phi}_m - \Phi_0 \bar{} \right) \right) \left(\tilde{\Phi}_m - \tilde{\Phi}_0 \right) - {}_{O_2}(0) \exp\left(- {}_{O_2} \left(\bar{\Phi}_m - \Phi_0 \bar{} \right) \right) \tilde{} {}_{O_2}(0) \tag{10-50}$$

and the oscillating charing current can be defined as

$$^e \quad {}_c = (j \quad)^{} \quad (\Phi^e_m - \Phi^e_0) \tag{10-51}$$

the total current phasor is expressed as

$$\tilde{}_T = \tilde{}_c + \tilde{}_{O_2} \tag{10-52}$$

the total current phasor at the electrode surface is determined by an integral expression, which can be written as

$$\int_0 \tilde{}_T 2 \quad - \quad = 0 \tag{10-53}$$

The ohmic impedance could be derived as

$$_e = \quad - \quad _0 \tag{10-54}$$

where Z is the total impedance and $_0$ is the interfacial impedance

$$= \left(\frac{2}{_0^2 \bullet 0} \int^2 \frac{\tilde{} \quad , 0}{\Phi em} \right)^{-1} \tag{10-55}$$

$$_0 = \left(-\frac{2 \int^2 e \quad (\quad , 0)}{_0^2 \tilde{0}\, \Phi m - \tilde{\Phi}_0} \right)^{-1} \tag{10-56}$$

at the insulating surface, Γ_I can be written as

$$\mathbf{n}\Gamma_I \cdot \quad \overline{\Phi_\Gamma} \mp \underset{I}{0} \tag{10-57}$$

at the counter electrode boundary, the potential is governed by laplace expression

$$\overline{\Phi}=0 \tag{10-58}$$

and the bulk concentration

$$\bar{}_{O_2}(\infty) = -\bar{O}_2 \tag{10-59}$$

Assuming a linear concentration gradient within the diffusion layer thickness of Oxygen, δ_{O_2}, the steady-state current density can be expressed as

$$i_{O_2} = -4F D_{O_2} \frac{\bar{c}_{O_2}(\infty) - \bar{c}_{O_2}(0)}{\delta_{O_2}} \tag{10-60}$$

the steady-state oxygen concentration at the electrode surface can be written as

$$\bar{c}_{O_2}(0) = \frac{\bar{c}_{O_2}(\infty)}{\frac{i_{O_2}}{4FD_{O_2}\bar{c}_{O_2}(\infty)}\delta_{O_2}\exp\left(-b_{O_2}\bar{V}\right) + 1} \tag{10-61}$$

from equation (10-60), the oscillating mass-transfer limiting current density may be written as

$$\tilde{i}_{O_2} = -4FD_{O_2}\frac{\tilde{c}_{O_2}(\infty) - \tilde{c}_{O_2}(0)}{\delta_{O_2}} \tag{10-62}$$

where $\tilde{c}_{O_2} = \tilde{c}_{O_2}/\bar{c}_{O_2}(0)$ is the dimensionless oscillating concentration, $\tilde{c}'_{O_2}$ is the derivative of $\tilde{c}_{O_2}$ with respect to the dimensionless position, $\eta = x/\delta_{O_2}$, and δ_{O_2} is the diffusion layer thickness. As stated by Orazem and Tribollet [122], the concentration $\tilde{c}_{O_2}(0)$ can be eliminated in equations (10-50) and (10-62) to achieve the faradaic impedance

$$Z_{F,O_2} = \frac{\tilde{V}}{\tilde{i}_{O_2}} = R_{t,O_2} + Z_{D,O_2} \tag{10-63}$$

where the charge-transfer resistance, R_{t,O_2}, is given by

$$R_{t,O_2} = \frac{1}{K_{O_2} b_{O_2} \bar{c}_{O_2}(0) \exp\left(-b_{O_2}\bar{V}\right)} \tag{10-64}$$

and the diffusion impedance is defined as

$$Z_{D,O_2}(\omega) = \frac{\delta_{O_2}}{4FD_{O_2}\bar{c}_{O_2}(0) b_{O_2}} \left(\frac{1}{i_{O_2}(0)}\right) \tag{10-65}$$

equation (10-65) could be rewritten as

$$Z_{D,O_2}(\ ) = R_{D,O_2}\left(-\frac{1}{\ _{O_2}(0)}\right) \tag{10-66}$$

the expression for $-\frac{1}{\ _{O_2}(\theta)}$ is derived by Orazem and Tribollet [122].

10.4.2 Impedance Results

Synthetic impedance spectroscopy data was obtained from the finite-element simulation of the electrochemical systems with faradaic reactions presumed as mass-transfer influenced Oxygen reduction reactions. The concentration of Oxygen species was 25 mol/m^3 in an electrolyte for a disk electrode with a rotation speed of 800 rpm. The ohmic impedance, $_e$ associated with the non-uniform current and potential distributions in the electrochemical system was obtained by subtracting the interfacial impedance, $_0$ from the total impedance, Z as shown in equations (10-54) through (10-56). The simulation results showed the potentials where Havriliak-Negami shape could be obtained for the electrochemical system considered. The parameters used for the numerical simulation in COMSOL multphysics are presented in Table 10-1. Following the electrochemical reactions considered, only the cathodic kinetic parameter was considered. The double-layer potential, V was varied from -1.4 V to 1.4 V. The frequency points used in the numerical model varied from 3 MHz to 1 mHz. The polarization curve for the reaction are presented in Figure 10-12. The points on the curves are potentials considered for the analysis which are -0.5 V and 1.0 V respectively. The mass-transfer-limited current for the oxygen-reduction reaction showed a negative plateau at low potentials from -1.0 V to -1.5 V. The steep slope in the middle of the curve corresponds to the electron transfer kinetics and the concentration of species at the electrode surface. The electrochemical system studied was oxygen reduction, hence, no positive current plateau was observed in this trend.

The impedance data for ohmic impedance obtained from the numerical simulation are summarized in Figure 10-14, as functions of potentials. The potentials considered were selected from the polarization curve shown in Figure 10-13(a) for positive potential (+1.0 V) at the

Table 10-1. Parameters used in the simulation of mass-transfer influenced oxygen reduction for a rotating disk electrode.

Parameter	Values
$_c$, A cm/mol	0.1
$_c$, V^{-1}	19.9
$_0$, F/cm^2	50
, cm^2/s	0.01
, cm^2/s	10^{-5}
Ω, rpm	800

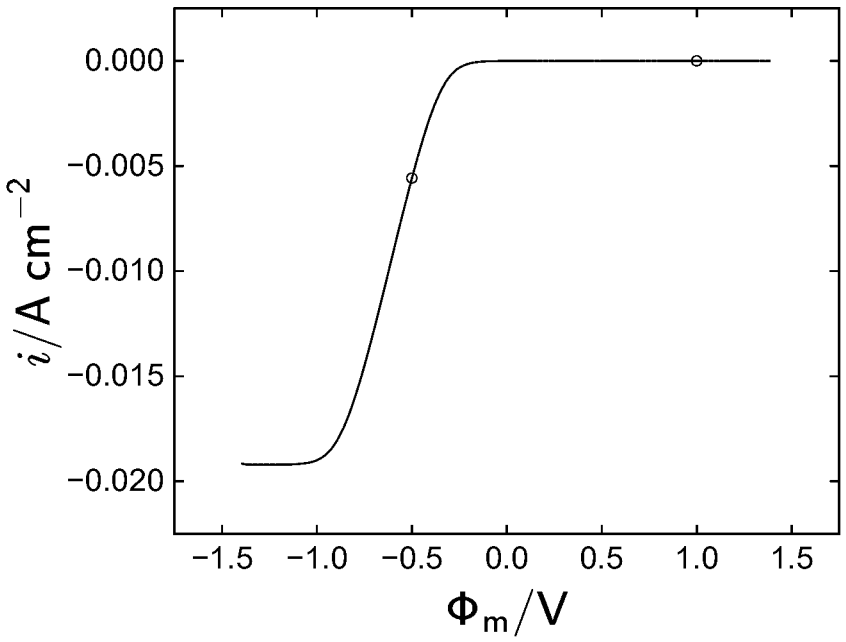

Figure 10-12. Polarization curve for Oxygen reduction influenced by mass transfer. The open circles represent the potentials evaluated.

mass-transfer limited region of the curve, and negative potential (-0.5 V) at the middle where there is a combination of kinetics and diffusion processes. The ohmic-impedance response for the +1.0 V are shown in Figure 10-13(a). The impedance response show characteristic of the Havriliak-Negami shape, common for complex systems with geometry-induced non-uniform current and potential distributions. At negative potentials of -0.5 V depicted in Figure 10-13(b), the ohmic impedance show nearly perfect Havriliak-Negami response, with a small inductive loop observed at 0.1 Hz, indicating surface inhomogeneity and frequency dispersion due to a distribution of relaxation time.

The magnitudes of ohmic impedance are presented in Figure 10-14 as a function of potentials. The resulting magnitudes for +1.0 V are shown in Figure 10-14(a). At low frequencies, the total impedance is dominated by charge transfer resistance and mass transfer. As frequency increases, the double-layer capacitance become smaller and the impedance response primarily reflects the ohmic resistance. At -0.5 V, the magnitude of ohmic impedance presented in Figure 10-14(b) showed a less sharp frequency response at low frequency points below 0.1 Hz. The low-frequency transition suggests more frequency dispersion at the electrode due to surface heterogeneity and kinetic effects at the negative potential. The possibility of obtaining a Havriliak-Negami ohmic impedance response is dependent on potential and faradaic reactions in the electrochemical system studied.

The phase-angle of ohmic impedance spectra are presented in Figure 10-15 a as function of potentials. At a positive potential of +1.0 V presented in Figure 10-15(a), the trend showed a peak in phase angle of -1.6 degrees around 10 kHz, with values close to zero at both lower and higher frequency points. The phase behavior suggest double-layer capacitance with a well-defined relaxation time at 10 kHz. The phase angle presented for the impedance spectra for -0.5 V in Figure 10-15(b) displayed a similar peak around 10 kHz with a broader distribution with a small deviation at low frequency points below 0.1 Hz suggesting a small distribution in relaxation times due to complex reaction kinetics at the electrode surface.

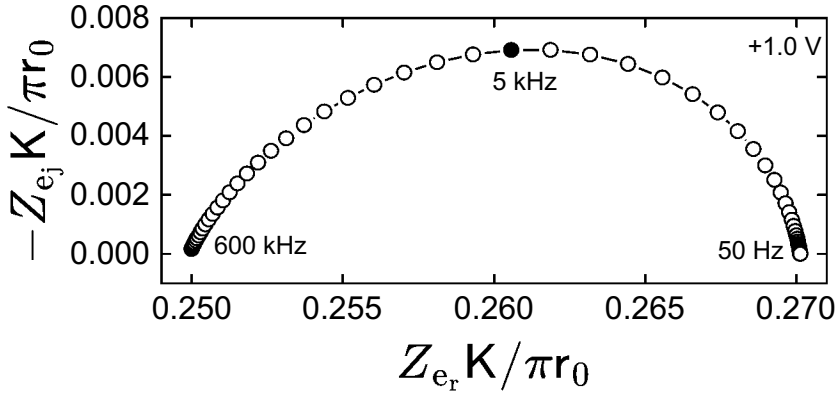

(a)

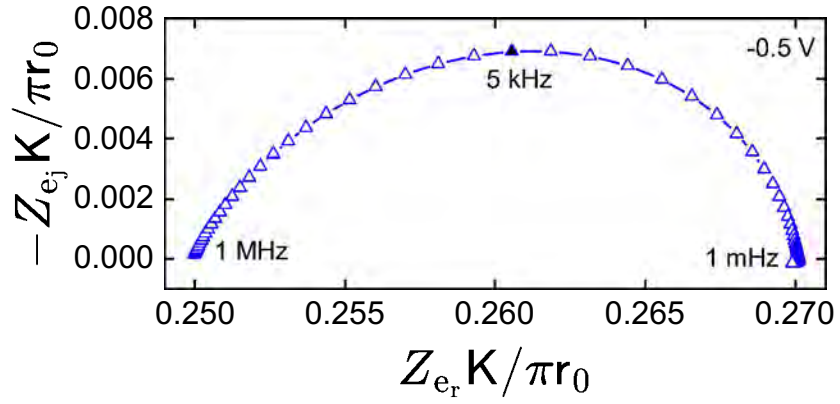

(b)

Figure 10-13. Simulation results for Ohmic impedance of mass-transfer influenced Oxygen reduction on a rotating disk electrode geometry as a function of potential: a) impedance spectra for 1.0 V, and b) impedance spectra for -0.5 V.

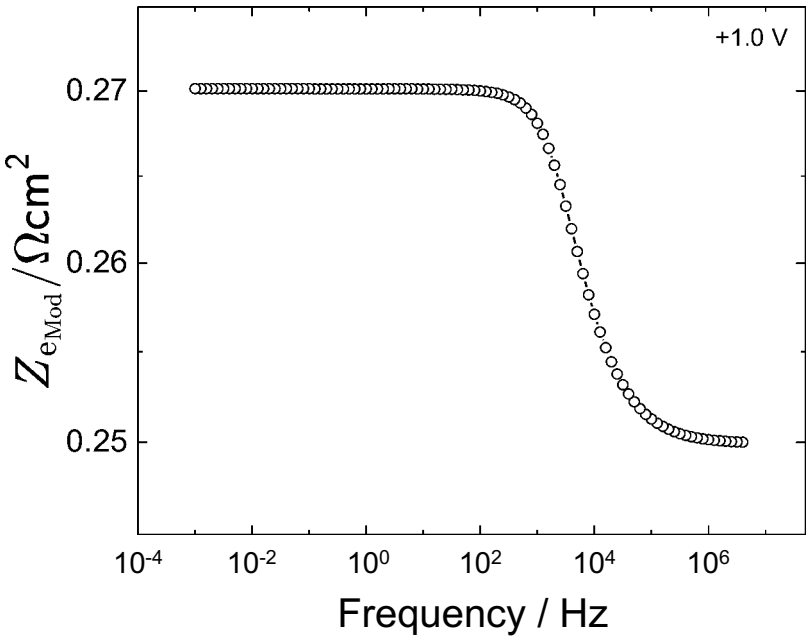

(a)

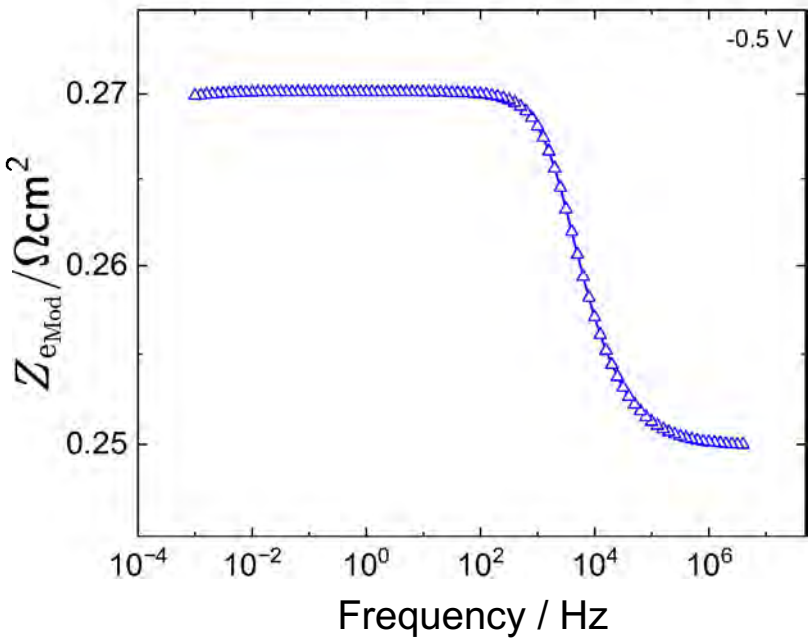

(b)

Figure 10-14. Magnitude for Ohmic impedance for mass-transfer influenced Oxygen reduction on a rotating disk electrode geometry as a function of potential: a) impedance magnitude for 1.0 V, and b) impedance magnitude for -0.5 V.

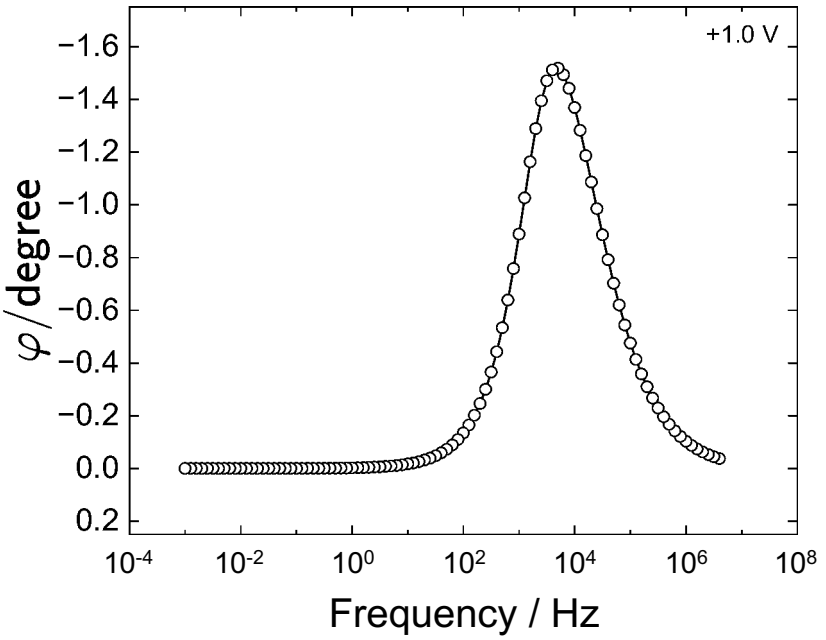

(a)

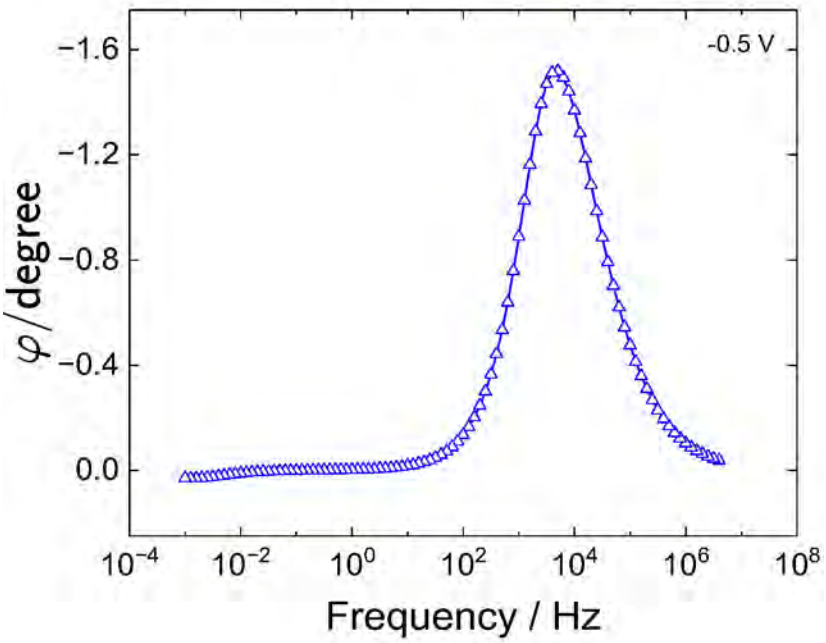

(b)

Figure 10-15. Phase angle for Ohmic impedance for mass-transfer influenced Oxygen reduction on a rotating disk electrode geometry as a function of potential: a) Phase angle for 1.0 V, and b) Phase angle for -0.5 V.

CHAPTER 11
CONCLUSIONS

The electrochemical properties of sputtered iridium oxide film (SIROF) ultramicroelectrodes developed for neural stimulation was characterized in vitro. The impedance spectra of the electrode devices were obtained at open-circuit condition. Regression of the measurement model to the impedance data confirmed the consistency of the data with the Kramers–Kronig relation. A stochastic-error-structure model was used to weight the regression of impedance spectra to filter experimental instability. The impedance spectroscopy analysis revealed the importance of accounting for parasitic capacitance introduced by cables and connectors. Through accuracy contour plot (ACPs) of open-lead and shorted-lead configurations, the operational frequency and impedance limits of the potentiostat and brain-stimulation devices were validated. A value of 10 TΩ and 1 Ω was obtained as the high and low impedance limits of the Gamry potentiostat, respectively. At high frequencies above 10 kHz the ultramicroelectrodes (20 m^2 and 80 m^2) exhibited impedance magnitudes attributable to the influence of parasitic capacitance, whereas the microelectrodes (4000 m^2) were primarily affected by ohmic impedance.

The process model captured the complex electrochemical interactions at the electrode–electrolyte interface, including redox reactions of the Iridium Oxide (IrOx) coating, double-layer charging via constant-phase elements, parasitic contributions from connecting cables, and mass-transfer-limited oxygen reduction. The extracted parameters were statistically significant across all electrode configurations. The study identified 2 methodologies for estimating capacitance. 1) the measurement model approach, and 2) the estimation of capacitance using the Brug's formula under the assumption of surface distribution of time constants. The extracted model parameters informed the development of a transient mathematical framework for neural stimulation, incorporating Laplace's equation and finite element simulations. These simulations demonstrated how geometry-induced non-uniform current and potential distributions, coupled with mass-transfer-limited faradaic reactions, shape the impedance response of ultramicroelectrodes.

The findings in this present work provide a robust analytical framework for interpreting impedance data from neural stimulation electrodes. The integration of accuracy contour plots, measurement model regression, stochastic-error-structure model, and statistical analysis offers a comprehensive methodology for characterizing electrochemical behavior in both in vitro and in vivo settings. These approaches are especially relevant for brain stimulation applications in preclinical and clinical environments, where accurate identification of faradaic and charging processes at the electrode–electrolyte interface is critical for device optimization and long-term functionality.

CHAPTER 12
FUTURE WORK

The recommendations for future studies on the impedance spectroscopy analysis and data interpretation of G4 devices are discussed in section 12.1. Future mathematical modeling directions for voltage transient response to biphasic current pulsing are discussed in section 12.2, and prospective studies on ferrocyanide oxidation can be found in section 12.3.

12.1 Measurement Modeling and Interpretation of G4 Device

The generation 4 (G4) device presented in Figure 12-1 consists of ultra-thin high density (HD) ultramicroelectrode arrays (UMEAs). The device was built using the NeuroNexus fabrication procedure. A photolithographic technique was used to create electrode sites on the 6-inch wafer. Each array was 5.5 m thick, made up of a 4.4 m silicon layer and a 1.1 m amorphous silicon carbide (a-SiC) layer. The electrodes vary in size, with spacing between sites (pitch) ranging from 6 m to 20 m depending on the layout as shown in Figure 12-1.

The project aims to examine the electrochemical properties of four generations (G1–G4) of ultramicroelectrode arrays (UMEAs) developed by NeuroNexus. The current study concentrates on experimental studies, data analysis, and interpretation models of impedance measurements for G1, G2, and G3 devices, as described in Chapter 3. The in vitro measurements of G4 device could guide the development of process model for the device in vivo. The G4 arrays incorporates loops and terminal traces for accessing the low-impedance and high-impedance regions of the accuracy contour plots. The experimental results for the G4 ultramicroelectrodes can be evaluated using the measurement model software developed by Watson and Orazem [97, 132] measurement model program. The regression analysis will generate the stochastic error structures of impedance data, error model and process model that will account for the faradaic reactions in the system and the overall behavior of the electrodes. Measurement model analysis will be used to determine the consistency of the data with Kramers–Kronig relations and provide accurate interpretation of impedance data.

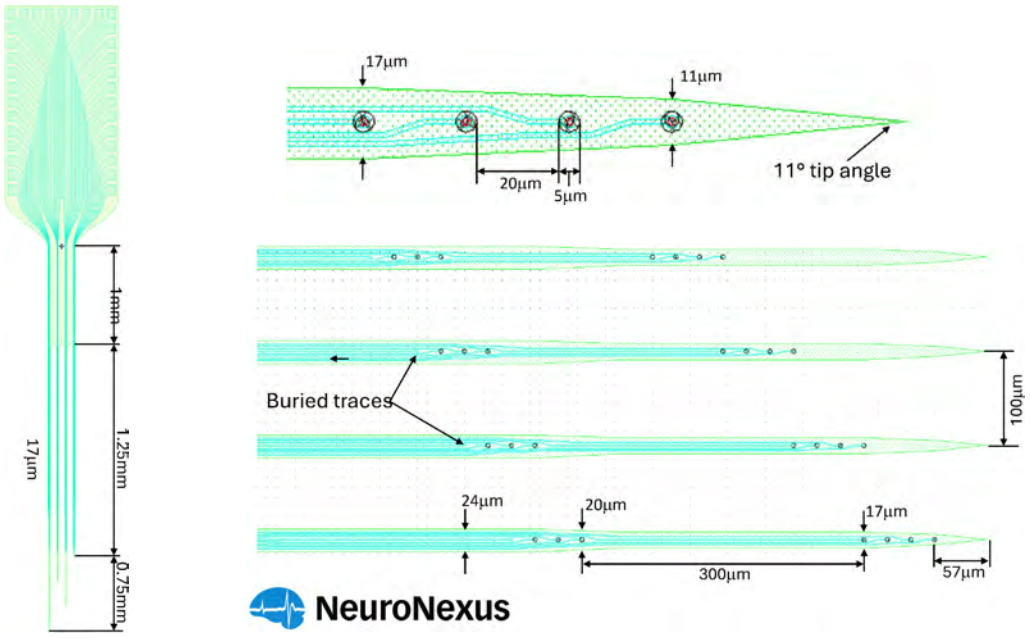

Figure 12-1. Schematics representation of generation 4 (G4) array device featuring 4 shanks. G4 device has looped traces for low-impedance assessment, and terminal traces for high-impedance assessment of the accuracy contour plot. The device was provided by NeuroNexus.

12.2 Potential Transient Response to Current Pulse

The parameters extracted from the measurement model analysis of SIROF ultramicroelectrodes could provide parameters for mathematical models and finite-element simulations. Numerical modeling of potential transients are used in neural stimulation studies to evaluate the maximum positive and negative polarization across the electrode/electrolyte interface. The interpretation models for G2 and G3 devices accounted for the changes in iridium oxidation state discussed in section 7.1.3. Previous numerical simulations on time-dependent response of double-layer potential to biphasic current pulsing presented in section 10.3.3.2 were performed without considering the influence of mass transfer associated with the changes in oxidation states of iridium. The voltage transient response to the biphasic current pulsing shown in Figure 12-2 could be remodeled to account for the concentrations of iridium redox process. The simulation results could provide information about faradaic processes and mass-transfer effects on stimulation parameters. Electrodes exhibit constant-phase-element (CPE) behavior, therefore, the finite-element model could be used to study the constant-phase-element behaviors of MEAs and UMEAs from the frequency domain to the time-dependent domain. In addition, the conditions that might lead to the failure of the electrodes could be studied, and the impedance at which the failure occurred could be determined.

12.3 Oxidation of Ferrocyanide

The electrochemical reaction for oxidation of ferrocyanide can be written as

$$[Fe(CN)_6]^{4-} \rightarrow [Fe(CN)_6]^{3-} + e^- \qquad (12\text{-}1)$$

the faradaic current density may be expressed as

$$F_a = a_{4(0)} \exp(a(\Phi_m - \Phi_0)) \qquad (12\text{-}2)$$

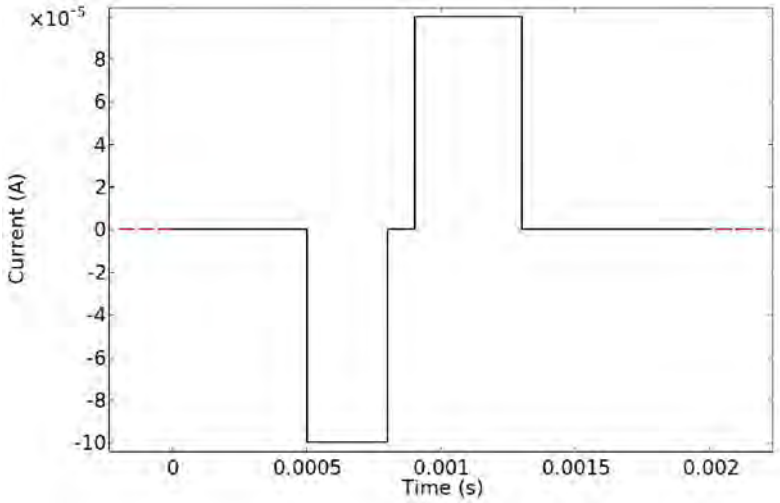

Figure 12-2. Schematic representation of the biphasic current pulsing. The time step was modeled with a piecewise function.

the oscillating current phasor may be obtained from the Taylors series expansion of equation 12-2 as

$$\tilde{}_F = \quad a \quad a \quad \bar{}_{4(0)} \exp(\quad a(\Phi\overline{m} - \Phi 0))(\overline{\Phi m} - \tilde{\Phi} 0) + \tilde{}a\exp(\quad a(\Phi m - \Phi 0)) \quad \bar{}\tilde{}_{4(0)} \quad \bar{} \tag{12-3}$$

the oscillating charing current can be defined as

$$\tilde{} \quad c = (\quad) \quad (\Phi\tilde{m} - \Phi 0) \tilde{} \tag{12-4}$$

The total current phasor at the electrode surface is defined as

$$\tilde{}_T = \tilde{}_c + \tilde{}_{Fa} \tag{12-5}$$

The total current phasor at the electrode surface is determined by an integral expression, which can be written as

$$\int_0 \tilde{}_T \, 2 \qquad - \quad = 0 \tag{12-6}$$

The ohmic impedance could be derived as

$$_{e} = \quad - \quad _{0} \tag{12-7}$$

where Z is the total impedance and $_{0}$ is the interfacial impedance

$$= 2\left(\frac{2}{_{0}^{2}} \int_{0}^{2} \frac{e \quad (\quad 0)}{\Phi_{m}} \right)^{-1} \tag{12-8}$$

$$_{0} = \left(\frac{2}{_{0}^{2}} \int_{0}^{2} \frac{(\quad , 0),}{\Phi_{m} - \Phi_{0}} \right)^{-1} \tag{12-9}$$

at the insulating surface, Γ_I can be written as

$$\mathbf{n}\Gamma_{I} \cdot \quad \Phi_{\Gamma} = 0 \tag{12-10}$$

at the counter electrode boundary, the potential is governed by laplace expression

$$\Phi = 0 \tag{12-11}$$

and the bulk anodic concentration

$$_{4}(\infty) = _{4} \tag{12-12}$$

The detailed derivation of the faradaic impedance and diffusion impedance associated with the reversible oxidation of Ferrocyanide was derived by You et al.[6].

12.3.1 Preliminary Results

Electrochemical impedance spectroscopy data were generated using finite-element simulations of disk electrode systems, with the faradaic reaction modeled as mass-transfer-limited ferrocyanide oxidation. The simulated electrolyte contained 10 mol/m^3 of oxidized ferrocyanide, and the disk electrode was rotated at 800 rpm. The system's ohmic impedance were estimated using equation (12-7). The simulation results identified electrode potentials at which the system

exhibited a Havriliak-Negami impedance response. The parameters used for the simulation are summarized in Table 12-1.

12.3.2 Polarization Curve for Ferrocyanide Oxidation

The electrochemical modeling was performed using only the anodic kinetic parameter, $_a$. The double-layer potential was varied from –0.5 V to 0.5 V, and impedance was simulated across a frequency range from 3 MHz to 1 mHz. The polarization curve for the system is displayed in Figure 10-12. The data points at –0.4 V, and 0 V mark the specific potentials analyzed in detail. For the oxidation of Ferrocyanide, the current approaches a positive mass-transfer-limiting value between –0.2 V and –0.5 V, as shown in Figure 10-12. The steep region of the plot arises from the interactions between electron-transfer kinetics and reactant concentration at the electrode interface. Since the analysis focused on the oxidation of ferrocyanide, no mass-transfer-limited plateau was found at negative currents within the potential window.

12.3.3 Impedance Response of Ferrocyanide Oxidation

The simulated ohmic impedance values as a function of applied potential are presented in Figure 12-4. Potentials were selected based on significant points identified on the polarization curve shown Figure 12-3, including a zero potential, and a negative mass-transfer-limited region of –0.4 V. The resulting nyquist plots for ohmic impedance response are displayed in Figure 12-4. The ohmic impedance, $_e$ was normalized by ohmic resistance to yield a dimensionless value, $_e$ K/ r_0. The impedance spectrum at -0.4 V shown in Figure 12-4(a) displays features in good agreement with the Havriliak-Negami model, indicating pronounced frequency dispersion due to

Table 12-1. Parameters used in the simulation of mass-transfer influenced oxygen reduction for a rotating disk electrode.

Parameter	Values
$_a$, A cm/mol	500
$_c$, V^{-1}	19.5
$_0$, F/cm^2	20
, cm^2/s	0.01
$_4$, cm^2/s	7.39×10^{-6}
, Ωcm	3.52
Ω, rpm	800

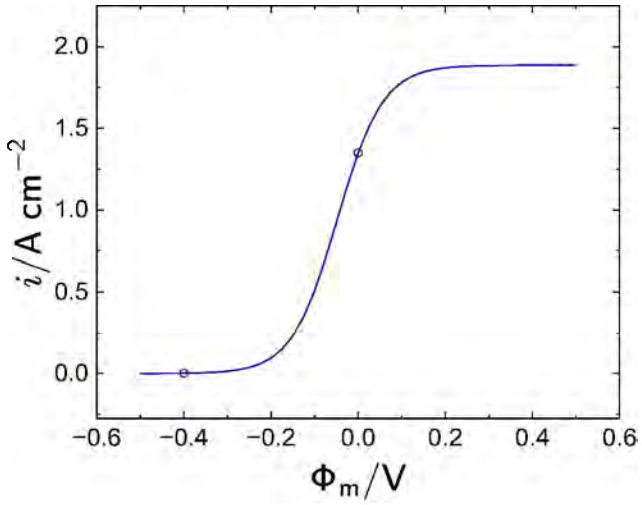

Figure 12-3. Polarization curve for oxidation of Ferrorcyanide influenced by mass transfer. The open circles represent the potentials evaluated.

geometric effects and non-uniform current and potential profiles. At 0 V, the impedance more closely follows a non-ideal Havriliak-Negami shape as shown in Figure 12-4(b), with an inductive loop observed near 0.1 Hz, reflecting surface heterogeneity and a spread of relaxation times at the electrode surface.

The Nyquist plot for the total impedance, Z are summarized in Figure 12-5. The resulting impedance spectra for -0.4 V are shown in Figure 12-5(a). The plot features a semicircular arc, typical of an electrochemical system dominated by charge transfer reactions with resistance and capacitance. At high frequency points, the impedance response is dominated by ohmic resistance and at lower frequencies the impedance behavior is controlled by charge-transfer resistance and double-layer capacitance. The impedance response suggest a kinetically limited region with minimum influence of mass transfer at these potentials. At a potential of 0 V displayed in Figure 12-5(b), the impedance response show two peaks, suggesting the appearance of additional adsorption effects, or contribution of multiple time constants. The lower impedance loop reflects demonstrate more favorable electrode kinetics at the electrode surface. The numerical results could be analyzed with the measurement model and interpreted using the Havrilliak-Negami equation following the procedure outlined elsewhere [6].

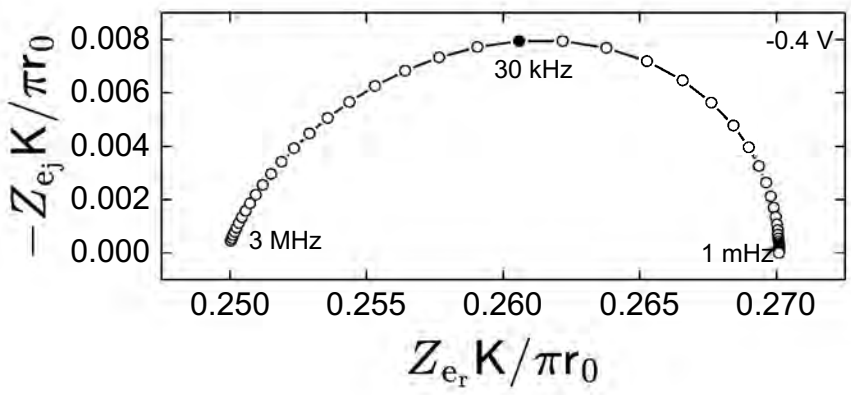

(a)

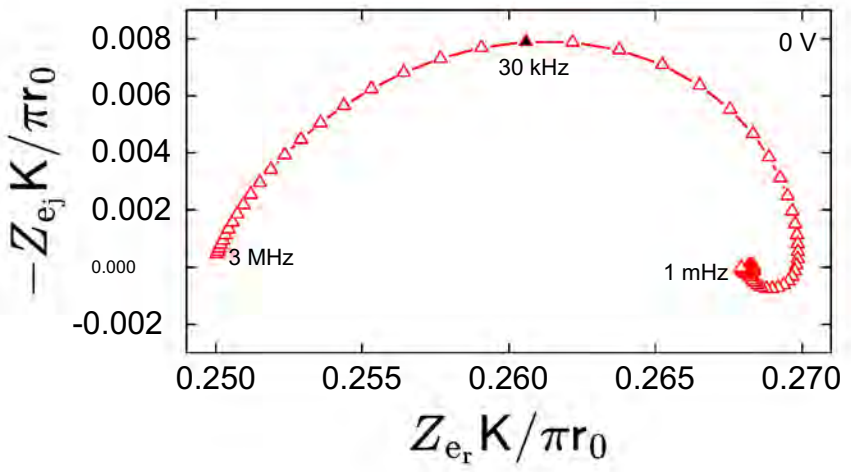

(b)

Figure 12-4. Simulation results for Ohmic impedance of mass-transfer influenced Oxygen reduction on a rotating disk electrode geometry as a function of potential: a) for -0.4 V, b) for 0 V.

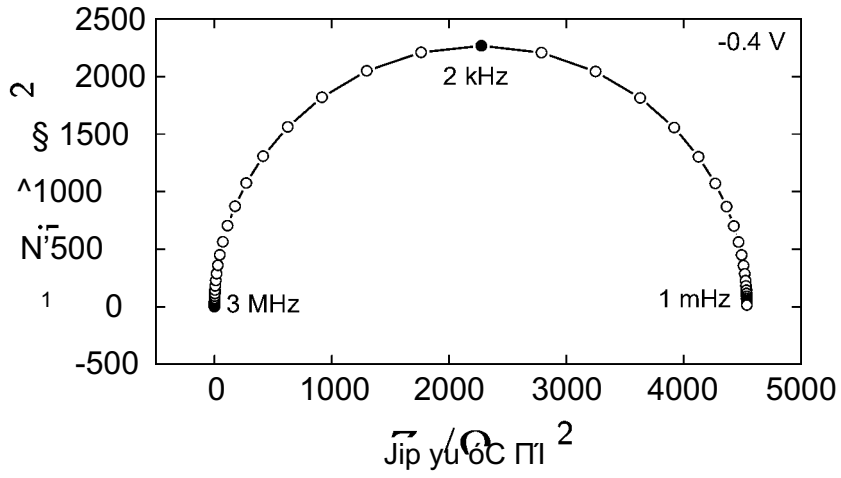

(a)

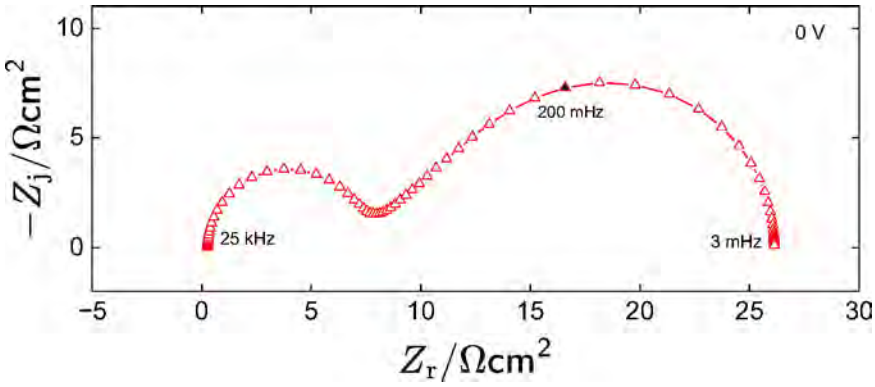

(b)

Figure 12-5. Simulation results for the total impedance for the oxidation of Ferrocyanide on a rotating disk electrode geometry as a function of potential: a) for -0.4 V, b) for 0 V.

APPENDIX
CAPACITANCE CALCULATION

This section details the procedure for calculating both the effective double-layer capacitance, $C_{eff,dl}$, and the pore capacitance, $C_{p_{ore}}$, using the parameters listed in Table 8-3 for a G3 electrode with an area of 20 m^2.

$$C_{eff,dl} = \left[\left(1.546 \text{ mF s}^{1-} \text{ cm}^{-2} \right)^{0.88} \times 0.023713 \ (\Omega \text{ cm}^2)^{\frac{1-0.88}{0.88}} \right] = 0.387 \text{ mF cm}^{-2} \quad \text{(A-1)}$$

$$C_{pore} = \left[\left(0.015 \text{ mF s}^{1-} \text{ cm}^{-2} \right)^{0.183} \times 380.78 \ (\Omega \text{ cm}^2)^{\frac{1-0.183}{0.183}} \right] = 0.00531 \text{ mF cm}^{-2} \quad \text{(A-2)}$$

Same procedure was followed to compute the capacitance of other electrodes.

LIST OF REFERENCES

[1] M. E. Orazem and B. Tribollet, *Electrochemical Impedance Spectroscopy* (Wiley, 2008).

[2] D. R. Merrill, M. Bikson, and J. G. Jefferys, “Electrical Stimulation of Excitable Tissue: Design of Efficacious and Safe Protocols,” *Journal of Neuroscience Methods*, **141** (2005) 171–198.

[3] P. Agarwal, M. E. Orazem, and L. H. Garcia-Rubio, “Measurement Models for Electrochemical Impedance Spectroscopy: I . Demonstration of Applicability,” *Journal of The Electrochemical Society*, **139** (1992) 1917–1927.

[4] P. Agarwal, M. E. Orazem, and L. H. Garcia-Rubio, “Application of Measurement Models to Impedance Spectroscopy: Iii . Evaluation of Consistency with the Kramers-Kronig Relations,” *Journal of The Electrochemical Society*, **142** (1995) 4159–4168.

[5] J. Min Goh, C. Eluagu, J. Babauta, and M. E. Orazem, “Comparison of Approaches for Assessing Linearity of Impedance Measurements,” *Journal of The Electrochemical Society*, **171** (2024) 036508.

[6] C. You, A. Dizon, M. Gao, V. Vivier, and M. E. Orazem, “Experimental Observation of Ohmic Impedance,” *Electrochimica Acta*, **413** (2022) 140177.

[7] J. Lei and K. Gillespie, “Projected Global Burden of Brain Disorders through 2050 (p7-15.001),” *Neurology*, **102** (2024).

[8] D. V. Parums, “A Review of the Current Status of Disease-Modifying Therapies and Prevention of Alzheimer’s Disease,” *Medical Science Monitor*, **30** (2024).

[9] B. Davidson, A. Bhattacharya, C. Sarica, G. Darmani, N. Raies, R. Chen, and A. M. Lozano, “Neuromodulation Techniques – from Non-Invasive Brain Stimulation to Deep Brain Stimulation,” *Neurotherapeutics*, **21** (2024) e00330.

[10] S. Alfihed, M. Majrashi, M. Ansary, N. Alshamrani, S. H. Albrahim, A. Alsolami, H. A. Alamari, A. Zaman, D. Almutairi, A. Kurdi, M. M. Alzaydi, T. Tabbakh, and F. Al-Otaibi, “Non-Invasive Brain Sensing Technologies for Modulation of Neurological Disorders,” *Biosensors*, **14** (2024) 335.

[11] A. J. Moshayedi, T. Mokhtari, and M. Emadi Andani, “Brain Stimulation Techniques in Research and Clinical Practice: A Comprehensive Review of Applications and Therapeutic Potential in Parkinson’s Disease,” *Brain Sciences*, **15** (2024) 20.

[12] C. S. R. Taylor and C. G. Gross, “Twitches Versus Movements: A Story of Motor Cortex,” *The Neuroscientist*, **9** (2003) 332–342.

[13] K. L. Clark, K. M. Armstrong, and T. Moore, “Probing Neural Circuitry and Function with Electrical Microstimulation,” *Proceedings of the Royal Society B: Biological Sciences*, **278** (2011) 1121–1130.

[14] C. Isitan, Q. Yan, D. D. Spencer, and R. Alkawadri, “Brief History of Electrical Cortical Stimulation: A Journey in Time from Volta to Penfield,” *Epilepsy Research*, **166** (2020) 106363.

[15] W. Alberts, B. Feinstein, G. Levin, and E. W. Wright, “Electrical Stimulation of Therapeutic Targests in Waking Dyskinetic Patients,” *Electroencephalography and Clinical Neurophysiology*, **20** (1966) 559–566.

[16] P. Limousin, J. D. Speelman, F. Gielen, M. Janssens, and study collaborators, “Multicentre European Study of Thalamic Stimulation in Parkinsonian and Essential Tremor,” *Journal of Neurology, Neurosurgery & Psychiatry*, **66** (1999) 289–296.

[17] M. R. Bergstro¨ m, G. G. Johansson, L. V. Laitinen, and P. Sipponen, “Electrical Stimulation of the Thalamic and Subthalamic Area in Cerebral Palsy,” *Acta Physiologica Scandinavica*, **67** (1966) 208–213.

[18] I. Cooper, “Effect of Chronic Stimulation of Anterior Cerebellum on Neurological Disease,” *The Lancet*, **301** (1973) 206.

[19] D. M. Thompson, A. N. Koppes, J. G. Hardy, and C. E. Schmidt, “Electrical Stimuli in the Central Nervous System Microenvironment,” *Annual Review of Biomedical Engineering*, **16** (2014) 397–430.

[20] M. E. Orazem, K. J. Otto, and C. L. Alexander, “Electrochemistry in Action-Engineering the Neuronal Response to Electrical Microstimulation,” *The Electrochemical Society Interface*, **32** (2023) 40–42.

[21] B. Hazelgrove, L. Matter, B. Raos, B. Harland, L. Cheng, M. Asplund, and D. Svirskis, “Electrochemical Impedance Spectroscopy in Vivo for Neurotechnology and Bioelectronics,” *Nature Reviews Electrical Engineering*, **2** (2025) 110–124.

[22] J. W. Salatino, K. A. Ludwig, T. D. Kozai, and E. K. Purcell, “Glial Responses to Implanted Electrodes in the Brain,” *Nature Biomedical Engineering*, **1** (2017) 862–877.

[23] A. Mercanzini, P. Colin, J.-C. Bensadoun, A. Bertsch, and P. Renaud, “In Vivo Electrical Impedance Spectroscopy of Tissue Reaction to Microelectrode Arrays,” *IEEE Transactions on Biomedical Engineering*, **56** (2009) 1909–1918.

[24] K. Krukiewicz, “Electrochemical Impedance Spectroscopy As a Versatile Tool for the Characterization of Neural Tissue: A Mini Review,” *Electrochemistry Communications*, **116** (2020) 106742.

[25] W. Adey, R. Kado, and J. Didio, “Impedance Measurements in Brain Tissue of Animals Using Microvolt Signals,” *Experimental Neurology*, **5** (1962) 47–66.

[26] R. Porter, W. R. Adey, and R. T. Kado, “Measurement of Electrical Impedance in the Human Brain: Some Preliminary Observations,” *Neurology*, **14** (1964) 1002–1012.

[27] T. Rose and L. Robblee, “Electrical Stimulation with Pt Electrodes. Viii. Electrochemically Safe Charge Injection Limits with 0.2 Ms Pulses (neuronal Application),” *IEEE Transactions on Biomedical Engineering*, **37** (1990) 1118–1120.

[28] D. B. McCreery, W. F. Agnew, T. G. H. Yuen, and L. A. Bullara, “Comparison of Neural Damage Induced by Electrical Stimulation with Faradaic and Capacitor Electrodes,” *Annals of Biomedical Engineering*, **16** (1988) 463–481.

[29] R. Shannon, “A Model of Safe Levels for Electrical Stimulation,” *IEEE Transactions on Biomedical Engineering*, **39** (1992) 424–426.

[30] A. Butterwick, A. Vankov, P. Huie, Y. Freyvert, and D. Palanker, “Tissue Damage by Pulsed Electrical Stimulation,” *IEEE Transactions on Biomedical Engineering*, **54** (2007) 2261–2267.

[31] S. F. Cogan, K. A. Ludwig, C. G. Welle, and P. Takmakov, “Tissue Damage Thresholds during Therapeutic Electrical Stimulation,” *Journal of Neural Engineering*, **13** (2016) 021001.

[32] W. M. Grill and J. Thomas Mortimer, “Electrical Properties of Implant Encapsulation Tissue,” *Annals of Biomedical Engineering*, **22** (1994) 23–33.

[33] K. A. Malaga, K. E. Schroeder, P. R. Patel, Z. T. Irwin, D. E. Thompson, J. Nicole Bentley, S. F. Lempka, C. A. Chestek, and P. G. Patil, “Data-Driven Model Comparing the Effects of Glial Scarring and Interface Interactions on Chronic Neural Recordings in Non-Human Primates,” *Journal of Neural Engineering*, **13** (2015) 016010.

[34] A. Prasad and J. C. Sanchez, “Quantifying Long-Term Microelectrode Array Functionality Using Chronicin Vivoimpedance Testing,” *Journal of Neural Engineering*, **9** (2012) 026028.

[35] T. D. Y. Kozai, N. B. Langhals, P. R. Patel, X. Deng, H. Zhang, K. L. Smith, J. Lahann, N. A. Kotov, and D. R. Kipke, “Ultrasmall Implantable Composite Microelectrodes with Bioactive Surfaces for Chronic Neural Interfaces,” *Nature Materials*, **11** (2012) 1065–1073.

[36] K. Otto, M. Johnson, and D. Kipke, “Voltage Pulses Change Neural Interface Properties and Improve Unit Recordings with Chronically Implanted Microelectrodes,” *IEEE Transactions on Biomedical Engineering*, **53** (2006) 333–340.

[37] K. P. O’Sullivan, M. E. Orazem, K. J. Otto, C. R. Butson, and J. L. Baker, “Electrical Rejuvenation of Chronically Implanted Macroelectrodes in Nonhuman Primates,” *Journal of Neural Engineering*, **21** (2024) 036056.

[38] M. Johnson, K. Otto, and D. Kipke, “Repeated Voltage Biasing Improves Unit Recordings by Reducing Resistive Tissue Impedances,” *IEEE Transactions on Neural Systems and Rehabilitation Engineering*, **13** (2005) 160–165.

[39] R. A. Frederick, P. R. Troyk, and S. F. Cogan, “Wireless Transmission of Voltage Transients from a Chronically Implanted Neural Stimulation Device,” *Journal of Neural Engineering*, **19** (2022) 026049.

[40] S. Cogan, P. Troyk, J. Ehrlich, T. Plante, and D. Detlefsen, “Potential-Biased, Asymmetric Waveforms for Charge-Injection With Activated Iridium Oxide (AIROF) Neural Stimulation Electrodes,” *IEEE Transactions on Biomedical Engineering*, **53** (2006) 327–332.

[41] B. Howell and W. Grill, *Design of Electrodes for Stimulation and Recording* (Elsevier, 2015) 59–93, 59–93.

[42] S. F. Cogan, “Neural Stimulation and Recording Electrodes,” *Annual Review of Biomedical Engineering*, **10** (2008) 275–309.

[43] D. McCreery, W. Agnew, T. Yuen, and L. Bullara, “Charge density and charge per phase as cofactors in neural injury induced by electrical stimulation,” *IEEE Transactions on Biomedical Engineering*, **37** (1990) 996–1001.

[44] D. McCreery, T. Yuen, W. Agnew, and L. Bullara, “Stimulus Parameters Affecting Tissue Injury during Microstimulation in the Cochlear Nucleus of the Cat,” *Hearing Research*, **77** (1994) 105–115.

[45] A. Ghazavi and S. F. Cogan, “Ultramicro-Sized Sputtered Iridium Oxide Electrodes in Buffered Saline: Behavior, Stability, and the Effect of the Perimeter to Area Ratio on Their Electrochemical Properties,” *Electrochimica Acta*, **423** (2022) 140514.

[46] T. Chung, J. Q. Wang, J. Wang, B. Cao, Y. Li, and S. W. Pang, “Electrode Modifications to Lower Electrode Impedance and Improve Neural Signal Recording Sensitivity,” *Journal of Neural Engineering*, **12** (2015) 056018.

[47] S. Pimenta, J. A. Rodrigues, F. Machado, J. F. Ribeiro, M. J. Maciel, O. Bondarchuk, P. Monteiro, J. Gaspar, J. H. Correia, and L. Jacinto, “Double-Layer Flexible Neural Probe with Closely Spaced Electrodes for High-Density in Vivo Brain Recordings,” *Frontiers in Neuroscience*, **15** (2021).

[48] S. Cogan, P. Troyk, J. Ehrlich, and T. Plante, “In Vitro Comparison of the Charge-Injection Limits of Activated Iridium Oxide (airof) and Platinum-Iridium Microelectrodes,” *IEEE Transactions on Biomedical Engineering*, **52** (2005) 1612–1614.

[49] Y. J. Lee, H. Kim, J. Y. Kang, S. H. Do, and S. H. Lee, “Biofunctionalization of Nerve Interface Via Biocompatible Polymer-Roughened Pt Black on Cuff Electrode for Chronic Recording,” *Advanced Healthcare Materials*, **6** (2017).

[50] E. Castagnola, A. Ansaldo, E. Maggiolini, T. Ius, M. Skrap, D. Ricci, and L. Fadiga, “Smaller, Softer, Lower-Impedance Electrodes for Human Neuroprosthesis: A Pragmatic Approach,” *Frontiers in Neuroengineering*, **7** (2014).

[51] S. Negi, R. Bhandari, L. Rieth, and F. Solzbacher, “In Vitro Comparison of Sputtered Iridium Oxide and Platinum-Coated Neural Implantable Microelectrode Arrays,” *Biomedical Materials*, **5** (2010) 015007.

[52] S. F. Cogan, A. A. Guzelian, W. F. Agnew, T. G. Yuen, and D. B. McCreery, “Over-Pulsing Degrades Activated Iridium Oxide Films Used for Intracortical Neural Stimulation,” *Journal of Neuroscience Methods*, **137** (2004) 141–150.

[53] J. Weiland, D. Anderson, and M. Humayun, “In Vitro Electrical Properties for Iridium Oxide Versus Titanium Nitride Stimulating Electrodes,” *IEEE Transactions on Biomedical Engineering*, **49** (2002) 1574–1579.

[54] K. A. Ludwig, N. B. Langhals, M. D. Joseph, S. M. Richardson-Burns, J. L. Hendricks, and D. R. Kipke, “Poly(3,4-Ethylenedioxythiophene) (pedot) Polymer Coatings Facilitate Smaller Neural Recording Electrodes,” *Journal of Neural Engineering*, **8** (2011) 014001.

[55] T. D. Y. Kozai, K. Catt, Z. Du, K. Na, O. Srivannavit, R.-u. M. Haque, J. Seymour, K. D. Wise, E. Yoon, and X. T. Cui, “Chronic in Vivo Evaluation of Pedot/cnt for Stable Neural Recordings,” *IEEE Transactions on Biomedical Engineering*, **63** (2016) 111–119.

[56] B. Chakraborty, A. Joshi-Imre, and S. F. Cogan, “Charge Injection Characteristics of Sputtered Ruthenium Oxide Electrodes for Neural Stimulation and Recording,” *Journal of Biomedical Materials Research Part B: Applied Biomaterials*, **110** (2021) 229–238.

[57] S. Cogan, T. Plante, and J. Ehrlich, “Sputtered Iridium Oxide Films (sirofs) for Low-Impedance Neural Stimulation and Recording Electrodes,” in *The 26th Annual International Conference of the IEEE Engineering in Medicine and Biology Society*, volume 4 of *IEMBS-04* (IEEE) 4153–4156.

[58] S. F. Cogan, J. Ehrlich, T. D. Plante, A. Smirnov, D. B. Shire, M. Gingerich, and J. F. Rizzo, “Sputtered Iridium Oxide Films for Neural Stimulation Electrodes,” *Journal of Biomedical Materials Research Part B: Applied Biomaterials*, **89B** (2008) 353–361.

[59] Q. Dong, C. Ezeh, Y. Wu, J. F. Hetke, S. Cogan, M. E. Orazem, and K. J. Otto, “Stability Assessment of Ultramicroelectrode Arrays in Neural Stimulation: An Electrochemical Impedance Spectroscopy Analysis,” in *2024 46th Annual International Conference of the IEEE Engineering in Medicine and Biology Society (EMBC)* (IEEE, 2024) 1–4.

[60] K. C. Fox, B. L. Foster, A. Kucyi, A. L. Daitch, and J. Parvizi, “Intracranial Electrophysiology of the Human Default Network,” *Trends in Cognitive Sciences*, **22** (2018) 307–324.

[61] C. L. Hughes, S. N. Flesher, J. M. Weiss, J. E. Downey, M. Boninger, J. L. Collinger, and R. A. Gaunt, “Neural Stimulation and Recording Performance in Human Sensorimotor Cortex Over 1500 Days,” *Journal of Neural Engineering*, **18** (2021) 045012.

[62] K. Woeppel, C. Hughes, A. J. Herrera, J. R. Eles, E. C. Tyler-Kabara, R. A. Gaunt, J. L. Collinger, and X. T. Cui, “Explant Analysis of Utah Electrode Arrays Implanted in Human Cortex for Brain-Computer-Interfaces,” *Frontiers in Bioengineering and Biotechnology*, **9** (2021).

[63] K. A. Ludwig, J. D. Uram, J. Yang, D. C. Martin, and D. R. Kipke, “Chronic Neural Recordings Using Silicon Microelectrode Arrays Electrochemically Deposited with a Poly(3,4-Ethylenedioxythiophene) (pedot) Film,” *Journal of Neural Engineering*, **3** (2006) 59–70.

[64] V. Castagnola, E. Descamps, A. Lecestre, L. Dahan, J. Remaud, L. Nowak, and C. Bergaud, “Parylene-Based Flexible Neural Probes with Pedot Coated Surface for Brain Stimulation and Recording,” *Biosensors and Bioelectronics*, **67** (2015) 450–457.

[65] S. R. Kane, S. F. Cogan, J. Ehrlich, T. D. Plante, D. B. McCreery, and P. R. Troyk, “Electrical Performance of Penetrating Microelectrodes Chronically Implanted in Cat Cortex,” *IEEE Transactions on Biomedical Engineering*, **60** (2013) 2153–2160.

[66] J. C. Barrese, N. Rao, K. Paroo, C. Triebwasser, C. Vargas-Irwin, L. Franquemont, and J. P. Donoghue, “Failure Mode Analysis of Silicon-Based Intracortical Microelectrode Arrays in Non-Human Primates,” *Journal of Neural Engineering*, **10** (2013) 066014.

[67] S. F. Lempka, S. Miocinovic, M. D. Johnson, J. L. Vitek, and C. C. McIntyre, “In Vivo Impedance Spectroscopy of Deep Brain Stimulation Electrodes,” *Journal of Neural Engineering*, **6** (2009) 046001.

[68] W. Franks, I. Schenker, P. Schmutz, and A. Hierlemann, “Impedance Characterization and Modeling of Electrodes for Biomedical Applications,” *IEEE Transactions on Biomedical Engineering*, **52** (2005) 1295–1302.

[69] C. M. Lewis, C. Boehler, R. Liljemalm, P. Fries, T. Stieglitz, and M. Asplund, “Recording Quality Is Systematically Related to Electrode Impedance,” *Advanced Healthcare Materials*, (2024).

[70] H. M. Lutz, Y. Wu, C. C. Eluagu, S. F. Cogan, K. J. Otto, and M. E. Orazem, “Analysis of Electrochemical Impedance Spectroscopy Data for Sputtered Iridium Oxide Electrodes,” *Journal of Neural Engineering*, (2025).

[71] A. Ghazavi, J. Maeng, M. Black, S. Salvi, and S. F. Cogan, “Electrochemical Characteristics of Ultramicro-Dimensioned Sirof Electrodes for Neural Stimulation and Recording,” *Journal of Neural Engineering*, **17** (2020) 016022.

[72] R. Meyer, S. Cogan, T. Nguyen, and R. Rauh, “Electrodeposited Iridium Oxide for Neural Stimulation and Recording Electrodes,” *IEEE Transactions on Neural Systems and Rehabilitation Engineering*, **9** (2001) 2–11.

[73] M. Vomero, F. Ciarpella, E. Zucchini, M. Kirsch, L. Fadiga, T. Stieglitz, and M. Asplund, “On the Longevity of Flexible Neural Interfaces: Establishing Biostability of Polyimide-Based Intracortical Implants,” *Biomaterials*, **281** (2022) 121372.

[74] S. Wilks, “Poly(3,4-Ethylene Dioxythiophene) (PEDOT) As a Micro-Neural Interface Material for Electrostimulation,” *Frontiers in Neuroengineering*, **2** (2009).

[75] C. Gabrielli, M. Keddam, and H. Takenouti, *Kramers-Kronig Transformation in Relation to the Interface Regulating Device* (ASTM International) 140–140–14, 140–140–14.

[76] V. Vivier and M. E. Orazem, “Impedance Analysis of Electrochemical Systems,” *Chemical Reviews*, **122** (2022) 11131–11168.

[77] J. E. B. Randles, “Kinetics of Rapid Electrode Reactions,” *Discussions of the Faraday Society*, **1** (1947) 11–19.

[78] E. Warburg, “Über Die Polarisationscapacität Des Platins,” *Ann Phys-new York*, **6** (1901) 125–135.

[79] J. R. Abbott, E. N. Jeakle, P. Haghighi, J. O. Usoro, B. S. Sturgill, Y. Wu, N. Geramifard, R. Radhakrishna, S. Patnaik, S. Nakajima, J. Hess, Y. Mehmood, V. Devata, G. Vijayakumar, A. Sood, T. T. Doan Thai, K. Dogra, A. G. Hernandez-Reynoso, J. J. Pancrazio, and S. F. Cogan, “Planar Amorphous Silicon Carbide Microelectrode Arrays for Chronic Recording in Rat Motor Cortex,” *Biomaterials*, **308** (2024) 122543.

[80] N. Alba, Z. Du, K. Catt, T. Kozai, and X. Cui, “In Vivo Electrochemical Analysis of a Pedot/mwcnt Neural Electrode Coating,” *Biosensors*, **5** (2015) 618–646.

[81] K. O’Sullivan, B. Philip, J. Baker, J. Rolston, M. Orazem, K. Otto, and C. Butson, “In Vivo and in Vitro Electrochemical Impedance Spectroscopy of Acute and Chronic Intracranial Electrodes,” *Data*, **9** (2024) 78.

[82] E. K. Purcell, D. E. Thompson, K. A. Ludwig, and D. R. Kipke, “Flavopiridol Reduces the Impedance of Neural Prostheses in Vivo without Affecting Recording Quality,” *Journal of Neuroscience Methods*, **183** (2009) 149–157.

[83] M. E. Urdaneta, N. G. Kunigk, J. D. Pen˜ aloza-Aponte, S. Currlin, I. G. Malone, S. I. Fried, and K. J. Otto, “Layer-Dependent Stability of Intracortical Recordings and Neuronal Cell Loss,” *Frontiers in Neuroscience*, **17** (2023).

[84] A. Prasad, Q.-S. Xue, R. Dieme, V. Sankar, R. C. Mayrand, T. Nishida, W. J. Streit, and J. C. Sanchez, “Abiotic-Biotic Characterization of Pt/ir Microelectrode Arrays in Chronic Implants,” *Frontiers in Neuroengineering*, **7** (2014).

[85] P. R. Patel, H. Zhang, M. T. Robbins, J. B. Nofar, S. P. Marshall, M. J. Kobylarek, T. D. Y. Kozai, N. A. Kotov, and C. A. Chestek, “Chronicin Vivostability Assessment of Carbon Fiber Microelectrode Arrays,” *Journal of Neural Engineering*, **13** (2016) 066002.

[86] B. J. Black, A. Kanneganti, A. Joshi-Imre, R. Rihani, B. Chakraborty, J. Abbott, J. J. Pancrazio, and S. F. Cogan, “Chronic Recording and Electrochemical Performance of Utah Microelectrode Arrays Implanted in Rat Motor Cortex,” *Journal of Neurophysiology*, **120** (2018) 2083–2090.

[87] N. L. Opie, S. E. John, G. S. Rind, S. M. Ronayne, D. B. Grayden, A. N. Burkitt, C. N. May, T. J. O'Brien, and T. J. Oxley, "Chronic Impedance Spectroscopy of an Endovascular Stent-Electrode Array," *Journal of Neural Engineering*, **13** (2016) 046020.

[88] B. Hirschorn, M. E. Orazem, B. Tribollet, V. Vivier, I. Frateur, and M. Musiani, "Constant-Phase-Element Behavior Caused by Resistivity Distributions in Films," *Journal of The Electrochemical Society*, **157** (2010) C458.

[89] B. Hirschorn, M. E. Orazem, B. Tribollet, V. Vivier, I. Frateur, and M. Musiani, "Determination of Effective Capacitance and Film Thickness from Constant-Phase-Element Parameters," *Electrochimica Acta*, **55** (2010) 6218–6227.

[90] M. R. Abidian and D. C. Martin, "Experimental and theoretical characterization of implantable neural microelectrodes modified with conducting polymer nanotubes," *Biomaterials*, **29** (2008) 1273–1283.

[91] V. Sankar, E. Patrick, R. Dieme, J. C. Sanchez, A. Prasad, and T. Nishida, "Electrode Impedance Analysis of Chronic Tungsten Microwire Neural Implants: Understanding Abiotic Vs. Biotic Contributions," *Frontiers in Neuroengineering*, **7** (2014).

[92] M. M. Straka, B. Shafer, S. Vasudevan, C. Welle, and L. Rieth, "Characterizing Longitudinal Changes in the Impedance Spectra of In-Vivo Peripheral Nerve Electrodes," *Micromachines*, **9** (2018) 587.

[93] C. Wang, E. Brunton, S. Haghgooie, K. Cassells, A. Lowery, and R. Rajan, "Characteristics of Electrode Impedance and Stimulation Efficacy of a Chronic Cortical Implant Using Novel Annulus Electrodes in Rat Motor Cortex," *Journal of Neural Engineering*, **10** (2013) 046010.

[94] C. Boehler, S. Carli, L. Fadiga, T. Stieglitz, and M. Asplund, "Tutorial: Guidelines for Standardized Performance Tests for Electrodes Intended for Neural Interfaces and Bioelectronics," *Nature Protocols*, **15** (2020) 3557–3578.

[95] G. Schiavone, X. Kang, F. Fallegger, J. Gandar, G. Courtine, and S. P. Lacour, "Guidelines to Study and Develop Soft Electrode Systems for Neural Stimulation," *Neuron*, **108** (2020) 238–258.

[96] S. K. Roy and M. E. Orazem, "Error Analysis of the Impedance Response of Pem Fuel Cells," *Journal of The Electrochemical Society*, **154** (2007) B883.

[97] W. Watson and M. E. Orazem, "Eis: Measurement Model Program," (2020).

[98] R. de Levie, "Electrochemical Responses of Porous and Rough Electrodes," in *Advances in Electrochemistry and Electrochemical Engineering*, P. Delahay, editor, volume 6 (New York: Interscience, 1967) 329–397.

[99] S. Wang, J. Zhang, O. Gharbi, V. Vivier, M. Gao, and M. E. Orazem, "Electrochemical Impedance Spectroscopy," *Nature Reviews Methods Primers*, **1** (2021).

[100] K. Sridhar, J. Evers, and M. Lowery, “Nonlinear Effects at the Electrode-Tissue Interface of Deep Brain Stimulation Electrodes,” *Journal of Neural Engineering*, **21** (2024) 016024.

[101] M. Sehlmeyer, M. Makarenko, N. Schoerner, M. B. Bhavsar, T. Blank, H. J. Maier, A. Kral, H. Maier, and S. Zimmermann, “Electrical Equivalent Circuit for Analyzing the Effect of Signal Shape on Power Distribution in Cochlear Implant Electrodes and Surrounding Tissue,” *Scientific Reports*, **15** (2025).

[102] J. Maeng, B. Chakraborty, N. Geramifard, T. Kang, R. T. Rihani, A. Joshi-Imre, and S. F. Cogan, “High Charge Capacity Sputtered Iridium Oxide Neural Stimulation Electrodes Deposited Using Water Vapor As a Reactive Plasma Constituent,” *Journal of Biomedical Materials Research Part B: Applied Biomaterials*, **108** (2019) 880–891.

[103] A. Lasia, *Electrochemical Impedance Spectroscopy and Its Applications* (Springer New York, 2014).

[104] E. Barsoukov and J. R. Macdonald, editors, *Impedance Spectroscopy: Theory, Experiment, and Applications*, 3rd edition (Hoboken: Wiley, 2018).

[105] J. R. Macdonald, *Impedance Spectroscopy* (New York: John Wiley & Sons, 1987).

[106] S. Erol, M. E. Orazem, and R. P. Muller, “Influence of Overcharge and Over-Discharge on the Impedance Response of Batteries,” *Journal of Power Sources*, **270** (2014) 92–100.

[107] M. Orazem, P. Wojcik, M. Durbha, I. Frateur, and L. Garcia-Rubio, “Applicationi of Measurement Models for Interpretation of Impedance Spectra for Corrosion,” *Materials Science Forum*, **289–292** (1998) 813–828.

[108] C. You, A. Titov, B. H. Kim, and M. E. Orazem, “Impedance Measurements on Qled Devices: Analysis of High-Frequency Loop in Terms of Material Properties,” *Journal of Solid State Electrochemistry*, **24** (2020) 3083–3090.

[109] M. Gao, M. S. Hazelbaker, R. Kong, and M. E. Orazem, “Mathematical Model for the Electrochemical Impedance Response of a Continuous Glucose Monitor,” *Electrochimica Acta*, **275** (2018) 119–132.

[110] M. E. Orazem and B. Tribollet, “A Tutorial on Electrochemical Impedance Spectroscopy,” *ChemTexts*, **6** (2020) 12.

[111] B. Hirschorn, M. E. Orazem, B. Tribollet, V. Vivier, I. Frateur, and M. Musiani, “Constant-Phase-Element Behavior Caused by Resistivity Distributions in Films,” *Journal of The Electrochemical Society*, **157** (2010) C452.

[112] C. You, M. A. Zabara, M. E. Orazem, and B. Ulgut, “Application of the Kramers–Kronig Relations to Multi-Sine Electrochemical Impedance Measurements,” *Journal of The Electrochemical Society*, **167** (2020) 020515.

[113] P. Agarwal, O. C. Moghissi, M. E. Orazem, and L. H. Garc´ıa-Rubio, “Application of Measurement Models for Analysis of Impedance Spectra,” *Corrosion*, **49** (1993) 278–289.

[114] P. Agarwal, O. D. Crisalle, M. E. Orazem, and L. H. Garc´ıa-Rubio, “Measurement Models for Electrochemical Impedance Spectroscopy: 2. Determination of the Stochastic Contribution to the Error Structure,” *Journal of the Electrochemical Society*, **142** (1995) 4149–4158.

[115] J. Newman, “Resistance for Flow of Current to a Disk,” *Journal of The Electrochemical Society*, **113** (1966) 501.

[116] J. S. Newman, “Current Distribution on a Rotating Disk below the Limiting Current,” *Journal of the Electrochemical Society*, **113** (1966) 1235–1241.

[117] W. H. Smyrl and J. Newman, “Detection of Nonuniform Current Distribution on a Disk Electrode,” *Journal of The Electrochemical Society*, **119** (1972) 208.

[118] W. R. Parrish and J. Newman, “Current Distribution on a Plane Electrode below the Limiting Current,” *Journal of The Electrochemical Society*, **116** (1969) 169.

[119] W. R. Parrish and J. Newman, “Current Distributions on Plane, Parallel Electrodes in Channel Flow,” *Journal of The Electrochemical Society*, **117** (1970) 43.

[120] J. S. Newman, “Frequency Dispersion in Capacity Measurements at a Disk Electrode,” *Journal of the Electrochemical Society*, **117** (1970) 198–203.

[121] V. M.-W. Huang, V. Vivier, M. E. Orazem, N. Pebere, and B. Tribollet, “The Apparent Constant-Phase-Element Behavior of a Disk Electrode with Faradaic Reactions,” *Journal of The Electrochemical Society*, **154** (2007) C99.

[122] M. E. Orazem and B. Tribollet, *Electrochemical Impedance Spectroscopy* (Wiley, 2017).

[123] K. Nisancioglu and J. S. Newman, “The Transient Response of a Disk Electrode,” *Journal of the Electrochemical Society*, **120** (1973) 1339–1346.

[124] K. Nisancioglu and J. S. Newman, “The Short-Time Response of a Disk Electrode,” *Journal of the Electrochemical Society*, **121** (1974) 523–527.

[125] N. Spinner, “Rotating Ring Disk Electrode Fundamentals Pine Research Instrumentation Store,” (2022).

[126] M. S. Harding, B. Tribollet, V. Vivier, and M. E. Orazem, “The Influence of Homogeneous Reactions on the Impedance Response of a Rotating Disk Electrode,” *Journal of the Electrochemical Society*, **164** (2017) E3418–E3428.

[127] J. Harper, “The Motion of Bubbles and Drops through Liquids,” in *Advances in Applied Mechanics* (Elsevier, 1972) 59–129.

[128] O. Gharbi, A. Dizon, M. E. Orazem, M. T. Tran, B. Tribollet, and V. Vivier, “From Frequency Dispersion to Ohmic Impedance: A New Insight on the High-Frequency Impedance Analysis of Electrochemical Systems,” *Electrochimica Acta*, **320** (2019) 134609.

[129] Y. Wu, *Influence of Structural Properties on the Electrochemical Performance of Iridium and Ruthenium Oxide Coatings for Neural Stimulating and Recording Electrodes*, Ph.D. dissertation, University of Texas at Dallas (2025).

[130] N. G. Kunigk, M. E. Urdaneta, I. G. Malone, F. Delgado, and K. J. Otto, "Reducing Behavioral Detection Thresholds Per Electrode Via Synchronous, Spatially-Dependent Intracortical Microstimulation," *Frontiers in Neuroscience*, **16** (2022).

[131] *Accuracy Contour Plots: Measurement and Discussion*, Technical report, Warminster, PA (2016).

[132] M. E. Orazem, "Measurement Model for Analysis of Electrochemical Impedance Data," *Journal of Solid State Electrochemistry*, **28** (2023) 1273–1289.

[133] P. Agarwal, O. D. Crisalle, M. E. Orazem, and L. H. Garcia-Rubio, "Application of Measurement Models to Impedance Spectroscopy: Ii . Determination of the Stochastic Contribution to the Error Structure," *Journal of The Electrochemical Society*, **142** (1995) 4149–4158.

[134] H. A. Kramers, "Die Dispersion Und Absorption Von Ro¨ ntgenstrahlen," *Physikalishce Zeitschrift*, **30** (1929) 522–523.

[135] R. de L. Kronig, "Dispersionstheorie Im Ro¨ ntgengebeit," *Physikalishce Zeitschrift*, **30** (1929) 521–522.

[136] Y. Sakamoto, M. Ishiguso, and G. Kitigawa, *Akaike Information Criterion Statistics* (Boston: D. Reidel, 1986).

[137] S. Zhang, Y. Song, S. Lv, L. Jing, M. Wang, Y. Liu, W. Xu, P. Jiao, S. Zhang, M. Wang, J. Liu, Y. Wu, and X. Cai, "Electrode Arrays for Detecting and Modulating Deep Brain Neural Information in Primates: A Review," *Cyborg and Bionic Systems*, **6** (2025).

[138] M. E. J. Obien, K. Deligkaris, T. Bullmann, D. J. Bakkum, and U. Frey, "Revealing Neuronal Function through Microelectrode Array Recordings," *Frontiers in Neuroscience*, **8** (2015).

[139] C. Erinmwingbovo and F. La Mantia, "Estimation and Correction of Instrument Artefacts in Dynamic Impedance Spectra," *Scientific Reports*, **11** (2021).

[140] E. Warburg, "Ueber Das Verhalten Sogenannter Unpolarisirbarer Elektroden Gegen Wechselstrom," *Annalen der Physik und Chemie*, **67** (1899) 493–499.

[141] G. Brug, A. van den Eeden, M. Sluyters-Rehbach, and J. Sluyters, "The Analysis of Electrode Impedances Complicated by the Presence of a Constant Phase Element," *Journal of Electroanalytical Chemistry and Interfacial Electrochemistry*, **176** (1984) 275–295.

[142] C. L. Alexander, B. Tribollet, and M. E. Orazem, "Contribution of Surface Distributions to Constant-Phase-Element (cpe) Behavior: 1. Influence of Roughness," *Electrochimica Acta*, **173** (2015) 416–424.

[143] B. Fan, B. Wolfrum, and J. T. Robinson, “Impedance Scaling for Gold and Platinum Microelectrodes,” *Journal of Neùral Engineering*, **18** (2021) 056025.

[144] H. Wang and L. Pilon, “Accurate Simulations of Electric Double Layer Capacitance of Ultramicroelectrodes,” *The Journal of Phyṡical Chemistry C*, **115** (2011) 16711–16719.

[145] J.-B. Jorcin, M. E. Orazem, N. Pe´be`re, and B. Tribollet, “CPE Analysis by Local Electrochemical Impedance Spectroscopy,” *Electrochimica Acta*, **51** (2006) 1473–1479.

[146] S.-L. Wu, M. E. Orazem, B. Tribollet, and V. Vivier, “The Influence of Coupled Faradaic and Charging Currents on Impedance Spectroscopy,” *Electrochimica Acta*, **131** (2014) 3–12.

BIOGRAPHICAL SKETCH

Cynthia Chiamaka Eluagu (Nee Ezeh) graduated with a first-class honors Bachelor of Engineering degree in materials and metallurgical engineering from the Federal University of Technology Owerri (FUTO) Nigeria. She was awarded the best graduating student of the department of materials and metallurgical engineering, ranking in the top 1% of her class in 2018. During her undergraduate study, she became the national vice president of the National Association of Materials and Metallurgical Engineering students (NAMMES) in Nigeria, and a recipient of the Agbami Medical and Engineering Professional Scholarship (AMEPS) award which covered her tuition and accommodation throughout her entire time at FUTO.

Cynthia started her doctoral studies at the University of Florida in August 2021 and joined Professor Mark E. Orazem's research group in September 2021. Her research focused on the electrochemical analysis and interpretation of impedance spectra for microelectrodes and ultramicroelectrodes intended for neural stimulation. During her time at the University of Florida (UF), she became a member of the Electrochemical Society, Society of Women Engineers, National Society of Black Engineers, and American Institute of Chemical Engineers (AIChE). Cynthia served in many leadership positions during her studies at UF. She became the social chair of the Graduate Association of Chemical Engineers (GRACE), and lab safety manager for Orazem research group in 2022. In 2023, she served as the graduate student council representative for GRACE, a member of the UF international student council, doctoral student peer mentor for the chemical engineering department, and a mentor for three undergraduate students in chemical engineering. In 2024, she served as the President of Graduate Association of Chemical Engineers and a member of worship committee at St. Augustine Catholic Church and Student Center, Gainesville, Florida.

Cynthia received many awards during her doctoral studies. In 2021 she received the Chemical Engineering Doctoral Excellence Award, the Board of Education Fellowship, and the Petroleum Technology Development Scholarship (PTDF) from Nigeria. In 2022, she was listed among the ten finalists in the 3MT thesis competition at UF and received the Outstanding

Achievement Merit Award from UF International Center. In 2023, she received the Women in Chemical Engineering (WIC) Travel Award from AIChE, the Chemical Engineering Doctoral Peer Mentoring Award, and the Alec Curtelis Award recognizing three exceptional international graduate students who demonstrated academic achievement and leadership. In 2024, she received the first place in oral talk at the GRACE symposium from the Department of Chemical Engineering. In 2025, she received the Graduating Board of Education Fellows Award from the University of Florida Graduate School and the Award of Excellence in Leadership and Service from the Department of Chemical Engineering at UF. Cynthia interned with Intel Cooperation in summer 2024. She worked with the Atomic Layer Deposition (ALD) back-end team in Oregon. She earned her master's degree in May 2025 from UF and graduated with doctoral degree in chemical engineering from the University of Florida in December 2025.